A transportable strontium-88 optical lattice clock

Inaugural-Dissertation

zur Erlangung des Doktorgrades (Dr. rer. nat.)
der Mathematisch-Naturwissenschaftlichen Fakultät
der Heinrich-Heine-Universität Düsseldorf

vorgelegt von
Dongliang Cong
aus Shandong, China

Düsseldorf, August 2025

Aus dem Institut für Experimentalphysik
der Heinrich-Heine-Universität Düsseldorf

Gedruckt mit der Genehmigung
der Mathematisch-Naturwissenschaftlichen Fakultät
der Heinrich-Heine-Universität Düsseldorf

Referent: Prof. Stephan Schiller, Ph.D.
Koreferent: Prof. Dr. Axel Görlitz

Tag der mündlichen Prüfung: 01.12.2025

Affidavit

I declare under oath that I have compiled my dissertation independently and without any undue assistance by third parties under consideration of the "Principles for the Safeguarding of Good Scientific Practice at Heinrich-Heine-University Düsseldorf".

Ich versichere an Eides Statt, dass die Dissertation von mir selbständig und ohne unzulässige fremde Hilfe unter Beachtung der „Grundsätze zur Sicherung guter wissenschaftlicher Praxis an der Heinrich-Heine-Universität Düsseldorf“ erstellt worden ist.

Düsseldorf,

Dongliang Cong

ABSTRACT

State-of-the-art optical clocks have instabilities and systematic uncertainties better by more than two orders of magnitude than atomic clocks operating on a microwave transition frequency, which raises the discussion of the redefinition of the SI second. With the unrivaled performance, optical clocks have a wide range of potential applications, from metrology to fundamental physics, geodesy to astronomy, etc. Relativistic geodesy measurements based on frequency comparisons of optical clocks were demonstrated by several groups. In the framework of the DFG-funded research unit "Clock Metrology: A Novel Approach to TIME in Geodesy", the time comparison of optical clocks via the Atomic Clock Ensemble in Space (ACES) is proposed to demonstrate relativistic geodesy. To this end, a transportable optical clock will be integrated, operated at Geodätisches Observatorium Wettzell (GOW).

In this dissertation, a transportable one-dimensional (1-D) optical lattice clock (SOC2) based on strontium-88 neutral atoms is described, which is planned to be transported to Wettzell. The clock has a compact physics package and compact, modular-designed laser systems, which make the clock easy to operate and transport.

The noise contributions from various sources to the clock instability were analyzed in this dissertation. The instability of the SOC2 clock against the PTB stationary optical lattice clock (Sr3) is $\sim 5.7 \times 10^{-16}/\sqrt{\tau}$, where τ is the averaging time in seconds. The frequency shifts due to all relevant effects were carefully characterized. The systematic uncertainty of the clock is 6.2×10^{-17} at low atom number ($\sim$ 240), and the main contribution is from the quadratic Zeeman shift; however, at high atom number ($\sim$ 2250), the systematic uncertainty is 1.26×10^{-16} with a high contribution from the lattice AC Stark shifts.

The isotope shift between strontium-88 and -87 was measured by comparing the frequency of the SOC2 and Sr3 clocks. The isotope shift is measured to be 62 188 134.032(35) Hz, which agrees well with the recently reported values. The isotope shift is also obtained by frequency comparison with the transportable optical lattice clock (Sr4) of PTB. This dissertation also describes direct measurements of the ^{88}Sr frequency ratio with respect to the indium ion clock ($^{115}\mathrm{In}^{+}$) and the electric octupole transition ($E3$) in the ytterbium ion clock ($^{171}\mathrm{Yb}^{+}$) at PTB, which are, to our knowledge, reported for the first time.

In order to further improve clock performance, some potential optimizations of the SOC2 clock are discussed, which could be implemented to meet the project goals. The achievable uncertainty of the SOC2 clock is less than 5.4×10^{-18}, if all effects are carefully controlled. Based on the performance described above, SOC2 will be an enabling element for time transfer between GOW and Potsdam to investigate relativistic geodesy via ACES.

Contents

List of Figures

List of Tables

Chapter 1

Introduction

1.1 Optical Clock

1.1.1 SI second and atomic clock

The definition of SI (International System of Units) second has evolved rapidly over the last century [1][2][3]. It was initially defined in astronomy as the fraction 1/86400 of a mean solar day. However, the Earth's rotation rate was observed to have unpredictable variations. Thus, the definition was revised in 1960 to be based on the motion of the Earth around the Sun, which is more stable.

Thanks to the microwave technology, which was invented and improved rapidly in the early 20th century, Louis Essen and Jack Parry invented the first cesium beam clock working in the microwave regime at National Physical Laboratory (NPL, United Kingdom) in 1955, which provided a more accurate and stable frequency [4]. Therefore, in the 13th General Conference on Weights and Measures (CGPM), 1967-1968, the definition of the SI second was referenced to the frequency of the ground state hyperfine transition in the caesium-133 atom. This is a historic step: the SI second entered quantum physics from astronomy. The SI second was initially linked to the motion of the Earth in astronomy, but is now determined by the frequency in quantum physics. The Standard Model holds that atomic resonance frequencies are universal and constant in time and space.

Since the late 20th century, techniques for laser cooling and trapping have been developed and rapidly improved. The atomic clocks that operate in optical frequency regimes, known as optical clocks, have been developed. Optical clocks have more than two orders of magnitude higher stability than clocks operating at the microwave transition frequency. Although the SI second is currently defined in the microwave regime, the redefinition of the SI second using optical clocks is being discussed, and a redefinition roadmap has been launched [3][5].

Apart from the potential redefinition of the SI second, due to their unrivaled performance, optical clocks have a wide range of applications, from metrology to fundamental physics, geodesy to astronomy, etc. (see Section 1.1.4).

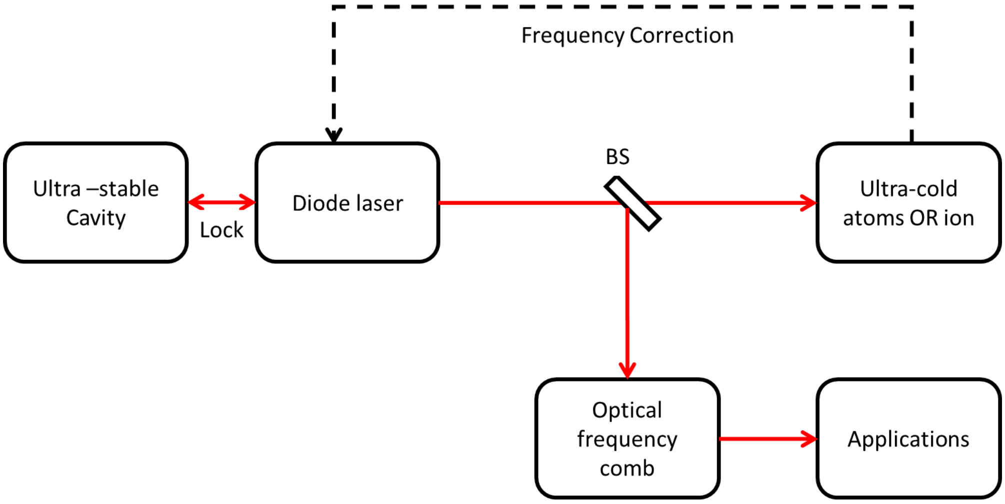

Figure 1.1: The principle of optical clocks. The clocks typically have two main parts: one periodic oscillator and one counter. For optical clocks, the ultra-narrow optical transitions of the ultra-cold neutral atoms or ions serve as the periodic oscillator and the optical frequency comb as the counter. The clock enables several applications via the comb. BS: beam splitter.

1.1.2 The principle of optical clocks

Usually, a clock comprises a periodic oscillator and a counter[1]. The microwave atomic clock utilizes a stable atomic hyperfine radio frequency (RF) transition as the oscillator and microwave counter to count time. However, in the optical clock, the electronic transition with optical frequency, called the clock transition, replaces the hyperfine RF transition as a periodic oscillator. The optical transition frequency, which is approximately hundreds of terahertz, was measured using complicated harmonic frequency chains before the invention of the optical comb. Since 1998, the frequency comb, a mode-locked femtosecond laser, has been used as a counter to measure optical transitions instead of harmonic frequency chains [6]. See Figure 1.1.

In order to excite the optical clock transition of cold atoms or ions, one ultra-narrow linewidth laser is employed as a local oscillator, which is first pre-stabilized to an ultra-stable cavity based on a spacer with ultra-low thermal expansion material, e.g., ULE (ultra-low expansion glass), crystalline silicon, sapphire, NEXCERA, and a pair of ultra-high finesse mirrors. Ultra-stable lasers typically have instabilities of $\leq 1 \times 10^{-15}$ at averaging time $1-10\,\mathrm{s}$. The best ultra-stable stationary laser worldwide, based on crystalline silicon spacer and dielectric mirror coating, has an instability of 4×10^{-17} at the averaging time $1-100\,\mathrm{s}$, operating in a cryogenic environment [7]. The instability of the best transportable ultra-stable laser worldwide, based on the ULE spacer and the crystalline mirror coating, reaches

---

[1] This dissertation only discusses passive atomic clocks.

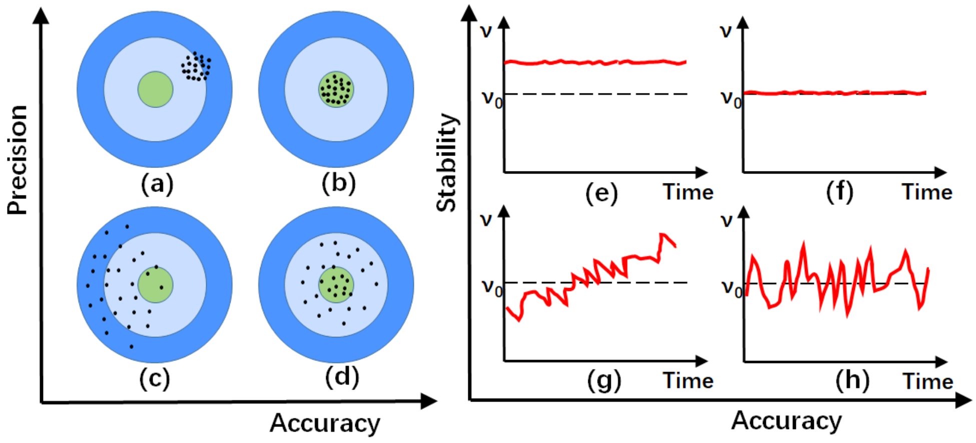

Figure 1.2: The comparison of shooting results and temporal output frequency to understand accuracy and stability properties. (a)-(d) show the shooting results with (a) precise but not accurate, (b) accurate and precise, (c) not accurate and not precise, and (d) accurate but not precise. (e)-(h) are corresponding temporal output frequency curves with (e) stable but not accurate, (f) stable and accurate, (g) not stable and not accurate, and (h) accurate but not stable. Building a highly accurate and stable clock is an ultimate goal. ν_0 is the true value of the output frequency.

1.6×10^{-16} at the averaging time $1 - 10\,\mathrm{s}$ [8].

The pre-stabilized laser light, called the clock laser, is delivered to the science chamber and probes the ultra-narrow clock transition of the ultra-cold neutral atoms or ions to have the frequency correction. The correction is usually sent to the laser via a double-pass AOM (Acousto-Optic Modulator) to keep the laser following the clock transition frequency, shown in Figure 1.1. For instance, the clock transition $(5s^2)^1S_0 \leftrightarrow (5s5p)^3P_0$ of neutral strontium-87 has a linewidth of ~1 mHz. Thus, the clock laser frequency ideally has the same linewidth as the ultra-narrow clock transition. Additionally, an optical frequency comb is employed to measure the clock laser frequency, to implement frequency comparisons with other optical clocks, or to down-convert to microwave frequency for RF applications.

The frequency oscillation sources, e.g. quartz crystal oscillators and atomic clocks, can be characterized by the following two properties: accuracy and stability. To easily understand both properties, a marksman's shooting results on a target are compared with the temporal output of a frequency oscillator [9], shown in Figure 1.2. The fewer scatterers there are, the better the stability. Ideally, developing a clock with highly accurate and stable output frequencies is the ultimate goal. However, in reality, the clock with low accuracy but high stability is acceptable if the frequency offset between the true frequency ν_0 and measured value ν is well known, shown in Figure 1.2(e).

1.1.3 The state of the art of strontium optical lattice clocks

Generally, optical clocks are divided into two groups based on the particles that provide narrow-linewidth transitions: optical lattice clocks, which use neutral atoms, and optical ion clocks, which use charged ions. After approximately two decades of development since the early 2000s, optical clocks have shown unparalleled performance, reaching the 10^{-19} regime. For example, the strontium lattice clock from Jun Ye's group at JILA recently reached a systematic uncertainty of 8×10^{-19} [10]. David Leibrandt et al. from NIST demonstrated a $^{27}\mathrm{Al}^{+}$ single-ion clock with a systematic uncertainty of 5.5×10^{-19} in 2025 [11].

Strontium optical lattice clocks with excellent performance have been set up in several national metrology laboratories and universities. Examples are JILA, NPL, LNE-SYRTE, PTB, NIM, RIKEN, USTC, NTSC, UoB, HHU, etc., as shown in Table 1.1. Most are stationary clocks for the SI second redefinition or fundamental research. Another avenue has been to develop transportable optical clocks that can be transported to various locations or laboratories to conduct frequency campaigns. PTB team implemented a trailer-based ^{87}Sr (strontium-87) transportable clock with a systematic uncertainty of 7.7×10^{-17} and used it successfully in several frequency campaigns [12][13], starting with one in Modane in France and Turin in Italy [12]. Now, the PTB team is operating their second-generation strontium transportable clock with a Pyramid MOT and a cryogenic BBR (Blackbody Radiation) shield [14], and also carried out several inter-institute frequency campaigns, for example, the ICON campaign [15]. A ^{88}Sr (strontium-88) transportable clock was built by a team from HHU, PTB, UoB, et al. with a systematic uncertainty of 2×10^{-17} in 2018 [16], which was aimed for space application. A pair of ^{87}Sr transportable clocks was developed by Katori's group at RIKEN and University of Tokyo, each with a systematic uncertainty of 5.5×10^{-18} in 2020 [17]. They were implemented in Tokyo Skytree to measure the gravitational red shift. One of them was transported to Europe to join the ICON frequency campaign [15]. Chang's team from NTSC reported on a transportable ^{87}Sr optical lattice clock aimed at space applications [18], which was already launched to the China Space Station in 2022, but is not running as a clock at the moment.

Institute	**Uncertainty**	**Instability**	**Transported**	**Reference**
PTB	2.7×10^{-18}	$2.1 \times 10^{-16}/\sqrt{\tau}$	No	[19]
	2.1×10^{-18}	$5 \times 10^{-16}/\sqrt{\tau}$ [2]	Yes	[14]
NPL	1.4×10^{-17}	$4 \times 10^{-16}/\sqrt{\tau}$ [3]	No	[15]
LNE-SYRTE	2.1×10^{-17}	$7 \times 10^{-16}/\sqrt{\tau}$ [4]	No	[20]
RIKEN & Uni. Tokyo	5.5×10^{-18}	$9 \times 10^{-16}/\sqrt{\tau}$ [5]	Yes	[17] [21]
NICT	5.4×10^{-17}	$7 \times 10^{-15}/\sqrt{\tau}$ [6]	No	[22]
NMIJ	1.1×10^{-16}	/	No	[23]
JILA	8.1×10^{-19}	/	No	[10]
NIM	7.2×10^{-18}	$1.18 \times 10^{-15}/\sqrt{\tau}$	No	[24]
NTSC	2.0×10^{-18}	$3.6 \times 10^{-16}/\sqrt{\tau}$	No	[25]
USTC	9.2×10^{-19}	$2.3 \times 10^{-16}/\sqrt{\tau}$	No	[26]
UMK	4.6×10^{-15}	/	No	[27]
HHU, UoB, PTB et al[8]	2.0×10^{-17}	$4.1 \times 10^{-16}/\sqrt{\tau}$ [7]	Yes clock laser only	[16]

Table 1.1: Latest progress of strontium optical lattice clocks. All clocks use strontium-87 (except UMK and HHU et al., which use strontium-88). Instabilities are obtained by interleaved self-comparison (unless otherwise specified). Full institute names are listed in the footnote. The averaging time τ is in seconds.

1.1.4 Applications of optical clocks

Due to their unparalleled performance, optical clocks have numerous potential practical applications. The redefinition of the seconds using optical clocks has been discussed. In

---

[2] Compared with stationary optical lattice clock at PTB

[3] Compared with RIKEN transportable clock at NPL.

[4] Compared with SrB at LNE-SYRTE

[5] Comparison between a pair of clocks

[6] The reference source is unclear.

[7] Compared with old stationary clock (Sr1, non-fuctional) at PTB.

[8] PTB: Physikalisch Technische Bundesanstalt, Braunschweig (DE); NPL: National Physical Laboratory, Teddington (UK); LNE: Laboratoire national de métrologie et d'essais, Paris (FR); SYRTE: SYstèmes de Référence Temps Espace (Observatoire de Paris), Paris (FR); RIKEN: Institute of physical and chemical research, Saitama (JPN); NICT: National Institute of Information and Communications Technology, Tokyo (JPN); NMIJ: National Metrology Institute of Japan, Tsukuba (JPN); JILA: Joint Institute for Laboratory Astrophysics, Boulder (USA); NIM: National Institute of Metrology, Beijing (CHN); NTSC: National Time Service Center, Xi'an (CHN); USTC: University of Science and Technology of China, Hefei (CHN); UMK: Uniwersytet Mikołaja Kopernika w Toruniu, Toruń (PL); HHU: Heinrich-Heine-Universität, Düsseldorf (DE); UoB: University of Birmingham, Birmingham (UK).

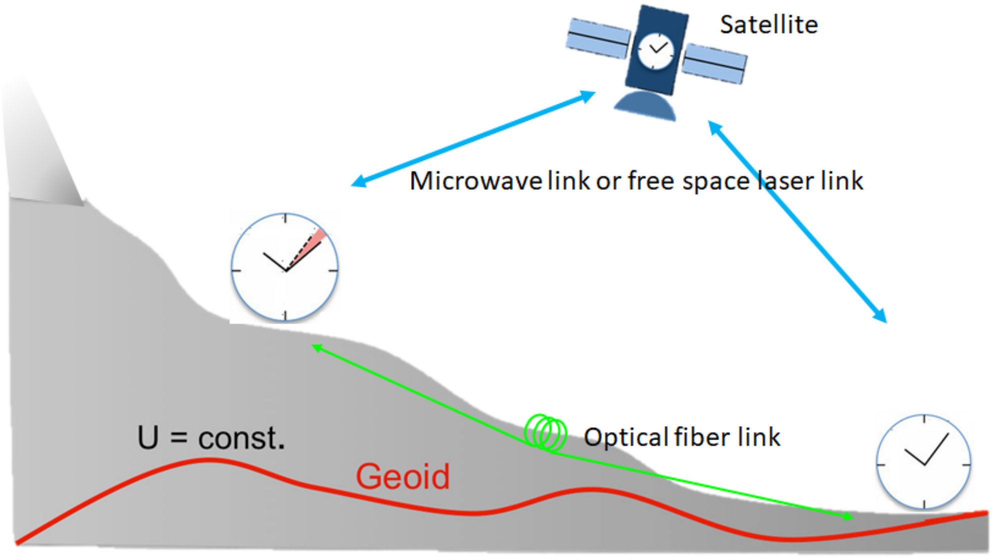

Figure 1.3: Clock application in relativistic geodesy and general relativity, adapted from Figure 1.4 in Ref. [29]. The frequency or time comparison can be implemented via optical fiber or satellite links.

2016, Consultative Committee for Time and Frequency (CCTF) established the first version of a roadmap to achieve this goal. A dedicated CCTF task force updated the roadmap in 2020 [3]. According to the roadmap, the redefinition is expected to be implemented by 2030. Meanwhile, optical clocks are already used to calibrate the TAI (International Atomic Time) scale [28].

Relativistic geodesy and general relativity are also studied using optical clocks, as shown in Figure 1.3. For example, the PTB group implemented long-distance chronometric leveling using a ^{87}Sr transportable optical clock, with the uncertainty of the geopotential difference equivalent to an height uncertainty of 27 cm [13]. A test of general relativity was conducted by the RIKEN group using a pair of transportable optical lattice clocks seperated by a height difference of 450 m [17]. An international frequency comparison using state-of-the-art transportable optical clocks from Japan and Europe determined geopotential height differences between NPL and PTB at the 4 cm level [15].

Recently, the constraints on the coupling of ultralight bosonic dark matter to photons are tightened by long-term comparisons of ^{87}Sr optical lattice clock and ^{171}Yb^{+} ion clock which operate at electric-octupole ($E3$) and electric-quadrupole ($E2$) transitions [30].

Apart from the above applications, optical clocks could also be applied to GNSS systems, astronomy, space exploration, testing quantum mechanics, and other fields.

Items	Research topics
Project 1	Galileo pseudolite calibration target used to consolidate time between space geodetic techniques
Project 2	Accurate active (and passive) time transfer from ground to ground via satellite link
Project 3	Integration, operation, and performance optimization of the optical clock "SOC2" at Wettzell and test of fundamental physics
Project 4	General Relativity and coherent time definition
Project 5	Determination of physical heights via time transfer
Project 6	Time as observable in integrated ground- and space-based GNSS analysis
Project 7	The application of time in closure as a novel strategy towards error-free space geodetic observations
Project 8	Specifying the atmospheric delay by means of accurate measurements of the atmospheric state
Project 9	Novel clock technologies for combination on ground and in space: operation and simulation
Project 10	Common treatment of clock ties and atmospheric ties in space geodesy

Table 1.2: Projects in the research unit of Clock Metrology [31]

1.2 Clock Metrology (FOR 5456)

FOR 5456 is a DFG-funded research unit "Clock Metrology: A Novel Approach to TIME in Geodesy" (https://clockmetrology.de/en/). This research unit was launched in 2023 and is coordinated by Prof. U. Schreiber (Geodätisches Observatorium Wettzell, Technische Universität München), Prof. S. Schiller (Heinrich-Heine-Universität Düsseldorf), and Dr. M. Seitz (Deutsches Geodätisches Forschungsinstitut, Technische Universität München). This unit aims to develop a new method for a highly accurate and long-term stable realization of geodetic reference systems by linking all space geodetic techniques to a common time system [31]. Ten projects operate under this research unit, listed in Table 1.2.

1.2.1 Introduction of Project 3

Background [32]

Project 3 is titled "Integration, operation, and performance optimization of the optical clock "SOC2" at Wettzell and test of fundamental physics". Prof. S. Schiller from Heinrich-Heine-Universität Düsseldorf is the principal investigator (PI) of this project.

The goal is to introduce the highly accurate optical clock 'SOC2' to the Geodätisches

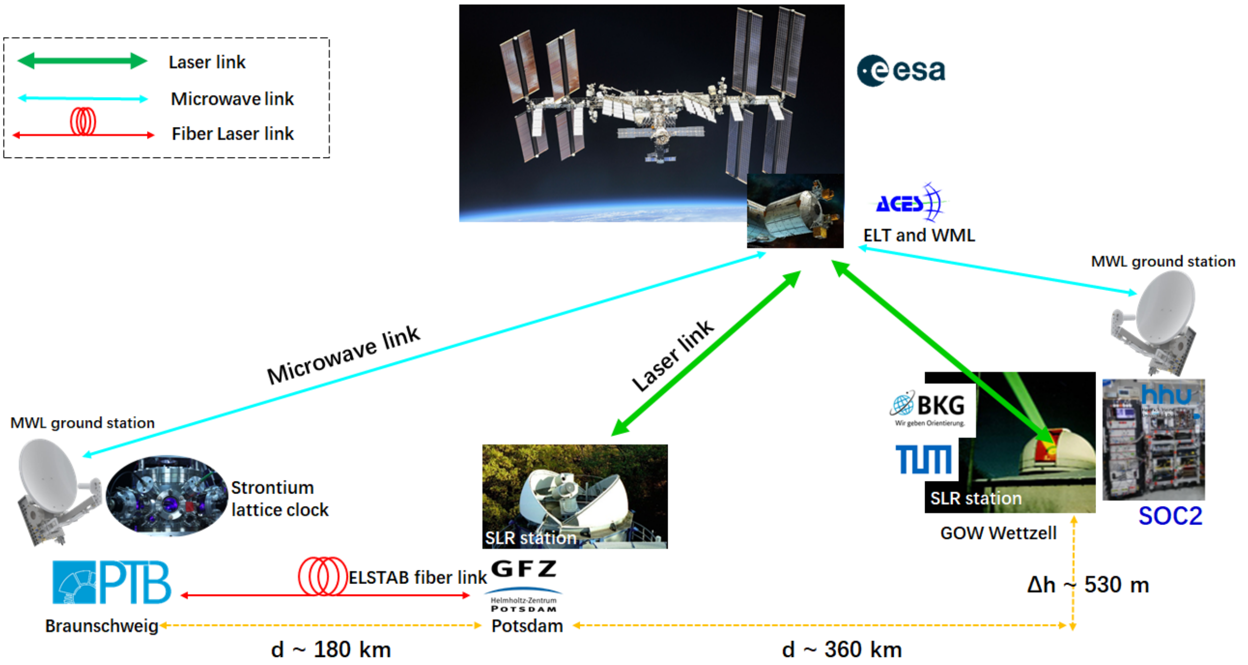

Figure 1.4: Accurate optical free-space and microwave time transfers via ACES. The SOC2 lattice clock will be relocated to GOW (Wettzell) in 2025. See the text for details. ACES: Atomic Clock Ensemble in Space; SLR: Satellite Laser Ranging; ELT: European Laser Time transfer link; MWL: MicroWave Link; ELSTAB: ELectronically STABilized fiber optic time and frequency distribution system.

Observatorium Wettzell (GOW). The initial phase will improve clock's performance, reliability, and robustness over two years. Subsequently, the clock will be relocated to GOW and integrated with the Satellite Laser Ranging (SLR) system to implement optical time transfer to ACES (Atomic Clock Ensemble in Space) via the European Laser Time Transfer (ELT) link. It will also be integrated with the GOW timing system and the ACES microwave link. This will be the first time an optical clock is available to a major geodetic observatory. With these facilities, this project will demonstrate accurate time transfer applications in geodesy and relativistic geodesy through repeated comparisons with the optical clocks at PTB and validating the universality of gravitational time dilation (GTD) (see Figure 1.4).

Scientific objectives [32]

This project will contribute to relativistic geodesy via time transfer (see Figure 1.4). At GOW, we will use an optical clock to apply the ELT technique for comparisons with other optical clocks. We will compare in common-view with PTB clocks via Potsdam and the ELSTAB link (Potsdam–Braunschweig), and in non-common-view with more distant European clocks and clocks on other continents (e.g., Tokyo, Washington, D.C.), provided that appropriate SLR ground stations with ELT electronics are available by 2025. In addition, GOW will host an ESA (European Space Agency)-provided microwave link (MWL) terminal, allowing us to verify the consistency of results obtained using fundamentally different time and frequency transfer methods–optical and microwave.

This project will contribute to measurements of gravitational time dilation in the fields of Earth, Moon, and Sun. This consists of three main parts:

- The GTD in the gravitational field of the Earth will be investigated by comparisons between ground clocks, e.g., the SOC2 clock at GOW and stationary clocks of metrology labs (e.g., PTB), and the cold Cs atom clock on board the ISS (International Space Station) during the ACES mission.
- The GTD due to the Sun and the Moon will be tested by the comparison of the SOC2 clock at GOW with clocks on other continents to determine whether the GTD from the Sun and the Moon follows the same law as Earth's GTD. By long measurement intervals and repeat measurements, the obtained frequency comparison data can then be analyzed for the presence of a daily and near-daily modulation. A non-observation of modulations would allow us to set limits for a hypothetical dependence of GTD on the nuclear composition of the body (Moon/Sun/Earth) generateing the GTD.
- Closure tests of Earth's GTD will be performed by simultaneously comparing three or more different ground stations. According to the theory, the sum of the fractional frequency differences caused by Einstein's gravitational time dilation must sum to zero, since the sum of the gravitational potential differences is zero.

Technical requirements of the SOC2 clock [32]

1. Establish systematic uncertainty $\leq 1\times10^{-17}$, instability $\leq 1\times10^{-14}$ at 100 s, $\leq 1\times10^{-16}$ at 1 h, $\leq 1\times10^{-17}$ at 2 d integration time.

   The links (ELT, ELSTAB, MWL) have timing errors of a few picoseconds (ps) after 100 s of integration time (contact time with ISS). Assuming that this is the only limitation of the timing errors, SOC2 must maintain an instability of less than 1×10^{-14} at 100 s. After 1 hour (approximately half the orbital period of ISS), the timing error of the links remains within a few ps. Therefore, SOC2 should achieve an instability of less than 1×10^{-16} at 1 hour. Given the necessity for repeated clock comparisons over at least a few days to allow an overall uncertainty of 1×10^{-17}, SOC2 is expected to achieve an instability of less than 1×10^{-17} at two days. In conjunction with this, the uncertainty of SOC2 shall be less than 1×10^{-17} at all time scales.

2. Achieve nearly uninterrupted operation for at least 1 week.

   More precisely, our preliminary analysis indicates that the 8 ps goal accuracy for a 1 week ($\simeq 10^6$ s) long time transfer via ELT is reachable: (1) if the clock laser is nearly always locked (2-second loss of lock at most every quarter-hour) and stable at 1×10^{-15} level, we can tolerate a $T_{\text{loss}} = 2\,\text{s}$ loss of atomic signal quite frequently (e.g., every 10 s). (2) But if T_{loss} is larger, the tolerable mean time between loss events will increase as T_{loss}^2. However, as we also want to be able to make comparisons via MWL, the requirement is more stringent. In order to take advantage of the MWL performance (better than ELT over day-long intervals), we aim to reach 1 ps uncertainty over 1 day. Laser lock loss is tolerable once every 2 hours if the dead time is 2 s.

   We need to ensure almost continuous clock operation for periods of up to 1 week, several times over a 2-year period, during clear weather. This will allow ELT time-transfer experiments with PTB and other stations worldwide via ACES.

3. Establish a robust optical-to-microwave frequency conversion at GOW, which will be the reference for GOW's time-and-frequency distribution system [33].

1.2.2 Outline of the thesis

In this dissertation, I will discuss the optimization, performance analysis, and potential improvements of the SOC2 clock, which will be transported and installed in Wettzell within the FOR 5456 framework. Chapter 2 will cover the principle of optical lattice clocks, specifically the strontium lattice clock. Chapter 3 will detail all components of the SOC2 apparatus, experimental methods, and results. Chapter 4 will analyze the contributions to clock instability from different noise sources, such as magnetic bias fields, probe light power, quantum projection noise (QPN), Dick effect, and others. Chapter 5 will evaluate the systematic uncertainty of the clock and present isotop shifts and frequency ratios relative to other atomic species, while Chapter 6 will discuss the potential improvements to the SOC2 clock. The conclusion will be presented in Chapter 7.

Chapter 2

Strontium Optical Lattice Clock

2.1 Atoms with two valence electrons and strontium atom

The alkaline-earth(-like) atoms

The alkaline-earth(-like) atoms have two valence electrons in the outer shell, e.g., beryllium (Be), magnesium (Mg), calcium (Ca), strontium (Sr), barium (Ba), radium (Ra), mercury (Hg), cadmium (Cd), and ytterbium (Yb). Consequently, the total spin could be zero, corresponding to a singlet state, or one, corresponding to a triplet state. According to the selection rule for electric dipole transition ($E1$), transitions between the singlet and triplet states are forbidden. For example, transitions from the ground state ${}^1S_0$ to the excited state ${}^3P_1$ are forbidden by spin conservation ($\Delta S = 0$). Another example is transitions from the ground state ${}^1S_0$ to the excited state ${}^3P_0$, which are doubly forbidden by spin conservation ($\Delta S = 0$) and total angular momentum requirements ($J = 0 \nRightarrow J = 0$). Nevertheless, the 'forbidden' does not mean thoroughly impossible. The $E1$ transitions of ${}^1S_0$ to ${}^3P_1$ are weakly allowed via spin-orbit interaction between ${}^1P_1$ and ${}^3P_1$. These transitions are called *intercombination transitions* and are used in the second-stage cooling of alkaline-earth(-like) atoms (see next section). The doubly forbidden transitions from ${}^1S_0$ to ${}^3P_0$ are partially allowed through nuclear and spin-orbit mixing in fermionic isotope atoms, providing ultra-narrow spectrum linewidth ($\sim$mHz), typically used for optical clocks—hence called *clock transition*. Thanks to this property, alkaline-earth(-like) atoms are widely utilized in optical clocks, atomic interferometers, dark matter searches, and studies of new physics, among other applications. The properties of these two types of 'forbidden' transitions are listed in Table 2.1.

	Intercombination transition $^1S_0$ to $^3P_1$		**Clock transition** $^1S_0$ to $^3P_0$		Reference
Elements	**Wavelength**	**Linewidth**	**Wavelength**	**Linewidth**	
^{24}Mg	457.1 nm	36 Hz	458 nm	-	[34]
^{40}Ca	657 nm	374 Hz	-	- [9]	[35]
^{87}Sr	689.2585 nm	7.5 kHz	698.4457 nm	1.35(3) mHz	[36]
^{88}Sr	689.2585 nm	7.5 kHz	698.4457 nm	$5.5 \times 10^{-12}/\mathrm{s}$	[37][38]
^{199}Hg	253.7 nm	1.3 MHz	265.6 nm	100 mHz	[39]
^{111}Cd	326 nm	66.6 kHz	332 nm	7.0 mHz	[40]
^{171}Yb	556 nm	182.4 kHz	578 nm	10 mHz	[41]

Table 2.1: The properties of the transitions between the singlet and triplet states of the alkaline-earth(-like) atoms, commonly used to build optical clocks.

Strontium atom

Strontium is one of the favored elements for building optical lattice clocks (see Chapter 1). Most major national metrology institutes worldwide are developing strontium optical lattice clocks. The reasons are: 1) Due to its two valence electrons, strontium has a transition with an ultra-narrow natural linewidth as its clock transition, and a laser system for this transition (≈698 nm) is readily available. 2) All the lasers used for cooling and trapping strontium atoms operate at visible-light wavelengths and can be easily constructed using external cavity diode lasers.

There are four stable and naturally existing isotopes: ^{84}Sr, ^{86}Sr, ^{87}Sr, ^{88}Sr. However, they have different natural abundances, shown in Table 2.2. Since ^{88}Sr has the highest natural abundance (∼82.58 %), it can provide a high atomic flux for experiments. Due to the lack of nuclear spin ($I = 0$), there is no hyperfine structure for the ^{88}Sr atoms. Thus, laser cooling and trapping for the ^{88}Sr atoms is straightforward and robust. The ^{88}Sr atoms are also insensitive to vector and tensor light shifts. Therefore, the ^{88}Sr atom is an excellent choice for optical clocks due to its simplicity and robustness. Nevertheless, ^{88}Sr optical lattice clocks have two drawbacks: 1) The clock transition $^1S_0 \leftrightarrow {}^3P_0$ cannot be directly probed, and the lifetime of $^3P_0$ is approximately 5800 years due to the $E1$ transition being doubly forbidden and lacking nuclear-spin-orbit interaction. To excite the clock transition, auxiliary techniques are required, such as electromagnetically induced transparency (EIT), magnetic-field-induced spectroscopy, or three-photon excitations (see Section 2.4). However, these techniques induce additional effects, including high probe light shifts and quadratic

---

[9] The intercombination transition $^1S_0$ to $^3P_1$ is used as clock transition in ^{40}Ca.

Isotope	Atomic Mass	Natural Abundance	Spin
^{84}Sr	83.913 425	0.56(1)%	0
^{86}Sr	85.909 260	9.86(1)%	0
^{87}Sr	86.908 877	7.00(1)%	9/2
^{88}Sr	87.905 612	82.58(1)%	0

Table 2.2: Properties of the stable and natural isotopes of stontium [42].

Zeeman shifts from magnetic-field-induced spectroscopy (see Chapter 5). 2) ^{88}Sr optical lattice clocks usually suffer from high collision shifts due to *s-wave* collisions between bosonic atoms. Although ^{88}Sr has these limitations, its simplicity, robustness, and transportability make it ideal for developing transportable ^{88}Sr optical lattice clocks. New techniques can also mitigate these drawbacks (see Chapter 6).

2.2 Laser cooling and trapping of strontium-88 atoms

Theory of laser cooling and trapping

The laser cooling and trapping technique was invented in the late 1970s and is a powerful tool for high-resolution spectroscopy [43][44][45]. Doppler cooling, a widely used laser cooling technique, relies on the Doppler effect: an atom moving with velocity $\overrightarrow{v_i}$ in the ground state absorbs a photon with wave vector $\overrightarrow{k}$ from a counterpropagating laser, exciting it to an excited state via stimulated absorption. The atom then spontaneously decays to the ground state through spontaneous emission. Since the atom absorbs photons from a specific direction but emits photons randomly, momentum conservation dictates that the atom experiences a net force opposing its motion (see Eqs. 2.1 and 2.2).

$$m\overrightarrow{v_i} + n \cdot \hbar \overrightarrow{k} = m\overrightarrow{v_f} \tag{2.1}$$

$$mv_i - n\hbar k = mv_f \tag{2.2}$$

where m is the atom mass; $\hbar$ is the reduced Planck constant; $\overrightarrow{v_f}$ is the final velocity of the atom after n times absorption and spontaneous cycles. Eq. 2.2 applies only for counter-propagating laser beams relative to atomic motion. However, this technique provides only a scattering force and cannot confine atoms. Typically, magnetic fields are combined with optical fields to cool and trap cold atoms, such as Zeeman slowers, magneto-optical trap (MOT).

Zeeman slowers are powerful tool to slow atoms from typically $\sim 400\,\mathrm{m/s}$ to a few m/s. They are commonly used after the atomic oven which provides a hot atom beam by heating to ∼ 450 °C for strontium atoms. Several methods exist for using Zeeman slowers, but here we consider using a fixed-frequency laser and a non-uniform magnetic field to maintain atomic resonance with the laser, thereby slowing atoms to the target velocity. The relation among the atomic transition frequency, the laser frequency, the magnetic field, and the atom velocity is expressed as

$$\omega_0 = \omega_L + kv(z) - (g_e M_e - g_g M_g)\mu_B B(z)/\hbar \tag{2.3}$$

where ω_0 is the unperturbed transition frequency between the ground state and the excited state, ω_L is the counterpropagating laser frequency, $v(z)$ is the atom velocity along atomic beam axis z, $g_{e,g}$ is the Landé g-factor, $M_{e,g}$ is the magnetic quantum number (the subscripts g and e denote ground and excited states), μ_B is the Bohr magneton and $B(z)$ is the position-dependent magnetic field along z axis. The second term on the right-hand side represents the Doppler shift, and the third term denotes the Zeeman shift due to the magnetic field.

A *Magneto-Optical Trap (MOT)* consists of three orthogonal pairs of σ^+- σ^- laser beams with circular polarization and a pair of magnetic field coils with anti-Helmholtz configuration (see Figure 2.1(a)). To explain the MOT mechanism, consider a transition from total angular momentum $J = 0$ to $J = 1$. The excited state $J = 1$ splits into three sub-levels with $M_J = 0, \pm 1$ due to the Zeeman effect. Since $J = 0$, the ground state has a single sub-level ($J = 0$, $M_J = 0$). Atoms resonate with counterpropagating σ^+ (or σ^-) laser beams via $J = 0$, $M_J = 0 \leftrightarrow J = 1$, $M_J = +1$ (or $J = 0$, $M_J = 0 \leftrightarrow J = 1$, $M_J = -1$) transitions. Each atom experiences a cooling force and a position-dependent restoring force, trapping it at the MOT center [46]:

$$F_{MOT} = -\alpha v - \frac{\alpha\beta}{k} z \tag{2.4}$$

where

$$\alpha = 4\hbar k^2 \frac{I}{I_{sat}} \frac{-2\delta/\Gamma}{[1 + (2\delta/\Gamma)^2]^2} \tag{2.5}$$

$$\beta = \frac{g_J \mu_B}{\hbar} \frac{dB}{dz} \tag{2.6}$$

Here, I_{sat} and I are the saturation and laser intensities, respectively. δ is the frequency detuning from resonance ($\delta = \omega_L - \omega_0 + kv$). Γ is the natural linewidth of the atomic transition. g_J is the Landé g-factor. The first term on the right-hand side in Eq. 2.4 is a damping force (α is the damping coefficient) due to the Doppler shift. The second term is a restoring force with spring constant $\alpha\beta/k$ from the Zeeman effect. Thus, the MOT cools and traps atoms at the center. It can cool and trap strontium atoms to a few μK after two-stage MOTs, as detailed later.

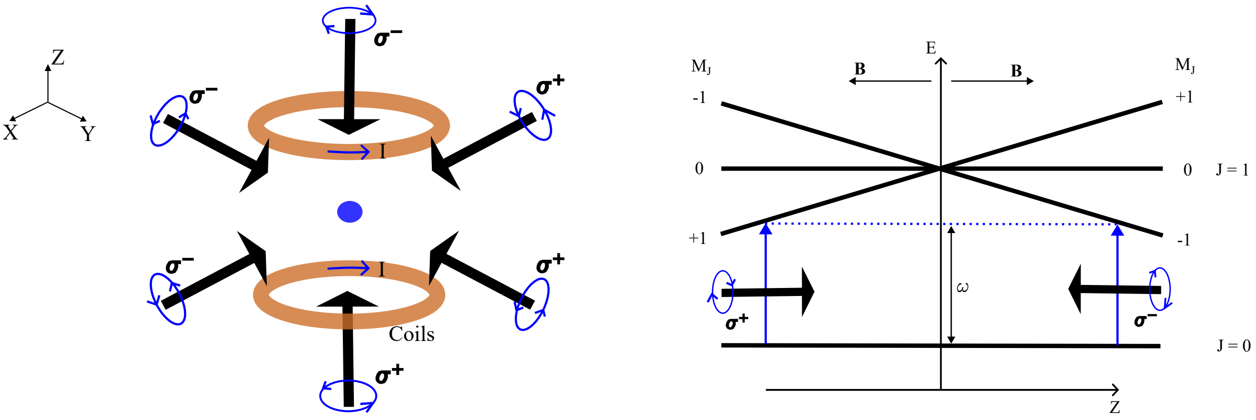

(a) (b)

Figure 2.1: Magneto-Optical Trap (MOT). (a) The configuration of 3-D MOT. (b) The mechanism of the MOT. More details in the text.

Doppler cooling cannot cool atoms below the *Doppler limit*, where equilibrium between cooling and heating mechanisms sets the minimum temperature [46]:

$$k_B T_D = \frac{\hbar\Gamma}{2} \tag{2.7}$$

where T_D is the Doppler limit and k_B is the Boltzmann constant. For strontium atoms, the Doppler limits of the cooling transitions are listed in Table 2.3.

When an atom emits (or absorbs) a single photon, the atom loses (or gains) momentum $\hbar k$ due to momentum conservation, which sets a laser cooling limit, the *recoil limit*.

$$k_B T_r = \frac{(\hbar k)^2}{m} \tag{2.8}$$

where T_r is the recoil limit temperature. For the strontium atoms, the recoil limits of the cooling transitions are shown in Table 2.3.

First stage cooling and trapping of strontium atoms

The $5s^2\,{}^1S_0 \leftrightarrow 5s5p\,{}^1P_1$ transition in the strontium atoms has 5 ns lifetime (corresponding to 32 MHz of linewidth), and a wavelength of 461 nm. Its Doppler limit temperature is 768 µK and the recoil limit is 1.03 µK (see Table 2.3). These properties make it suitable for laser cooling and trapping. We use it for the first-stage cooling and trapping, known as a blue MOT.

There is a decay channel from $5s5p\,{}^1P_1$ state to $5s5d\,{}^1D_2$ state, then atoms decay to $5s5p\,{}^3P_1$ and $5s5p\,{}^3P_2$ states via $5s5d\,{}^1D_2$ state. Atoms in the $5s5p\,{}^3P_1$ state (lifetime of 21 µs) can spontaneously decay to the ground state $5s^2\,{}^1S_0$, returning to the cooling cycle. However,

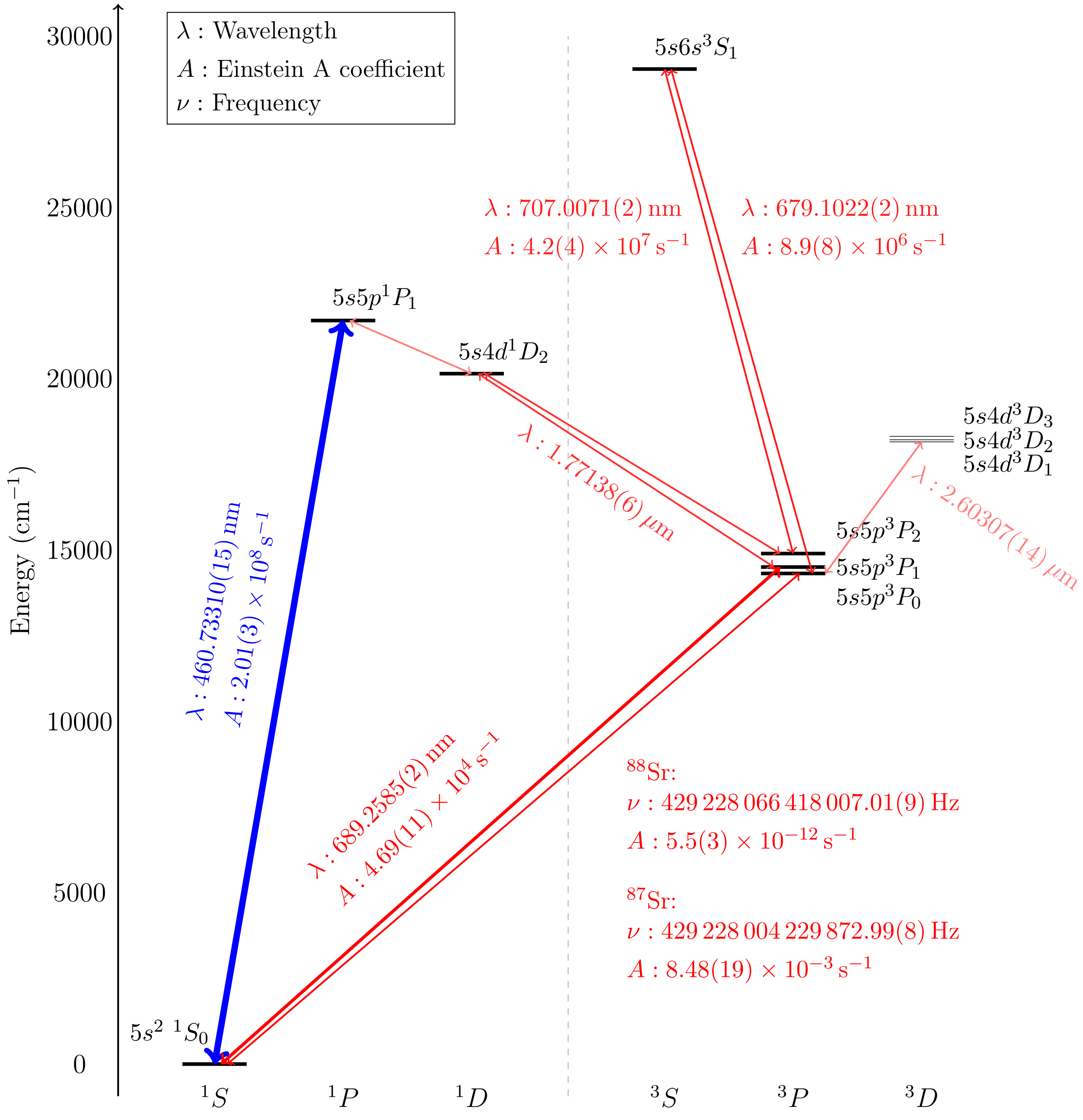

Figure 2.2: The relevant energy levels for strontium optical lattice clock, data from [3] [36] [38] [42].

	First Stage Cooling and Trapping	Second Stage Cooling and Trapping
Transition	$5s^2\,{}^1S_0 \leftrightarrow 5s5p\,{}^1P_1$	$5s^2\,{}^1S_0 \leftrightarrow 5s5p\,{}^3P_1$
Wavelength λ	460.733 10(15) nm	689.2585(2) nm
Einstein A coefficient	$2.01(3) \times 10^8\,\mathrm{s}^{-1}$	$4.69(11) \times 10^4\,\mathrm{s}^{-1}$
Lifetime τ	5.0(1) ns	21.3(5) µs
Linewidth $\Gamma/2\pi$	32.0(5) MHz	7.5(2) kHz
Saturation intensity I_{sat}	$42.8(6)\,\mathrm{mW/cm^2}$	$2.98(7)\,\mathrm{\mu W/cm^2}$
Doppler limit $T_{Doppler}$	768(11) µK	179(4) nK
Recoil limit T_{recoil}	1.03 µK	0.46 µK
Maximum acceleration a_{max}	$9.9(1) \times 10^5\,\mathrm{m/s^2}$	$154(4)\,\mathrm{m/s^2}$

Table 2.3: The cooling transition parameters for two-stage MOTs. The data in this table is sourced from or based on [42].

atoms in the $5s5p\,{}^3P_2$ state (lifetime of 520 s) cannot spontaneously decay to the ground state $5s^2\,{}^1S_0$ within typical clock cycle times (∼ seconds) [47]. To pump the atoms from this dark state back to the cooling cycle, we apply 707 nm and 679 nm lasers corresponding to $5s5p\,{}^3P_2 \leftrightarrow 5s6s\,{}^3S_1$ and $5s5p\,{}^3P_0 \leftrightarrow 5s6s\,{}^3S_1$ transitions, respectively. These lasers repump atoms back to the cooling cycle via $5s5p\,{}^3P_1$ state. Ultimately, the atoms can be cooled to ∼1-2 mK in the blue MOT.

Second stage cooling and trapping of strontium atoms

For the second stage cooling and trapping, we use the intercombination transition $5s^2\,{}^1S_0 \leftrightarrow 5s5p\,{}^3P_1$ which has 21 µs of lifetime, corresponding to 7.5 kHz of linewidth and wavelength at 689 nm. Its Doppler limit temperature is 179 nK, and the recoil limit temperature is 0.46 µK (see Table 2.3). These properties make it suitable for laser cooling and trapping. We use it for the second stage cooling and trapping, known as a red MOT.

After the first cooling stage, atoms have a temperature of approximately a few mK. To cover atoms with a range of velocities, the red MOT beam is modulated to broaden its laser linewidth (known as broadband cooling). The atoms are then cooled to approximately 100 µK. Subsequently, the modulation is turned off, and the red MOT transitions to single-frequency cooling and trapping to obtain even colder atoms at a few µK, called a single-frequency MOT.

Other cooling schemes

For the SOC2 setup, the repumping scheme with $5s5p\,{}^3P_2 \leftrightarrow 5s6s\,{}^3S_1$ (707 nm) and $5s5p\,{}^3P_0 \leftrightarrow 5s6s\,{}^3S_1$ (679 nm) transitions is applied to pump atoms out of the dark states, since the diode lasers at these wavelengths are readily available. Besides this scheme, single-repumping schemes through the $^3D_2$ states are implemented in other groups [48][49]. The $5s5p\,^3P_2 \leftrightarrow 5s4d\,^3D_2$ transition is addressed by 3.0 µm laser and atoms decay into the $5s5p\,^3P_1$ state to ultimately reach the ground state $5s^2\,^1S_0$. Similarly, $5s5d\,^3D_2$ and $5s6d\,^3D_2$ can be used, though with different laser wavelengths (497 nm and 403 nm, respectively). Recently, repumping has also been demonstrated via the $5s5p\,^3P_2 \leftrightarrow 5p^2\,^3P_2$ (481 nm) transition [50].

In addition to the two-stage MOTs (blue and red MOTs) mentioned above, which are applied in the SOC2 apparatus, different-colour MOTs have also been proposed and implemented in other groups, for example, infrared MOT [51][52] and green MOT [52]. Hobson et al. [51] conducted an infrared MOT operation on $5s5p\,^3P_2 \leftrightarrow 5s4d\,^3D_3$ transition (2.9 µm) and directly transferred the atomic cloud from the blue MOT to the infrared MOT, cooling it to a final temperature of 6 µK. Akatsuka et al. [52] implemented three-stage MOTs using $5s^2\,^1S_0 \leftrightarrow 5s5p\,^1P_1$ (461 nm, blue MOT), $5s5p\,^3P_2 \leftrightarrow 5s5d\,^3D_3$ transition (496 nm, green MOT) and $5s5p\,^3P_2 \leftrightarrow 5s4d\,^3D_3$ transition (2.9 µm, infrared MOT), achieving a cold atomic cloud at a temperature of 2.5(2) µK. Both groups used ^{87}Sr atoms to demonstrate the MOT schemes.

2.3 Optical lattice and magic wavelength

2.3.1 Introduction of the optical lattice: Geometry and trap properties

After the two stages of cooling and trapping of the strontium atoms, the cold atoms are loaded into an optical lattice. The optical lattice is a periodic optical potential composed of a pair of overlapping counter-propagating beams, which can easily produced by a single beam with its retro-reflection beam [53][54]. The electric fields for these beams are

$$E_0 \sin(kz - \omega t + \phi_1) \tag{2.9}$$

and

$$E_0 \sin(kz + \omega t - \phi_2) \tag{2.10}$$

where E_0 is the electric field amplitude. The resulting electric field for the optical lattice is

$$E(z,t) = 2E_0 \sin(kz - \Phi) \cos(\omega t - \varphi) \tag{2.11}$$

where $\Phi = (\phi_2 - \phi_1)/2$ and $\varphi = (\phi_1 + \phi_2)/2$. If the origin phase is chosen such that $\Phi = \pi/2$, the time-averaged periodic potential is

$$\begin{aligned} U(z) &= -U_0 \cos^2(kz) \\ &= -\frac{\alpha(\omega)}{2}(2|E_0|)^2 \cos^2(kz) \\ &= -4\alpha(\omega)\frac{I_0}{c\varepsilon_0}\cos^2(kz) \end{aligned} \tag{2.12}$$

where U_0 is the amplitude of the periodic potential, $\alpha(\omega)$ is the polarizability, $I_0 = c\varepsilon_0(2|E_0|)^2/2$ is the intensity corresponding to E_0, c is the speed of light in vacuum, and ε_0 is the permittivity of free space.

2.3.2 Energy band structure and sideband spectroscopy in the optical lattice

Bloch theorem

The Bloch theorem is a powerful tool for studying a quantum particle in a periodic potential [55]. In this theorem, the wavefunction of the particle in a 1-D lattice can be expressed as

$$\psi_q(z) = u_q(z)e^{iqz} \tag{2.13}$$

where u_q is periodic over the lattice in real space, and q is the quasi-momentum belonging to the reciprocal lattice.

Since it is periodic over the lattice with period $\lambda_L/2$ (where λ_L is lattice laser wavelength), u_q can be expanded into a Fourier series [55]:

$$\begin{aligned} u_q(z) &= \sum_m c_m^{(q)} e^{im\frac{4\pi}{\lambda_L}z} \\ &= \sum_m c_m^{(q)} e^{im2kz} \end{aligned} \tag{2.14}$$

thus the wavefunction becomes

$$\psi_q(z) = \sum_m c_m^{(q)} e^{i(q+m2k)z} \tag{2.15}$$

which is a series of plane waves with momenta $\hbar(q + m2k)$, $m \in \mathbb{Z}$.

The Schrödinger equation for $\psi_q(z)$ is

$$\left[\frac{\hat{p}^2}{2M} + U(\hat{z})\right] \psi_q(z) = E(q)\psi_q(z) \tag{2.16}$$

where $\hat{p}$ is the momentum operator $\hat{p} = -i\hbar\frac{d}{dz}$, $\hat{z}$ is the position operator, M is the particle mass, and $E(q)$ is the eigenenergy of $\psi_q(z)$. The Schrödinger equation can be rewritten without dimensions:

$$\left[-\frac{d^2}{dz_k^2} - u_0 \cos^2(z_k)\right] \psi_q(z_k) = \epsilon(q)\psi_q(z_k) \tag{2.17}$$

where all quantities are dimensionless: the position $z_k = kz$, the lattice depth $u_0 = U_0/E_r$, and the eigenenergy $\epsilon(q) = E(q)/E_r$. E_r is the recoil energy corresponding to the lattice laser.

Using the wavefunction in Eq. 2.15, the Schödinger equation Eq. 2.17 can be numerically solved; the spectrum of the eigenenergies $\epsilon_n(q) = E_n(q)/E_r$ is shown in Figure 2.3 with different lattice potentials. The above description is in the first Brillouin zone $q \in [-k, k]$. The energy interval spanned by $E_n(q)$ for q in the first Brillouin zone is called the n^{th} energy band.

Energy bands

The energy spectrum is the usual parabola folded within the first Brillouin zone for a free particle. In the shallow trap potential, $U_0 \lesssim E_r$, the energy bands are close to that of a free particle. However, in the deep lattice, the energy bands are almost independent of q, and the energy spectrum resembles that of a harmonic oscillator due to the strong confinement.

$$E_n(q) \simeq (n + 1/2)\hbar\omega_0 \tag{2.18}$$

where ω_0 is the harmonic frequency along the z axis.

$$\omega_0 = \sqrt{\frac{2U_0k^2}{M}} \tag{2.19}$$

For the intermediate lattice depth, e.g., 25 E_r, the energy bands are close to the harmonic energy for deeply bound particles; however, unbound particles are close to the free particles. Figure 2.3 shows the band structure of the lattice at different trap potentials. Our optical clock typically operates at $U_0 \gg E_r$; thus, the harmonic oscillator approximation is valid for deeply bound bands.

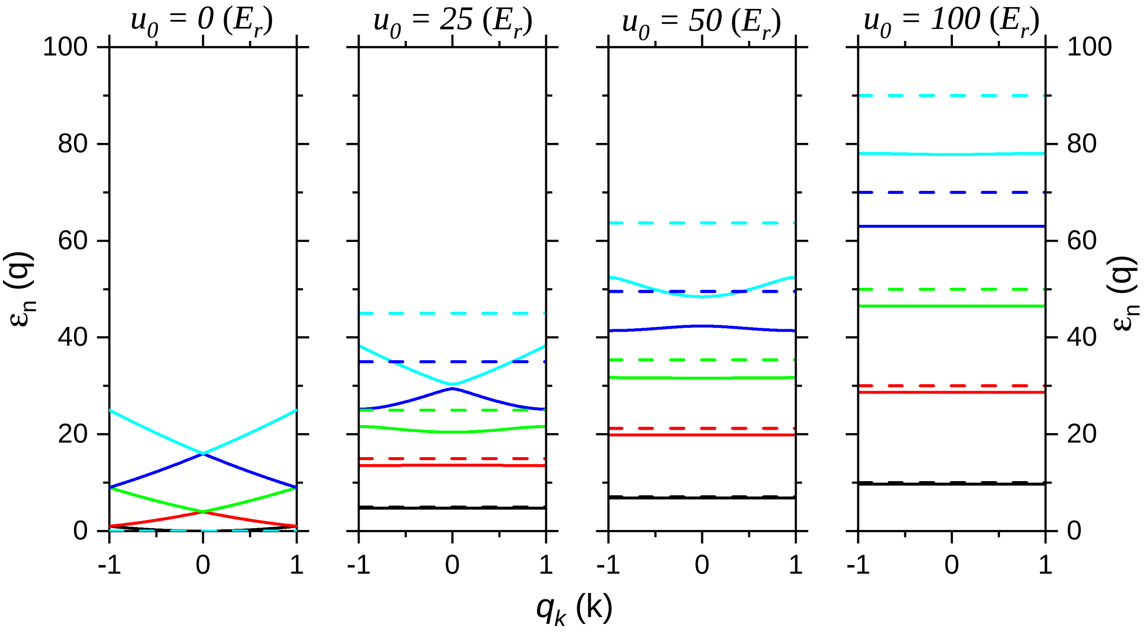

Figure 2.3: Band structure at different lattice potentials. Different color lines show different energy bands; for example, the black, red, green, blue, and cyan lines are $n = 0, 1, 2, 3, 4$ bands, respectively. The dashed lines correspond to the energy bands of the harmonic oscillator. All the energies are in units of recoil energy E_r: the lattice depth $u_0 = U_0/E_r$, and the eigenenergy $\epsilon_n(q) = E_n(q)/E_r$. The quasi-momentum is in units of k: $q_k = q/k$. In the deep bound band, the eigenenergy can be expressed by the energy band in the harmonic oscillator.

Lamb-Dicke regime

	Clock laser	Lattice laser
Wavelength	$\lambda_p = 698.445\,61\,\mathrm{nm}$	$\lambda_L = 813.427\,57\,\mathrm{nm}$
Wave number	$k_p = 8\,995\,955.063\,m^{-1}$	$k_L = 7\,724\,332.859\,m^{-1}$
Recoil energy	$E_{r\_p} = 3.083\times10^{-30}\,\mathrm{J}$	$E_r = 2.273\times10^{-30}\,\mathrm{J}$
Recoil frequency	$\nu_{r\_p} = 4.653\,\mathrm{kHz}$	$\nu_r = 3.430\,\mathrm{kHz}$

Table 2.4: Property clock and lattice lights based on ^{88}Sr.

For optical lattice clocks, to eliminate the Doppler effect of the atom's motion, the atoms are confined in the Lamb-Dicke regime, where the atom's motion is confined to a region much smaller than the wavelength of the probe light [56][57]. The degree of confinement is quantified by the Lamb-Dicke parameter η_z

$$\eta_z = k_p z_0 \tag{2.20}$$

where k_p is the wave vector of the probe light (clock laser), and z_0 is the extension of the wave function along the z axis

$$k_p = \frac{2\pi}{\lambda_p} \tag{2.21}$$

$$z_0 = \sqrt{\frac{\hbar}{4\pi m \nu_z}} \tag{2.22}$$

where m is the atom mass and $\nu_z = \omega_0/2\pi$ is the trap frequency along z axis (see Eq. 2.19).

For the strontium-88 optical lattice clock, the wavelengths, the wave numbers, and the recoil-related quantities of clock and lattice lasers are listed in Table 2.4. The axial trap frequency $\nu_z = 53.14\,\mathrm{kHz}$ when lattice depth $U_0 = 60E_r$ and corresponding wave function extension $z_0 = 32.9\,\mathrm{nm}$. Thus, the parameter η_z is ~ 0.3, which is much less than 1 and satisfies the Lamb-Dicke regime condition:

$$z_0 \ll \lambda_p \tag{2.23}$$

and

$$\nu_{r\_p} \ll \nu_z \tag{2.24}$$

where $\nu_{r\_p} = \hbar k_p/m$ is the recoil velocity of the probe light. In the Lamb-Dicke regime, the probe light would not cause Doppler broadening because of strong spatial confinement of the atoms.

The transitions between the initial state i and the final state j are illustrated in Figure 2.4. The dipole matrix element for the transition is $\langle n_j|e^{ik_p z}|n_i\rangle$, when the probe

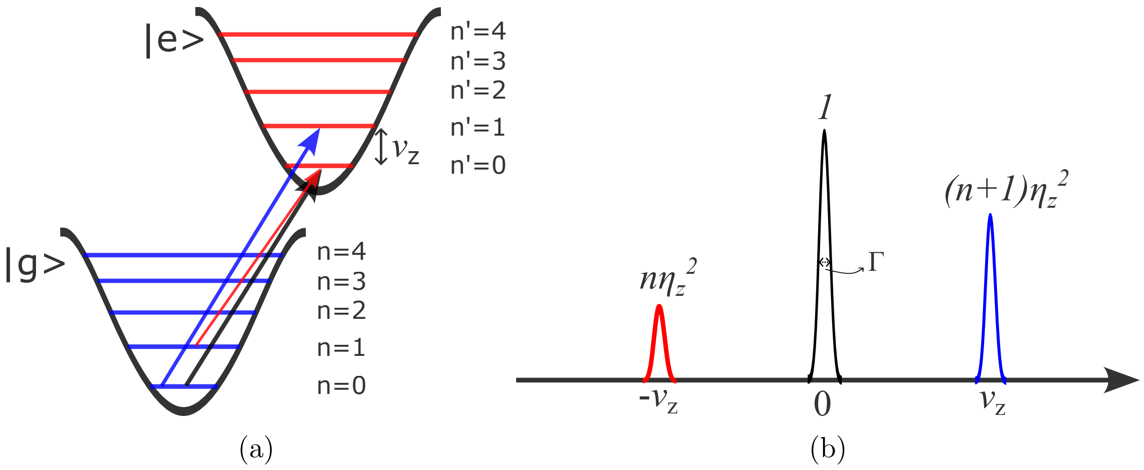

Figure 2.4: The schematic of lattice spectroscopy and the relative transition strength. The transitions with motional states $\Delta n = 0$, $\Delta n = -1$, and $\Delta n = +1$ correspond to carrier, red sideband, and blue sideband in (b), respectively. Compared to carrier transition, the red sideband and blue sideband are suppressed by $n\eta_z^2$ and $(n+1)\eta_z^2$, respectively. In (b), the effect of radial motion is not considered.

light field is described by a traveling plane wave. Here, n denotes the motional state. Using the raising and lowering operators, the exponential at z_0 can be expanded, and the matrix element becomes [19]

$$\begin{aligned}\langle n_j|e^{ik_pz}|n_i\rangle &\approx \langle n_j|1|n_i\rangle + \langle n_j|ik_pz|n_i\rangle \\ &= \delta_{n_i,n_j} + ik_pz_0(\langle n_j|\hat{a} + \hat{a}^\dagger|n_i\rangle) \\ &= \delta_{n_i,n_j} + ik_pz_0(\sqrt{n_i}\delta_{n_i+1,n_j} + \sqrt{n_i+1}\delta_{n_i-1,n_j})\end{aligned} \tag{2.25}$$

Only three terms remain when squaring the matrix element:

$$|\langle n_j|e^{ik_pz}|n_i\rangle|^2 = \delta^2_{n_i,n_j} + \eta_z^2(n_i\delta^2_{n_i+1,n_j} + (n_i+1)\delta^2_{n_i-1,n_j}) \tag{2.26}$$

The strongest transition occurs when the motional state remains unchanged ($\Delta n = 0$), called the carrier transition with Rabi frequency Ω_0. The transitions where $\Delta n = -1$ (from n to $n' - 1$) are the first red sideband, suppressed by $n\eta_z^2$ relative to the carrier transition. The transitions where $\Delta n = +1$ (from n to $n' + 1$) are the first blue sideband, suppressed by $(n+1)\eta_z^2$. In optical lattice clocks, these three transitions are typically probed via sideband spectroscopy, as illustrated in Fiugre 2.4.

Resolved and unresolved sideband spectroscopy

Whether the sidebands are resolved depends on the linewidth Γ of the electronic transition

$|g\rangle \rightarrow |e\rangle$ and the trap frequency ν_z of the potential. When $\Gamma > \nu_z$, the sidebands overlap and are unresolved. Conversely, when $\Gamma < \nu_z$, the sidebands are resolved. See Figure 2.4. For our strontium-88 optical lattice clock, the linewidth of the clock transition ${}^1S_0 \leftrightarrow {}^3P_0$ is $\sim 1\,\mathrm{Hz}$, while the axial trap frequency is a few tens of kHz, satisfying the condition of resolved sideband spectroscopy.

Sideband spectroscopy in the Lamb-Dicke regime with resolved sidebands is a powerful tool for evaluating lattice properties (see the next chapter).

The confinement in the radial axis

We also need to consider the Gaussian beam's transverse profile in a 1-D lattice, which provides the confinement in the radial direction [19][58]. Thus, the potential becomes

$$U(r, z) = -4\alpha(\omega)\frac{I_0}{c\varepsilon_0}e^{-2r^2/w^2(z)}\cos^2(kz) \tag{2.27}$$

where $w(z)$ is the beam radius at a longitudinal distance z from the beam focus, and r is the radial distance from the beam center.

In radial confinement, the Lamb-Dicke parameter is [58]

$$\eta_r = \frac{\delta\theta_m}{\lambda_p}\sqrt{\frac{h}{2m\nu_r}} \tag{2.28}$$

where ν_r is the radial trap frequency and $\delta\theta_m$ is the misalignment angle between the probe and the lattice lights. In the 1-D optical lattice, the radial confinement is much weaker than axial confinement ($\nu_z \gg \nu_r$).

For low atom temperatures and small misalignment between the probe and the lattice lights, the excitation probability from the ground state to the excited state is approximated as [58]

$$p_e(t) \simeq \frac{1}{2} + \frac{1-z_r}{2}\frac{z_r\cos[\phi(1-\eta_r^2)] - \cos\phi}{1 + z_r^2 - 2z_r\cos(\phi\eta_r^2)} \tag{2.29}$$

where $z_r = e^{-h\nu_r/(k_B T_r)}$ and $\phi = 2\pi t\Omega_0 e^{-\eta_r^2/2}e^{-\eta_z^2/2}$. t is the probe pulse length, Ω_0 is the Rabi frequency in units of Hz, and T_r is the radial temperature. At zero misalignment ($\delta\theta_m = 0$), the excitation probability can be reduced to $\sin^2(\phi/2)$, as shown in Figure 2.5. Oscillation dephases more rapidly as the misalignment angle $\delta\theta_m$ increases. Minimizing $\delta\theta_m$ (typically $\delta\theta_m \leq 0.1\,\mathrm{mrad}$ in SOC2 clock, as shown in Section 3.4.6) is essential.

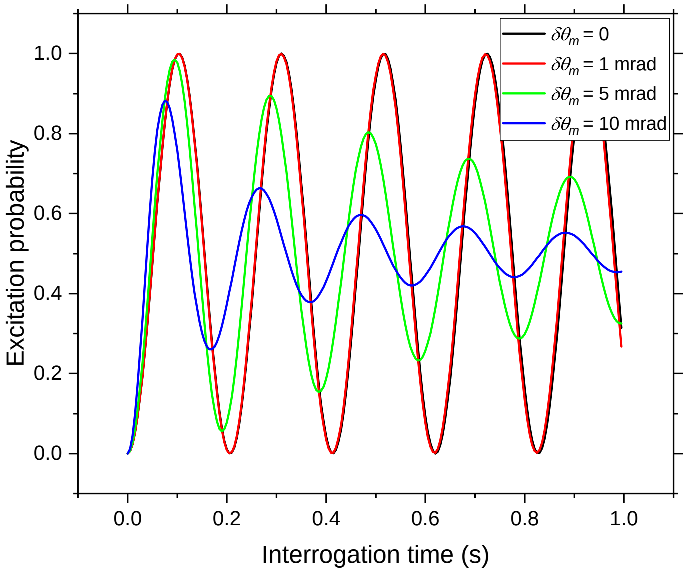

Figure 2.5: Effect of radial motion on Rabi oscillations. The oscillation is dephasing faster as the misalignment angle $\delta\theta_m$ increases. The simulation condition is based on the experimental result in Figure 3.33: the lattice depth 101 E_r, the longitudinal trap frequency $\nu_z = 69\,\mathrm{kHz}$, the radial temperature $T_r = 4.8\,\mathrm{\mu K}$. The simulation shows $\delta\theta_m \leq 1\,\mathrm{mrad}$ is desirable.

2.3.3 A vertical optical lattice

The orientation of the 1-D optical lattice axis is crucial for the tunneling effect between adjacent lattice sites [19][59]. In a horizontal lattice, adjacent lattice sites have degenerate energy levels, causing wavefunctions to delocalized and extend over the entire lattice. Atoms could tunnel between lattice sites and the tunneling rate causes a frequency shift; for example, in a horizontal optical lattice with a depth of 50 E_r, the tunneling frequency shift is approximately 0.42 Hz, corresponding to 1.0×10^{-15} in fractional units for the strontium clock transition [60]. However, in a vertically oriented optical lattice, tunneling is suppressed by gravity, lifting the degeneracy between lattice sites by $mg\lambda_L/2$ (Wannier-Stark ladder), as illustrated in Figure 2.6, where λ_L is the lattice laser wavelength. The lattice potential becomes

$$U(r,z) = -4\alpha(\omega)\frac{I_0}{c\varepsilon_0}e^{-2r^2/w^2(z)}\cos^2(kz) + mgz \tag{2.30}$$

As a consequence of the vertical orientation, the maximum tunneling-induced frequency at a lattice depth of 50 E_r is approximately 0.4 µHz , corresponding to 9×10^{-22} in fractional units for the strontium clock transition [59]. Compared to other contributions (shown in Chapter 5), this shift is negligible.

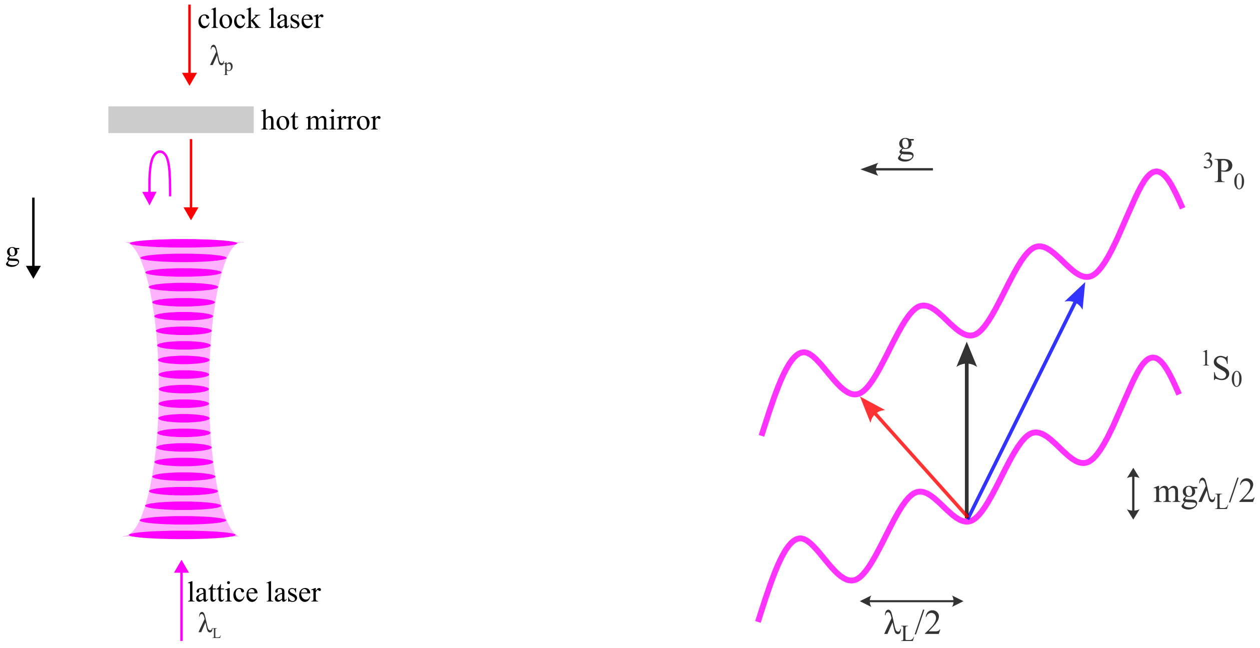

(a) (b)

Figure 2.6: (a) The configuration of vertical optical lattice: 'pancake'. (b) The external potential seen by the atoms in the vertical optical lattice which is aligned with respect to local gravitational acceleration g. The different-colored arrows indicate the transitions between different orders of Wannier-Stark sidebands.

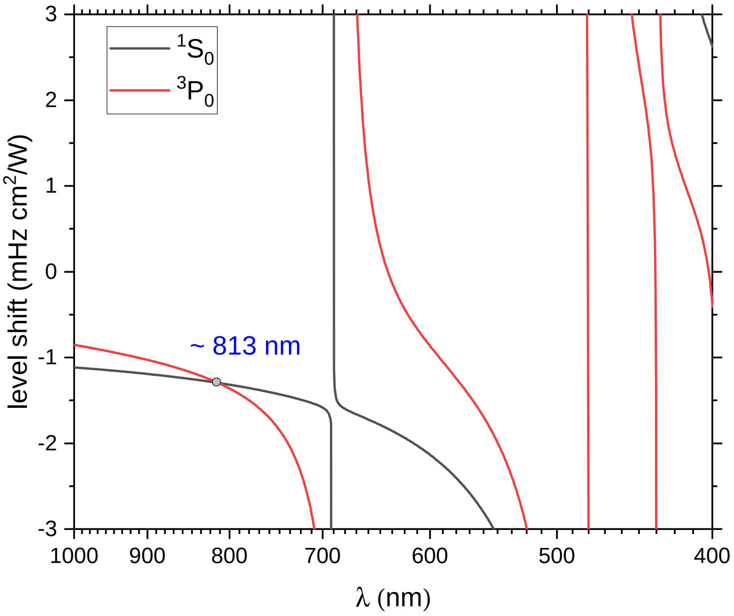

Figure 2.7: Lattice light AC Stark shifts of clock states $^1S_0$ and $^3P_0$ of strontium atoms. The red far-detuned magic wavelength of the clock transition $^1S_0 \leftrightarrow {}^3P_0$ of strontium-88 is 813.42757(62) nm [63]. The level shift data is taken from [64].

2.3.4 Magic wavelength of optical lattice for the clock transition

The laser light modifies the energy levels of atoms compared to unperturbed levels, a phenomenon known as the AC Stark shift, especially in deep optical lattices. The AC Stark shift for the clock transition $^1S_0 \leftrightarrow {}^3P_0$ due to the lattice light is [29][61]

$$\delta\nu_{clock} = -\frac{4\Delta\alpha(\lambda_L)}{c\varepsilon_0 h} I_0 + O(I_0^2) \tag{2.31}$$

where $\Delta\alpha(\lambda_L) = \alpha_{^3P_0}(\lambda_L) - \alpha_{^1S_0}(\lambda_L)$ is the differential AC Stark polarizability of the $^1S_0$ and $^3P_0$ states, which depends on the lattice wavelength λ_L and is independent of the light polarizability due to $J = 0$ which exhibits a scalar light shift.

To eliminate the lattice light shift, Katori et al. proposed operating a neutral strontium optical lattice clock at a 'magic' wavelength in 2003 [62]. At this wavelength, $\Delta\alpha(\lambda_L) = 0$, which is independent of the intensity of lattice light. The lattice AC Stark shift of the clock transition $^1S_0 \leftrightarrow {}^3P_0$ is eliminated by adjusting the lattice light to this wavelength, if the higher-order corrections $O(I_0^2)$ are negligible. The AC Stark shifts of the $^1S_0$ and $^3P_0$ states of strontium atoms are shown in Figure 2.7, and the red far-detuned magic wavelength of the clock transition $^1S_0 \leftrightarrow {}^3P_0$ of strontium-88 is 813.42757(62) nm [63].

2.4 Excitation of clock transition of the bosonic strontium-88 atom

The singlet to triplet transitions of alkaline-earth(-like) atoms, i.e., $^1S_0 \leftrightarrow {}^3P_0$ are of interest for metrology and new physics research, e.g., optical lattice clocks, atomic interferometers, gravitational wave detectors, dark matter searches.

For fermionic isotopes, the $^1S_0 \leftrightarrow {}^3P_0$ transition is weakly dipole-allowed through hyperfine interaction of the nuclear spin. However, for bosonic isotopes, the transition is double-forbidden ($\Delta S = 1$ and $\Delta J = 0$ with $J = 0 \leftrightarrow J = 0$). Several methods have been proposed to excite the transition of the bosonic isotopes, such as the magnetic-field-induced spectroscopy, the three-photon excitation, and the electromagnetically induced transparency.

2.4.1 Magnetic Field-induced Spectroscopy

Magnetic field-induced spectroscopy uses a single clock laser combined with a DC magnetic field to mix excited states $^3P_1$ and $^3P_0$, thereby allowing single-photon excitation of the transition $^1S_0 \leftrightarrow {}^3P_0$ [65], shown in Figure 2.8. The effective Rabi frequency for the excitation is [65]

$$\Omega_{12} = \frac{\Omega_L \Omega_B}{\Delta_{32}} \tag{2.32}$$

where Ω_B and Ω_L are the Rabi frequencies corresponding to couplings between $^3P_0$ and $^3P_1$ states and between $^1S_0$ and $^3P_1$ states, respectively. Δ_{32} is the splitting frequency between $^3P_0$ and $^3P_1$ states. In terms of applied magnetic field $\mathbf{B}$ and laser light intensity I, the effective Rabi frequency can be rewritten as [65]

$$\Omega_{12} = \alpha\sqrt{I}|\mathbf{B}|\cos\theta \tag{2.33}$$

where α is the coupling coefficient (e.g., $\alpha = 198\,\mathrm{Hz}/(\mathrm{T}\sqrt{\mathrm{mW/cm^2}})$ for strontium-88 atoms) and θ is the angle between linearly polarized light field $\mathbf{E}$ and magnetic field $\mathbf{B}$. Typically, the bias field $\mathbf{B}$ and the optical field $\mathbf{E}$ are parallel, so $\theta = 0$.

The frequency shifts due to the magnetic field and laser light must be carefully studied for clock applications. The first-order Zeeman shift is eliminated in magnetic field-induced spectroscopy due to $J = 0$ for the clock transition. The second-order Zeeman shift is given

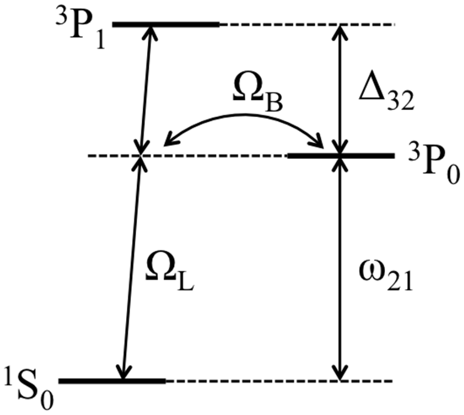

Figure 2.8: Magnetic field-induced excitation of a strongly forbidden transition. For example, the clock transition $^1S_0 \leftrightarrow {}^3P_0$ in bosonic isotopes of alkaline-earth(-like) elements (Yb, Sr, Ca, Hg, and Mg). The figure is taken from [29]. More details in the text.

by

$$\Delta\nu_B = -\frac{\Omega_B^2}{\Delta_{32}} = \beta|\mathbf{B}|^2 \tag{2.34}$$

where β is the second-order Zeeman shift coefficient ($\beta = -23.3\,\mathrm{MHz/T^2}$ for ^{88}Sr [65]). The probe laser AC Stark shift is given by

$$\Delta\nu_L = \frac{\Omega_L^2}{4\Delta_{32}} = kI \tag{2.35}$$

where k is the coefficient of the AC Stark shift ($k = -18\,\mathrm{mHz/(mW/cm^2)}$ for ^{88}Sr [65]).

The frequency shifts due to the magnetic field and clock laser light are the primary contributors to the systematic uncertainty of neutral bosonic atom optical lattice clocks, as shown in Chapter 5.

2.4.2 Multi-Photon Excitations

Hong et al. proposed using three-photon resonance to excite the double-forbidden $^1S_0 \leftrightarrow {}^3P_0$ transition in the bosonic isotopes, which is based on the concept of electromagnetically induced transparency and absorption (EITA) and predicted that the light shift could be limited below 10^{-18} [66].

Recently, Carman et al. and He et al. demonstrated the coherent three-photon excitation of the strontium clock transition. He et al. used ^{84}Sr atoms [67], however Carman et al used ^{88}Sr atoms and all three laser beams are collinear [68]. Carman et al. also claim that their scheme reduces the Zeeman shift and eliminates the overall probe light shift with an appropriate choice of laser detunings.

Jun Ye's group proposed using two lasers to establish coherent coupling between ${}^1S_0 \leftrightarrow {}^3P_0$ and the broad ${}^1P_1$ as an intermediate state to exploit the phenomenon of electromagnetically induced transparency (EIT) [69].

The multi-photon excitations of a strongly forbidden transition, e.g., EITA and EIT, are complicated to realize in terms of alignment of laser beams and may cause significant light shifts that are not easily eliminated. For our SOC2 apparatus, we utilize magnetically induced spectroscopy which is single-photon excitation. After careful investigation, the uncertainty in the quadratic Zeeman shift and the clock laser light AC Stark shift can be controlled to the 10^{-17} level, as shown in Chapter 5.

Chapter 3

SOC2 Optical Lattice Clock

3.1 Overall apparatus

History of SOC2

The SOC2 apparatus was inherited from the Space Optical Clock project. The first stage of the Space Optical Clock (SOC) project began in 2007, funded by ESA and coordinated by Prof. S. Schiller of Heinrich-Heine-Universität Düsseldorf. It studied the feasibility of operating an optical lattice clock in space. SOC was the natural follow-on mission to the ACES mission, which was launched on April 21, 2025. The goal of SOC was to achieve at least one order of magnitude better stability and accuracy compared to ACES. A compact transportable clock was demonstrated in Florence [70].

The second stage of the SOC project, also known as the SOC2 project, started in 2011 as a follow-on to the preliminary study of the SOC project. Two transportable optical lattice clocks based on strontium [71] and ytterbium atoms [72], respectively, were developed. The strontium optical lattice clock was moved to PTB after successfully characterizing the optical lattice trap at the University of Birmingham. The ytterbium optical lattice clock was transported from Universtät Düsseldorf to INRiM[10] and put into operation there, and later transported back.

The characterization and further development of the strontium clock were implemented in PTB [16], which was partially funded by the Marie Curie action Future Atomic Clock Technology (FACT) and, since 2017, in the framework of the I-SOC ESA mission study. Figure 3.1 shows a photo of the SOC2 apparatus in 2018.

Since 2023, the SOC2 apparatus has been part of the Clock Metrology research unit, funded by the DFG. The goal is to integrate, operate, and optimize the performance of the SOC2 apparatus at Wettzell, as well as to test fundamental physics. Figure 3.2 shows photos of the SOC2 apparatus in 2024.

---

[10] Istituto Nazionale di Ricerca Metrologica, Turin, Italy.

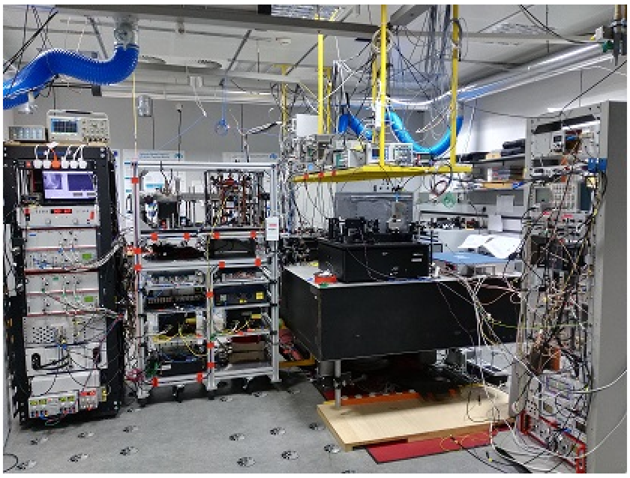

Figure 3.1: The SOC2 optical clock in 2018. The photo was taken at PTB. The atomic package is located at the top of the rack in the middle, with the laser subsystems mounted below. The electronics are mounted on a separate rack on the left. The clock laser is situated on top of the large optical table, and its corresponding electronics are located on the right rack.

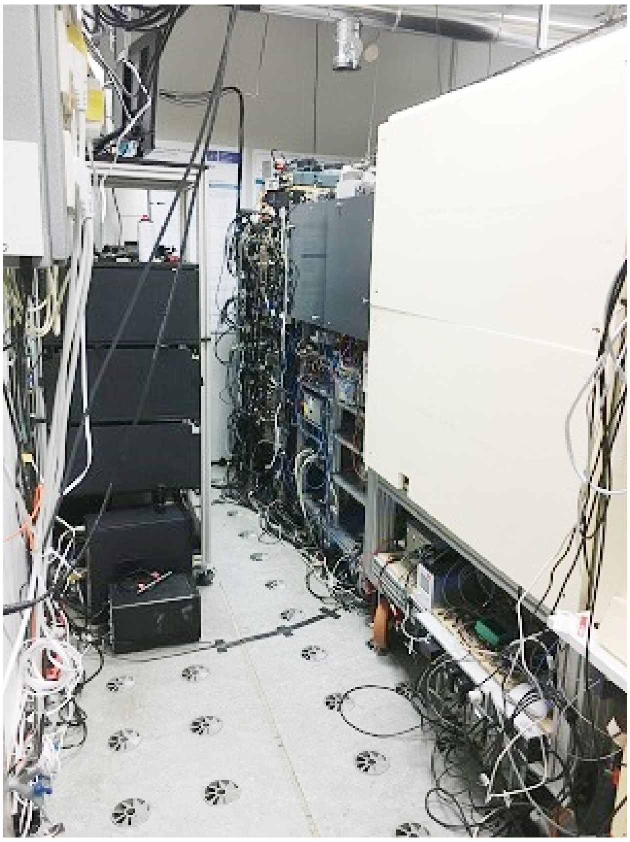

Figure 3.2: The SOC2 optical clock currently (2024), still at PTB, in the same laboratory space. In the foreground right is the enclosed new clock laser. The atomics package is at the center, covered with black panels. On the left is a rack containing laser subsystems.

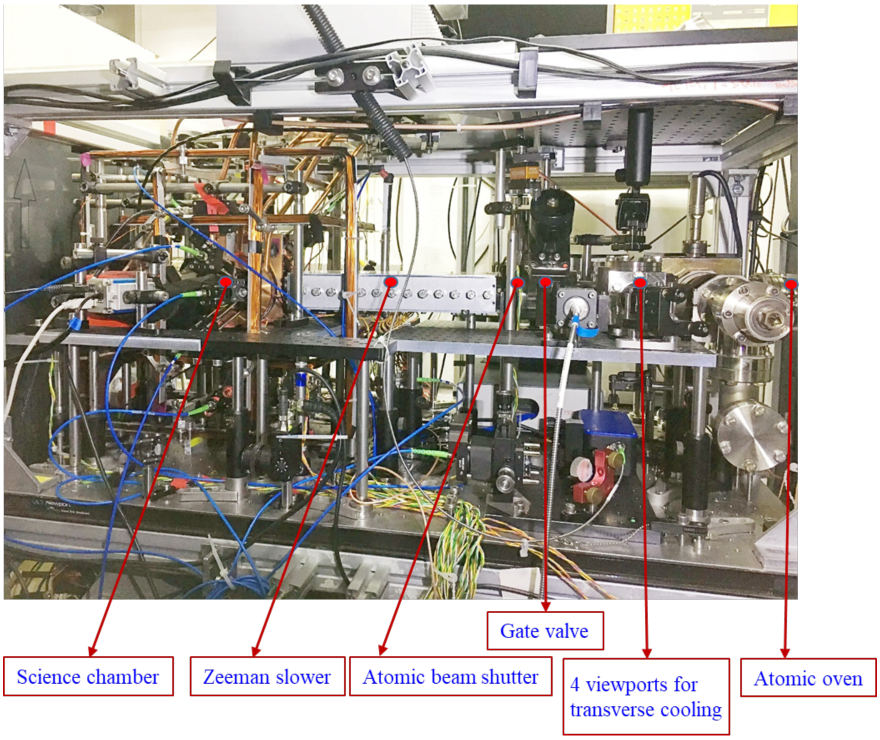

Figure 3.3: The compact physics package of the SOC2 apparatus.

3.2 Compact physics package

The compact physics package of the SOC2 apparatus is shown in Figure 3.3. The total volume is 143 l, and the mass is 50 kg, including the breadboard [29]. The following paragraphs will introduce all the components from right to left in the figure.

Atomic Oven:

A thermal strontium beam is effused from a strontium oven attached to a port aligner with a CF35 flange, shown in Figure 3.4. The oven is heated to 400 ∼ 500 °C by a tantalum wire housed in an alumina multibore tube. The oven is a modified version of the PTB design. The divergence of the beam is ∼ 50 mrad. A 25 l ion pump (25S Gamma Vacuum) is installed through one 4-way cross to maintain a high vacuum for the oven. Usually, in operation, the pressure of the oven is $\sim 2 \times 10^{-9}$ mbar.

Transverse cooling:

The 6-way cross with 4 viewports for transverse cooling is installed next to the 4-way cross. To increase atomic flux to the science chamber, the atomic beam divergence is decreased by transverse cooling. The atom number is increased by approximately three times compared to that without transverse cooling.

(a) The atomic oven installed on a CF35 flange.

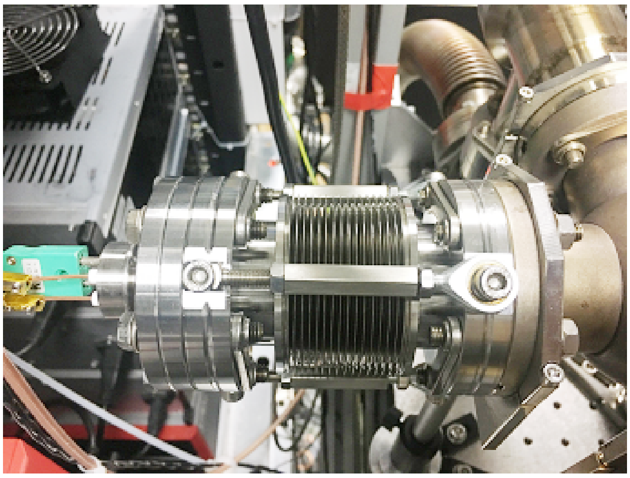

(b) The port aligner.

Figure 3.4: The atomic oven and port aligner used to align the oven to the science chamber.

Gate valve and atomic beam shutter:

One gate valve separates the vacuum between the science chamber and oven, making it flexible for partially breaking the vacuum, for example, replacing the oven, etc. In order to eliminate the frequency shift due to blackbody radiation (BBR shift) from the oven, a flag shutter (CF35 Pneumatic Viewport Shutter from Kurt J. Lesker) is installed adjacent to the gate valve. The shutter is driven by a servo motor (model SB2272MG from Savöx), and opened only during the first-stage MOT (blue MOT phase, shown in 3.21). A 2.5 mm pinhole just next to the flag shutter and before the Zeeman slower acts as a differential pump stage, across which a pressure ratio of 100 is expected.

Zeeman slower:

A Zeeman slower is implemented to slow the atoms effused from the oven to the capture velocity of the MOT. The Zeeman slower is based on a 2-D array of neodymium permanent magnets with transverse field [73], as shown in Figure 3.5. In order to measure velocity of the atoms after the Zeeman slower, I delivered a 461 nm blue laser beam from the PTB stationary strontium optical lattice clock (Sr3) lab as a detection beam. The blue laser beam is split from a 461 nm DL pro diode laser, whose frequency is monitored by the beat note with a TA-SHG pro laser in the Sr3 lab. The laser beam for Zeeman slowing is from another TA-SHG pro laser in the SOC2 lab. Both fundamental wavelengths of TA-SHG pro lasers are locked to their own 922 nm reference optical cavity, respectively. More details of the SOC2 SHG laser locking to Frequency Stabilization System (FSS) can be found in Ref. [74]. The sketch of measurement scheme is shown in Figure 3.6a.

The detection beam has an angle θ_z with respect to the thermal atomic beam, and its frequency ν_{detec} can be tuned by the piezoelectric component of 461 nm DL pro laser in Sr3 lab. First, starting the experiment with $\theta_z = 90\,^\circ$, which means that the detection beam is orthogonal to the atomic beam to find the center resonance frequency f_0 of atoms with zero velocity $v_a = 0$. Then, fixing the angle θ_z at 45 ° and scanning the detection beam frequency f to obtain the velocity distribution. The relation between atom velocity v_a and detection beam frequency f can be expressed as

$$k_{detec} v_a \cos\theta_z = 2\pi(f - f_0) \tag{3.1}$$

where k_{detec} is the wave number of the detection beam. The detuning of the detection beam, $f - f_0$, can be directly read from the spectrum analyzer, shown in Figure 3.6a. The velocity distribution of atoms after the Zeeman slower by scanning the detection beam frequency f is shown in Figure 3.6b.

Ultimately, strontium atoms are slowed down to $\sim$ 160 m/s by this slower before

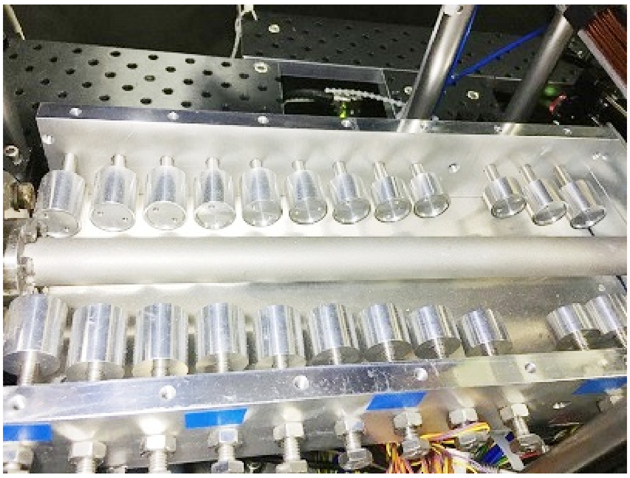

Figure 3.5: The photo of Zeeman slower which is based on a 2-D array of neodymium permanent magnets with transverse field.

entering the science chamber (see Figure 3.6b). The relationship between atom velocity and laser polarization direction has also been observed. When the polarization direction is aligned with the magnetic field direction, only one group of slowed atoms is obtained. However, several groups of slowed atoms are observed when a laser beam is applied with the polarization direction orthogonal to the magnetic field direction. In the first case, the laser only addresses ${}^1S_0 \leftrightarrow {}^1P_1, m_J = 0$ transition and the magnetic field cannot vary the energy level of this transition which means the Zeeman slower is not working in this case. In the second case, the laser addresses ${}^1S_0 \leftrightarrow {}^1P_1, m_J = +1$ (or $m_J = -1$) transition and the Zeeman slower works in this case; however, due to unsmooth magnetic fields, several groups of slowed atoms are observed [73].

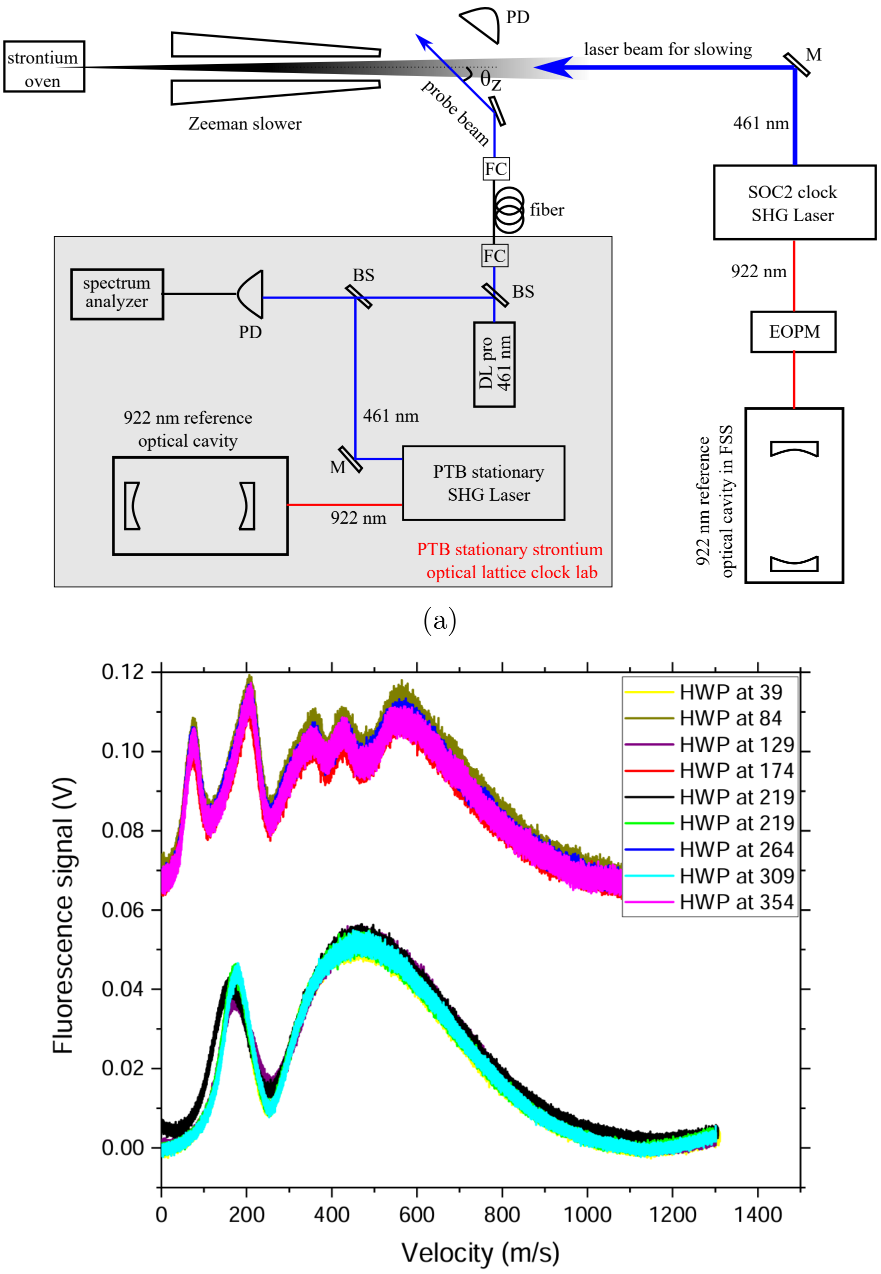

(a)

(b)

Figure 3.6: Measurements of the velocity distribution of atoms after the Zeeman slower. (a) Schematics of the measurement setup. The detection beam is provided by the PTB stationary strontium optical lattice clock (Sr3) lab, which is from a 461 nm DL pro diode laser. The PTB SHG laser is as a frequency reference for the DL pro laser. The slowing laser is produced from theSOC2 SHG laser, which is stabilized to one of the FSS cavities. (b) The velocity distribution of atoms after the Zeeman slower. The upper curves have been offset by 0.7 V for clarity. Here shows the polarization effect of the Zeeman slower as well. The SHG lasers are TA-SHG pro lasers from Toptica. More details in the text. SHG: second harmonic generation, EOPM: waveguide electro-optic phase modulator, PD: photodetector, BS: beam splitter, FC: fiber collimator/coupler, M: mirror, FSS: Frequency Stabilization System, shown in the next section.

Science chamber:

A compact science chamber has been installed, 51 mm in diameter and 22 mm in thickness, made of titanium. The total length, including the tubes to connect to the rest of the vacuum system, is 130 mm. The advantages of the compact science chamber are: 1) reducing the size and weight of the whole vacuum system for easy transportation. 2) making MOT coils with a relatively small size, which means that the power consumption and heat produced are lower. It is sufficient to use TEC (thermoelectric cooling element) peltiers to cool the MOT coils instead of water cooling, thereby decreasing the temperature inhomogeneity around the science chamber and, ultimately, reducing ambient BBR shifts.

There are 8 windows made out of BK7 installed around the science chamber: 6 lateral windows with a diameter of 10 mm and 2 windows with a diameter of 40 mm on the horizontal plane, as shown in Figure 3.7a. All windows are accessible for laser beams, including MOT beams, repump beams, lattice laser beams, and clock laser beam, via 16 mm cage systems that are either directly attached to the science chamber or connected via viewport adapters.

The MOT coils are attached to the science chamber, and three pairs of compensation coils are installed to compensate for the background magnetic field. Other components, such as the PMT (Hamamatsu H11526-110-NF) and the CCD camera (pco.pixelfly USB), as well as photodetectors for monitoring laser powers, are installed around the science chamber, as shown in Figure 3.7b.

To maintain the vacuum of the chamber, an ion getter pump (SAES NexTorr D100-5) with the volume of 0.5 l and the mass of 2.2 kg is attached. Due to the presence of getter elements, the pumping speed is 100 l/s for H_2 and 40 l/s for N_2. The capacity of the getter pump is maintaining the vacuum of less than 1×10^{-10} mbar, even during clock operation with the hot oven.

At the end of the vacuum system, opposite the oven side, there is a sapphire window from Kurt J. Lesker, which provides access for the blue laser beam of the Zeeman slower. The sapphire window, which has a higher temperature resistance, can be heated to 150 °C to remove strontium deposits that are from the collimated atomic beam effusing from the atomic oven [49]. Heating the sapphire window is expected to be implemented in the future.

Major upgrades of the physics package:

Regarding the physics package, further information can be found in Refs. [29] and [75] for the details. The important upgrades we have made since 2018 are: **1)** Using the PTB oven design, which is simpler and easier to install compared to the old design [76]. **2)** Installation of the oven with the port aligner to easily align the atomic beam with the science chamber. **3)** Implementation of a 6-way cross for transverse cooling to reduce the divergence of the

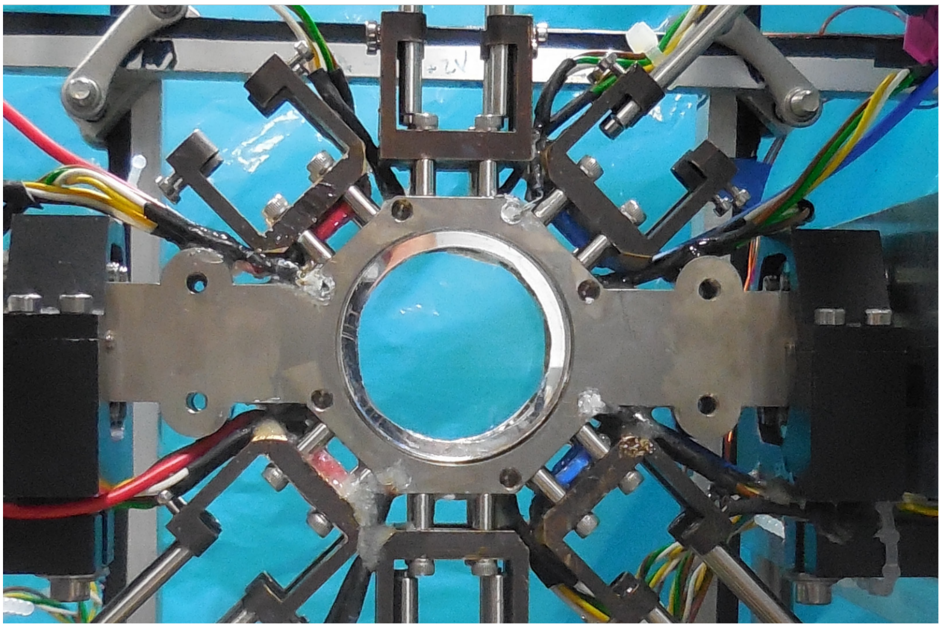

(a) Photo of the science chamber before installation of the magnetic coils. Taken from Ref. [29].

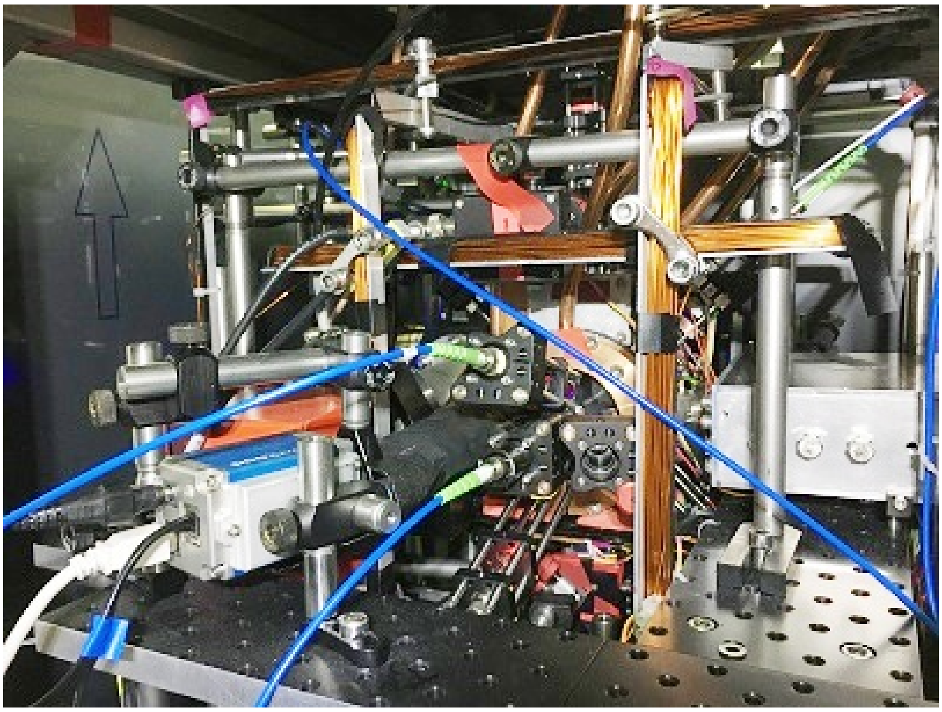

(b) Photo of the science chamber with all the components around it.

Figure 3.7: The science chamber.

atomic beam. **4)** Installation of the gate valve before the atomic beam shutter to isolate the vacuum between the oven and the science chamber if necessary.

3.3 Laser systems

For a strontium optical lattice clock, six laser systems are needed, with differrent wavelengths at 461 nm, 679 nm, 689 nm, 698 nm, 707 nm, 813 nm, and all laser systems are compact, transportable, and modular in design. The overall schematics of the laser systems are shown in Figure 3.8.

Blue laser system (461 nm):

One TA-SHG pro from Toptica provides the 461 nm blue lasers used for the Zeeman slower, blue MOT, transverse collimation, and atom detection in the trap. There is approximately 200 mW blue light sent from the TA-SHG to the distribution breadboard. Using polarizing beamsplitters (PBS), the laser beam is split into four branches for different purposes, shown in Figure 3.9. For example, we have a beam branch for the Zeeman slower with 78 mW power, for the blue MOT with 28 mW, for transverse cooling with 13 mW, and for detection with 1.4 mW. Here, all the beam power is measured before the fiber couplers. The coupling efficiency of all the fiber couplers is $> 50\,\%$. Each branch has one single-passed acousto-optic modulator (AOM) to shift the laser frequency—different branches have different laser frequencies. Figure 3.10 shows each laser beam's detuning from the resonance of blue transition ($^1S_0 \leftrightarrow {}^1P_1$).

The fundamental wave at 922 nm of the TA-SHG pro is stabilized to our frequency stabilization system (FSS) [74] via the Pound-Drever-Hall (PDH) locking technique, resulting in the 461 nm laser having approximately 1 MHz linewidth.

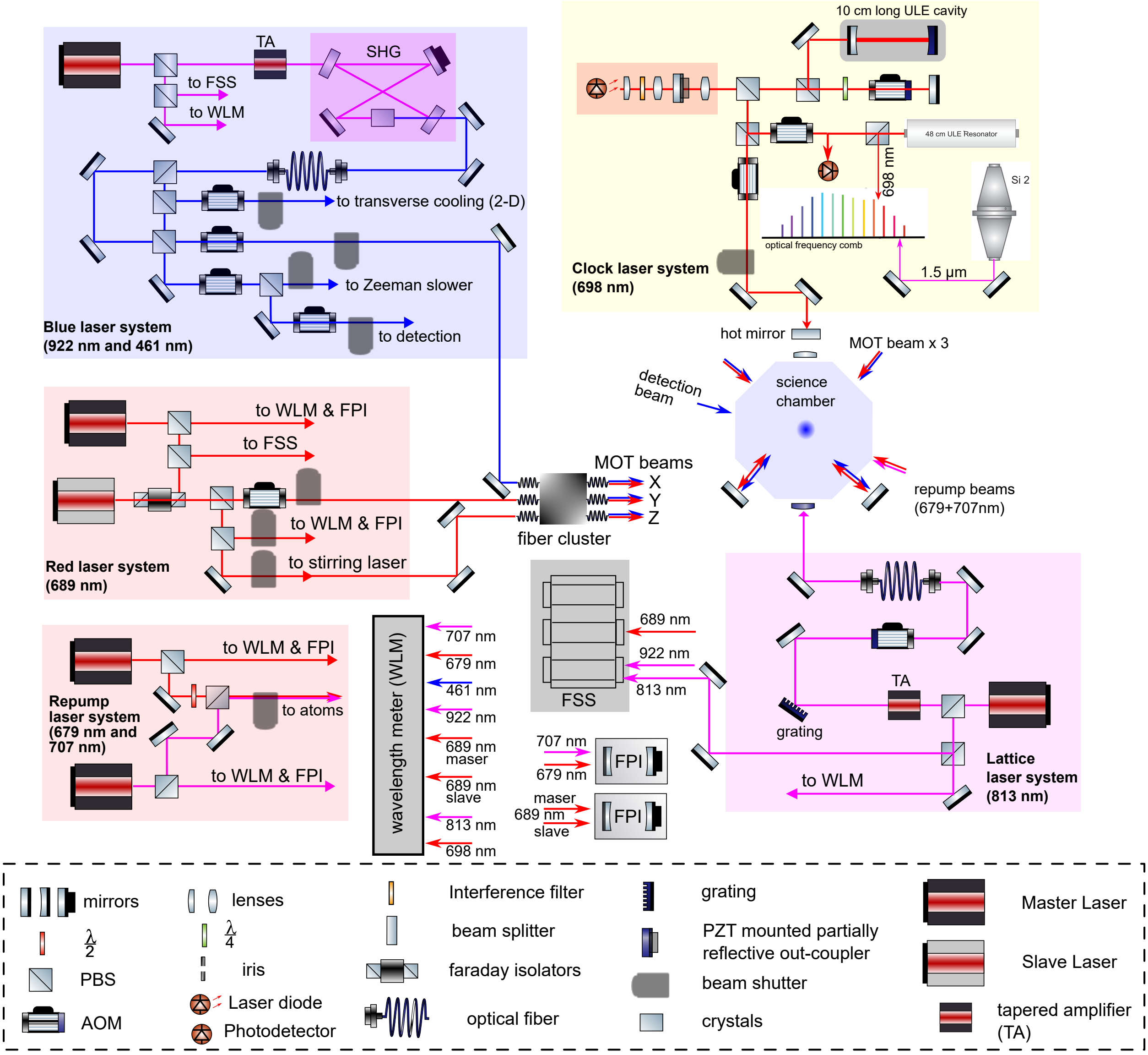

Figure 3.8: Overall schematics of the laser systems. The stirring laser is only used for strontium-87 atoms. More details are in the following text. TA: tapered amplifier, SHG: second harmonic generation, FSS: Frequency Stabilization System, WLM: wavelength meter, 2-D: two-dimensional, FPI: Fabry-Perot interferometer, ULE: ultra-low expansion glass, Si2: PTB cryogenic silicon cavity, MOT: magneto-optical trap, AOM: acousto-optic modulator, PBS: polarizing beamsplitter.

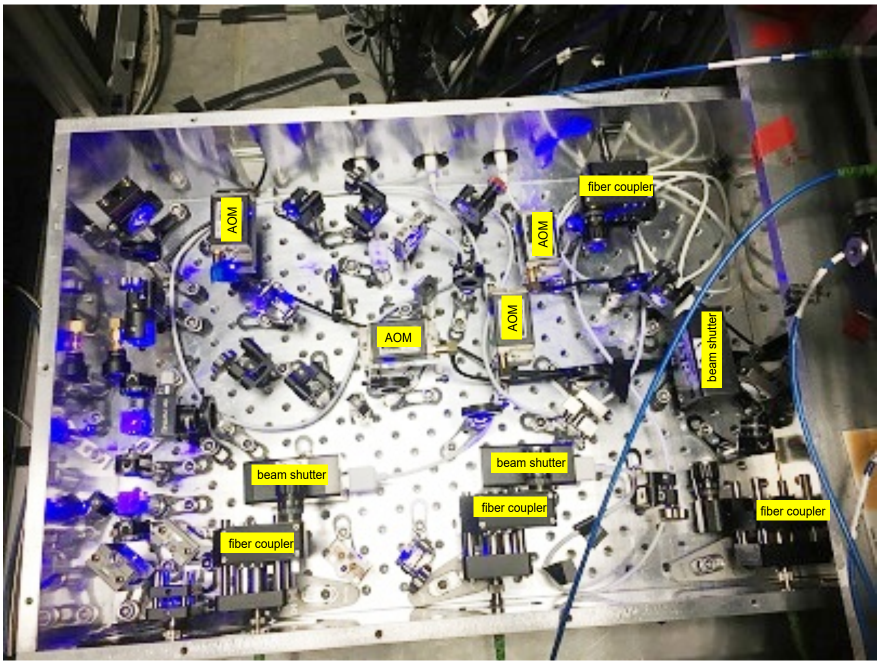

(a) Photo of the blue laser distribution breadboard.

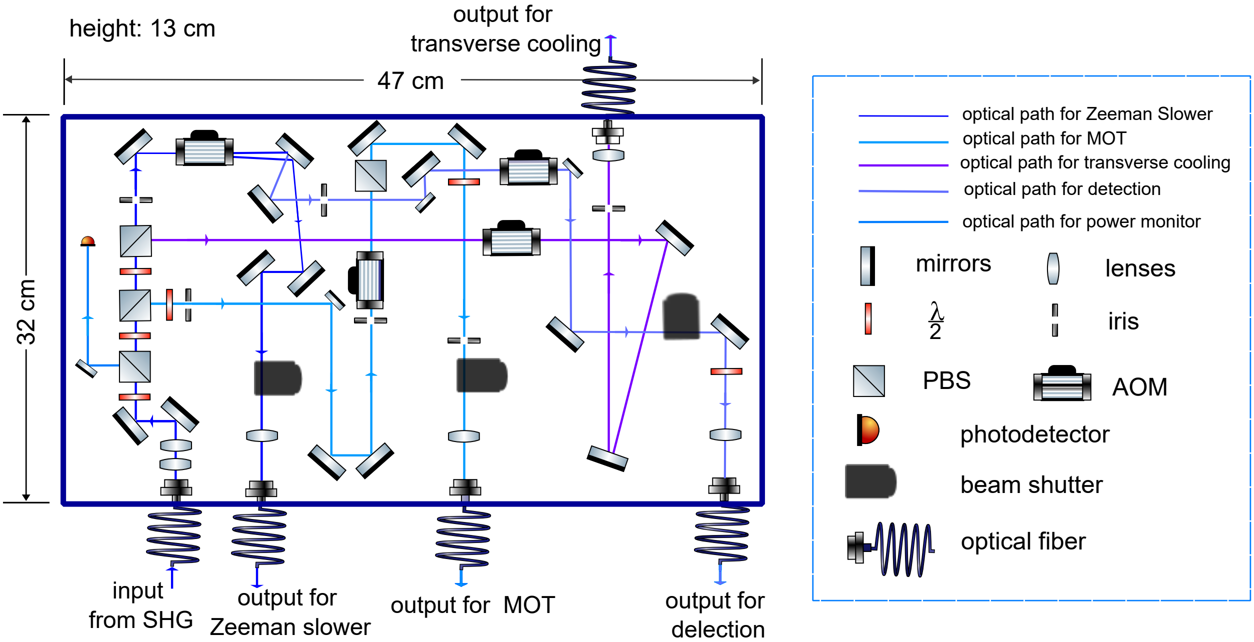

(b) Schematics of the blue laser distribution breadboard. The first order diffracted beam of each AOM is shown here, except for the top left AOM with zero and first orders. The other beam dumps are left out for clarity.

Figure 3.9: Blue laser distribution breadboard. The laser beam is split into four branches for different purposes. The top left AOM is More details in the text. SHG: second harmonic generation; AOM: acousto-optic modulator; MOT: magneto-optical trap; PBS: polarizing beamsplitter.

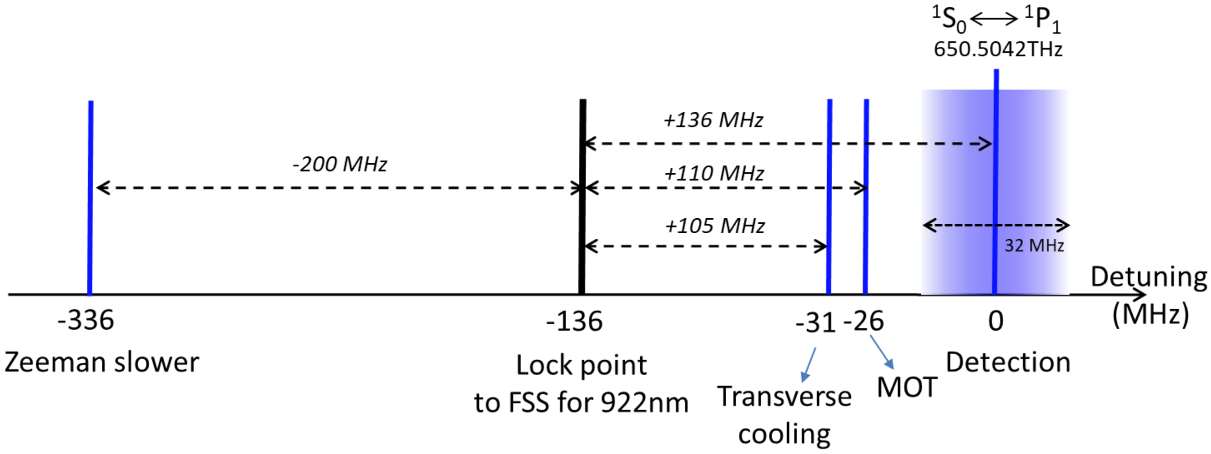

Figure 3.10: Frequency detuning of each blue beam from the resonant $^1S_0 \leftrightarrow {}^1P_1$ transition. The italic labels on the double arrow lines indicate RF frequencies of AOMs. The blue-shaped area shows the natural linewidth of the $^1S_0 \leftrightarrow {}^1P_1$ transition. The frequency axis is not to scale. AOM: Acoustic Optical Modulator.

Red laser system (689 nm):

The 689 nm laser system consists of a DL pro laser from Toptica and a slave laser, which is injection locked to the DL pro, to provide sufficient laser power for the red MOT, wavelength meter, and an extended output. The extended output is for the injection system of the stirring and the spin polarization lights when shifting to ^{87}Sr optical lattice clock. The master laser provides a laser beam of 6.5 mW to the FSS, reducing the laser spectrum linewidth to approximately 1 kHz [29]. The slave laser can provide a 21 mW laser beam for the red MOT. Figure 3.11 shows the red laser system schematics.

Usually, the second-stage MOT (red MOT) has two phases: broadband-frequency (BB) and single-frequency (SF) MOTs (see Section 3.4 for details). We use an AOM to vary the red MOT beam frequency to transfer the atoms from the BB red MOT to the SF red MOT. The detunings of both phases from the resonance of the $^1S_0 \leftrightarrow {}^3P_1$ transition are shown in Figure 3.12. Figure 3.13 indicates the modulated spectrum of the BB red MOT beam in operational condition.

For traditional magneto-optical traps, three orthogonal beams with retro-reflection beams comprise six beams to cool down and trap atoms. To simplify the system, a polarization-maintaining (PM) optical fiber array from Evanescent Optics Inc. with three inputs and three outputs is employed in the SOC2 apparatus. The array combines the lights for the blue MOT, the red MOT, and the stirring, and then splits the combined light into three outputs as three orthogonal MOT beams.

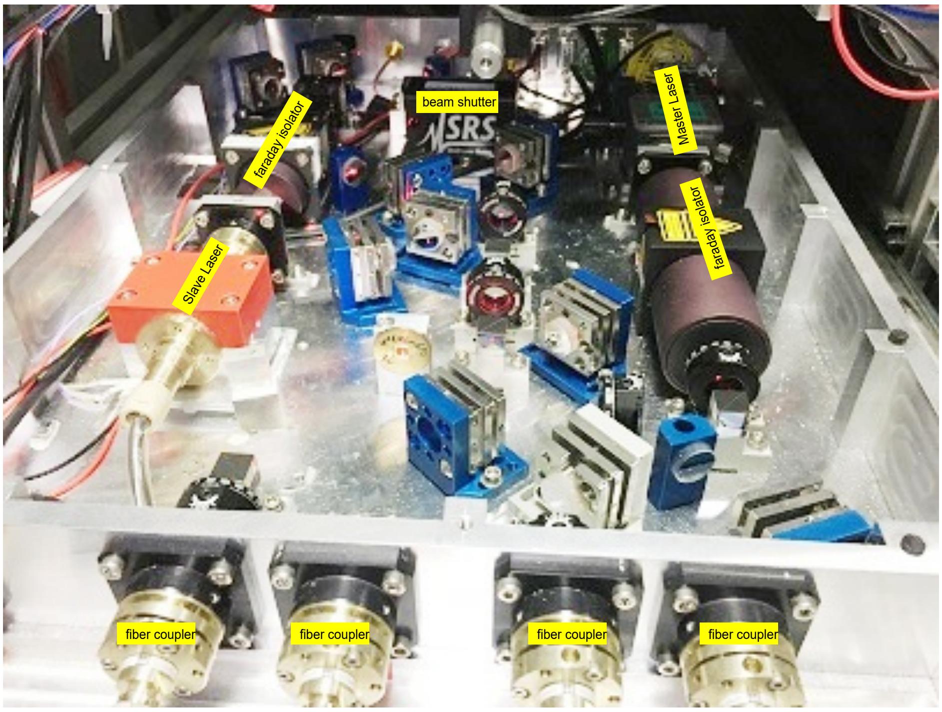

(a) Photo of the red laser distribution breadboard.

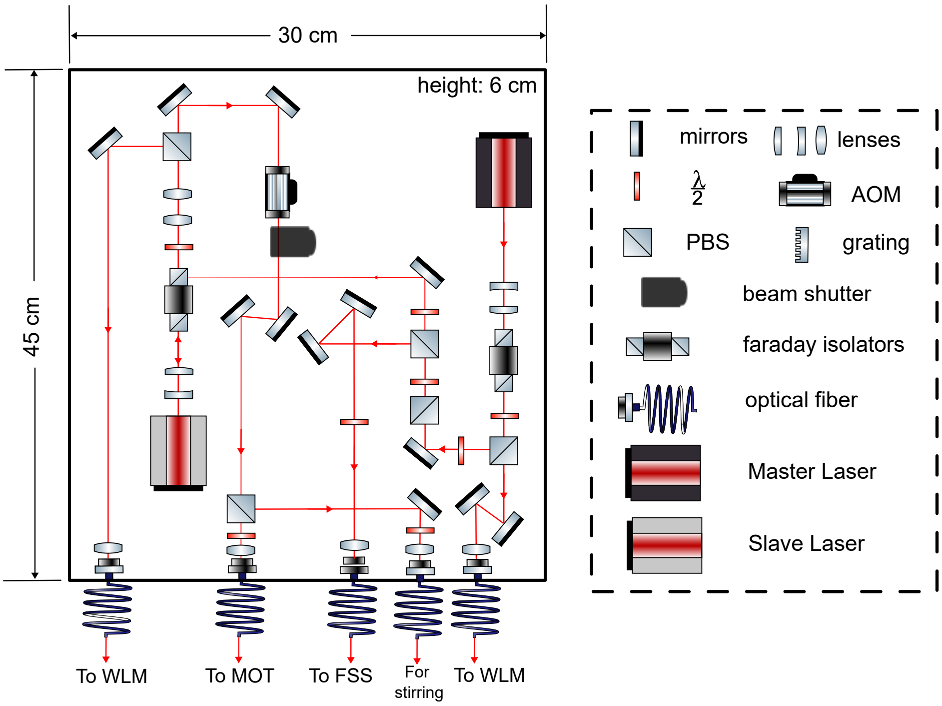

(b) Schematics of the red laser distribution breadboard. The first order diffracted beam of the AOM is shown here. The other beam dumps are left out for clarity.

Figure 3.11: Red laser distribution breadboard. FSS: frequency stabilization system; AOM: acousto-optic modulator; MOT: magneto-optical trap; WLM: wavelength meter; PBS: polarizing beamsplitter.

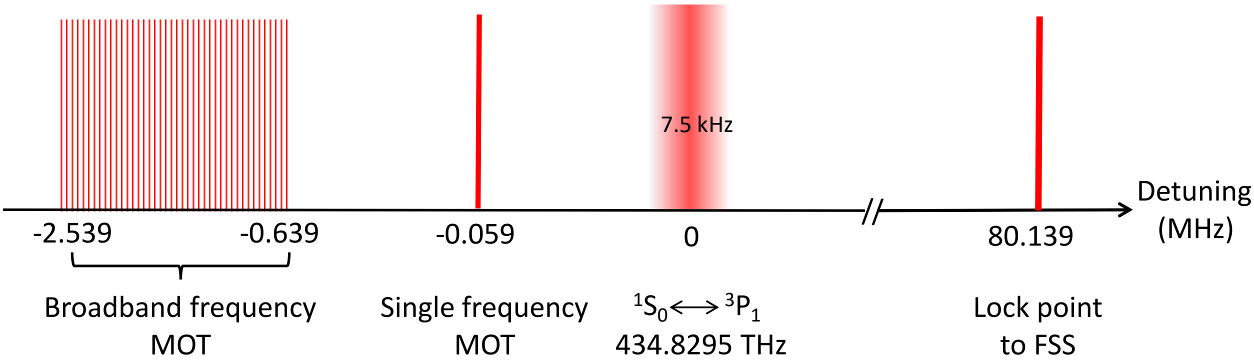

Figure 3.12: Frequency detuning of the red light from the resonance of the $^1S_0 \leftrightarrow {}^3P_1$ transition. The red area at resonance indicates the natural linewidth of the transition. The multiple lines around at 1.5 MHz detuning show the modulated frequency for the first phase of the red MOT. The frequency axis is not to scale. FSS: frequency stabilization system; MOT: magneto-optical trap.

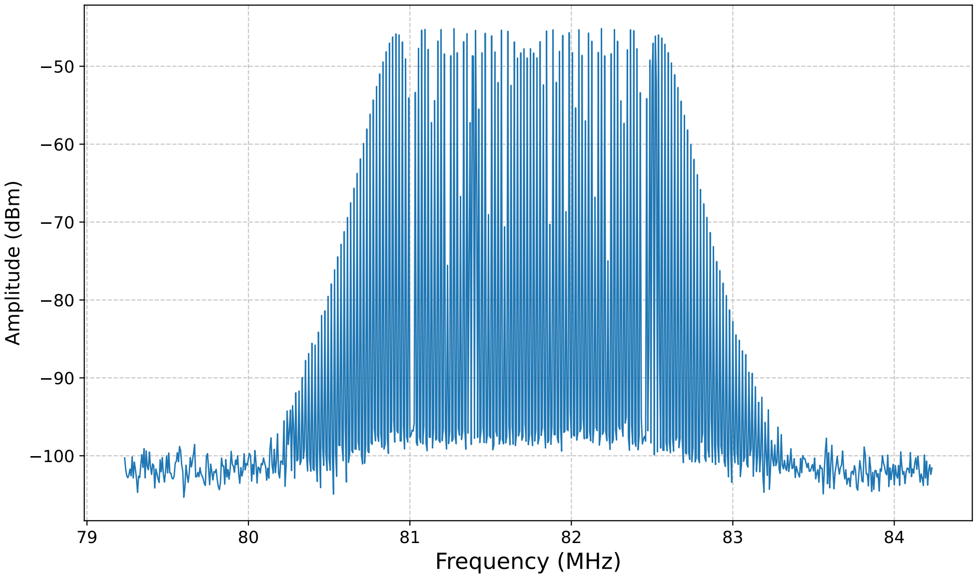

Figure 3.13: RF spectrum of the AOM for the BB red MOT beam. The spectrum analyzer has Resolution Bandwidth (RBW) and Video Bandwidth (VBW) both at 100 Hz. MOT: magneto-optical trap; AOM: acousto-optic modulator; RF: radio frequency; BB: broadband.

Repump laser system (679 nm and 707 nm):

To bring atoms back to the cooling cycle in the first-stage cooling and to repump atoms from the $^3P_0$ state to the $^1S_0$ state via the $^3S_1$ state during the detection phase, the lasers with wavelengths of 707 nm and 679 nm are employed, which address the transitions of $^3P_2 \leftrightarrow {}^3S_1$ and $^3P_0 \leftrightarrow {}^3S_1$, respectively. Both lasers are external cavity diode lasers (ECDLs) from Toptica. The 707 nm and 679 nm laser beams are combined via a PBS and delivered to the cold atoms with a total power of 13 mW via a PM optical fiber. Both lasers have separate optical paths to the wavelength meter via fibers, shown in Figure 3.14.

(a) Photo of the distribution breadboard of the repump lasers.

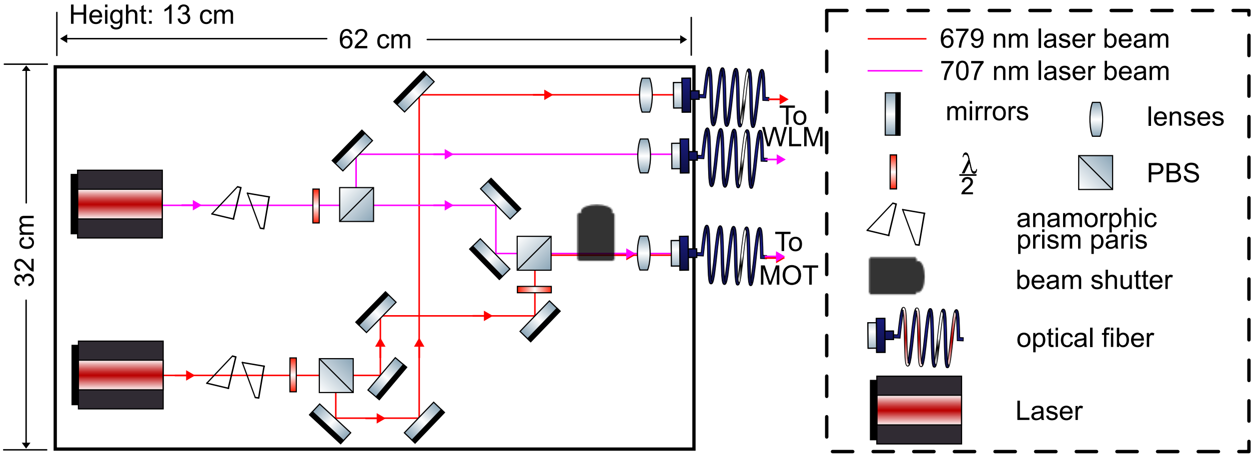

(b) Schematics of the distribution breadboard of the repump lasers.

Figure 3.14: The distribution breadboard of the repump lasers. More details are shown in the text. MOT: magneto-optical trap; WLM: wavelength meter; PBS: polarizing beamsplitter.

Lattice laser system (813 nm):

Our lattice laser system is based on one tapered amplifier (TA) module from Toptica, which includes an 813 nm DL pro diode laser (master laser) and a TA chip. A portion of the master laser beam is delivered to the FSS system, reducing the laser linewidth to a few kHz. Another portion (less than 1 mW) is directed to the wavelength meter for frequency diagnose. The main beam from the master laser serves as seed light for the TA module, producing up to 1.8 W of total output. The TA light then pass through an AOM and couples into a PM fiber (as shown in Figure 3.15). A grating-based filter, as shown in Figure 3.16, is used to suppress amplified spontaneous emission (ASE) due to the tapered amplifier. In the end, approximately 350 mW of laser power constitutes the optical lattice in the science chamber. A photodetector is installed in the lattice laser distribution breadboard to monitor the retro-reflection beam from a hot mirror, which reflects 813 nm light to form the optical lattice with the incoming light, shown in Figure 3.20.

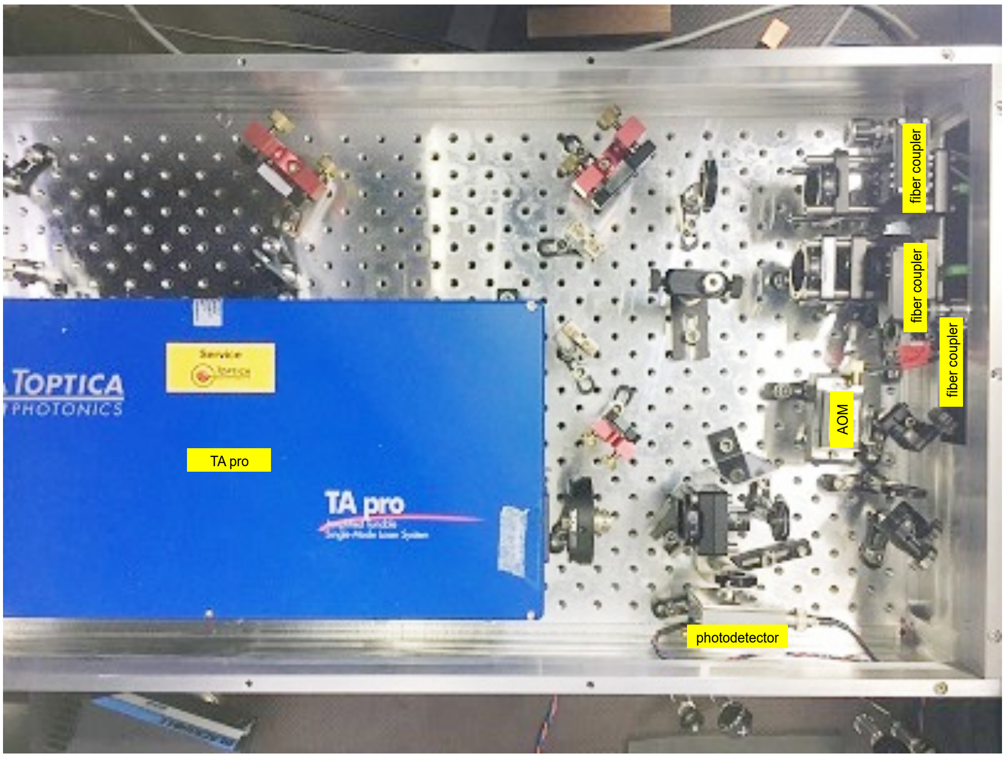

(a) Photo of the lattice laser distribution breadboard.

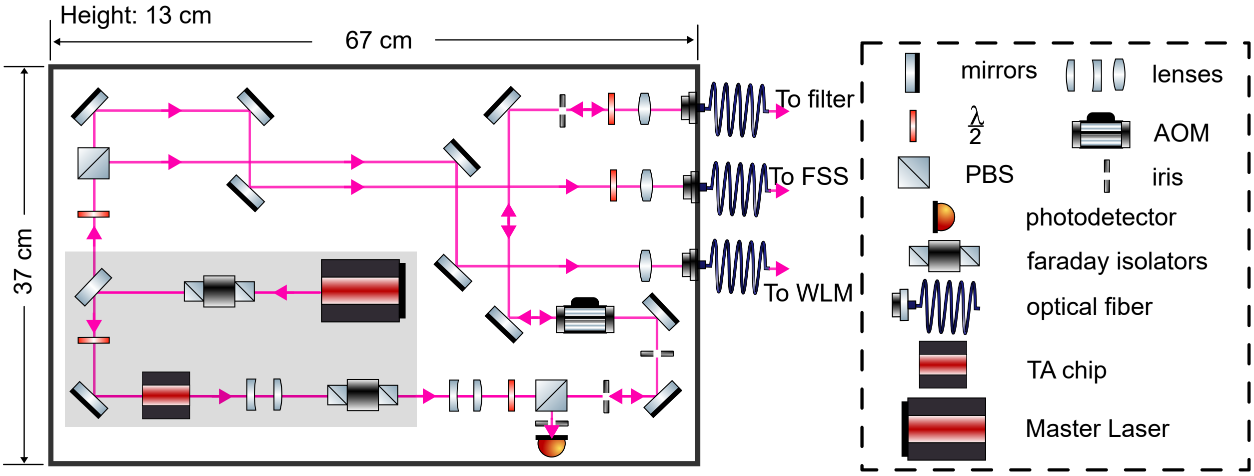

(b) Schematics of the lattice laser distribution breadboard. The first order diffracted beam of the AOM is shown here. The other beam dumps are left out for clarity.

Figure 3.15: Lattice laser distribution breadboard. FSS: frequency stabilization system; AOM: acousto-optic modulator; WLM: wavelength meter; PBS: polarizing beamsplitter; TA: tapered amplifier.

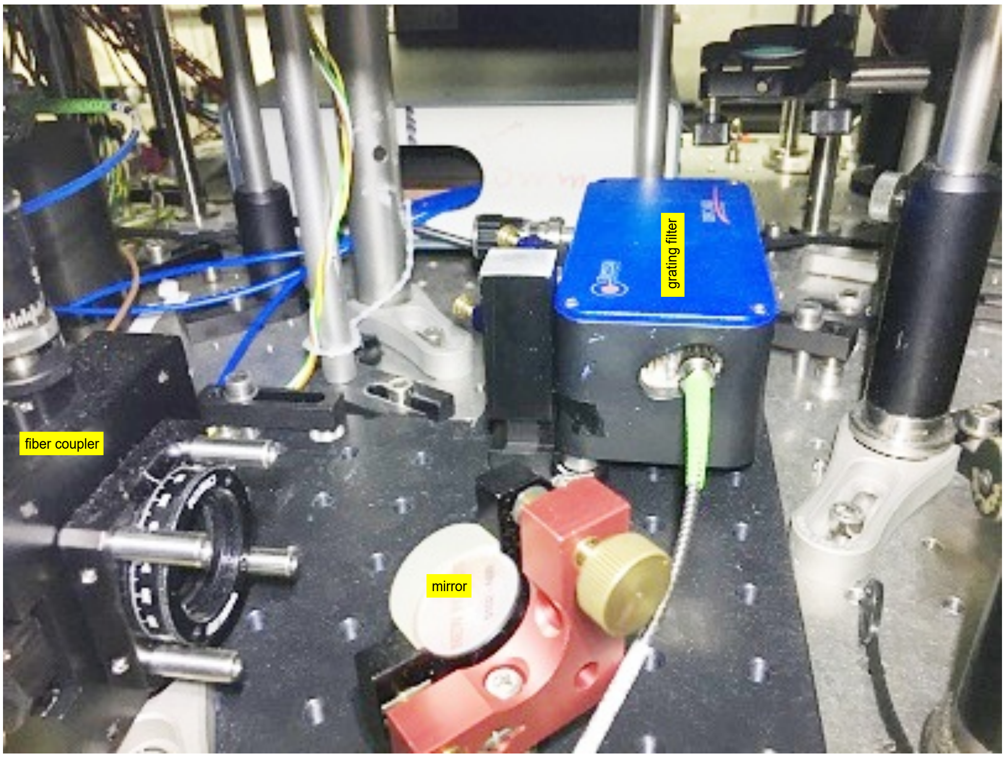

(a) Photo of the distribution breadboard.

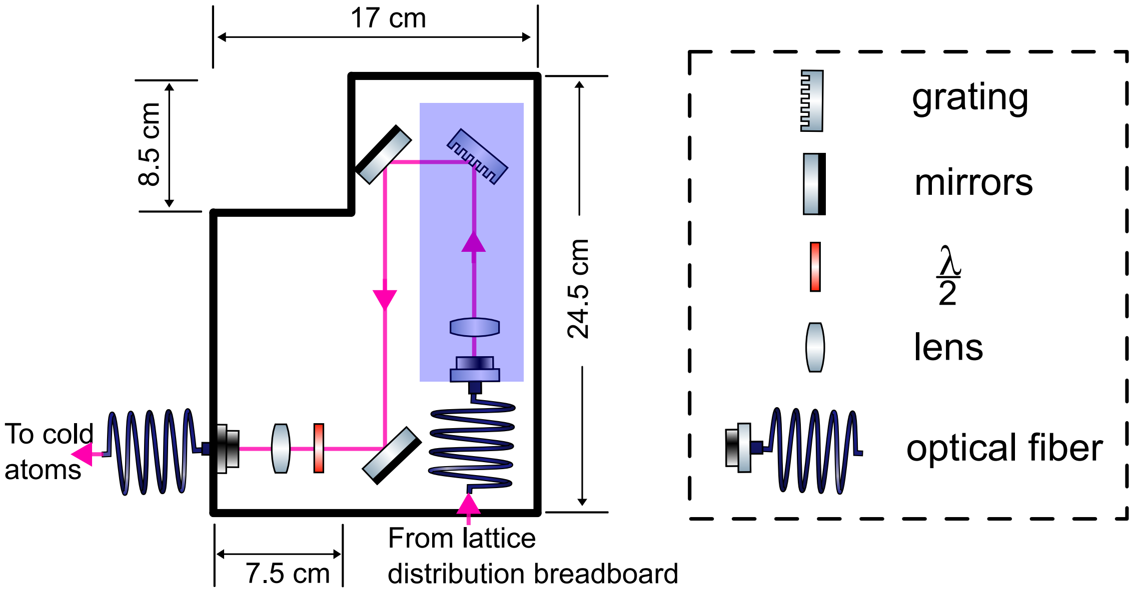

(b) Schematics of the distribution breadboard. The light blue rectangle area shows the filter.

Figure 3.16: The distribution breadboard of the grating-based filter for the lattice light. This filter is used to suppress amplified spontaneous emission (ASE) due to the tapered amplifier (TA).

Clock laser system (698 nm):

A homemade 698 nm laser based on an interference filter (IF) is implemented as the clock laser, shown in Figure 3.17a (inside the white foam box) and red area of Figure 3.17b. The output power of the IF laser is approximately 20 mW. A light leak from the isolator is used to diagnose it by the wavelength meter. The distribution breadboard has three optical paths for a 10 cm long ULE optical cavity [77], the phase locking to a 48 cm long ULE cavity [78], and the interrogation light to cold atoms, as shown in Figure 3.17. Both optical cavities are operated at room temperature. Usually, the 48 cm ULE cavity is further stabilized to a cryogenic single crystal silicon cavity [7] by transfer locking via optical frequency comb and, consequently, has the stability of approximately 4×10^{-17} at $1 \sim 100$ s. Those stabilization links are illustrated in Ref. [29] in detail. Ultimately, our clock laser could provide ultra-stable light to cold atoms with the same performance as the cryogenic silicon cavity. In order to reduce fiber noise, fiber noise cancellations are implemented for the laser beams to the 48 cm long ULE cavity (a light green area in Figure 3.17b) and cold atoms (a gray area in Figure 3.17b).

This distribution breadboard was operated in the daily experiments. However, since mid-2022, the original 10 cm cavity became unavailable. Therefore, we had to modify another 10 cm long ULE optical cavity for our strontium optical clock application, which was originally designed for a calcium lattice clock. At almost the same time, we noticed that the IF laser was no longer as stable as before, as it was running in multiple modes. Therefore, we installed a DL pro from Toptica to replace the IF laser and made slight modifications to the distribution breadboard. The results of the SOC2 clock in Chapters 4 and 5 are obtained using the new 10 cm ULE optical cavity and the DL pro laser; however, the results in Section 3.4 are still acquired with the original configuration.

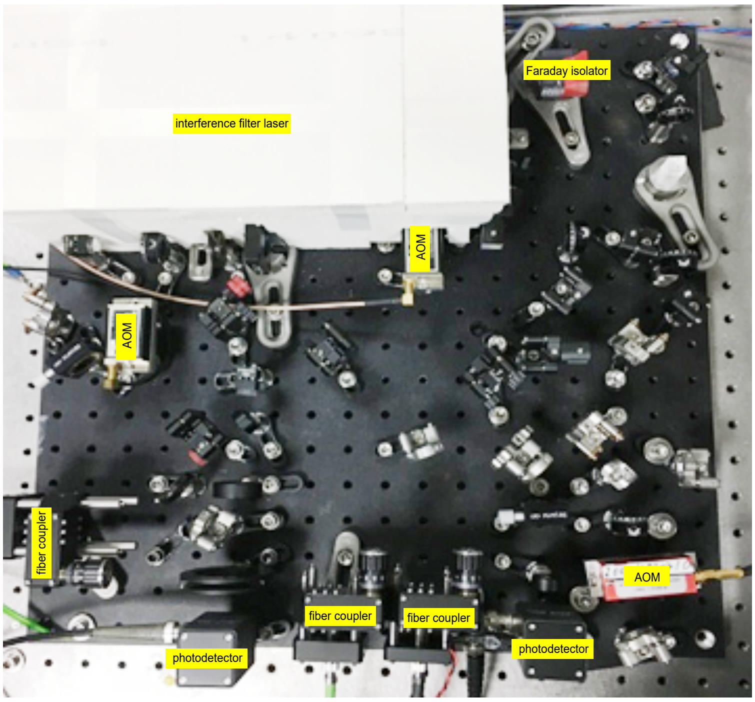

(a) Photo of the distribution breadboard.

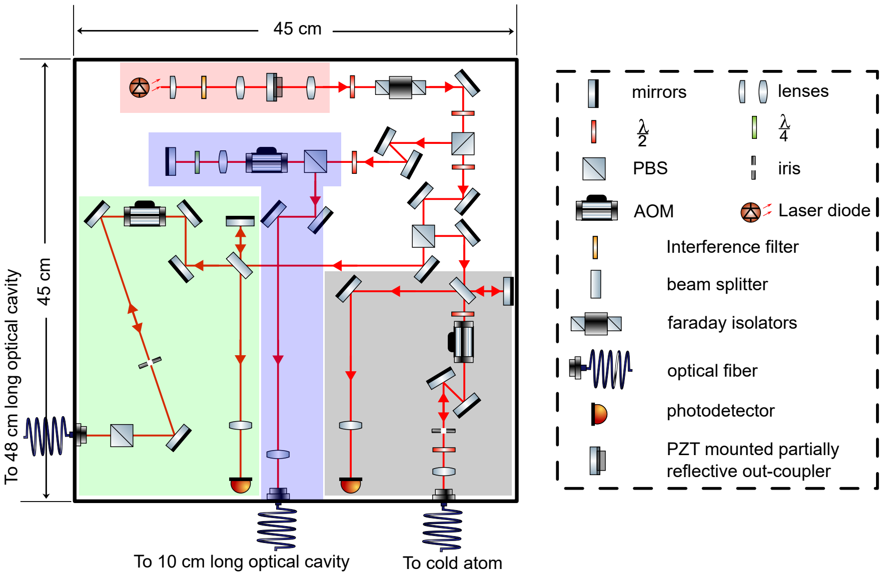

(b) Schematics of the distribution breadboard. The first order diffracted beam of each AOM is shown here. The other beam dumps are left out for clarity.

Figure 3.17: The distribution breadboard of the 698 nm clock laser, which has three optical paths for a 10 cm long ULE optical cavity (light blue area), phase locking to a 48 cm long ULE cavity (light green area), and interrogation light to cold atoms (light gray area). The light red area shows the homemade 698 nm diode laser based on an interference filter. Fiber noise cancellations are implemented for the laser beams to the 48 cm long ULE cavity and cold atoms. AOM: acousto-optic modulator; PBS: polarizing beamsplitter.

Frequency stabilization system (FSS):

As mentioned above, the frequency stabilization system stabilizes the lattice and first- and second-stage cooling lasers via the Pound-Drever-Hall (PDH) technique [74]. There are three cavities in a single ULE block that is sealed in the vacuum together with basic electronics; shown in Figure 3.18a. Theoretically, one cavity in the FSS could stabilize lasers of two different wavelengths, e.g., 813 and 922 nm lasers, 689 and 698 nm lasers, and 679 and 707 nm lasers; therefore, the FSS can stabilize six lasers. However, we only stabilize 813 nm, 922 nm, and 689 nm via the FSS due to the non-necessity to stabilize the 679 and 707 nm lasers and insufficient stability for stabilizing the 698 nm laser.

In the FSS system, the sideband locking technique is employed to bridge the laser frequency and cavity resonance frequency [74]. Each EOM in FSS is modulated with two frequencies, one for bridging the offset ω_{gap} between laser and cavity and another one with minor modulation frequency Ω_{pdh} for PDH locking to sideband at the frequency ω_{gap} from the laser frequency. The main advantage of this technique is that it is easy to change the laser frequency over a few hundred MHz range without losing lock.

Unfortunately, after its operation for a few years, the vacuum of the FSS was gradually worsening and repaired by installing an additional new ion pump, shown in Figure 3.18b. The FSS system can stabilize 689 nm, 813 nm and 922 nm lasers into approximately 1 kHz, a few kHz, and hundreds kHz levels, respectively.

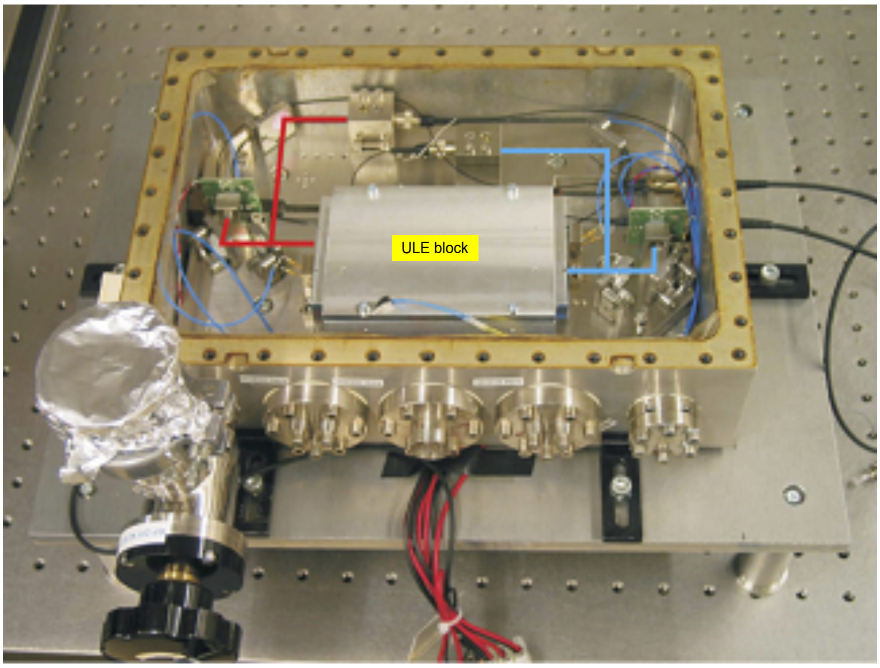

(a) The vacuum chamber[71].

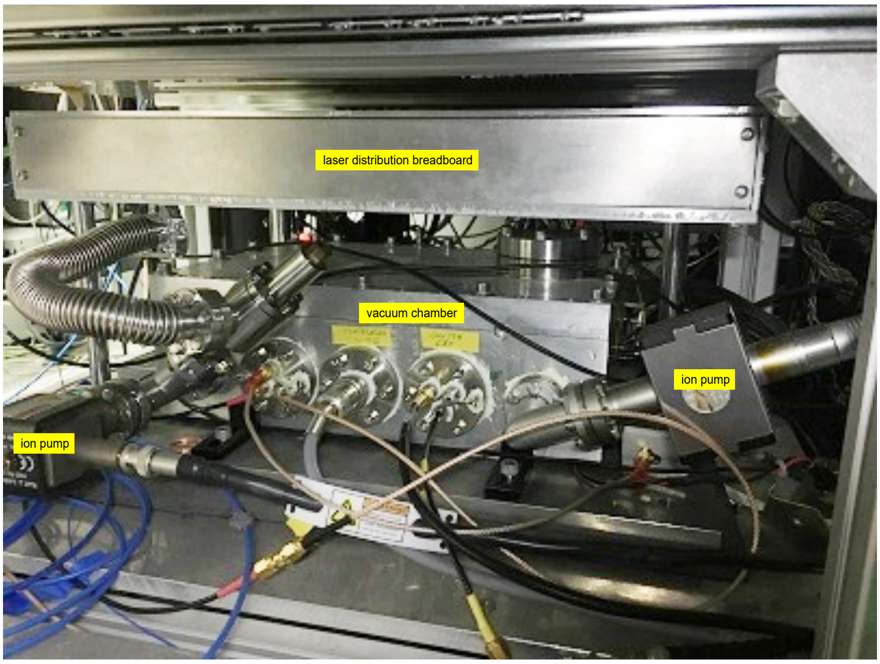

(b) Whole setup with the laser distribution breadboard, vacuum chamber and ion pumps.

Figure 3.18: The frequency stabilization system.

The distribution breadboard for laser frequency diagnosis:

A small portion of power of the 689 nm lasers (master and slave lasers) and repump lasers is delivered to one distribution breadboard for laser diagnosis, shown in Figure 3.19. We combine the 689 nm master and slave lasers and couple the combined light to one scanning Fabry-Pérot interferometer (SA200-5B, Thorlabs) and one fiber for a wavelength meter (WS-6, HighFinesse). The scanning Fabry-Pérot interferometer monitors the laser frequency spectrum to ensure the laser operates in single mode, a crucial tool for verifying the seeding of the injection slave laser. We also combine the repump lasers (679 nm and 707 nm) and couple the light to another scanning Fabry-Pérot interferometer (SA200-5B, Thorlabs) to verify whether the lasers operate in single mode, while both repump lasers have separate optical paths to the wavelength meter to monitor the laser frequency. The diagnosis distribution breadboard is crucial for continuously monitoring the laser frequencies.

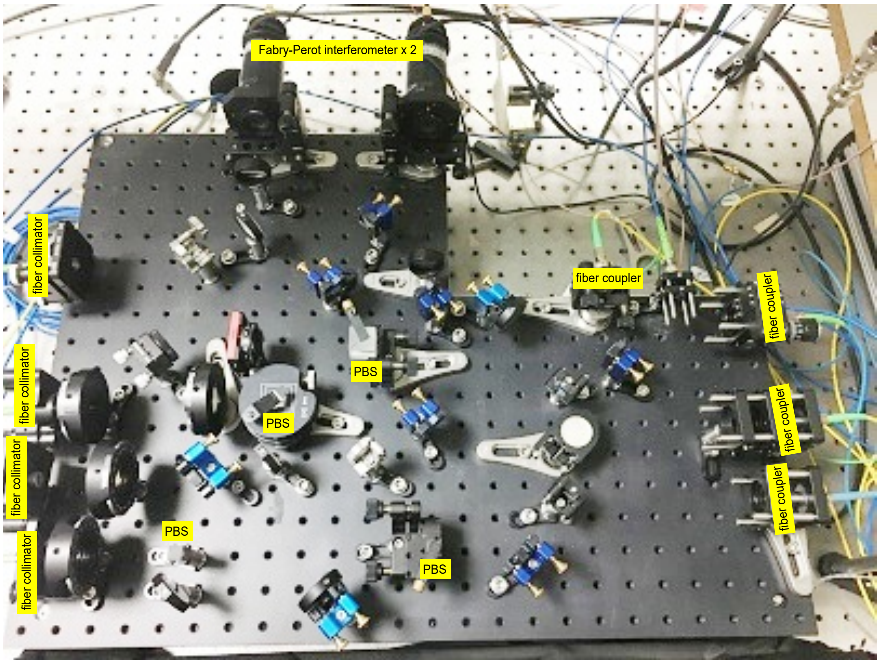

(a) Photo of the distribution breadboard

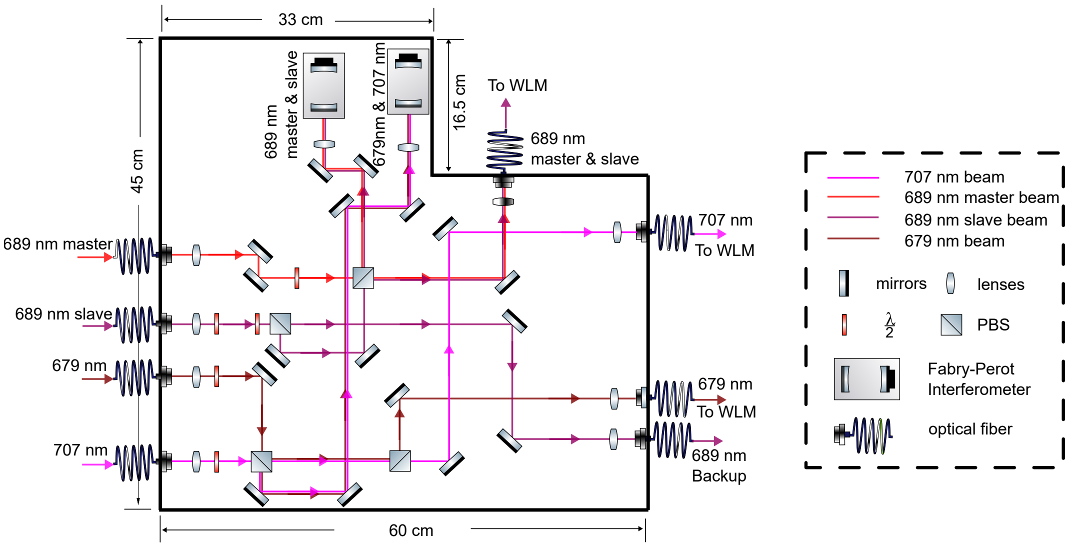

(b) Schematics of the distribution breadboard

Figure 3.19: The distribution breadboard for laser frequency diagnosis of the 689 nm and repump lasers. WLM: wavelength meter; PBS: polarizing beamsplitter.

Lattice and clock laser beams to science chamber:

The lattice laser beam is delivered from the lattice laser distribution breadboard via a PM fiber to the cage system, which is attached to the science chamber. Then the lattice beam is collimated using a lens with a focal length of 6.2 mm, passes through additional optics, then is focused at the center of the science chamber with a waist approximately 35 µm by a 75 mm lens. In order to form an optical lattice, another lens with a 75 mm focal length and a hot mirror are installed to provide the retro-reflection beam. The hot mirror can reflect the lattice laser beam (813 nm) and transmit the clock laser beam (698 nm) to easily overlap those two beams. The schematics of the optics of the clock laser beam are similar to that of the lattice beam, except for the propagation direction and the beam shaping lenses. The lattice beam propagation direction is from the bottom to the top of the science chamber; however, the clock beam direction is from the top to the bottom. Ultimately, the beam waist of the clock beam is approximately 110 µm after passing through the lens with a focal length of 75 mm. In order to stabilize the clock and lattice beam power, four photodetectors are installed to monitor the beam power within and outside the stabilization loop, respectively. The schematics are shown in Figure 3.20, and some details can also be found in Ref. [29].

Fluorescence collection systems:

In order to observe the atomic transition, the fluorescence from spontaneous emission is typically employed because of its convenience and simplicity. In our setup, there are two devices with dedicated optics to collect atomic fluorescence: PMT (Hamamatsu H11526-110-NF) and the CCD camera (pco.pixelfly USB) which are attached to the science chamber via the cage systems, as shown in Figures 3.7 and 3.20.

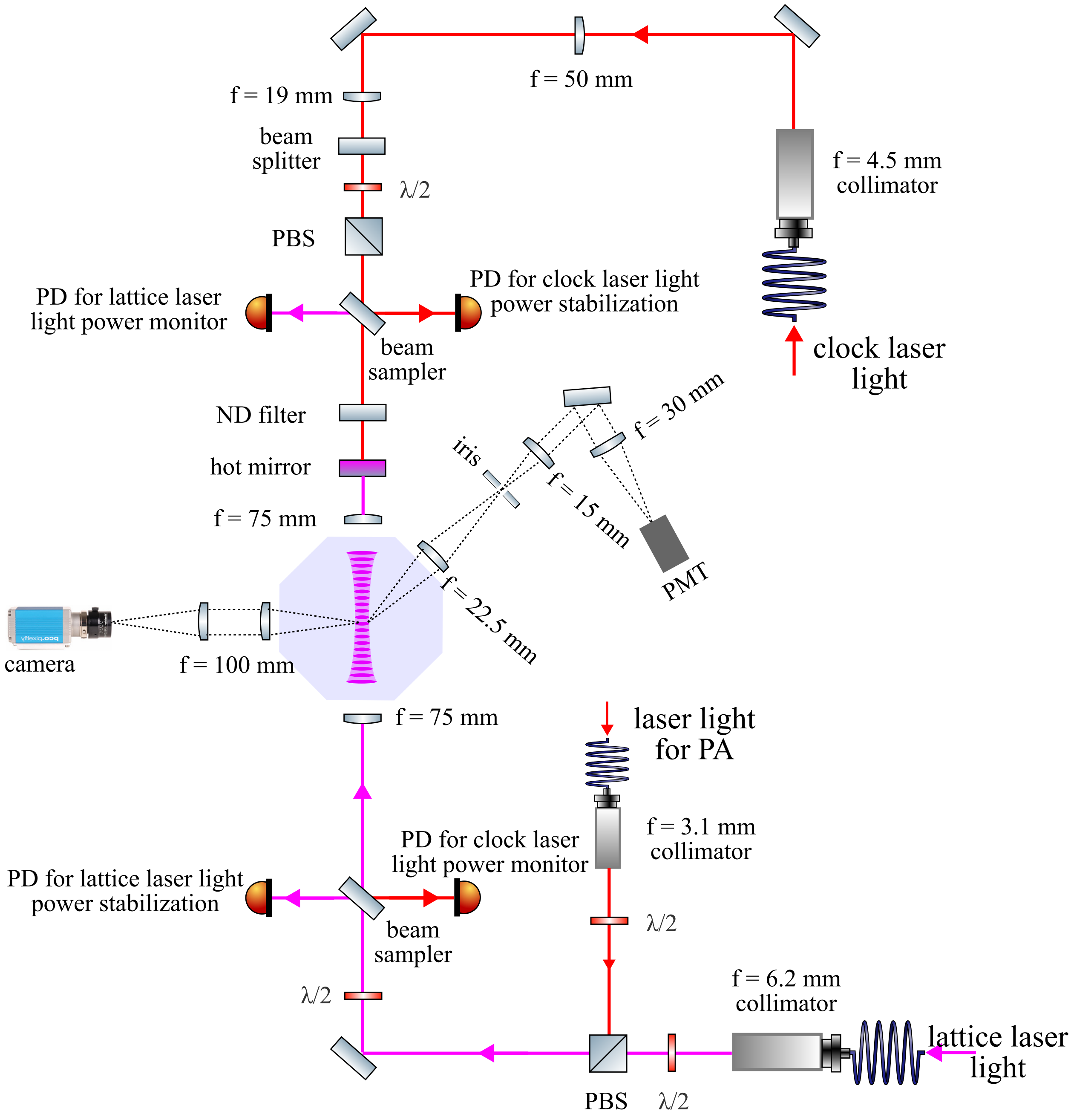

Figure 3.20: Schematics of the optics for the lattice and the clock beams to the science chamber and the fluorescence collection systems. The lattice beam propagation direction is from the bottom to the top of the science chamber; however, the clock beam direction is from the top to the bottom. The laser light for PA is only used in Section 6.4 of this dissertation. More details show in the text. PBS: polarizing beamsplitter; PD: photodetector; ND: neutral density; PMT: photomultiplier; PA: photoassociation.

Major upgrades of laser systems:

Several upgrades have been implemented since 2018: **1)** Rebuild all laser distribution breadboards except the red cooling distribution breadboard, especially building a compact distribution breadboard for the two repump lasers to replace two separated distribution breadboards. **2)** Build a new diode laser based on an interference filter that is used for probing the clock transition. **3)** Build a new diagnostic distribution breadboard for the 689 nm lasers (master and slave lasers) and the 679 nm and 707 nm lasers (repump lasers) to continuously monitor laser frequency. **4)** Implement an independent detection beam to replace the previous scheme, which used two MOT beams as detection beams. **5)** Install the new CCD camera and PMT with newly designed optics for fluorescence collection. **6)** Add a blue laser beam to implement transverse cooling after the oven to increase atom flux to the science chamber. **7)** Upgrade the vacuum system of the FSS by adding a new ion pump.

3.4 Experimental methods and results

3.4.1 Timing sequence of the clock operation

The clock operation generally has six phases in one clock cycle; see Figure 3.21.

- **A: Atom loading and blue MOT.** The hot atomic beam is effused from the oven and slowed by the Zeeman slower beam. The slowed atoms are then captured by the blue MOT, which is called the atom loading and blue MOT phase.

- **B: Low-power blue MOT.** At the end of the blue MOT stage, the blue MOT beam power is reduced to allow the atom cloud to expand by itself; consequently, atoms can reach a lower temperature, $\sim 1\,\mathrm{mK}$. This stage is called the low-power blue MOT phase. In this phase, the atomic beam shutter, transverse cooling beam, and Zeeman slower beam are switched off, and the power of the blue MOT beam is gradually decreased through two steps. Each step has 4 ms duration. During these first two phases, repump beams should be applied to drive the atoms from the dark states back to the cooling cycle; more details are shown in Section 2.2. The repump beams are turned off before transferring to the red MOT phase.

- **C: Broadband red MOT.** After cooling atoms to approximately 1 mK, the atoms are transferred to the second cooling and trapping stage, called red MOT, which uses $^1S_0 \leftrightarrow {}^3P_1$ transition with a linewidth of 7.5 kHz. In order to cover more atoms with different velocities, we first modulate the frequency of the red laser from the original

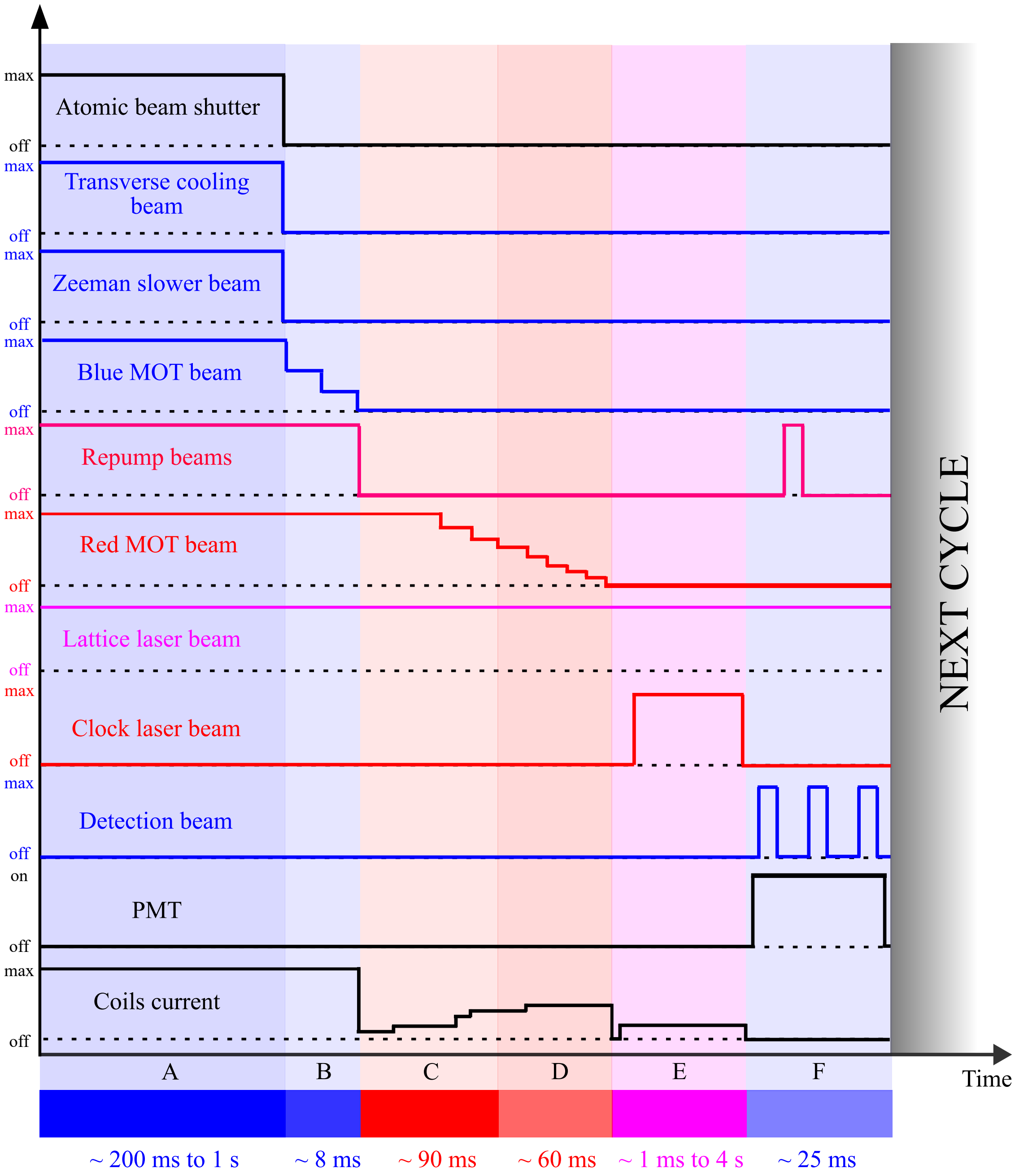

Figure 3.21: Timing sequence of the clock operation. A-F shows the different phases of the operation. A: atoms loading and blue MOT. B: low-power blue MOT. C: broadband red MOT. D: single-frequency red MOT. E: interrogation. F: detection. The color bars at the bottom of the diagram show the different phases of a clock cycle. The numbers under the color bar are the time duration of each phase. The y-axis shows the power of each laser beam or the strength of the coils current. For PMT, the y-axis shows the PMT on or off. *'max'* means the laser beam power at maximum value, and *'off'* means the laser beam is turned off. PMT is photomultiplier tubes. The axes are not scaled. More details in text.

linewidth of 1 kHz to 1.9 MHz via an AOM, shown in Section 3.3. This is the first step of the second cooling and trapping stage, called broadband red MOT. During the blue MOT phases, the broadband red MOT beams are also maintained to cool atoms to even lower temperatures and enhance the transfer efficiency of atoms from the blue MOT to the red MOT.

- **D: Single-frequency red MOT.** The second step of the second cooling and trapping stage is the single-frequency red MOT phase, in which the frequency of the red laser is without modulation, and atoms can be cooled down to a few microkelvin (µK).

- **E: Interrogation.** When the atom temperature reaches a few µk, we switch off the red MOT beam and load the atoms into an optical lattice, in which the atom temperature is approximately a few µK.

  During the phases of blue and red MOTs, the magnetic field coils are in the anti-Helmholtz configuration to create the quadrupole magnetic field for MOTs. However, during the atoms and probe laser (clock laser) interaction phase, called the interrogation phase, the atoms should sit in a homogeneous magnetic field (also named bias field) created by configuring the magnetic field coils in Helmholtz configuration. Due to the relaxation procedure of changing the coils from anti-Helmholtz configuration to Helmholtz configuration, we switch on the coil current 100 ms ahead of the clock laser pulse. The pulse length depends on the Rabi frequency, which should always be a π pulse during clock operations.

- **F: Detection.** The detection phase follows the interrogation phase, which typically consists of three pulses to determine the excitation probability p_e. The first pulse is to detect the atoms in the ground state $^1S_0$ and the PMT-collected fluorescence signal s_g is proportional to the atom number in the ground state. All the atoms in the ground state are kicked out of the optical lattice trap by the strong interaction with the detection pulse. Before the second pulse, the repump lasers are turned on to pump the atoms from the excited state $^3P_0$ to the ground state $^1S_0$ via intermediate state $^3S_1$. After all the atoms from the excited state are transferred to the ground state, the second pulse is applied to detect atoms in the ground state. Hence, the fluorescence signal s_e collected from PMT is now proportional to the atom number in the excited state. The third pulse is used to obtain the background signal s_{bk} from the stray light of the detection beam. According to those three signals, the excitation probability can be calculated by

  $$p_e = \frac{s_e - s_{bk}}{s_e + s_g - 2s_{bk}} \tag{3.2}$$

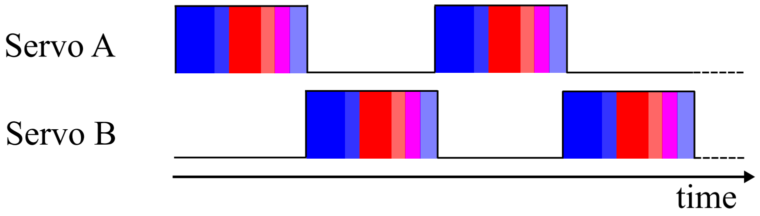

Figure 3.22: Timing sequence of interleaved measurements. Servo A and B are independent locking servos, which alternatively probe atoms. Usually, servo A and B have different experimental conditions. Color bars show the different phases of the single operation, which are A-F in Figure 3.21. Servo A and B are also called cycle A and B sometimes in the following text.

Figure 3.21 shows the timing sequence of the clock operation. We program the timing sequence based on LabVIEW according to the timing diagram and upload it into an FPGA (NI-PXI-7842R from National Instruments) to control all the devices for the sequence, e.g., the AOMs and the laser beam shutters in the diagram.

Timing sequence of interleaved measurements

To evaluate the systematic effects, interleaved measurements are applied, which include two independent locking servos, servo A and B, shown in Figure 3.22. Usually, servo A and B alternatively probe atoms under different experimental conditions. For example, servo A has probe light intensity I_a, while servo B has probe light intensity I_b to evaluate the probe light AC Stark shift, shown in Chapter 5. Servo A and B are also called cycle A and B sometimes in the following text.

3.4.2 The time-of-flight method

The atom temperature is crucial for ultra-cold atom experiments, e.g., optical lattice clocks, atom interferometers. How can we evaluate the temperature of atoms in the MOT? We usually use the time-of-flight method (TOF), which investigates the cloud size evolution related to the atom temperature when a cold atomic cloud expands in the absence of magnetic and laser light fields. We assume that the atom cloud has a Gaussian distribution due to the Gaussian intensity distribution of the MOT beams. The relation between the cloud size and the temperature is [79]

$$\sigma^2(t) = \sigma_0^2 + \frac{k_B T}{m} t^2 \tag{3.3}$$

where $\sigma(t)$ is the standard deviation of the atom cloud size at flight time t, σ_0 is the standard deviation of the atom cloud size at $t = 0$, k_B is the Boltzmann constant, m is atomic mass, and T is the atom temperature. Here, we only discuss the atom temperature in the MOTs and ignore the effects of gravity.

3.4.3 The first stage MOT

The first stage MOT has two phases: blue MOT and low-power blue MOT, shown in Figure 3.21. We use 3 mW for each pair of MOT beams with the saturation parameter $s = 0.18$ and the magnetic field gradient of 45 G/cm. Based on TOF measurements, the atoms are cooled to 4.9(4) mK on the x-axis and 5.0(9) mK on the y-axis in the blue MOT, shown in Figure 3.23.

The blue MOT is followed by the low-power blue MOT, in which we lower the MOT beam power to lower the trap potential and let the atomic cloud expand by itself and the hot atoms out of the trap. Ultimately, cold atoms can reach a temperature below the Doppler limit, for example, the temperature is typically 561(21) µK on the x-axis and 635(63) µK on the y-axis for our experiments, as shown in Figure 3.24.

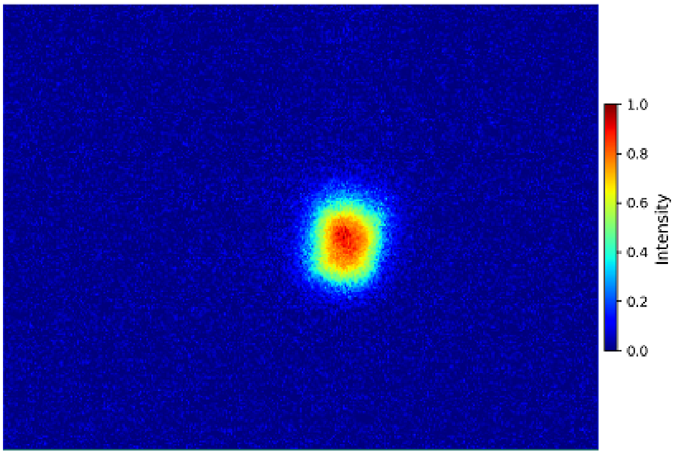

(a) The image of the blue MOT with waiting time $t = 0.5\,\mathrm{ms}$.

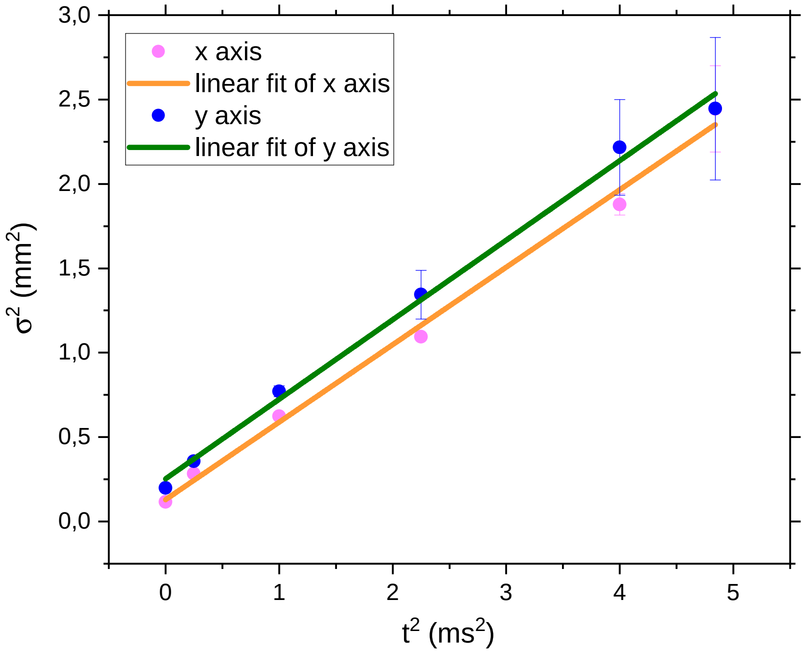

(b) TOF measurements of the blue MOT. The temperature of the cold atom cloud is 4.9(4) mK on the x-axis and 5.0(9) mK on the y-axis determined from the linear fits of Eq. 3.3.

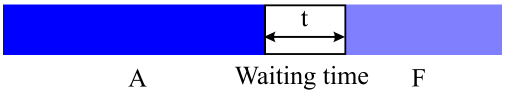

(c) The timing sequence of the TOF measurement of blue MOT. A: atoms loading and blue MOT, F: detection phase; more details in Figure 3.21.

Figure 3.23: The time-of-flight (TOF) measurement of the blue MOT.

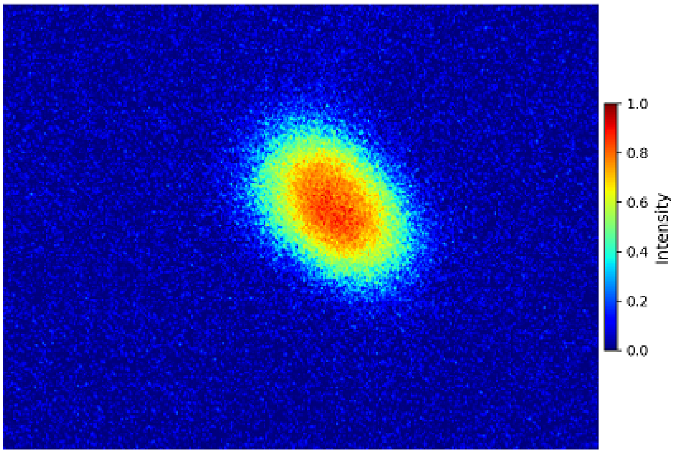

(a) The image of the low-power blue MOT at $t = 0\,\mathrm{s}$.

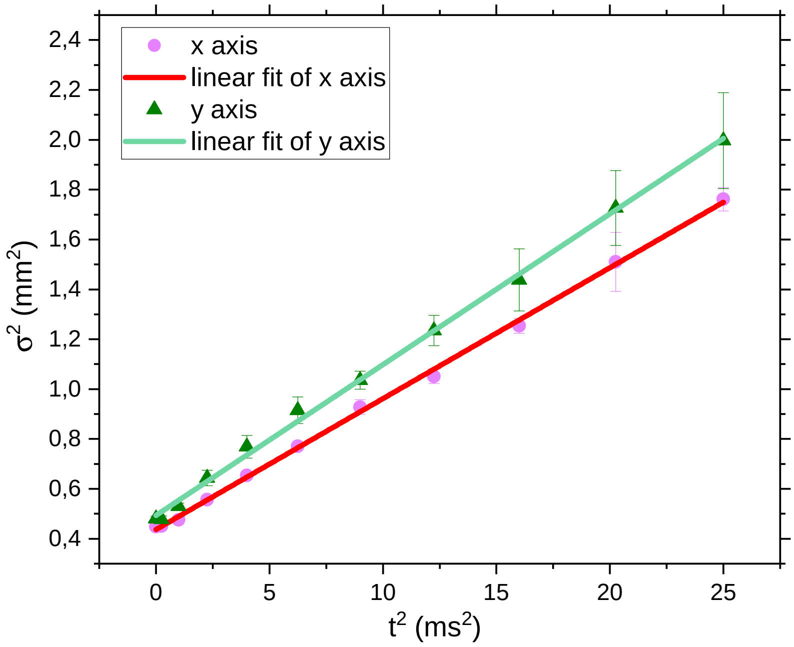

(b) TOF measurements of the low-power blue MOT. The temperature of the cold atom cloud is 561(21) µK on the x-axis and 635(63) µK on the y-axis determined from the linear fits of Eq. 3.3.

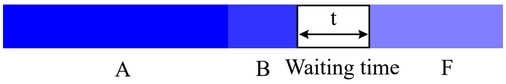

(c) The timing sequence of the TOF measurement of the low-power blue MOT. A: atoms loading and blue MOT, B: low-power blue MOT, F: detection phase; more details in Figure 3.21.

Figure 3.24: The time-of-flight (TOF) measurement of the low-power blue MOT.

3.4.4 The second stage MOT

The second stage MOT has two phases: broadband red MOT and single-frequency red MOT. In the broadband red MOT, we modulate the frequency of the red MOT beam to cover cold atoms with various velocities as broadly as possible, which can increase the transfer efficiency from the low-power blue MOT to the red MOT. The frequency spectrum and detuning are shown in Figure 3.12 and 3.13. Meanwhile, the magnetic field is gradually increasing to compress the atomic cloud. The atom temperature can reach less than 100 µK in the broadband red MOT. The deformation of the cold atomic cloud in BB red MOT is observed due to gravity, shown in Figure 3.25a. Hence, the temperature of the x-axis, which is parallel to gravity, is not evaluated by the TOF measurements. The temperature of 95(11) µK on the y-axis is obtained, shown in Figure 3.25.

To make the atoms even colder and be able to load them into an optical lattice, we implement the single-frequency red MOT. During this process we stop the modulation of red MOT beams, lower the beam power, and increase the magnetic field gradient. Figures 3.26 and 3.27 show the shape evolution of the cold atomic cloud in single-frequency red MOT with increasing frequency detuning and TOF waiting time, respectively. Shape deformations are significantly observed in these cold clouds due to the influence of gravity. The atom temperature can reach a few µK after the single-frequency red MOT phase. The atoms can be easily loaded into an optical lattice.

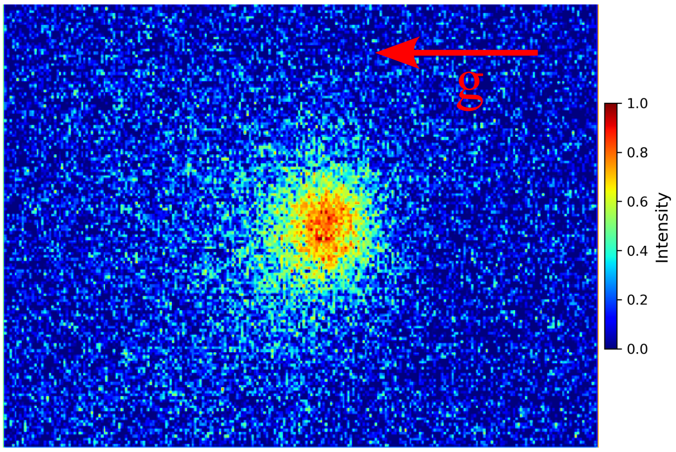

(a) The image of the broadband red MOT.

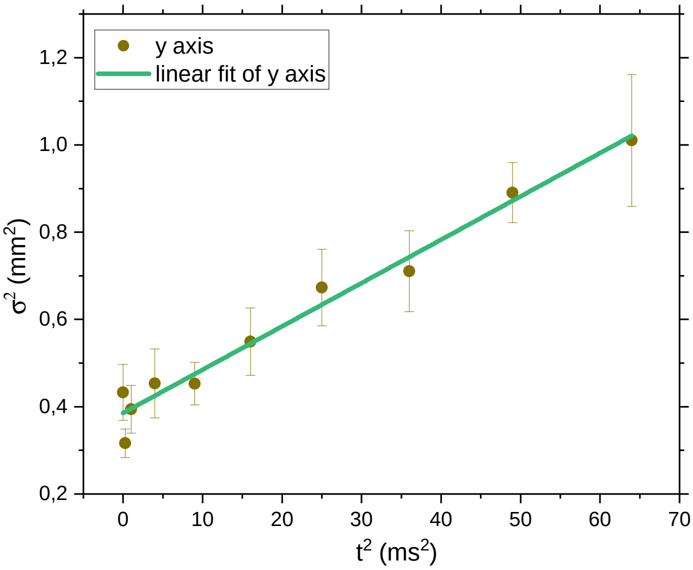

(b) TOF measurements of the broadband red MOT. The temperature of the cold atom cloud is 95(11) µK on y-axis from the linear fit of Eq. 3.3.

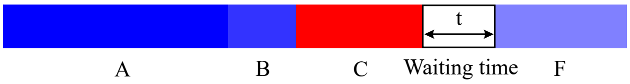

(c) The timing sequence of TOF measurement of broadband red MOT. A: atoms loading and blue MOT, B: low-power blue MOT, C: broadband red MOT, F: detection; more details in Figure 3.21.

Figure 3.25: The time-of-flight (TOF) measurements of the broadband red MOT. The temperature on the y-axis is only shown here. An appropriate Gaussian fit cannot be obtained since cold atoms drop along the x-axis, which is aligned with the gravity direction, shown in the image in (a). The arrow g indicates the direction of gravity in (a).

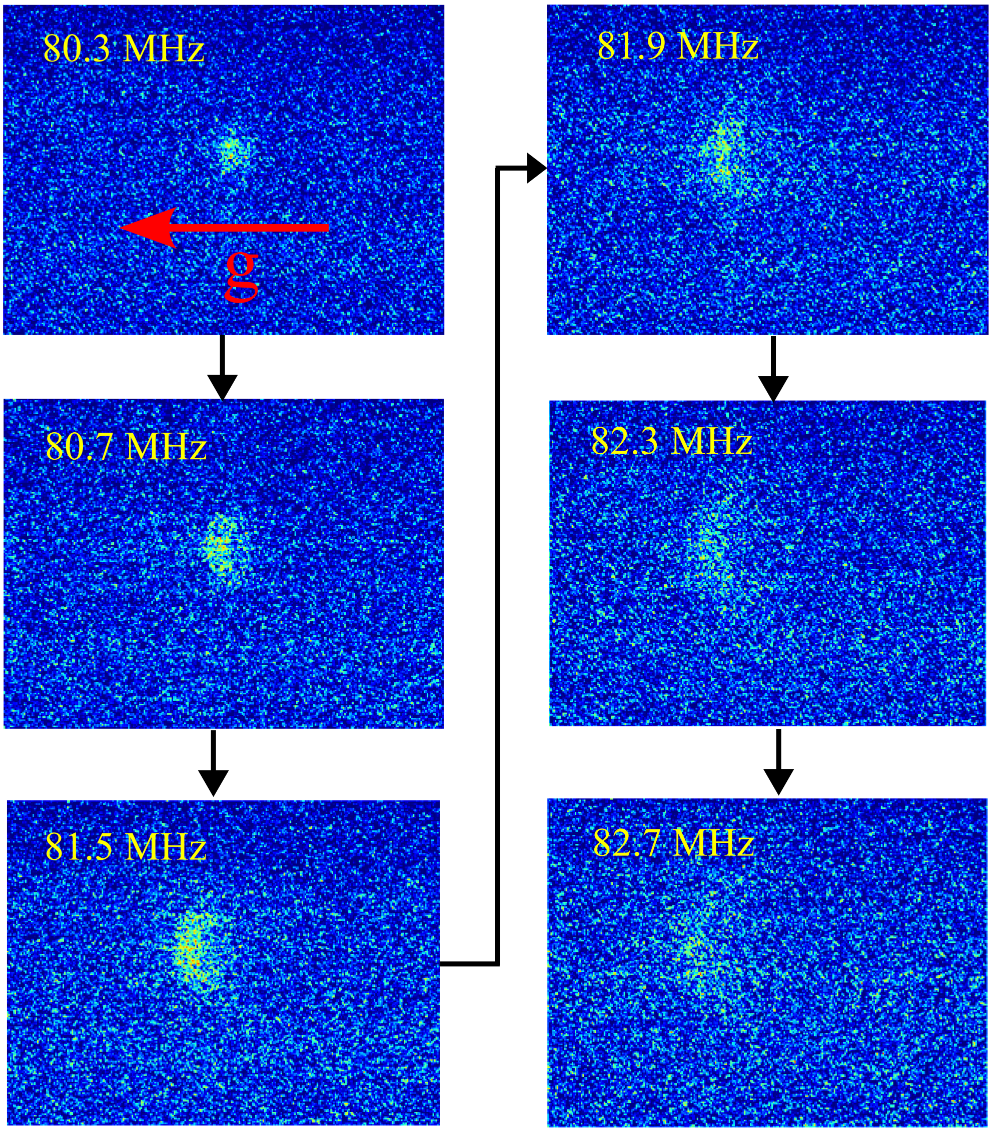

Figure 3.26: The shape evolution of the cold atomic cloud in the single-frequency MOT with increasing red detuning from the resonance of ${}^1S_0 \leftrightarrow {}^3P_1$ transition. The frequency on the top left corner of each image shows the AOM frequency modulating the red MOT beam, shown in Figure 3.11 and 3.12. The arrow g indicates the direction of gravity.

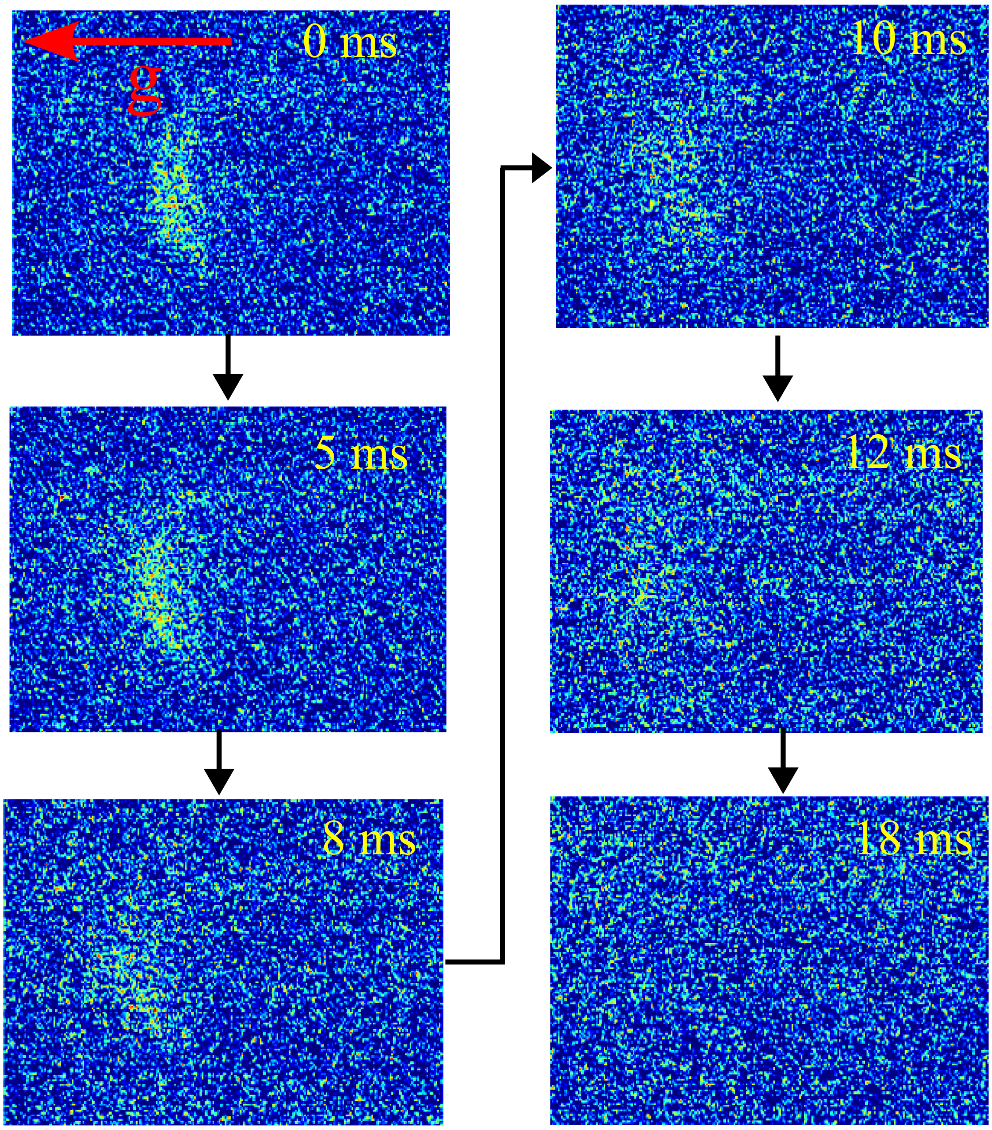

Figure 3.27: The shape evolution of the cold atomic cloud in the single-frequency MOT during the time-of-flight (TOF). The arrow g indicates the direction of gravity.

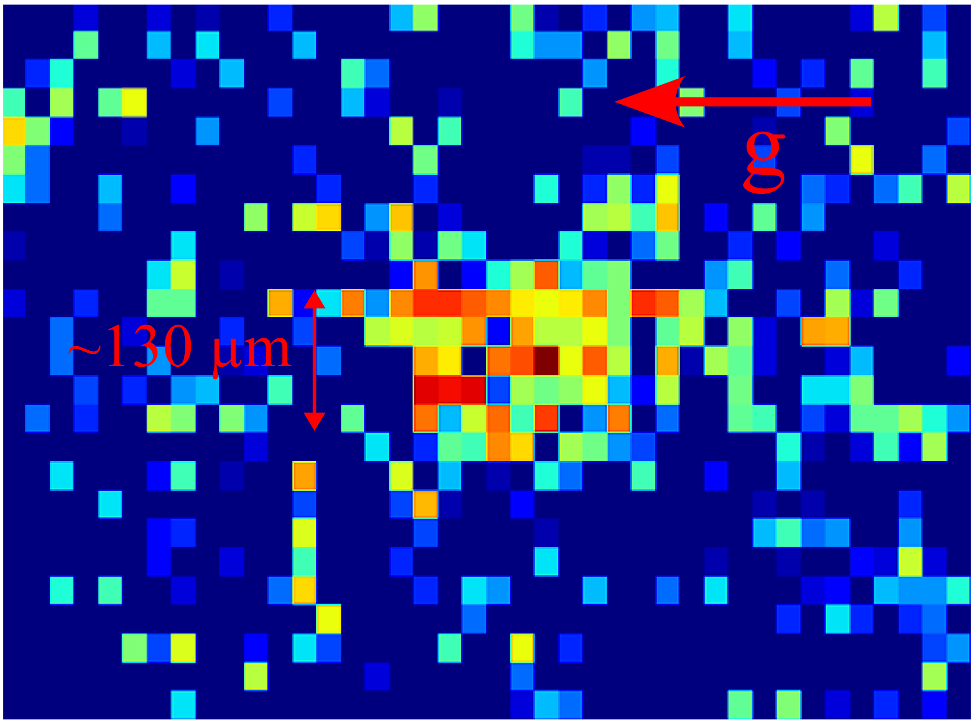

Figure 3.28: An image of the optical lattice. The arrow g indicates the direction of gravity.

3.4.5 Optical lattice

After the single-frequency red MOT phase, atoms can be loaded into the optical lattice with a trap potential of a few µK, then the magnetic field and MOT beams can be switched off. The fluorescence image of the atoms in the optical lattice is shown in Figure 3.28. The lattice beam is aligned with the gravity direction (x-axis in the image). Therefore, the atoms are a bit more widely spread on the x-axis. The fluorescence signal collected by the PMT is used to calculate the atom number in the optical lattice by carefully considering the radiant sensitivity of the PMT, the solid angle of the collection system optics, and other factors. The atom number is approximately 6.2×10^3 in the optical lattice with a depth of $\sim 410\,E_r$. Here, the lattice depth is estimated by the lattice laser beam power and the efficiencies of the optical path. The atom temperature in the lattice can be evaluated by sideband spectroscopy of the clock transition [58], which can also be used to evaluate the lattice depth, shown in Figure 3.33.

3.4.6 Observation of the clock transition

Overlapping between clock and lattice laser beams

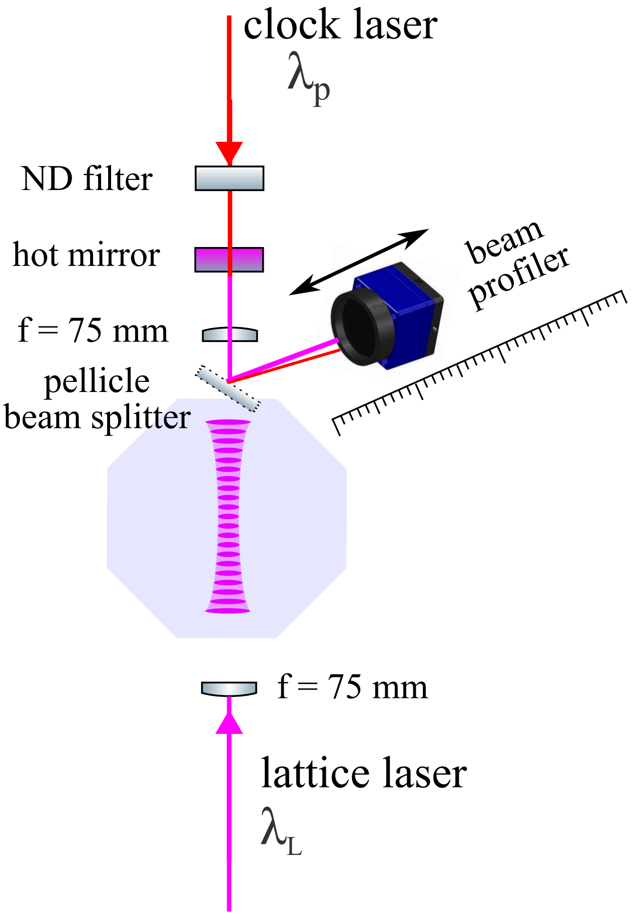

Figure 3.29: Overlapping measurement scheme. A beam profiler is used to check the beam spot offset between clock and lattice laser beams at different positions along the beam axis.

The overlap between the clock and the lattice laser beams is critical for the clock transition and coherence time as shown in Figure 2.5. To accurately measure the misalignment angles between clock and lattice laser beams, we insert a pellicle beam splitter between the upper 75 mm lens and top window of the science chamber and use a beam profiler(CinCam CMOS-1201-Pico) from Cinogy Technologies to check the beam spot offset between clock and lattice laser beams at different positions along the beam axis, shown in Figure 3.29; then fit the offset data (see Figure 3.30). Here I give the misalignment angles along with the x and y axes and the long-term drift of the angles, shown in Figure 3.31. The angles are ≤ 0.1 mrad and meet the requirement of clock transition excitation, which is discussed in Section 2.3.2.

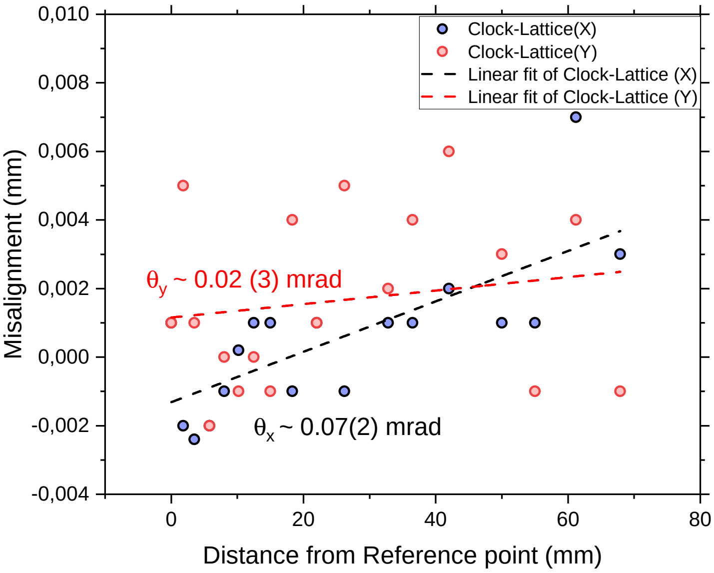

Figure 3.30: The offset and misalignment angles between the clock and lattice laser beam axes. θ_x and θ_y are the misalignment angles along x and y axes, respectively. Both angles are less than 0.1 mrad, which meets the requirement of clock transition excitation.

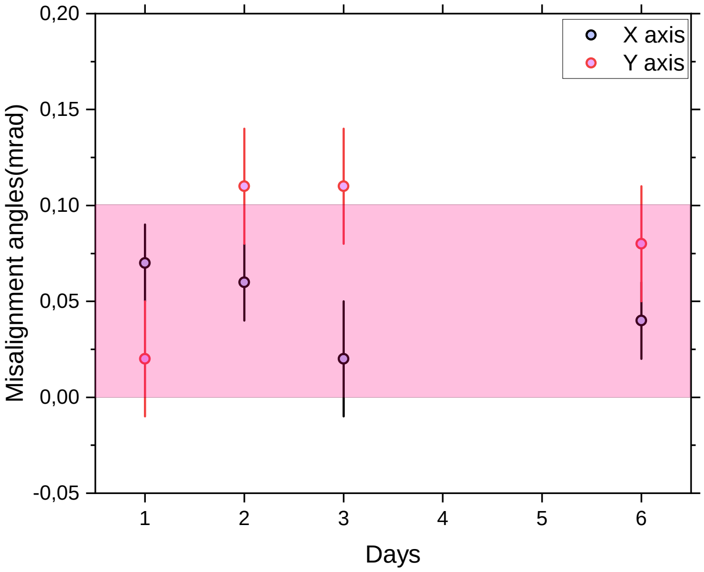

Figure 3.31: The long-term drift of the misalignment angles between the clock and lattice laser beam axes. The angles are ≤ 0.1 mrad and meet the requirement of clock transition excitation.

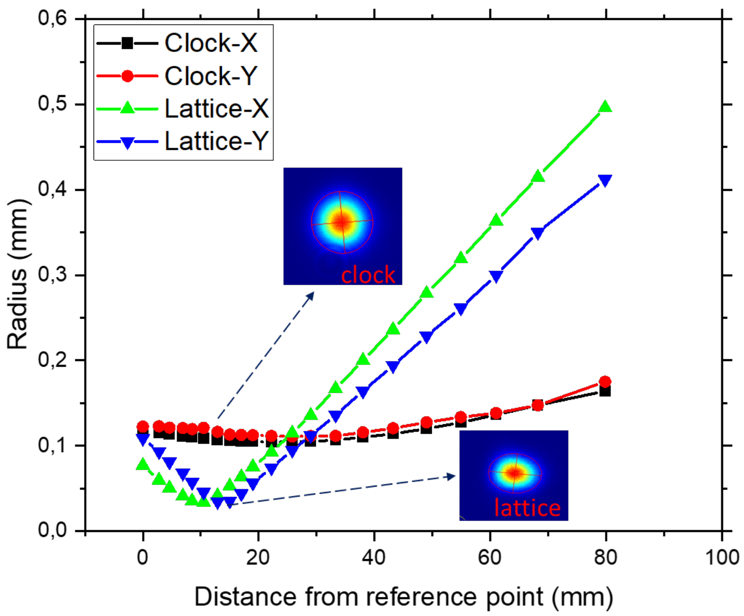

Figure 3.32: The beam radii of the clock and lattice laser beams. The beam profiles at the beam waists are shown in the insert images. The clock beam waist ($\sim 110\,\mu$m) is more than twice as large as the lattice beam waist ($\sim 35\,\mu$m).

To ensure that the atoms experience homogeneous probe light intensity in the optical lattice, the clock laser beam waist is typically larger than that of the lattice laser beam. To confirm this, the beam radii along the x and y axes are plotted in Figure 3.32. The lattice beam waist is approximately $35\,\mu$m, while the clock beam waist is $\sim 110\,\mu$m, which shows that the clock beam waist is more than twice as large as the lattice beam waist.

Sideband spectroscopy

A straightforward method for searching for clock transitions in the optical lattice is through sideband spectroscopy. By increasing the Rabi frequency through the bias magnetic field and probe light intensity, sideband spectroscopy can be easily observed, as shown in Figure 3.33. After determining the clock transition frequency, we can decrease the Rabi frequency to achieve a narrow clock transition.

Sideband spectroscopy is also a powerful tool for characterizing optical lattice properties [58], such as trap frequency, trap depth, motional states, and atom temperatures along both axial and radial directions. The relation between the trap frequency along the z axis and lattice depth is [58]

$$\nu_z = 2\nu_r\sqrt{u_0} \tag{3.4}$$

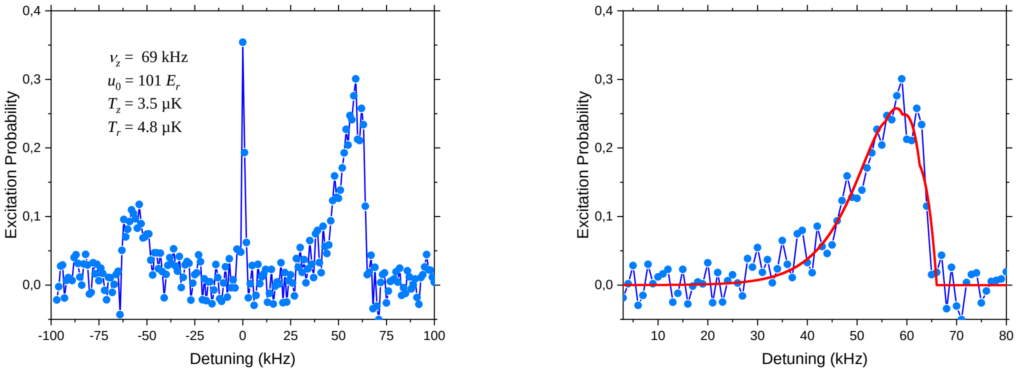

(a) (b)

Figure 3.33: The sideband spectroscopy of the clock transition. (a) The middle peak is the carrier of the transition, and the other two sidebands are the blue and red sidebands, respectively, according to the frequency detuning. (b) The blue sideband with fitted curve (red line) using Eq. 3.7. After analysis, the trap parameters are: longitudinal trap frequency $\nu_z = 69\,\text{kHz}$, lattice depth $u_0 = 101\,E_r$, longitudinal temperature $T_z = 3.5\,\mu\text{K}$, and radial temperature $T_r = 4.8\,\mu\text{K}$.

where ν_z is the longitudinal trap frequency; ν_r is the recoil frequency of the lattice laser light; u_0 is lattice depth in unit of E_r which is the recoil energy of the lattice laser light. There is no contribution from the $n_z = 0$ state to the red sideband cross section because there is no motional state with $n_z < 0$, thus the ratio of integrated sideband absorption cross sections is [58]

$$\frac{\sigma_{red}^{total}}{\sigma_{blue}^{total}} = \frac{\sum_{n_z=1}^{N_z} e^{-E_{n_z}/k_B T_z}}{\sum_{n_z=0}^{N_z} e^{-E_{n_z}/k_B T_z}} = 1 - \frac{e^{-E_0/k_B T_z}}{\sum_{n_z=0}^{N_z} e^{-E_{n_z}/k_B T_z}} \tag{3.5}$$

where σ_{red}^{total} and σ_{blue}^{total} are the integrated sideband absorption cross sections of the red and blue sidebands, respectively; N_z is the number of states in the trap along the z axis, $N_z \simeq \sqrt{u_0}/2$; E_{n_z} is the energy of the state n_z neglecting the coupling term; T_z is the atom temperature along longitudinal axis. From Eq. 3.5, the longitudinal atom temperature T_z can be extracted.

The approximate line shape of the blue sideband as a function of the detuning δ from the carrier for the motional state n_z: [58]

$$\sigma_{blue}^{n_z}(\delta) = \frac{\alpha^2}{\widetilde{\gamma}(n_z)}[1 - \frac{\delta}{\widetilde{\gamma}(n_z)}]e^{-\alpha[1-\delta/\widetilde{\gamma}(n_z)]}\Theta[\widetilde{\gamma}(n_z) - \delta] \tag{3.6}$$

where $\alpha = [\widetilde{\gamma}(n_z)/\nu_r](h\nu_z/k_B T_r)$, T_r is the radial temperature of the atoms, $\widetilde{\gamma}(n_z) = \nu_z - \nu_r(n_z+1)$, and the term of Θ is the Heaviside function. The thermally averaged blue sideband absorption cross section is expressed as [58]

$$\sigma_{blue}(\delta) \propto \sum_{n_z=0}^{N_z} e^{-E_{n_z}/k_B T_z} \sigma_{blue}^{n_z}(\delta) \tag{3.7}$$

which is the Boltzmann-weighted superposition of single (z axis) state sidebands shifted by the anharmonicity of the longitudinal trap. The coupling term between the longitudinal and transverse traps smears the blue sideband out toward the carrier, shown in Figure 3.33b. By fitting the blue sideband shape, the radial temperature of the atoms can be estimated.

By analyzing Figure 3.33 using Eq. 3.5 and Eq. 3.7, I find that the axial trap frequency is 69 kHz, the trap depth is 101 E_r, and atom temperatures are 3.5 µK and 4.8 µK for the axial and radial directions, respectively.

Rabi oscillations

In this dissertation, the Rabi interrogation scheme is employed to excite the clock transition. In general, atoms are first prepared in their ground states, then excited by a Rabi pulse, such that the probability of finding a two-level atom in the excited states is [80]

$$P_e(\Delta\omega, t) = \frac{{\Omega_R}^2}{{\Omega_R}^2 + \Delta\omega^2} \sin^2 \frac{\sqrt{{\Omega_R}^2 + \Delta\omega^2} t}{2} \tag{3.8}$$

where Ω_R is the Rabi frequency, $\Delta\omega$ is the frequency detuning between the probe light and the clock transition. Figure 3.34 shows one example of Rabi oscillations with $\Delta\omega = 0$. Here, a significant decay is observed, which may be due to cold collisions between atoms in the same lattice site.

The clock transition is observed at different interrogation times, shown in Figure 3.35. For each spectroscopy, the interrogation time t is fixed, while the detuning $\Delta\omega$ is scanned. For instance, a π pulse is when t satisfies $\Omega_R t = \pi$, and 2π and 3π pulses are for $\Omega_R t = 2\pi$ and $\Omega_R t = 3\pi$, respectively. The Rabi frequency Ω_R is approximately $2\pi \cdot 12$ Hz, the scanning frequency step is 2 Hz and each data point is four times averaged in Figure 3.35.

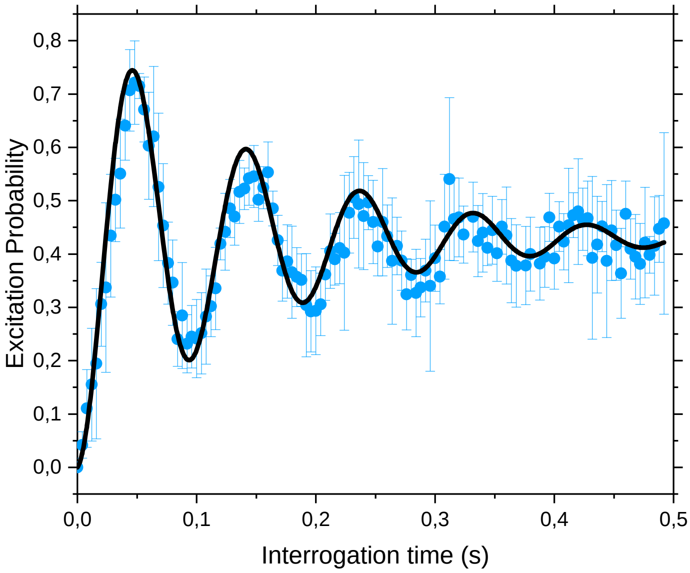

Figure 3.34: Rabi oscillation. The light blue dots represent experimental data, and the black line shows the fit from Eq. 3.8 with exponential decay. The Rabi frequency Ω_R is approximately $2\pi \cdot 12\,\mathrm{Hz}$.

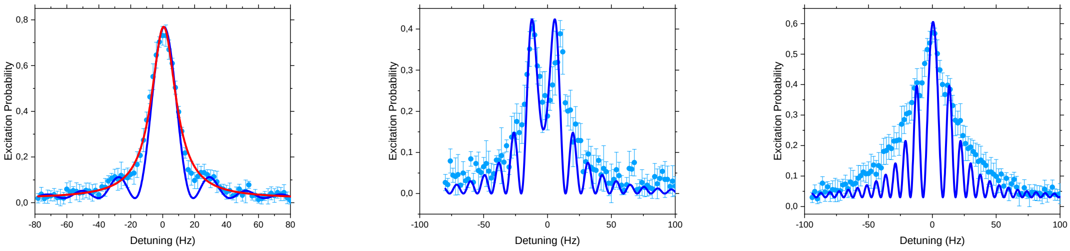

(a) π pulse

(b) 2π pulse

(c) 3π pulse

Figure 3.35: The clock spectroscopy at different interrogation times corresponding to Rabi oscillation in Figure 3.34. The light blue dots represent experimental data, and the blue lines represent fits from Eq. 3.8. The red line in (a) shows the Lorentz fit with a linewidth of 18.5 Hz, which is approximately the Fourier limit linewidth of the π pulse here. The Rabi frequency Ω_R is approximately $2\pi \cdot 12\,\mathrm{Hz}$, the scanning frequency step is 2 Hz and each data point is four times averaged.

Clock transitions with narrow linewidth

By reducing the Rabi frequency through decreasing the bias magnetic field strength and probe light power, the narrower clock transitions are observed. Figure 3.36a shows a clock transition with a linewidth of 0.7 Hz at 1 s interrogation time, which is approximately at the Fourier limit. However, Figure 3.36b shows a clock transition with a linewidth of 0.4 Hz at 3 s interrogation time, which is approximately 50% larger than the Fourier limit linewidth, which may be due to cold collisions broadening. On the other hand, the transition in Figure 3.36b shows a poor signal-to-noise ratio, which would lead to poor clock frequency stability. Hence, in our clock operation, we use 1 s interrogation time and transition with 0.7 Hz linewidth. Another reason for using 1 s interrogation time is that our future clock laser has a coherence time of approximately 1 s.

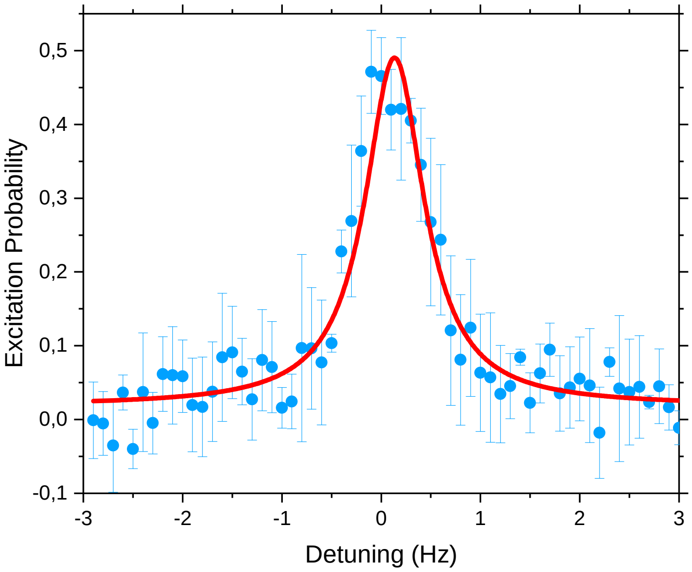

(a) The clock transition with 0.7 Hz linewidth at 1 s interrogation time.

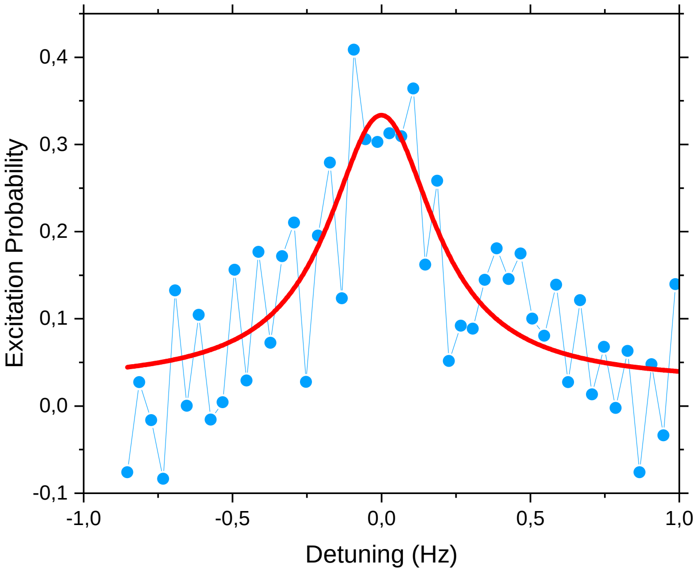

(b) The clock transition with 0.4 Hz linewidth at 3 s interrogation time.

Figure 3.36: The narrow clock transitions. The light blue dots represent experimental data, and the red lines represent Lorentz fits. (a) shows a clock transition with a linewidth of 0.7 Hz at 1 s interrogation time, which is approximately at the Fourier limit. (b) shows a clock transition with a linewidth of 0.4 Hz at the 3 s interrogation time, which is approximately 50% larger than the Fourier limit linewidth, which may be due to cold collision broadening.

Chapter 4

Instability of the SOC2 Clock

The clock stability is fundamentally limited by quantum projection noise (QPN), which is related to the number of particles (atoms or ions) in the traps during the interrogation time. Another critical limitation factor is the Dick effect from the clock laser, which is aliasing noise due to non-continuous interrogation. Additionally, the SOC2 clock is an optical lattice clock based on bosonic atoms strontium-88 requiring a strong magnetic field and high-power probe light to induce clock transition. The stabilities of the magnetic field and probe light power are important contributions to the clock stability as well. Moreover, the power fluctuations of the lattice laser also cause fluctuations in the clock transition frequency, thereby worsening the clock stability. Furthermore, electronic noise, photon shot noise, and other factors also contribute to clock instability [81]. In this chapter, I will discuss all these noise contributions to the clock instability.

4.1 Detection noise

In this section, I will discuss detection noise from different noise sources, e.g., quantum projection noise, electronic noise, photon shot noise, and detection laser noise, which contribute to clock instability through the noisy excitation probabilities.

4.1.1 Quantum projection noise

Quantum Projection Noise is the fundamental noise that arises from the quantum superposition state of each individual uncorrelated atom as it projects to the ground or excited state. QPN scales with $\sqrt{N}$ while the signal scales with the number of atoms N. By this, an increase in N can reduce QPN contribution to excitation probability noise, expressed as [81]

$$\sigma_{QPN}(p_e) = \frac{\sqrt{p_e(1-p_e)N}}{N} \tag{4.1}$$

where $\sigma_{QPN}(p_e)$ is the QPN noise and p_e and $1-p_e$ are the probabilities of an atom projecting to excited and ground states, respectively. To evaluate QPN, the excitation probability p_e

and atom number N should be known. The excitation probability can be obtained from the atomic fluorescence signals, shown in Eq. 3.2. The atom number can be acquired by atomic fluorescence and its collection efficiency. Taking into account the atomic fluorescence signal, Eq. 4.1 can be rewritten as

$$\sigma_{QPN}(p_e) = \sqrt{\frac{p_e(1-p_e)}{\varrho s_{at}}} \tag{4.2}$$

where $\varrho = 10(3)$ atoms per count is the conversion factor between the fluorescence signal s_{at}, measured in counts, and the atom number. s_{at} is the integral fluorescence signal corresponding to the total atom number which equals $s_e + s_g - 2s_{bk}$. According to Eq. 4.2, the noise from QPN is approximately proportional to $\frac{1}{\sqrt{s_{at}}}$. I calculated the upper bound of the QPN contribution to the excitation probability noise using $\varrho = 7$, shown in Figure 4.5 together with other noise contributions.

4.1.2 Electronic noise

Electronic noise refers to the noise generated by electronic devices within the detection system, such as the dark current of a photomultiplier tube (PMT), amplifier, analog-to-digital converter (ADC), and electronic devices used for transmitting signals to a computer. Noise appears in all three integral detection fluorescence signals, s_g, s_e, s_{bk}. The total noise contribution from electronic noise $\sigma_{ele}(p_e)$ can be expressed as

$$\sigma_{ele}(p_e) = \sqrt{(\frac{\partial p_e}{\partial s_g}\sigma_{ele})^2 + (\frac{\partial p_e}{\partial s_e}\sigma_{ele})^2 + (\frac{\partial p_e}{\partial s_{bk}}\sigma_{ele})^2} \tag{4.3}$$

where σ_{ele} is the electronic noise. The same electronic noise level is assumed for s_g, s_e, s_{bk}.

According to Eq. 3.2 and Eq. 4.3, $\sigma_{ele}(p_e)$ is proportional to $1/s_{at}$, which indicates more atoms interact with the probe light and less relative noise appears.

The electronic noise σ_{ele} is measured when running the clock sequence without atoms and without laser light being present. The electronic noise σ_{ele} is equivalent to 0.61 counts (with an electronic offset of 19 counts). The contribution from electronic noise to the excitation probability is shown in Figure 4.5.

4.1.3 Photon shot noise

Photon shot noise is inherent to the quantum nature of light and arises from the fundamental randomness of the photon flux. The shot noise is $\sqrt{N_p}$, where N_p photons are detected in a given interval. A PMT collects fluorescence photons in the SOC2 apparatus, and shot noise

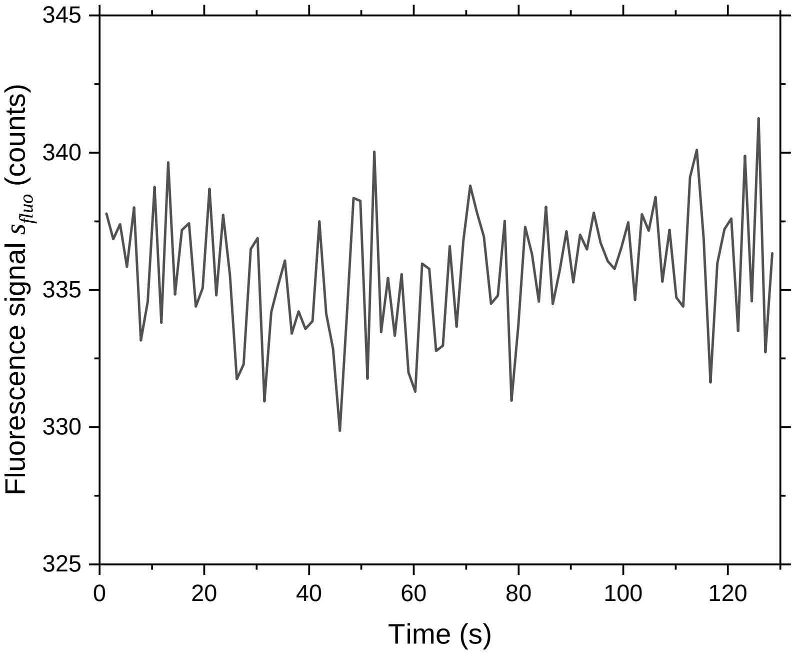

Figure 4.1: Photon shot noise measurement. An external flashlight is the light source, and the PMT collects fluorescence photons.

appears in the excited state fluorescence signal s_e and the ground state fluorescence signal s_g.

An external flashlight is used as a shot noise-limited light source to investigate the photon shot noise [81]. The measurements are implemented at different light intensities. The raw data of an example of photon shot noise measurements is shown in Figure 4.1. To remove the influence of the slow drift of light intensity of the flashlight, the first point of the Allan Deviation is equivalent to shot noise. To extract the actual fluorescence signals, the electronic background is removed from s_e and s_g. The measurements are shown in Figure 4.2. The red line is the fit using

$$\begin{aligned}\sigma_{sn} &= \sqrt{N_p} \\ &= \sqrt{n_p s_{fluo}}\end{aligned} \tag{4.4}$$

where σ_{sn} is the photon shot noise due to the fluorescence signal, s_{fluo} is the fluorescence signal which could be s_e, s_g or s_{bk}, and n_p is the detected photons per count. According to the fit, n_p is 0.0170(5). However, only s_e and s_g suffer from photon shot noise, so the noise contribution to the excitation probability is expressed similarly to Eq. 4.3 without the term

s_{bk}, which is expressed by

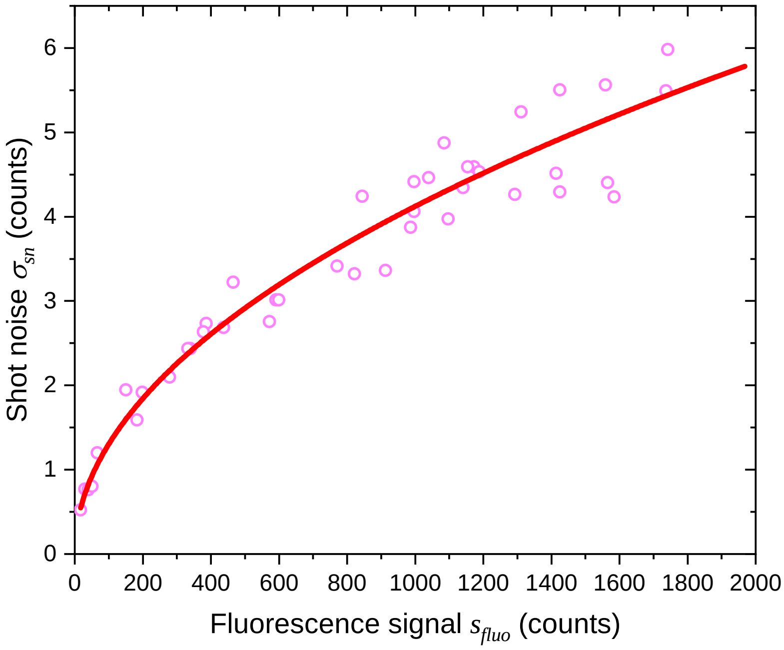

Figure 4.2: The photon shot noise as a function of the fluorescence signal.

$$\sigma_{sn}(p_e) = \sqrt{(\frac{\partial p_e}{\partial s_g}\sigma_{sn})^2 + (\frac{\partial p_e}{\partial s_e}\sigma_{sn})^2} \tag{4.5}$$

The resulting contribution to the excitation probability $\sigma_{sn}(p_e)$ is illustrated in Figure 4.5.

4.1.4 Detection laser noise

In the strontium lattice clock, we use the ${}^1S_0 \leftrightarrow {}^1P_1$ transition (461 nm) to detect atoms in the ground state ${}^1S_0$; the detection scheme can be found in Section 3.4.1. The frequency noise and intensity noise of the detection laser beam can cause excitation probability noise. As shown in Section 3.3, the detection laser (461 nm) is stabilized to the FSS system and narrowed down to ∼1 MHz linewidth. The linewidth is much smaller than the natural linewidth of ${}^1S_0 \leftrightarrow {}^1P_1$ transition, ∼32 MHz, thus the frequency noise is not significant to the detection noise. The intensity fluctuations of the detection beam are also negligible in our 461 nm system based on the beam power data in Section 3.3 and the analysis in Ref. [81].

4.1.5 Total detection noise

In the previous sections, the noise contributions to the excitation probabilities are discussed, e.g., QPN, electronic noise, photon shot noise and detection laser noise, are shown in Figure 4.5. Assuming that the noises from different sources are uncorrelated, the total detection noise can be modeled as [81]

$$\sigma_{p_e} = \sqrt{\sigma^2_{QPN}(p_e) + \sigma^2_{ele}(p_e) + \sigma^2_{sn}(p_e)} \tag{4.6}$$

Based on the previous analysis and this noise model, the total detection noise is shown in Figure 4.5. In order to verify this model, I implemented the detection noise measurement, which should not include the noise caused by the clock laser. To this end, a Rabi $\pi/2$ probe pulse at resonance is used instead of a π pulse at a half-width frequency detuning which is usually applied in a stabilization sequence [81]. In this scheme, the atoms are prepared at superposition states with the excitation probability at 0.5. An example of the measurements with raw data is shown in Figure 4.3 and the results of all the measurements at various atom numbers are shown in Figure 4.4. The measurements show that a higher atom number leads to a lower excitation probability noise. The experimental data are also illustrated in Figure 4.5 (blue dots), which are consistent with the analysis, especially in high population.

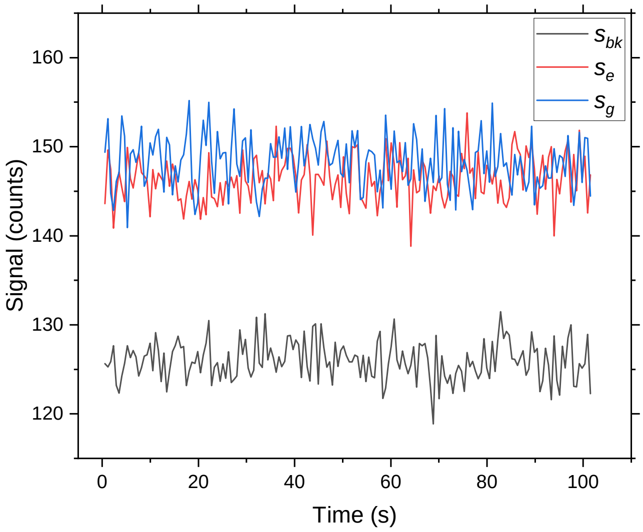

Figure 4.3: An example of the excitation probability noise measurements. A Rabi $\pi/2$ probe pulse at resonance prepares atoms at superposition states with the excitation probability at 0.5. In this measurement, the length of the $\pi/2$ pulse is 4 ms and all three integral detection fluorescence, s_{bk}, s_g, s_e are 126(2) counts, 148(3) counts, 146(3) counts, repectively. The resulting excitation probability noise is 0.047. This measurement corresponds to the first data point in Figure 4.4.

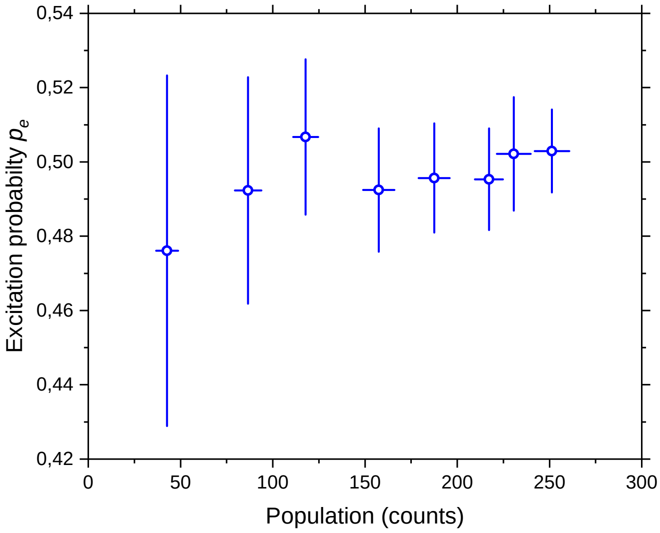

Figure 4.4: The excitation probability noise measurements at different atom numbers. The first data point corresponds to the measurement in Figure 4.3. The measurements show that a higher atom number has less excitation probability noise.

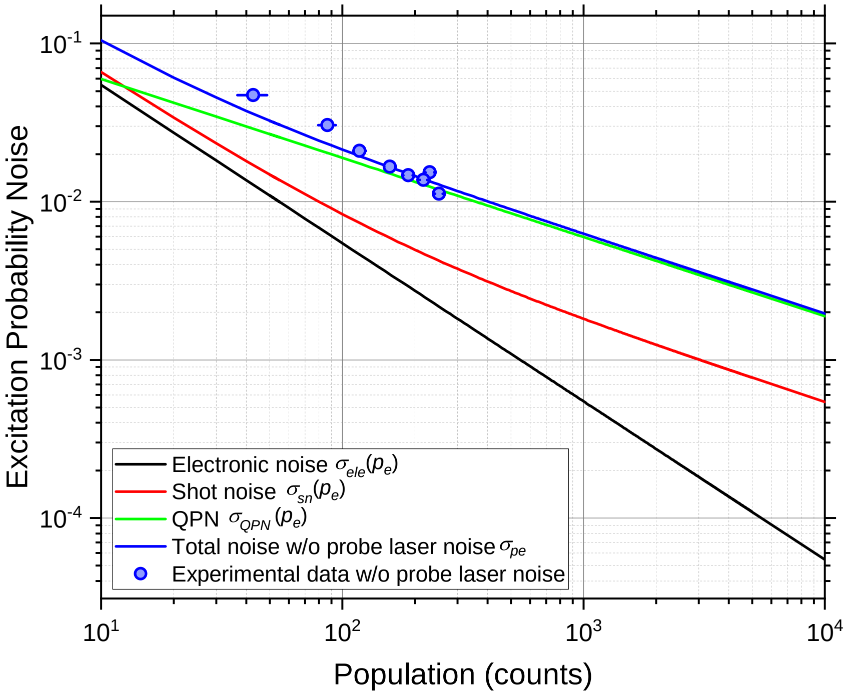

Figure 4.5: The estimated excitation probability noise from different noise source contributions: QPN (green line), electronic noise (black line), shot noise (red line). The experimental results are shown in blue dots, which are consistent with the analysis, especially in high population scenarios. Here, there is no contribution from the probe laser (clock laser) noise.

4.2 Clock laser frequency noise and Dick effect

The clock laser interrogates the cold atoms to extract frequency corrections from the clock transition and then sends the feedback to the clock laser. However, the frequency noise of the clock laser worsens the clock's instability. The frequency noise contribution of the clock laser to the clock instability can generally be expressed by

$$\sigma_y^2 \propto \int S_y(f)\,|W(f)|^2 df \tag{4.7}$$

where $S_y(f)$ is the single-sided power spectral density of the clock laser spectrum, and $W(f)$ is the normalized Fourier transform of the sensitivity function $w(t)$.

The *sensitivity function* $w(t)$ describes the response of the detected excitation probability to the interrogation laser frequency changes [81][82],

$$\delta p_e = \frac{1}{2}\int_0^T 2\pi\,\delta\nu(t)\,w(t)dt \tag{4.8}$$

where $\delta\nu(t)$ is the fluctuation of the clock laser frequency and T is the complete stabilization cycle time, $T = n\,T_c$. T_c is a single clock cycle time, and n is the number of interrogations in each stabilization cycle.

However, cold atoms can only be interrogated during the interrogation phase (phase E in Figure 3.21) with a probe pulse of length T_π in the Rabi interrogation scheme. The remaining time of the clock cycle T_c is the dark time T_D during which the probe light is switched off.

When the π pulse is centered at $t = T_\pi/2$, the sensitivity function $w(t)$ is described by [81][82]

$$w(t) = \begin{cases} \sin^2\vartheta\,\cos\vartheta\,[(1-\cos\Omega_2)\sin\Omega_1 + (1-\cos\Omega_1)]\sin\Omega_2 & \text{during pulse,} \\ 0 & \text{elsewhere} \end{cases} \tag{4.9}$$

with

$$\vartheta = \frac{\pi}{2} - \arctan(2T_\pi\Delta) \tag{4.10}$$

and

$$\Omega_1 = \pi\sqrt{1+(2T_\pi\Delta)^2}\,\frac{t}{T_\pi} \tag{4.11}$$

$$\Omega_2 = \pi\sqrt{1+(2T_\pi\Delta)^2}\,\frac{T_\pi - t}{T_\pi} \tag{4.12}$$

where Δ is the detuning (in Hz) of the interrogation laser from resonance.

The Fourier components g_k of $w(t)$ can be expressed by [81][83]

$$g_k = \int_0^T w(t) e^{\frac{-2i\pi kt}{T}} dt \tag{4.13}$$

where k is the index of the Fourier coefficient. For $k = 0$,

$$g_0 = \int_0^T w(t) dt \tag{4.14}$$

According to Eq. 4.8, the dc Fourier coefficient g_0 can be rewritten as

$$g_0 = \frac{1}{\pi} \frac{dP_e}{d\nu} = \frac{1}{\pi} D \tag{4.15}$$

where D is the discriminant of the clock transition. The discriminant D of Rabi interrogation with a π pulse of length T_π at a half-width point of the clock transition can be expressed as [81][84]

$$D = \frac{dP_e}{d\nu} \approx \pm 1.9\, T_\pi \tag{4.16}$$

S_y is evaluated in multiples of the inverse of the total duration T of a complete stabilization cycle. Now, the noise contribution to the clock instability from clock laser noise can be rewritten as [81]

$$\begin{aligned} \sigma^2_{y,Dick}(\tau) &= \frac{1}{\tau} \sum_{k=1}^{\infty} S_y(k/T) |W(k/T)|^2 \\ &= \frac{1}{\tau} \frac{1}{|g_0|^2} \sum_{k=1}^{\infty} S_y(k/T) |g_k|^2 \end{aligned} \tag{4.17}$$

where k is the index of the Fourier coefficient. This aliasing of noise from the probe laser due to the non-continuous interrogation of the atoms [82] is called Dick effect, which is the main limiting factor for the instability of optical lattice clocks.

The timing sequence of the clock operation is shown in Chapter 3.4.1 and the typical cycle time T_c is 2.311 s with the interrogation time $T_\pi = 1$ s and the dark time 1.311 s. The normalized Fourier components $|g_k|^2/|g_0|^2$ of the sensitivity function $w(t)$ are shown in Figure 4.6.

The clock laser is first pre-stabilized to a 10 cm room-temperature ULE cavity, then phase-locked to a 48 cm room-temperature ULE cavity, finally transfer-locked to a 21 cm cryogenic silicon cavity (called Si2) via an optical comb. The schematics of the clock laser

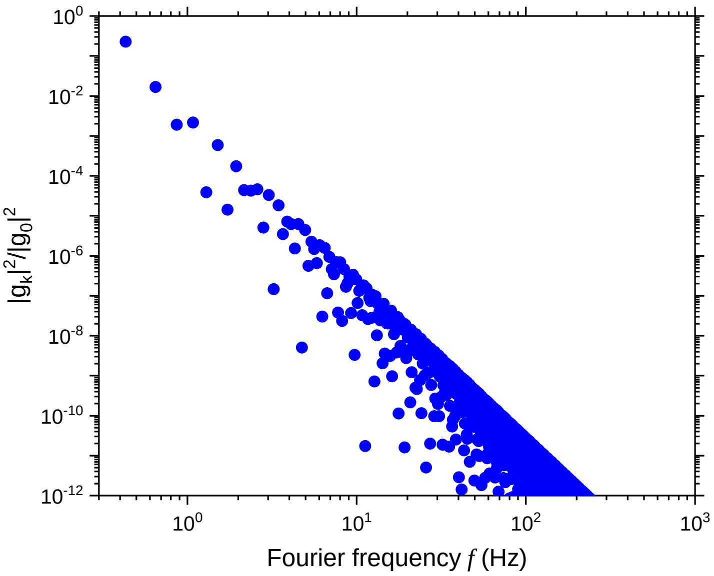

Figure 4.6: Normalized Fourier components $|g_k|^2/|g_0|^2$ during the SOC2 clock operation: cycle time $T_c = 2.311\,\mathrm{s}$, interrogation time $T_\pi = 1\,\mathrm{s}$. The Fourier frequency f is k/T, where k is the index of the Fourier coefficient.

frequency stabilization chain can be found in Chapter 3. Thus the clock laser has the same performance as the 1.5 µm laser which is locked to the Si2 cavity.

The frequency instability of the Si2 laser is measured by the three-cornered-hat comparisons with another similar cryogenic silicon cavity (called Si3) and the 48 cm room-temperature ULE cavity [7]. The spectral power density of the Si2 laser is shown in Figure 4.7, which is derived from the frequency instability of Si2 shown in Figure 1 of Ref. [7].

Based on the data shown in Figure 4.6 and Figure 4.7, the Dick effect can be evaluated by Eq. 4.17 and then visualized in Figure 4.8. The contribution of $9.57 \times 10^{-17}/\sqrt{\tau}$ from the Dick effect is obtained when the cycle time T_c is 2.311 s, the interrogation time T_π is 1 s and the clock laser is transfer-locked to Si2.

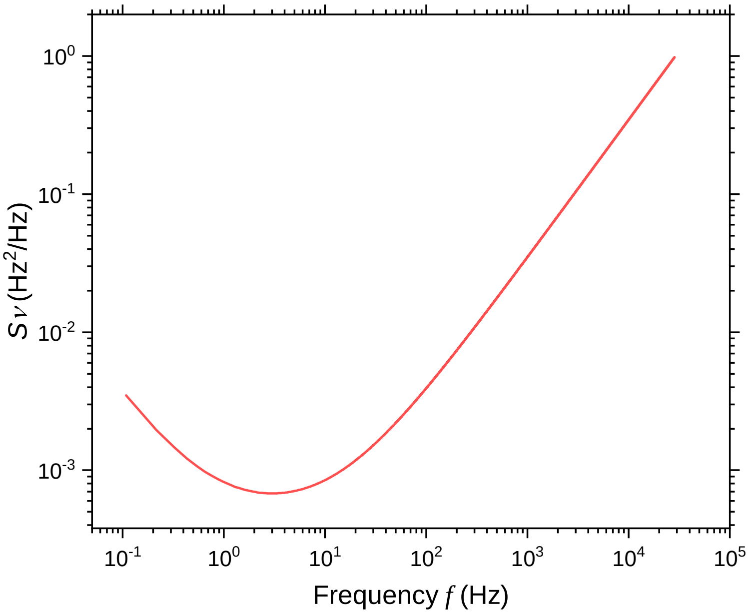

Figure 4.7: The single-sided power spectral density (PSD) of frequency fluctuations $S_\nu = \nu_0^2 S_y$ of the interrogation laser. The PSD is derived from the frequency instability of Si2 shown in Figure 1 of Ref. [7]. ν_0 is the clock transition frequency.

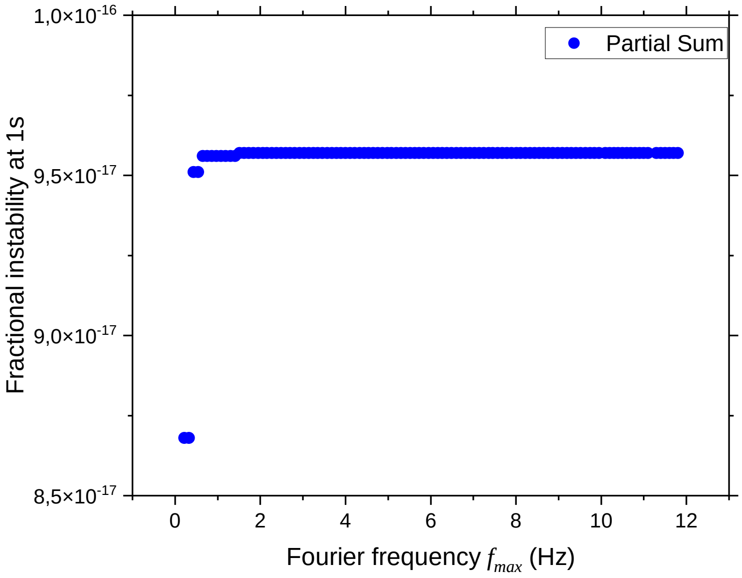

Figure 4.8: Dick effect contribution to the clock instability at 1 s averaging time as a function of the Fourier frequency $f_{max} = k_{max}/T$. The partial sum is from Eq. 4.17.

4.3 Coil current stabilization of the bias magnetic field

The quadratic Zeeman shift due to the magnetic field, shown in Section 2.4, it is expressed by [65]

$$\Delta\nu_B = -\frac{\Omega_B^2}{\Delta_{32}} = \beta|\mathbf{B}|^2 \tag{4.18}$$

For ^{88}Sr atoms, the coefficient is $\beta = -23.8(3)\,\mathrm{MHz/T^2}$. The relation between the fractional frequency variation and the magnetic field noise is

$$\frac{\delta\Delta\nu_B}{\nu_0} = \frac{2\beta|\mathbf{B}| \cdot \delta|\mathbf{B}|}{\nu_0} \tag{4.19}$$

where $\delta|\mathbf{B}|$ is the noise of the magnetic field and $\delta\Delta\nu_B$ is the corresponding frequency fluctuation of the quadratic Zeeman shift. According to Eq. 4.19, the magnetic field noise can directly contribute to the clock instability. To reduce the noise, a coil current stabilization of the bias magnetic field is built.

The bias current stabilization consists of a coil current switch, software, and electronic modules[11]. The coil current switches can set the coils into an anti-Helmholtz or Helmholtz configurations. For example, switches S1, S4, and S5 are used for a Helmholtz coil configuration to create a bias magnetic field for Rabi interrogations, shown in Figure 4.9. The blue arrows show the current direction of the Helmholtz coil in Figure 4.9. Other switches are used for the anti-Helmholtz configuration and another Helmholtz configuration with opposite direction of bias magnetic field [29]. The coil current switch module has two digital multimeters (DMMs) for monitoring coil current in-loop and out-of-loop, respectively. Both are connected to a software module based on Python via USB to a computer. When it is triggered by the clock timing sequence, DMM-1 acquires the in-loop current data and transfers it to the Sample and Hold sub-module via USB. Then, the first 100 ms of the current pulse is averaged and sent to a digital PID (proportional-integral-derivative) controller, where the averaged value is compared to the setpoint. The output of the digital PID is sent to Arduino in the Electronic Module. The control voltage for the VCA (voltage controlled amplifier) is generated using a 16-bit DAC (digital-to-analog converter) module. As the VCA operates within the control range of 0 to -2 V, an inverting amplifier with a gain of 0.5 is applied as an attenuator after the DAC. The FPGA provides the VCA's pre-setpoint, which should be as close as possible to the expected control voltage as the VCA has a strong non-linear transfer curve. By amplifying the VCA output twice, the Electronic Module's output is then sent to

---

[11] The software was developed by Rene Oswald and me, and the coil current switch and electronic modules were built by Stefano Origlia.

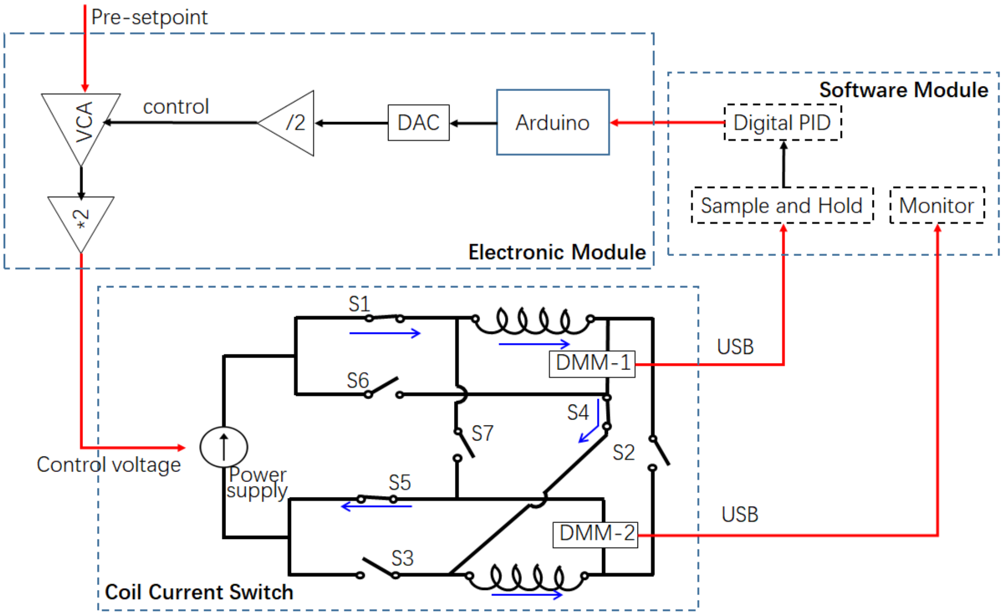

Figure 4.9: Schematics of the bias current stabilization. More details in the text. DMM: digital multimeter; VCA: voltage controlled amplifier; DAC: digital-to-analog converter; PID: proportional-integral-derivative controller; S1-S7: coil current switches.

the power supply unit as the control voltage.

Stabilization results in single-mode. The bias current stabilization loop is run at 0.215 A, and current stabilities of less than 3×10^{-3} are obtained for in-loop and out-of-loop currents, as shown in Figure 4.10. Both can reach below 1×10^{-5} after 10,000 s of averaging time.

Stabilization results in interleaved mode. The stabilization results in interleaved mode are shown in Figure 4.11. Cycle A, with a current of 1 A, has an instability of less than 4×10^{-4}, and Cycle B, with 1.5 A, has an instability of less than 3×10^{-4}. The reason for the difference in instability between cycles A and B will be discussed in the following text.

Long-term stabilization. To evaluate the long-term current stability, the stabilization loop is run for 60 hours at 0.215 A and 1.25 A, respectively, in the single-mode. From Figure 4.12, the fractional current instabilities are less than 5×10^{-6} for both at long averaging times.

Discussion. Figure 4.13 shows the coil current stabilities in interleaved and single modes. The fractional current instability at a set value of 0.215 A is higher than at other currents, see Figure 4.13a, but the noise contribution to fractional frequency shifts is lower than at other currents due to the lower current value, as shown in Figure 4.13b. According to Figure 4.13, the less bias magnetic field applied, the less noise contributions to fractional

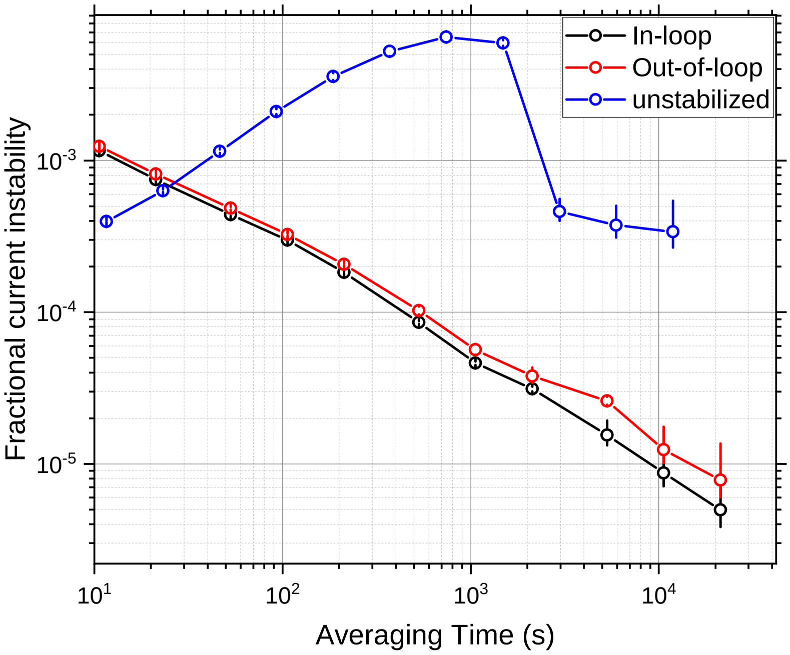

Figure 4.10: Bias current stabilization results in single-mode.

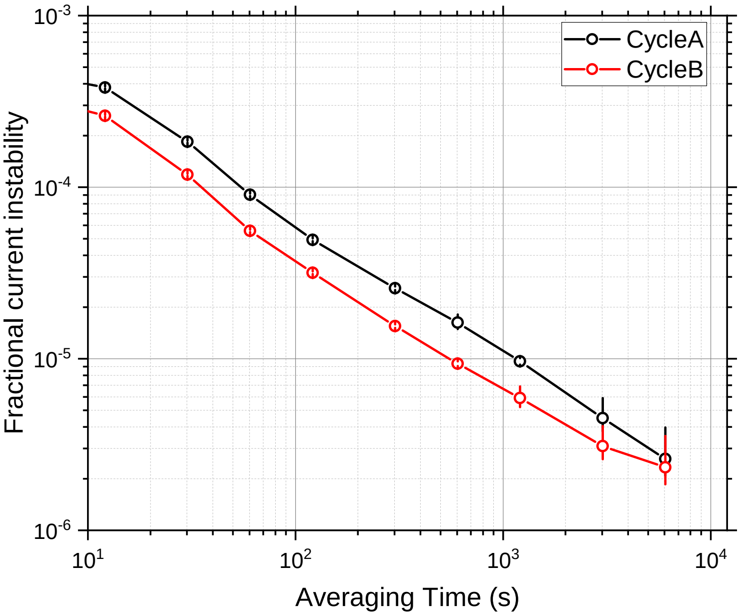

Figure 4.11: The out-of-loop results of bias current stabilization in interleaved mode: Cycle A at a current of $i = 1\,\mathrm{A}$, Cycle B at a current of $i = 1.5\,\mathrm{A}$

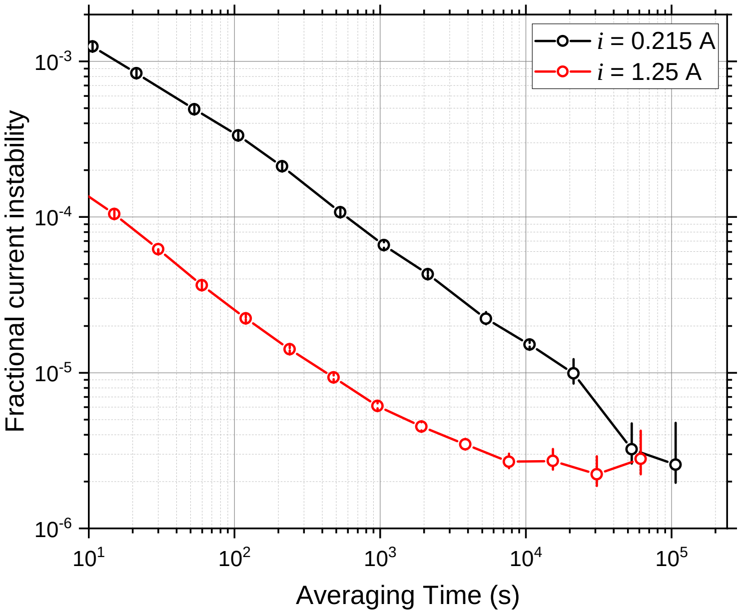

Figure 4.12: Bias current long-term stabilities at 0.125 A and 1.25 A, respectively. Both are out-of-loop data and acquired in single-mode.

frequency shift [12]. According to the magnetic field-induced excitation, shown in Section 2.4, the effective Rabi frequency is proportional to the bias field strength, $\Omega_{12} \propto |\mathbf{B}|$. Thus, the π pulse length T_π is proportional to $1/|\mathbf{B}|$, $T_\pi = \pi/\Omega_{12} \propto 1/|\mathbf{B}|$. The longer the π pulse length, the less bias current is required, resulting in a more stable clock with respect to the quadratic Zeeman shift.

---

[12] The fractional current stability of the current at 1.25 A is abnormally low compared to the currents at 1.5 A and 1 A. The reason is unclear.

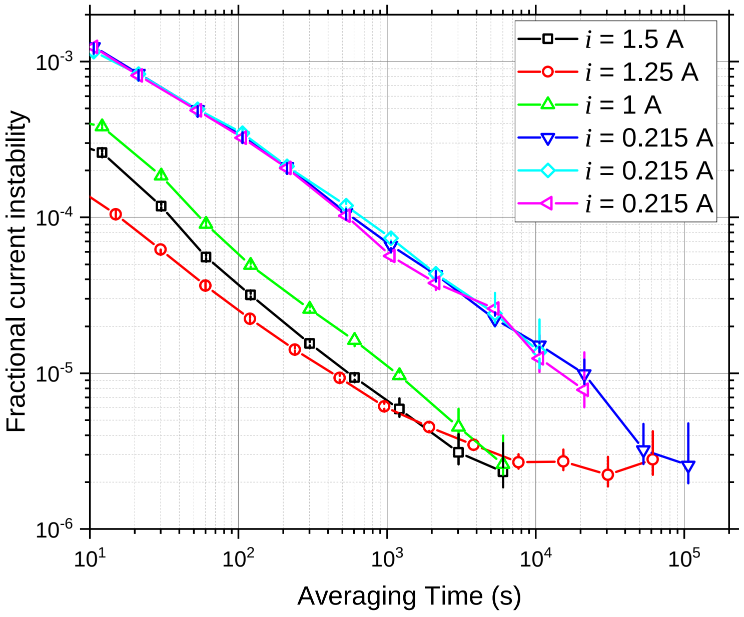

(a) Fractional current stability results at various currents.

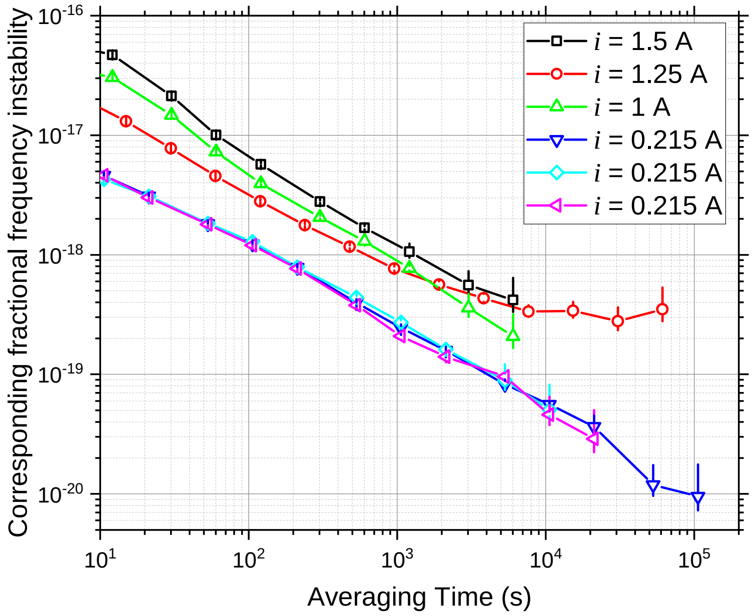

(b) Corresponding fractional frequency stability results at various currents.

Figure 4.13: The results of the coil current stabilization. All plots are from out-of-loop data.

4.4 Stabilization of the clock laser power

For magnetically induced spectroscopy, the frequency shift due to the probe light should also be considered. The AC Stark shift due to the probe light is expressed as [29][65]

$$\Delta\nu_L = \frac{\Omega_L^2}{4\Delta_{32}} = kI \tag{4.20}$$

where $k = -18\,\mathrm{mHz}/(\mathrm{mW}/\mathrm{cm}^2)$ for ^{88}Sr and I is the probe light (clock laser) intensity. The explanations of the other parameters can be found in Section 2.4. The instability of the probe light power can cause AC Stark frequency shift instable, ultimately worsening the clock frequency stability. The relation between the probe light power fluctuation δI and the noise of the AC Stark shift $\delta\Delta\nu_L$ is

$$\delta\Delta\nu_L = k \cdot \delta I \tag{4.21}$$

The fractional frequency noise is

$$\frac{\delta\Delta\nu_L}{\nu_0} = \frac{k \cdot \delta I}{\nu_0} \tag{4.22}$$

where ν_0 is the clock transition frequency, for ^{88}Sr $\nu_0 \approx 429.228\,\mathrm{THz}$. The fluctuation of the probe light power directly worsens the clock stability. To suppress the noise, the probe light power stabilization is implemented.

Stabilization scheme. The clock laser beam goes through an Acousto-Optic Modulator (AOM), then splits one small portion for the laser power stabilization loop, while the main branch goes into the science chamber and interacts with cold atoms in the optical lattice. The stabilization of the clock laser power is based on a homemade power regulator (PR), which compares the desired voltage (setpoint) with the photodetector (PD) voltage converted from the sample clock laser beam, shown in Figure 4.14. The PD voltage is also sent to the Sample and Hold module via the analog input of the NI DAQ card. The Sample and Hold module is implemented by a Python-based script that samples the first 100 ms of the laser beam pulse and averages it, then sends it to the PID module. By comparing averaged PD voltage with the pre-setpoint, the PID algorithm gives a desired voltage, which is actually the setpoint of the PR for the next cycle.

By comparing the PD voltage with the setpoint, the PR outputs the differential value of them as one input of the summing amplifier. Another input of the summing amplifier is a square voltage waveform generated by the pattern generator. The output of the summing amplifier controls the output power of the RF amplifier and, via the AOM, modulates the clock laser power. Another Sample and Hold module collects the summing amplifier output,

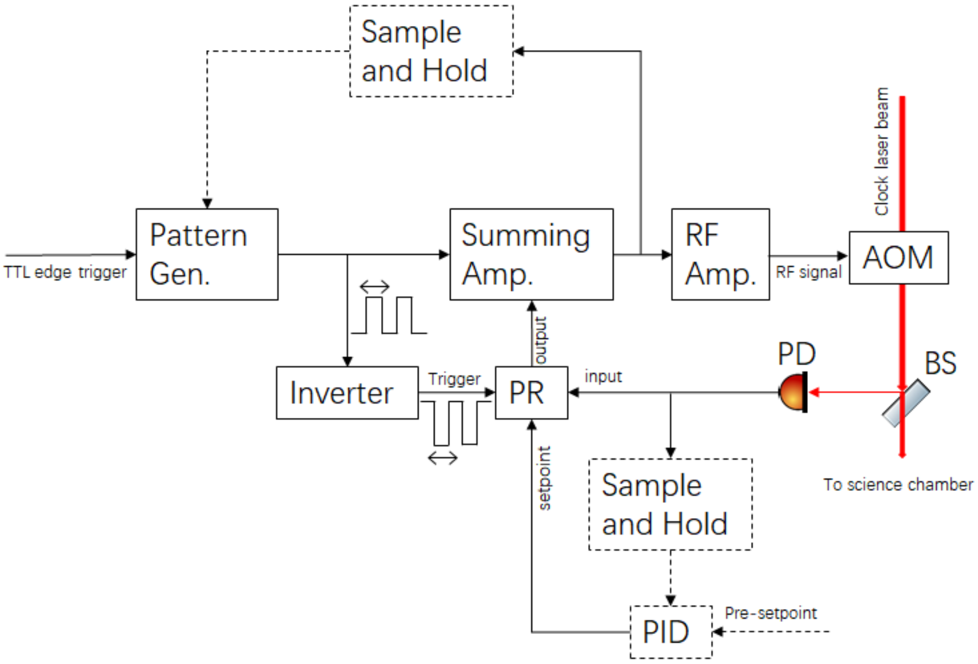

Figure 4.14: Schematics of the clock power stabilization. The dash line rectangle blocks are implemented by Python scripts. More details in the text. Pattern Gen.: Pattern Generator; Summing Amp.: Summing Amplifier; RF Amp.: RF Amplifier; AOM: Acousto-Optic Modulator; BS: Beam Splitter. PD: Photodetector; PR: Power Regulator.

samples the first 100 ms of data, averages it, and sends it to the pattern generator as the pre-set value for the next cycle.

The clock laser is only needed during the interrogation phase to perform Rabi spectroscopy. This means that the pulsed clock laser beam should be off during the cold atom preparation phase and on only during the interrogation phase. Therefore, the pattern generator is also used to produce different pulse lengths of square voltage waveforms to satisfy the π pulse of the clock spectroscopy during interrogation time. The trigger signal of PR is inverted from the pattern generator output (PR is low TTL enabled). In Figure 4.14, the dash line rectangle blocks are implemented by Python scripts. All hardware components, such as the pattern generator, the summing amplifier, the RF amplifier, the power regulator, and the phase inverter, are homemade.

Calibrations of probe light power. According to Eq. 4.22, the intensity of the clock laser beam, which interacts with cold atoms in the lattice, should be known accurately to calculate the noise contribution from the fluctuation of the clock laser power. The probe light intensity can be calibrated using two approaches: one is based on Rabi oscillations with different probe light powers; the other method relies on probe light shift measurements. The second method is implemented in this dissertation. From probe light shift measurements in

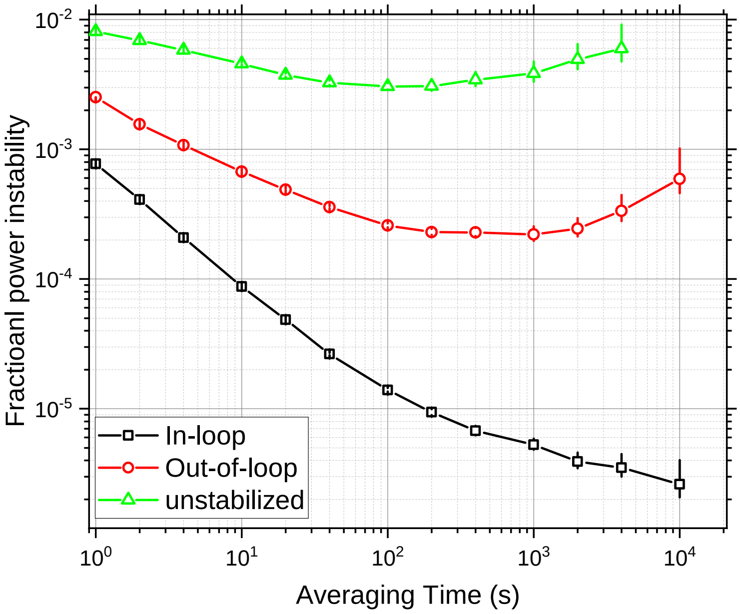

Figure 4.15: Probe laser power stabilization results in single-mode.

Chapter 5, the conversion factor of the PD voltage to intensity of the probe light power is $22.36\,(\mathrm{mW/cm^2})/\mathrm{V}$.

Stabilization results in single mode. Figure 4.15 shows the results with a PD voltage of 1 V in single mode. For comparison, the unstabilized result is also shown in the figure.

Stabilization results in interleaved mode. The pattern generator can generate different lengths of clock laser pulses for the interleaved mode of probe light shift measurements. Figure 4.16 shows the results of the clock power stabilizations in interleaved mode. Cycle A has a PD voltage of 2.5 V, and Cycle B has a PD voltage of 1 V. Similar clock laser power instabilities are obtained for cycles A and B and reach a relative power instability of 2×10^{-3}. According to Eq. 4.22 and the conversion factor, the noise contribution to the clock instability from the probe light power fluctuations can be easily calculated. Figure 4.16b shows that the lower the power, the lower the noise contribution to the clock instability. In typical clock operation conditions, the clock runs at 1.2 V PD voltage to have Rabi pulse at 1 s. The upper bound of the probe light power intensity fluctuations contribution to the clock instability is $\sim 2.25 \times 10^{-18}$, which is minor compared to the instability goal of 1×10^{-17}. The bump at the averaging time of $\sim 600\,\mathrm{s}$ is actually temperature fluctuation of the laboratory, which is also observed in other stabilization measurements.

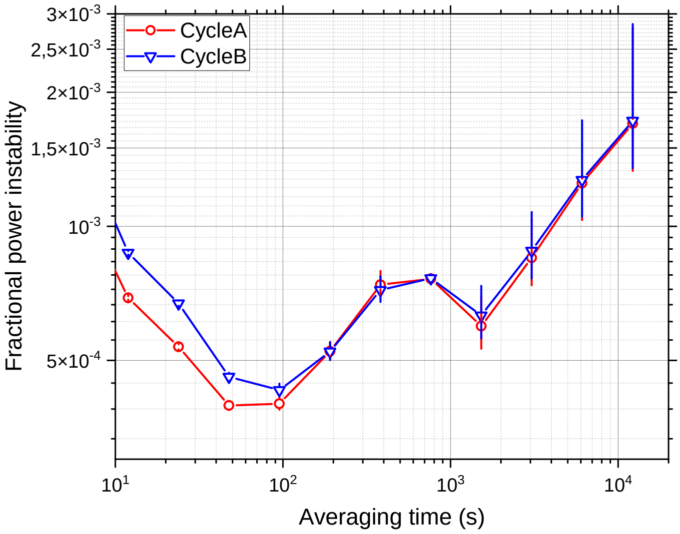

(a) Fractional probe light power stability results in interleaved mode.

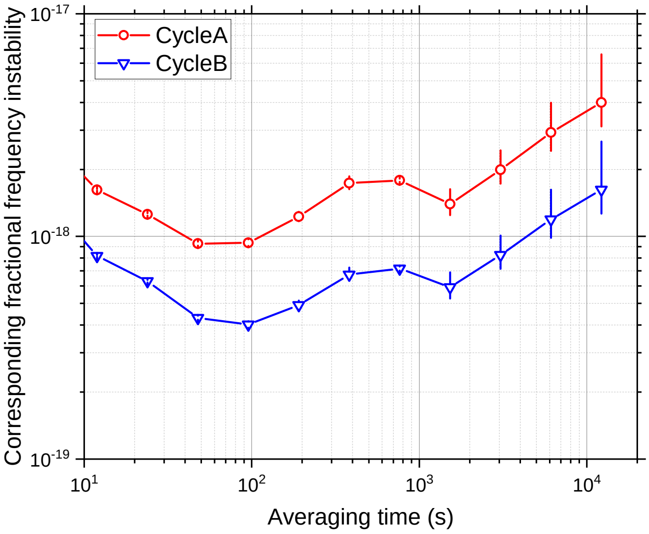

(b) Corresponding fractional frequency stability results in interleaved mode.

Figure 4.16: Clock power stabilization results in interleaved mode. Cycle A has a PD voltage of 2.5 V, and Cycle B has a PD voltage of 1 V. All plots are from out-of-loop data.

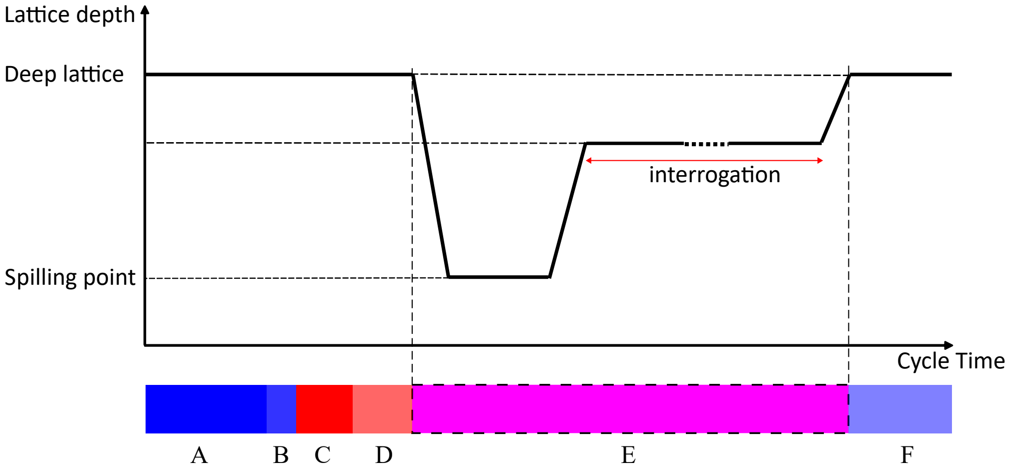

Figure 4.17: Atoms spilling in the lattice during interrogation phase (not to scale). The coloured bar A-F shows the different phases of the clock operation, which is the same as in Figure 3.21. More details in text. A: atoms loading and blue MOT. B: low-power blue MOT. C: broadband red MOT. D: single-frequency red MOT. E: interrogation. F: detection.

4.5 Stabilization of the lattice laser power

If the lattice laser power is unstable, it would cause fluctuations in the lattice depth, and induce instability in clock frequency via the lattice AC Stark shift. To eliminate the power fluctuation, I implemented the lattice power stabilization.

Lattice depth spilling process. To remove hot atoms from the lattice and keep the remaining atoms at the same motional states for different clock cycles, the 'spilling' process is added in the clock cycle, as shown in Figure 4.17. First, cold atoms are prepared (from phase A to phase D) and loaded into the deep lattice (typically $\sim 115\,E_r$) in the end of the single-frequency red MOT phase (D), then the lattice depth is adiabatically decreased to the shallow lattice (typically $\sim 35\,E_r$) in 15 ms, thus hot atoms are removed from the lattice; after that, the lattice depth is adiabatically increased to the desired lattice depth in 15 ms. Atoms and clock laser interact under the desired lattice depth which then is adiabatically increased to the original depth (typically $\sim 115\,E_r$) in the detection phase (F). The spilling process is only implemented in the interrogation phase (E), which can also be used to control the collision shift of ^{88}Sr atoms at the same order of magnitude for different cycles by keeping the atom number at the same level.

Lattice laser power stabilization scheme. To continuously stabilize lattice laser power, I implemented the power stabilization based on an analog controller (Power Regulator), Figure 4.18. A pattern generator is employed to create setpoints for the analog controller, which compares these setpoint voltages with the value from the in-loop photodetector and

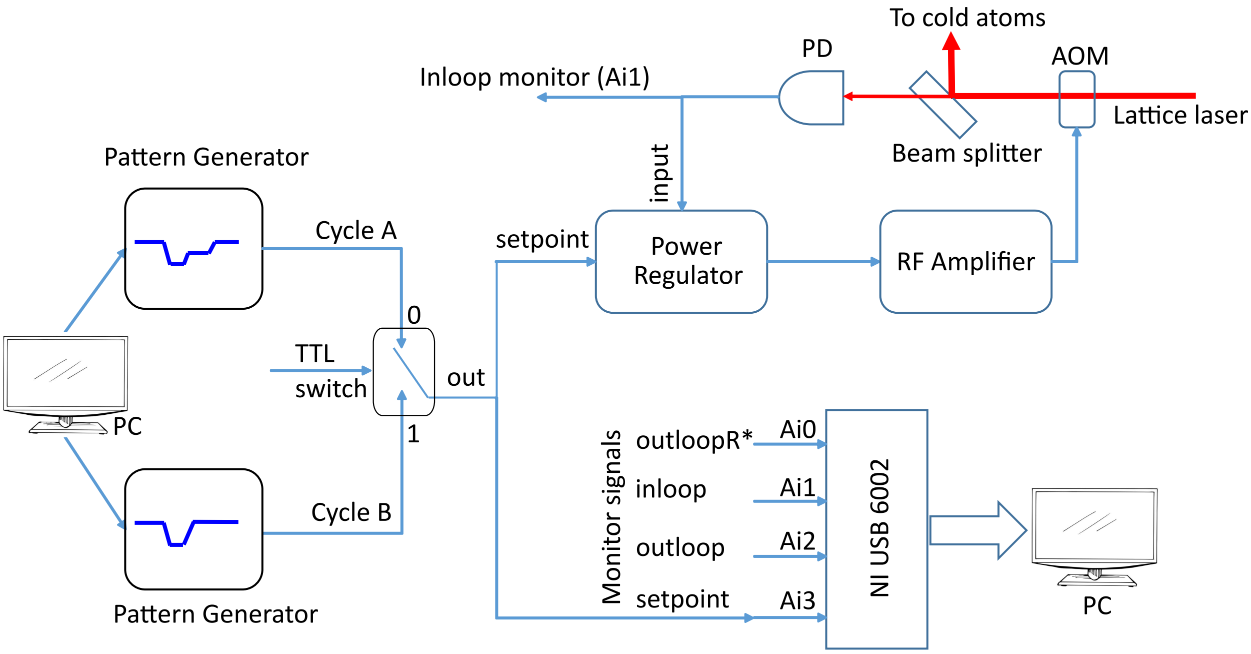

Figure 4.18: Schematics of lattice power stabilization. 'outloopR*' indicates the out-of-loop monitor signal on lattice laser distribution breadboard, shown in Figure 3.15. More details in text. PD: Photodetector; AOM: Acousto-Optic Modulator; TTL: Transistor-Transistor Logic signal; RF: Radio Frequency; Ai: Analog input port.

then use an analog PID to maintain the lattice power always at the desired setpoints. The setpoints have a similar pattern as Figure 4.17 to conduct the spilling process. The output from the power regulator controls the lattice laser power via one RF amplifier and an AOM. To evaluate the power stability, a 4-channel monitor system based on a DAQ NI USB 6002 was built. It monitors in-loop power, out-of-loop power, and the setpoint during the interrogation phase.

To conduct magic wavelength measurements (interleaved mode), I added another pattern generator to create a reference setpoint and a 2-channel switch to select which pattern generator would be used. I implemented optical lattices at different depths and compared their relative frequency shifts to find the magic wavelength of the clock transition, shown in Figure 5.8.

Stability results in single-mode. This stabilization loop runs first at the single stabilization mode (single mode) and the setpoint of the lattice power is set at 0.3 V. From the monitor system, monitor signals can be acquired and analyzed. The Allan deviations of the fractional laser powers are shown in Figure 4.19. The figure shows that the lattice power can be stabilized within less than 5%. However, there is one big bump at approximately 600 s averaging time. Without the bump, the stability could be less than 1% from 1 s to 10,000 s

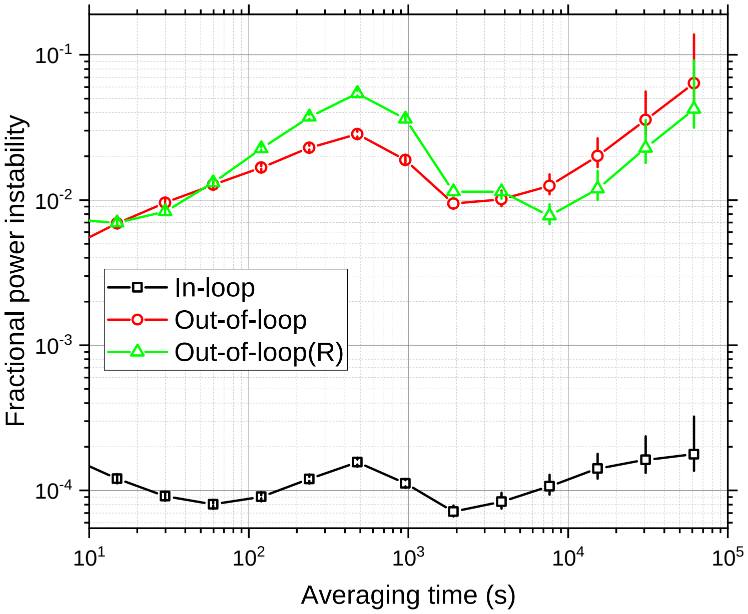

Figure 4.19: The instability of the lattice power in the single-mode operation. 'Out-of-loop(R)' refers to the monitor signal of 'outloopR*' in Figure 4.18.

averaging time. Nevertheless, the bump at 600 s is also observed in the in-loop signal.

To investigate the reason for the bump, the laboratory temperature is monitored, and a bump is also observed at 600 s, as shown in Figure 4.20. Thus, one can conclude that this bump is due to temperature-sensitive components in the stabilization loop. However, the in-loop signal should not fluctuate since the stabilization loop maintains the setpoints and suppresses oscillations. In addition, I monitored the setpoints of the analog controller and surprisingly observed a bump at 600 s averaging time, as shown in Figure 4.21. But the oscillation is small, less than 0.0003%. It could not cause the in-loop signal oscillating at 0.02%. Therefore, the noise from the in-loop signal may be due to the parameter settings of the analog controller and could not suppress the oscillation caused by temperature fluctuations.

Stability results in interleaved mode. Magic wavelength measurements can be carried out by switching the power stabilization to the interleaved stabilization mode using two pattern generators to stabilize the lattice at two different lattice depths, shown in Figure 4.18. One is used as a reference depth, and the other varies to several lattice depths. As an example, the interleaved stabilization mode runs with cycle A setting at 0.2 V and cycle B setting at 0.4 V, shown in Figure 4.22. The out-of-loop power instabilities are almost identical for both cycles.

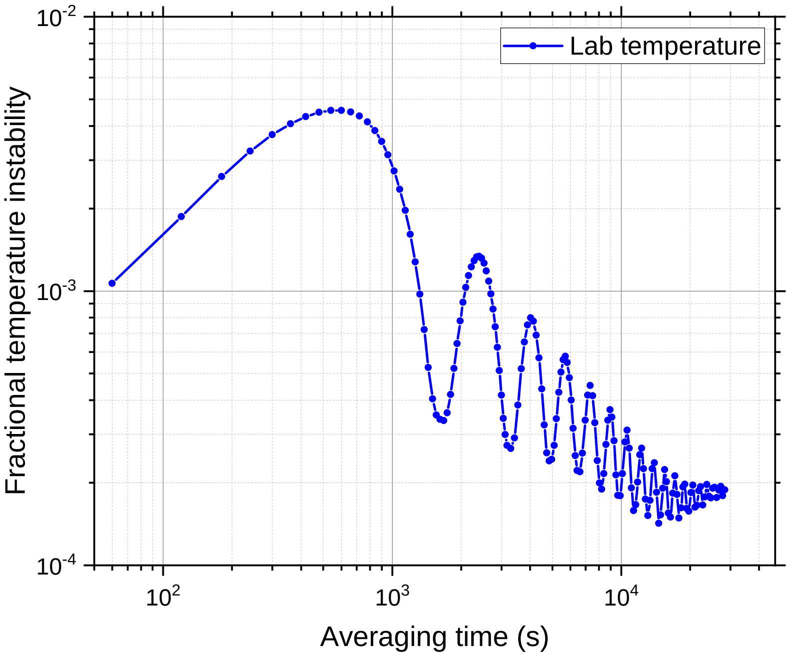

Figure 4.20: The instability of the lab temperature

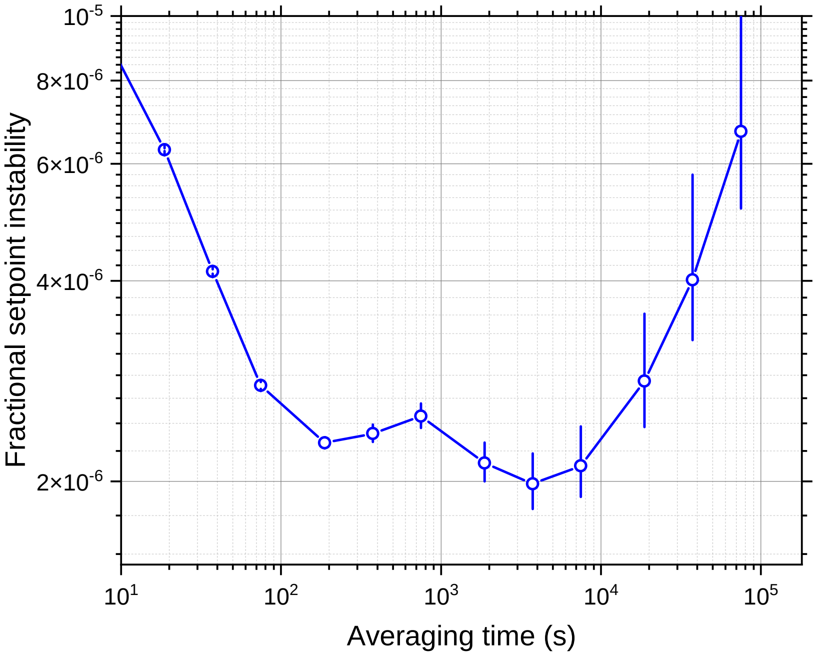

Figure 4.21: The instability of the setpoint of the lattice power stabilization

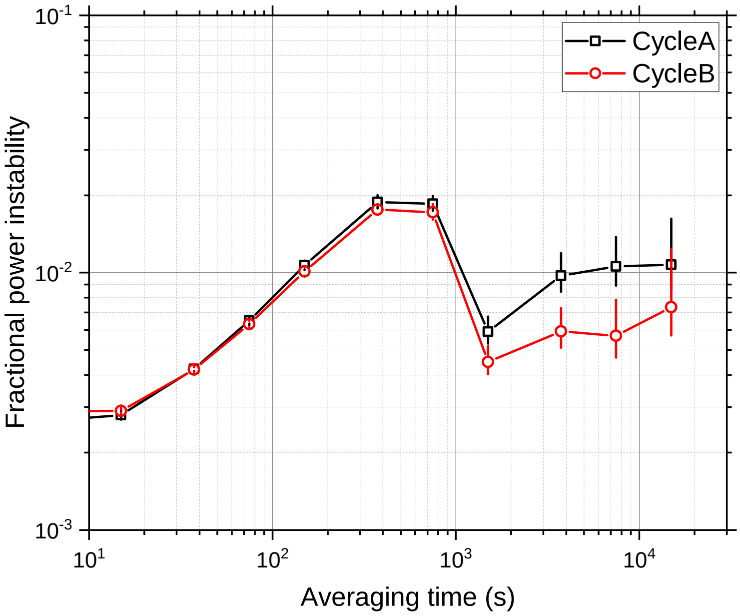

Figure 4.22: The instabilities of the lattice power in interleaved mode operation. The setpoint of cycle A is 0.2 V, while cycle B at 0.4 V. Both are out-of-loop data.

Contributions to the clock instability. We are interested in the clock instability caused by lattice power fluctuations. Assuming that the lattice frequency is $\Delta_m = 25\,\text{MHz}$ off from the magic wavelength, an upper bound on the clock instability can be obtained according to Eq. 4.23.

$$\sigma_\nu = \varkappa \Delta_m U_0 \sigma_{LP} \tag{4.23}$$

where $\varkappa$ is the differential $E1$ polarizability ($= 17.35(13)\,\mu\text{Hz}/\text{MHz}/E_r$ [85]), U_0 is the lattice depth in units of E_r and σ_{LP} is the fractional power instability.

To obtain lattice depths from different lattice powers, I calibrated the lattice depth according to the sideband spectroscopy at different lattice laser powers and then fit the result to obtain an empirical formula,

$$U_0(E_r) = -8(3.5) + 0.664(26) \times U_{PD}(mV) \tag{4.24}$$

where U_{PD} is the monitor voltage of the lattice laser power.

Eqs. 4.23 and 4.24 allow me to easily calculate the clock instability contribution from the lattice power fluctuations, shown in Figure 4.23. The contribution is much smaller than 5×10^{-18}.

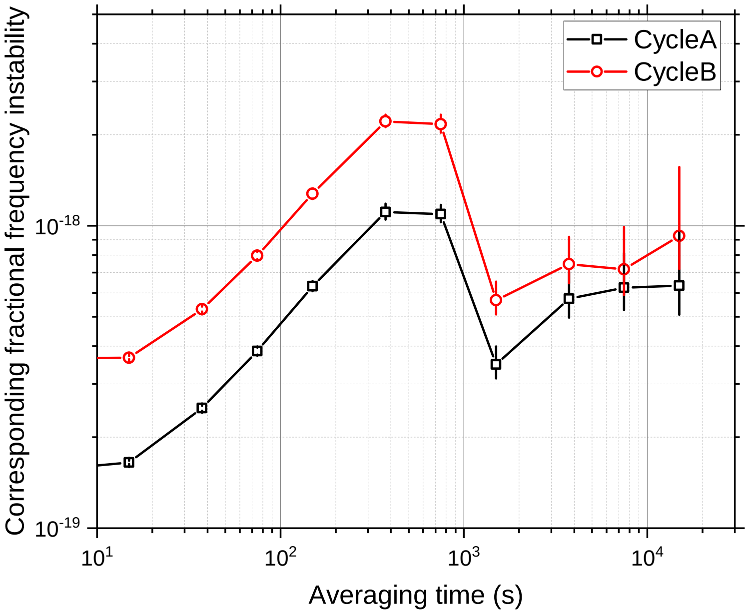

Figure 4.23: The clock instability contribution from lattice power fluctuation, which corresponds to the data in Figure 4.22.

4.6 Instability of the SOC2 clock vs the PTB stationary clock

Summary of all the known noise contributions to the SOC2 instability. In the above sections, I analyzed the noise contributions to the clock instability, for example, the noises from the bias field, the probe laser power, the lattice laser power, and the detection noise. The contributions of the frequency and power noises of the detection beam (461 nm) to the clock instability were considered as well; however, they are small compared to the noise mentioned above and are thus ignored [81]. The noise contributions are summarized in Figure 4.24.

Measured instability of the SOC2 clock against the stationary PTB clock (Sr3). The 6-hour frequency stability data were obtained while I implemented the magic wavelength measurements, and meanwhile Sr3 was operating. The instability of the SOC2 clock against Sr3 is $5.7 \times 10^{-16}/\sqrt{\tau}$, shown in Figure 4.24. According to the Sr3 self-comparison data, the interleaved instability of the Sr3 clock is $\sim 4.4\times10^{-16}/\sqrt{\tau}$, and the instability contributions from the Sr3 clock to the frequency comparison with the SOC2 clock is estimated as $\sim 2.2\times10^{-16}/\sqrt{\tau}$. According to the above analysis, the estimated contribution to the instability from all noise sources together with the contribution of the Sr3 clock is $\sim 2.7 \times 10^{-16}/\sqrt{\tau}$.

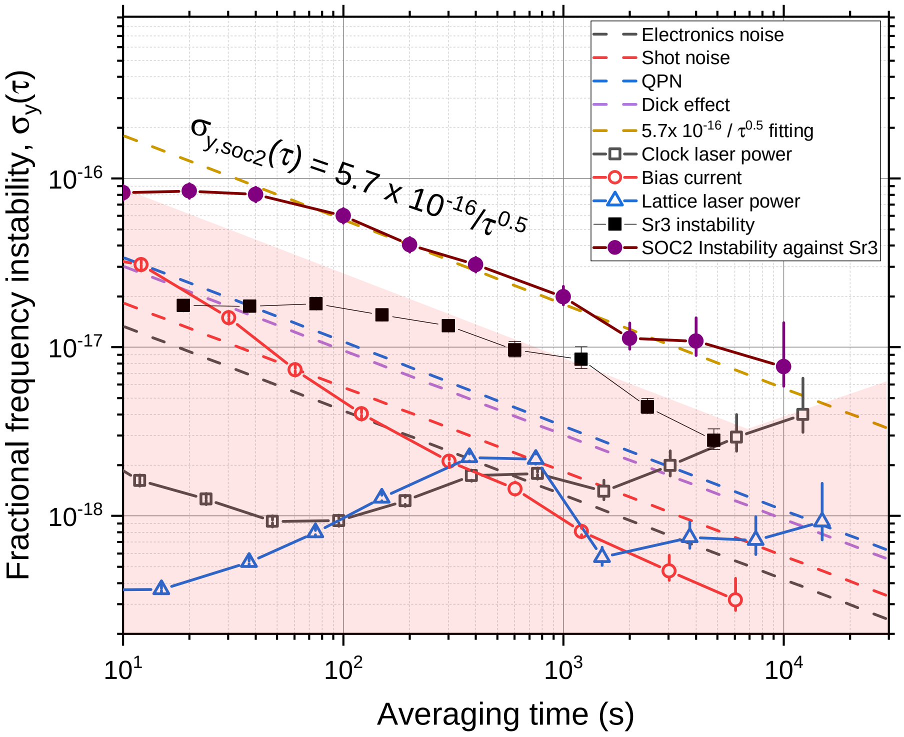

Figure 4.24: Various contributions to the SOC2 instability from different noise sources and the PTB stationary optical lattice clock (Sr3). The light red area shows the total noise contribution with an upper bound at $\sim 2.7 \times 10^{-16}/\sqrt{\tau}$ at the averaging time from 10 s to 7 000 s. The instability at an even longer averaging time is limited by the noise from the clock laser power. Black square dot line shows the contribution from the Sr3 clock, which can be estimated as $\sim 2.2 \times 10^{-16}/\sqrt{\tau}$ used for the total noise contribution calculation (light red area). The measured frequency instability of the SOC2 clock against the Sr3 clock is $\sim 5.7 \times 10^{-16}/\sqrt{\tau}$, which is dominated by the instability of the SOC2 clock. Therefore, there are still unidentified noise sources that contribute to the instability of the SOC2 clock. τ is the averaging time in seconds.

Therefore, there are still unidentified noise sources that contribute to the instability of the SOC2 clock.

Chapter 5

Uncertainty of the SOC2 Clock

To evaluate the uncertainty of the clock, the frequency shifts due to all relevant effects should be carefully characterized. This chapter presents the methods and results of the evaluations of each effect.

5.1 Blackbody Radiation shift

For strontium optical lattice clocks operated at room temperature, the blackbody radiation (BBR) shift is the main contribution to the clock frequency shift. The BBR shift of the clock transition at temperature T is described as [64][86]

$$\Delta\nu_{BBR}(T) = \Delta\nu_{stat}(T) + \Delta\nu_{dyn}(T) \tag{5.1}$$

where $\Delta\nu_{stat}$ is the static BBR shift that depends on the differential dc polarizability between the excited and ground states of the clock transition, $\Delta\nu_{dyn}$ is the dynamic BBR shift.

The static frequency shift in the temperature T can be expressed by [86]

$$\Delta\nu_{stat}(T) = \Delta\nu_{stat}(T_0)\left(\frac{T}{T_0}\right)^4 \tag{5.2}$$

where the static coefficient $\Delta\nu_{stat}(T_0)$ is the frequency shifts at the reference temperature $T_0 = 300\,\mathrm{K}$. The dynamic frequency shift in the temperature range from 50 to 350 K can be expressed by [64]

$$\Delta\nu_{dyn}(T) \approx \eta_6\left(\frac{T}{T_0}\right)^6 + \eta_8\left(\frac{T}{T_0}\right)^8 + \eta_{10}\left(\frac{T}{T_0}\right)^{10} \tag{5.3}$$

where the coefficients are

$$\begin{aligned} \eta_6 &= -0.12998\,\mathrm{Hz} \\ \eta_8 &= -0.01211\,\mathrm{Hz} \\ \eta_{10} &= -0.00844\,\mathrm{Hz} \end{aligned} \tag{5.4}$$

The static and dynamic coefficients are $\Delta\nu_{stat}(T_0) = -2.13023(6)\,\mathrm{Hz}$ [86] and $\Delta\nu_{dyn}(T_0) = -150.51(43)\,\mathrm{mHz}$ [64], respectively.

To accurately evaluate the BBR shift due to the environment, the temperature T surrounding the science chamber must be known accurately. To this end, 17 temperature sensors are attached to the compact science chamber. The representative temperature is obtained from the highest temperature (T_{max}) and the lowest (T_{min}) using a rectangular probability distribution model, $T = (T_{min} + T_{max})/2$ with uncertainty $\Delta T = (T_{max} - T_{min})/\sqrt{12}$. Under clock operation conditions, T and ΔT are 298.60 K and 0.16 K, respectively. The frequency shift due to BBR is -2236.8 mHz with an uncertainty of 4.9 mHz, which corresponds to $-5211.2(115) \times 10^{-18}$ in fractional units.

At the beginning of the accuracy characterization of the SOC2 clock in 2024, the atomic beam shutter was installed, and thus the BBR shift due to the atomic oven was zero. However, after a few weeks, the atomic beam shutter was unfortunately broken. Thus, there is a frequency shift due to the hot atomic oven, which is usually heated to approximately 450 °C. The atomic oven is located 640 mm away from the cold atomic cloud, shown in Figure 5.1. There is a pinhole with a diameter of 2.5 mm placed between the flag shutter and the Zeeman slower (more details in Section 3.2), which limits the solid angle of the atomic oven to cold atoms. The pinhole is 375 mm away from the cold atoms. The solid angle can be expressed as

$$\Omega_s = A/R^2 = \frac{\pi (r_0 R/l)^2}{R^2} \tag{5.5}$$

where A is the partial area of the oven seen by the cold atoms through the pinhole (the red area in Figure 5.1), R is the distance between the atomic oven and the cold atoms, l is the distance between the pinhole and the cold atoms, r_0 is the radius of the pinhole. The resulting solid angle Ω_s is 35(10) µsr (sr = steradian), in which 10% length measurement error is assumed. After considering the solid angle, the frequency shift due to the BBR of the oven is -0.465(167) mHz, which corresponds to $-1.08(39) \times 10^{-18}$ in fractional units.

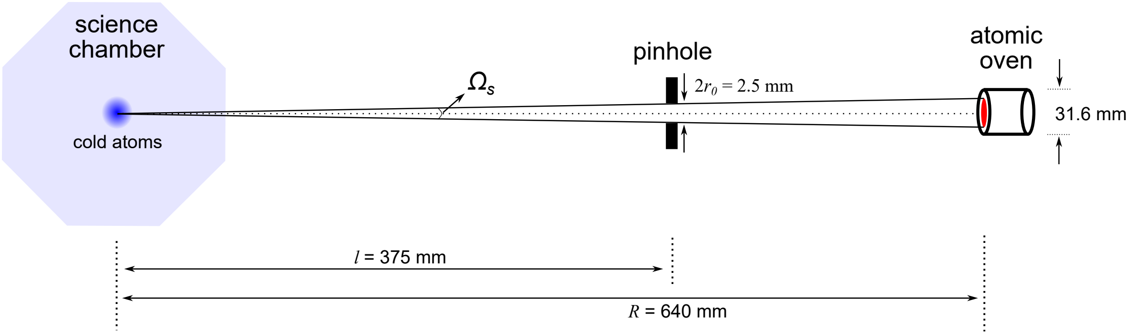

Figure 5.1: The solid angle Ω_s of the atomic oven to the cold atoms. The red area is the partial area of the oven seen by the cold atoms through the pinhole, A in Eq. 5.5. l is the distance between the cold atoms and the pinhole. R is the distance between the cold atoms and the atomic oven. r_0 is the radius of the pinhole. The diameter of the oven is 31.6 mm. The resulting solid angle Ω_s is 35(10) µsr (sr = steradian).

Another frequency shift related to BBR is the BBR transmitted by the windows of the science chamber, which is less than 3×10^{-19} [16]; thus, it is negligible.

5.2 Quadratic Zeeman shift

Benefiting from the absence of nuclear spin of bosonic isotope, there is no first-order Zeeman shift. However, the bosonic clock suffers a significant second-order Zeeman shift due to the clock excitation via magnetic field-induced spectroscopy; more details are given in Section 2.4.

Before conducting the quadratic Zeeman shift measurement, three pairs of Helmholtz coils were used to compensate for the perpendicular background field $\overrightarrow{B}_\perp$ with respect to the bias magnetic field $\overrightarrow{B}$, illustrated in Figure 5.2. The ${}^1S_0 \leftrightarrow {}^3P_1$ transition was applied for the evaluation of the background magnetic field. The details of the compensation can be found in the Appendix A.

Ideally, the background magnetic field can be suppressed to zero by applying the compensation field. However, in reality, there is still a residual background magnetic field present at the position of cold atoms, shown in Figure 5.2. The residual background field $\overrightarrow{B}_r$ is decomposed into $\overrightarrow{B}_{//}$ and $\overrightarrow{B}_\perp$, which are parallel to the z-axis and perpendicular to the z-axis in the xy plane, respectively. φ indicates the angle between $\overrightarrow{B}_{//}$ and $\overrightarrow{B}_r$.

The bias magnetic field $\overrightarrow{B}$ is produced by Helmholtz coils and the second-order Zeeman shift can be expressed by

$$\Delta\nu_B = \beta(|\overrightarrow{B} + \overrightarrow{B}_{//}|^2 + |\overrightarrow{B}_\perp|^2) \tag{5.6}$$

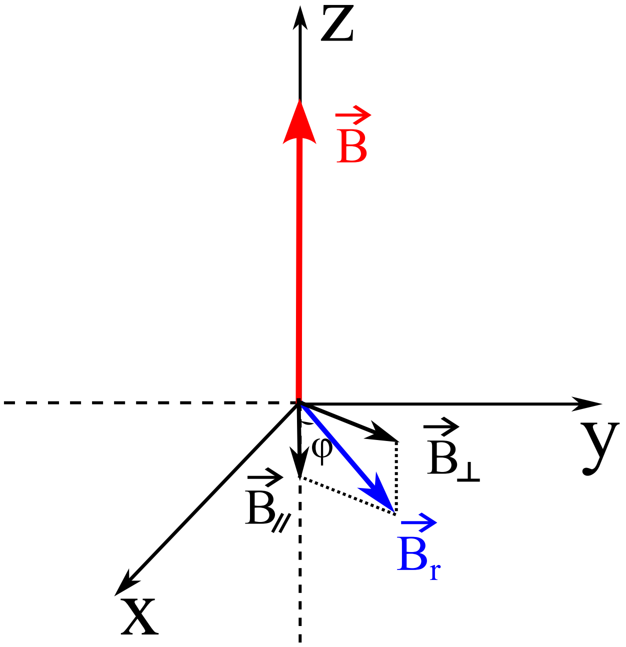

Figure 5.2: Bias magnetic field $\overrightarrow{B}$ and residual background field $\overrightarrow{B}_r$. The residual background field $\overrightarrow{B}_r$ is decomposed into $\overrightarrow{B}_{//}$ and $\overrightarrow{B}_{\perp}$.

where β is the second-order Zeeman shift coefficient, $\beta = -23.3(3)$ MHz/T^2 for ^{88}Sr [65].

The interleaved measurement is used to evaluate the quadratic Zeeman shift, in which the currents of the Helmholtz configuration coils for the bias magnetic field (called bias current) are varied. The timing sequence of interleaved measurements can be found in Section 3.4.1. For example, servo A has a bias current i_a, while servo B has a bias current i_b. The quadratic Zeeman shifts for servo A and servo B are

$$\Delta\nu_{Ba} = \beta(|\overrightarrow{B}_a + \overrightarrow{B}_{//}|^2 + |\overrightarrow{B}_{\perp}|^2) \tag{5.7}$$

and

$$\Delta\nu_{Bb} = \beta(|\overrightarrow{B}_b + \overrightarrow{B}_{//}|^2 + |\overrightarrow{B}_{\perp}|^2) \tag{5.8}$$

where the subscripts a and b show the parameters in servo A and servo B, respectively. Thus, the differential quadratic Zeeman shift in the interleaved measurements is expressed as

$$\Delta\nu_{ba} = \beta(|\overrightarrow{B}_b + \overrightarrow{B}_{//}|^2 - |\overrightarrow{B}_a + \overrightarrow{B}_{//}|^2) \tag{5.9}$$

Five interleaved measurements are implemented:

- Self-comparison at $i_1 = 0.625$ A.

- Self-comparison at $i_3 = -0.625\,\mathrm{A}$.
- Interleaved measurement with $i_2 = 0.938\,\mathrm{A}$ and $i_1 = 0.625\,\mathrm{A}$.
- Interleaved measurement with $i_4 = -0.938\,\mathrm{A}$ and $i_3 = -0.625\,\mathrm{A}$.
- Interleaved measurement with $i_5 = 1.25\,\mathrm{A}$ and $i_1 = 0.625\,\mathrm{A}$.

First method to analyze the quadratic Zeeman shift is: parabola fitting. With respect to the coil current, the fractional differential quadratic Zeeman shift is [16]

$$\delta\Delta\nu_B = \zeta((i_B - i_{0,z})^2 - (i_{B,r} - i_{0,z})^2) \tag{5.10}$$

where $i_{0,z}$ is the unknown current necessary to compensate for the background magnetic field in z direction, $i_{B,r}$ is the reference current which is 0.625 A here, i_B is the coil current, and ζ is the coefficient of quadratic Zeeman shift with respect to the coil current. From the fit of Figure 5.3, unfortunately, there is a high residual frequency at 0.938 A which causes the fit $\chi^2 \gg 1$. The reason is that the reference point is not the same for positive and negative current measurements, for example, the third and fifth measurements have a current reference at 0.625 A, however, the fourth measurement has a current reference at -0.625 A. Using this method, I cannot obtain the correct quadratic Zeeman shift.

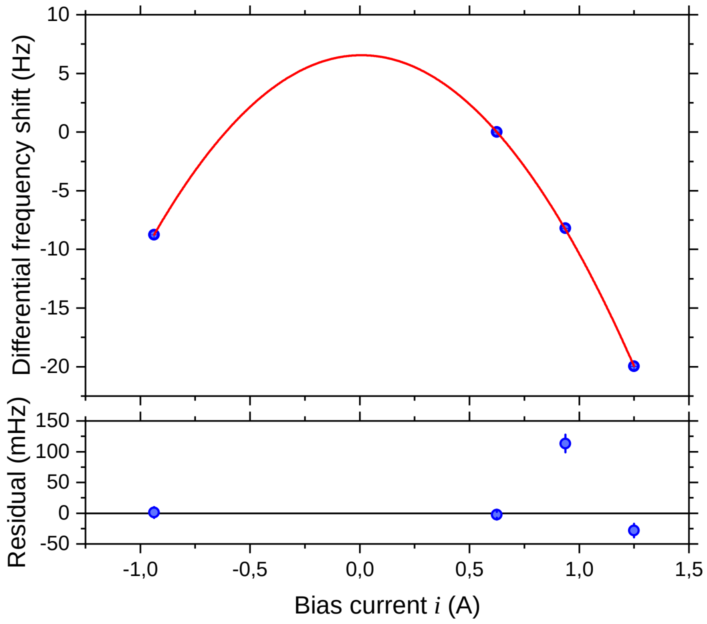

Figure 5.3: Differential quadratic Zeeman shift measurement. The fit function is Eq. 5.10. There is a high fit residual offset at 0.938 A. More details in text.

The second method is to analyze the interleaved measurements results to obtain quadratic Zeeman shift. For the third and fourth measurements, the differential quadratic Zeeman shifts are

$$\begin{aligned} \Delta\nu_{21} &= \beta(|\overrightarrow{B}_2 + \overrightarrow{B}_{//}|^2 - |\overrightarrow{B}_1 + \overrightarrow{B}_{//}|^2) \\ \Delta\nu_{43} &= \beta(|\overrightarrow{B}_4 + \overrightarrow{B}_{//}|^2 - |\overrightarrow{B}_3 + \overrightarrow{B}_{//}|^2) \end{aligned} \tag{5.11}$$

where the subscripts of numbers, e.g. 1, 2, 3, 4, show the parameters corresponding to the interleaved measurements with currents $i = 1, 2, 3, 4$. For example, $\Delta\nu_{21}$ is the differential quadratic Zeeman shifts which corresponds to the third measurement with bias current i_2 and i_1; $\overrightarrow{B}_4$ shows the bias magnetic field which corresponds to the fourth measurement with bias current i_4.

Because $|\overrightarrow{B}| \propto i$, $i_4 = -i_2$ and $i_3 = -i_1$, therefore

$$\Delta\nu_{43} = \beta(|-\overrightarrow{B}_2 + \overrightarrow{B}_{//}|^2 - |-\overrightarrow{B}_1 + \overrightarrow{B}_{//}|^2) \tag{5.12}$$

The frequency difference between these two interleaved measurements is

$$\begin{aligned} \Delta\nu_{43} - \Delta\nu_{21} &= \beta(-4\overrightarrow{B}_2\overrightarrow{B}_{//} + 4\overrightarrow{B}_1\overrightarrow{B}_{//}) \\ &= 4\beta\overrightarrow{B}_{//}(-\overrightarrow{B}_2 + \overrightarrow{B}_1) \end{aligned} \tag{5.13}$$

Define $\xi_2 = \frac{|\overrightarrow{B}_2|}{|\overrightarrow{B}_1|} = \frac{i_2}{i_1}$, thus

$$\Delta\nu_{43} - \Delta\nu_{21} = 4\beta\overrightarrow{B}_{//}\overrightarrow{B}_1(-\xi_2 + 1) \tag{5.14}$$

For the third and fifth interleaved measurements, similarly, the differential quadratic Zeeman shifts are

$$\Delta\nu_{51} - \Delta\nu_{21} = \beta|\overrightarrow{B}_1|^2(\xi_5^2 - \xi_2^2) + 2\beta\overrightarrow{B}_1\overrightarrow{B}_{//}(\xi_5 - \xi_2) \tag{5.15}$$

where $\xi_5 = \frac{|\overrightarrow{B}_5|}{|\overrightarrow{B}_1|} = \frac{i_5}{i_1}$. The subscripts are labeled in the same way as in eq. 5.11.

During clock operation, the bias current i_1 is used for creating the bias magnetic field, and thus the quadratic Zeeman shift is

$$\begin{aligned} \Delta\nu_{B1} &= \beta(|\overrightarrow{B}_1 + \overrightarrow{B}_{//}|^2 + |\overrightarrow{B}_{\perp}|^2) \\ &= \beta|\overrightarrow{B}_1|^2 + 2\beta\overrightarrow{B}_1\overrightarrow{B}_{//} + \beta|\overrightarrow{B}_{//}|^2 + \beta|\overrightarrow{B}_{\perp}|^2 \end{aligned} \tag{5.16}$$

According to eq. 5.14 and 5.15, the quadratic Zeeman shift along the z-axis $\beta(|\overrightarrow{B}_1 + \overrightarrow{B}_{//}|^2)$ can be obtained which is -6.3413(221) Hz.

According to the background field compensation in the Appendix A, $\beta|\overrightarrow{B}_\perp|^2 = -4(17)$ µHz, which is negligible compared to the shift along the z-axis. Based on the analysis above, the quadratic Zeeman shift at the bias current $i_1 = 0.625$ A is -6.3413(221) Hz corresponding to $-1477.4(52) \times 10^{-17}$ in fractional units.

5.3 Probe light shift

The probe light for interacting with cold atoms induces an AC Stark shift for clock transition energy levels. Optical lattice clocks based on neutral bosonic isotopes typically suffer from high AC Stark shifts due to probe light [65].

To evaluate the probe light shifts, I conducted interleaved measurements with different powers of the probe light. I have already discussed stabilizing the clock laser power during interleaved measurements in Section 4.4. I performed interleaved measurements with reference probe light power at 1.2 V (the monitor voltage) and four measurement points at 0.8 V, 1.2 V, 1.6 V, and 1.8 V. The differential fractional clock transition shifts are obtained. Based on the differential clock transition shifts, the probe light shift can be derived by fitting the data with

$$\delta\Delta\nu_L = k'(U_{pd} - U_{ref}) \tag{5.17}$$

Where U_{pd} is the monitor voltage from the photodetector, U_{ref} is the reference voltage, and k' is the shift coefficient. The position of the photodetector is shown in Figure 3.20 in Chapter 3.

Figure 5.4 shows the result for the probe light shift measurements. The probe light shift at the reference point, which is the operational condition of our clock, can be derived by $\delta\Delta\nu_L = k'U_{ref}$. As a result, the probe light shift is -485.8(96) mHz, corresponding to $-113.2(22) \times 10^{-17}$ relative frequency shift.

From the above measurements, I observed a significant probe light shift due to the high probe light power, which is limited by the principle of clock transition excitation of bosonic atoms, as described by magnetically induced spectroscopy [65].

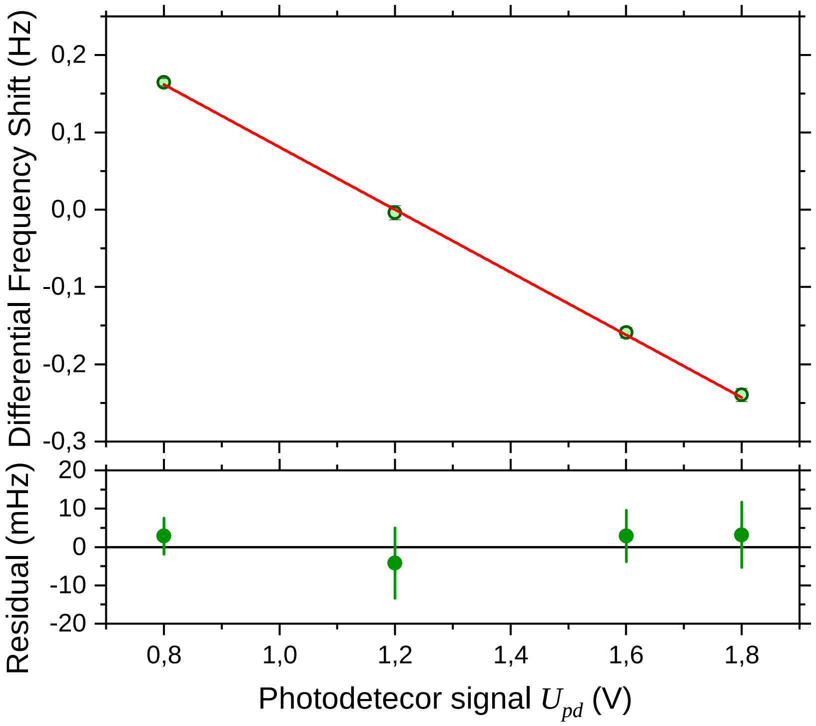

Figure 5.4: Probe light shift measurements. The green dots are experimental data and the red line is the fit with Eq. 5.17. The reference point is at 1.2 V and the resulting probe light shift is -485.8(96) mHz.

5.4 Cold collision shift

SOC2 is an optical lattice clock based on neutral bosonic strontium-88 atoms, which do not obey the Pauli exclusion principle. Thus, SOC2 experiences a larger collision shift compared to a neutral fermionic strontium-87 optical lattice clock.

To measure density shifts, interleaved measurements by varying the atom density are usually conducted. For the atom density, we must consider not only the number of atoms in the optical lattice but also the size of the atomic cloud. To this end, the most straightforward approach is to vary the number of atoms while maintaining size of the atomic cloud constant. One way to characterize the atomic cloud size is through the wavefunction extension of harmonic oscillations in an optical lattice, which can be evaluated by the motional state occupied by the atoms. In practice, the red cooling beam power of the breadboard red MOT is used to change the atom number; however, other parameters of clock operations remain the same, especially the parameters of the single—frequency red MOT. Thus, only the atom number is changed, and the atomic cloud size is kept the same. During density shift measurements, sideband spectroscopies are obtained at various atom numbers. The atom temperatures are extracted from the sideband spectroscopies and used to verify whether the montional state distribution remains the same for each measurement—the results show that it always does.

The density shifts are measured at shallow ($30\,E_r$) and deep ($58\,E_r$) lattices shown in Figure 5.5. At deep lattice, the density shift is -0.280(107) mHz per count, corresponding to $-6.5(25) \times 10^{-19}$ per count, and -0.431(121) mHz for shallow lattice, corresponding to $-10.0(28) \times 10^{-19}$ per count. In clock operation, the SOC2 clock always runs at a shallow lattice ($\sim 30\,E_r$); thus, the coefficient of $-10.0(28) \times 10^{-19}$ per count is used for the density shift evaluation. For example, for the atom number of 24(5) counts, the density shift is -8.7(27) mHz, corresponding to $-2.0(6) \times 10^{-17}$ in fractional units.

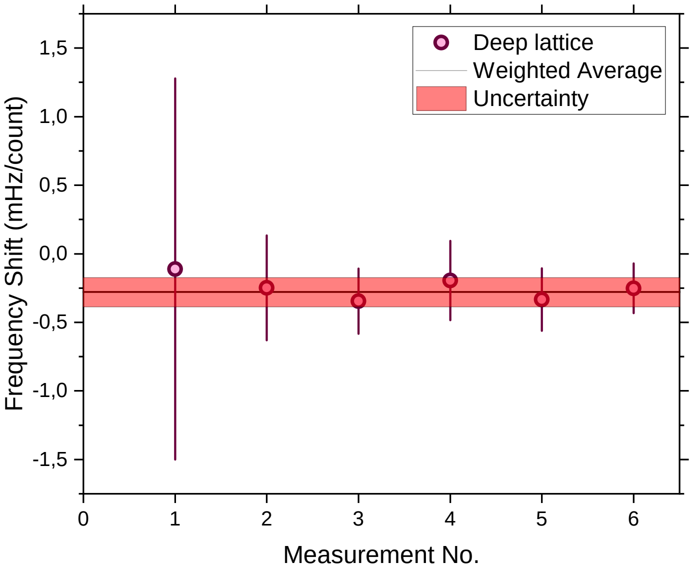

(a) Density shift measurements with a deep lattice with lattice depth of 58 E_r.

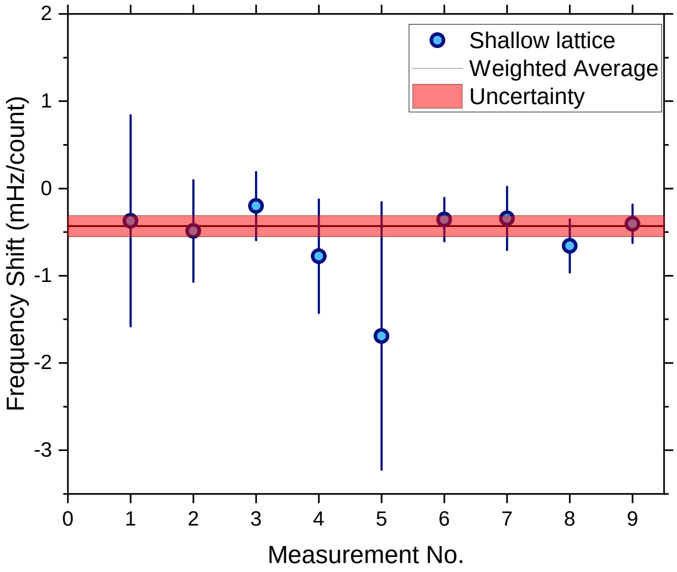

(b) Density shift measurements with a shallow lattice with lattice depth of 30 E_r.

Figure 5.5: Density shift measurements at the deep and shallow lattices. At the deep lattice, the density shift is -0.280(107) mHz per count, and -0.431(121) mHz per count for the shallow lattice.

5.5 Lattice light AC stark shift

Atoms in the optical lattice experience an AC Stark shift due to the lattice light, which provides the trap potential for atoms in the Lamb-Dicke regime; however, it also causes the frequency shift for the clock transition, ${}^1S_0 \leftrightarrow {}^3P_0$, which is undesirable in metrology. In order to suppress the lattice light shift of the clock transition, as mentioned in Chapter 2, the optical lattice at the 'magic' wavelength was proposed in which the AC Stark shift of the clock transition could be eliminated. However, to characterize the systematic uncertainty of optical clock to 10^{-18} level, the nonlinear dependence of the lattice light shift on trap depth due to higher multipolarizabilites from magnetic dipole (M1) and electric quadrupole (E2) contributions and hyperpolarizability should be carefully considered.

Based on the perturbative treatment in the harmonic motional state basis with consideration of longitudinal and transverse optical confinements, the lattice light AC Stark shift as a function of the lattice depth u_0 in units of E_r is expressed by [87]

$$\begin{aligned}\frac{\delta\nu_{clock}}{\nu_{clock}} &= n_5\Delta\alpha'_{M_1E_2} + [(n_1+n_2)\Delta\alpha'_{E1} - n_1\Delta\alpha'_{M_1E_2}]u_0^{\frac{1}{2}} \\ &\quad - [\Delta\alpha'_{E1} + (n_3+n_4+4n_5)\Delta\beta']u_0 + [2\Delta\beta'(n_1+n_2)]u_0^{\frac{3}{2}} - \Delta\beta' u_0^2\end{aligned} \tag{5.18}$$

where $\Delta\alpha'_{E1}$, $\Delta\alpha'_{M_1E_2}$, and $\Delta\beta'$ represent dimensionless differential electric dipole (E1) polarizability, M1/E2 polarizabilities and hyperpolarizability, respectively. $n_1 = n_z + 1/2$, $n_2 = [\sqrt{2}/(kw_0)][n_\rho + 1]$, $n_3 = (3/2)(n_z^2 + n_z + 1/2)$, $n_4 = [8/(3k^2w_0^2)](n_\rho^2 + 2n_\rho + 3/2)$, and $n_5 = 1/(\sqrt{2}kw_0)(n_z + 1/2)(n_\rho + 1)$ are intermediate factors that represent the temperatures of cold atom with longitudinal motional state n_z and transverse motional state $n_\rho = n_x + n_y$.

The observations of sideband spectroscopy at different lattice trap depths are implemented, as shown in Figure 5.6, and a linear scaling of the axial temperature with lattice depth u_0 is observed, shown in Figure 5.7. Based on the thermal model in Ref.[87], the averaged $<n_1>$, $<n_2> \propto \sqrt{u_0}$ and $<n_3>$, $<n_4>$, $<n_5> \propto u_0$ are obtained and Eq. 5.18 can be reduced to [87]

$$\frac{\delta\nu_{clock}}{\nu_{clock}} = -\alpha^* u_0 - \beta^* u_0^2 \tag{5.19}$$

where α^* and β^* are u_0-independent finite-temperature polarizabilities.

In order to roughly search for the magic wavelength, interleaved measurements with deep ($u_{0,d} \sim 56\,E_r$) and shallow ($u_{0,s} \sim 28\,E_r$) lattice depths are conducted at various lattice light frequencies, shown in Figure 5.8. The differential fractional frequency can be expressed

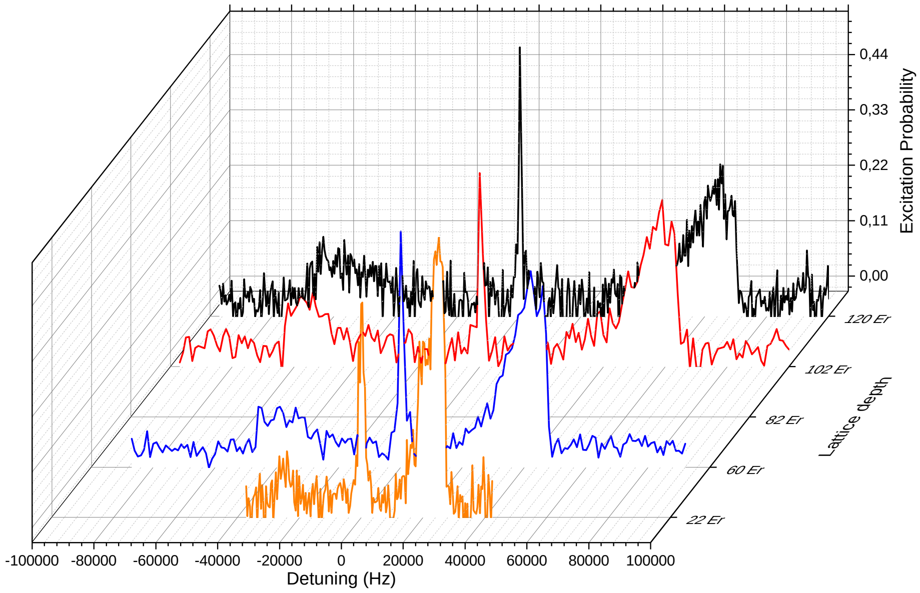

Figure 5.6: Sideband spectroscopy with multiple trap depths.

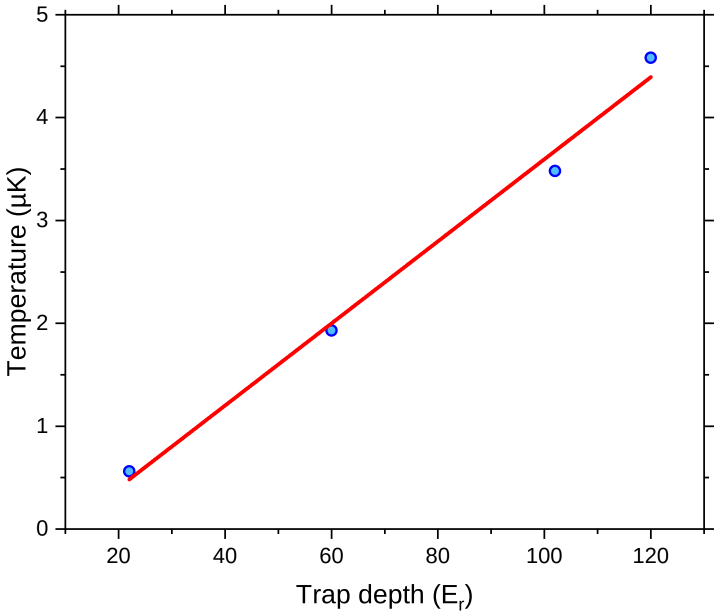

Figure 5.7: The linear scaling of longitudinal (axial) temperatures with lattice trap depths. The trap depths and temperatures are extracted from the sideband spectra in Figure 5.6, using the method shown in Section 3.4.6.

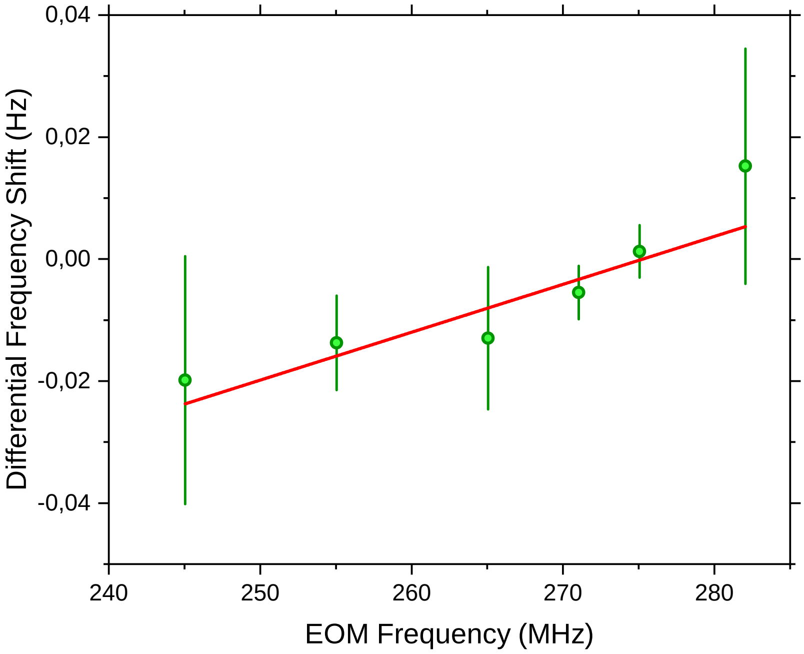

Figure 5.8: The effective magic wavelength searching by interleaved measurements with two lattice depths at various EOM frequencies which is for locking the lattice laser to FSS (frequency stabilization system, shown in Section 3.3). The density shift contributions are removed for all data points.

as

$$\begin{aligned} \Delta\frac{\delta\nu_{clock}}{\nu_{clock}} &= -\alpha^*(u_{0,d}-u_{0,s}) - \beta^*(u_{0,d}^2-u_{0,s}^2) \\ &= -\frac{\partial\alpha^*}{\partial\nu_l}(\nu_l-\nu_{zero})(u_{0,d}-u_{0,s}) - \beta^*(u_{0,d}^2-u_{0,s}^2) \end{aligned} \tag{5.20}$$

where ν_l and ν_{zero} are lattice laser frequency and the effective magic frequency, respectively. Since α^* is dependent on the laser frequency, I expressed it in terms of the partial derivative with respect to the laser frequency and the frequency detuning. The data of fractional differential frequency shifts are fitted by Eq. 5.20, and $\partial\alpha^*/\partial\nu_l$ and ν_{zero} can be obtained from the fitting. However, the coefficient of the quadratic term cannot be acquired by this fitting. If the frequency shift due to hyperpolarizability is ignored, the quadratic term in Eq. 5.19, the lattice AC Stark frequency shift could shift by about 2×10^{-18} which should be avoided if the optical lattice clock aims for 10^{-18} level.

From the measurements in Figure 5.8 and Eq. 5.20, it is impossible to calculate lattice

AC Stark shift and magic wavelength because β^* is unknown. To determine $\partial\alpha^*/\partial\nu_l$ and β^* accurately, measurements of differential AC Stark shifts as a function of lattice depth at various lattice laser frequencies need to be implemented, and then fitted by Eq. 5.20 [88][87][89]. Based on these two coefficients, the AC Stark shift at the operational wavelength and the effective magic wavelength can be easily determined. An operational magic wavelength at $\nu_{opmagic} \equiv (-2\beta^* u_0)/(\partial\alpha^*/\partial\nu_l) + \nu_{zero}$ is recommended in Ref. [87], at which the first-order frequency shift is insensitive to fluctuations in the corresponding u_0 and a negative linear light shift partially cancels the positive hyperpolarizability shift. The lattice laser frequency could be continuously monitored within $\sim 25\,\text{MHz}$ uncertainty around ν_{zero}, which can lead to a lattice shift uncertainty of 10^{-18}. Then Eq. 5.20 can be applied to calculate the AC Stark shift. However, the lattice laser frequency may drift because of the FSS cavity length drift, which needs to be compensated during measurements. Achieving lattice AC Stark shift in this way is complicated due to multiple measurements at different lattice depths and laser frequencies.

Another method to characterize the AC Stark shift in the lattice is to implement interleaved measurements with two lattice depths around the effective magic wavelength and using accurately determined atomic parameter coefficients: $\Delta\alpha'_{E1}$, $\Delta\alpha'_{M_1E_2}$, and $\Delta\beta'$, to determine the frequency detuning with respect to the effective magic wavelength via Eq. 5.18. After the determination of the frequency detuning, the lattice AC Stark shift can be calculated by Eq. 5.18 at operational lattice depth u_0, which can be evaluated by the sideband spectroscopy before starting the interleaved measurements. I ran the interleaved measurements with lattice depths of $\sim 56\,E_r$ and $\sim 28\,E_r$ at the EOM frequency of 271 MHz. The resulting differential fractional frequency shift is $-1.3(10)\times 10^{-17}$. Lattice AC Stark shift of this interleaved measurements is $-1.2(12)\times 10^{-17}$ by using atomic coefficients from Ref. [85]. The primary contribution to the uncertainty of this shift is the statistical uncertainty of the interleaved measurement, which can be improved by increasing the lever arm of the lattice depths and conducting longer measurements. The density shift contributions are removed from the frequency shift during the lattice AC Stark shift measurements.

Estimate of differential electric dipole polarizability. In order to precisely characterize the lattice AC Stark shift, the atomic coefficients, e.g. $\Delta\alpha'_{E1}$, $\Delta\alpha'_{M_1E_2}$, and $\Delta\beta'$, need to be accurately known according to Eq. 5.18. Here, a simple approach to determine the partial derivative of the differential dipole polarizability is shown.

According to the expression of Eq. 5.18, the differential fractional frequency shift between the deep and shallow lattice depth is

$$\begin{aligned}\Delta\frac{\delta\nu_{clock}}{\nu_{clock}} &= \{n_5^d\Delta\alpha'_{M_1E_2} - n_5^s\Delta\alpha'_{M_1E_2}\} \\ &+ \{[(n_1^d+n_2^d)\Delta\alpha'_{E1} - n_1^d\Delta\alpha'_{M_1E_2}]u_{0,d}^{\frac{1}{2}} - [(n_1^s+n_2^s)\Delta\alpha'_{E1} - n_1^s\Delta\alpha'_{M_1E_2}]u_{0,s}^{\frac{1}{2}}\} \\ &- \{[\Delta\alpha'_{E1} + (n_3^d+n_4^d+4n_5^d)\Delta\beta']u_{0,d} - [\Delta\alpha'_{E1} + (n_3^s+n_4^s+4n_5^s)\Delta\beta']u_{0,s}\} \\ &+ \{[2\Delta\beta'(n_1^d+n_2^d)]u_{0,d}^{\frac{3}{2}} - [2\Delta\beta'(n_1^s+n_2^s)]u_{0,s}^{\frac{3}{2}}\} - \{\Delta\beta' u_{0,d}^2 - \Delta\beta' u_{0,s}^2\}\end{aligned} \tag{5.21}$$

where the superscript d and s mean the quantities are for deep and shallow lattice, respectively. For two interleaved measurements at different lattice laser frequencies, the frequency shift difference is expressed

$$\begin{aligned}\Delta_1\frac{\delta\nu_{clock}}{\nu_{clock}} - \Delta_2\frac{\delta\nu_{clock}}{\nu_{clock}} &= \{(n_1^d+n_2^d)u_{0,d}^{\frac{1}{2}} - (n_1^s+n_2^s)u_{0,s}^{\frac{1}{2}}\}\frac{\partial\Delta\alpha'_{E1}}{\partial\nu_l}(\nu_{l1}-\nu_{l2})) \\ &- \{u_{0,d} - u_{0,s}\}\frac{\partial\Delta\alpha'_{E1}}{\partial\nu_l}(\nu_{l1}-\nu_{l2})) \\ &= \{(n_1^d+n_2^d)u_{0,d}^{\frac{1}{2}} - (n_1^s+n_2^s)u_{0,s}^{\frac{1}{2}} - u_{0,d} + u_{0,s}\}\frac{\partial\Delta\alpha'_{E1}}{\partial\nu_l}(\nu_{l1}-\nu_{l2}))\end{aligned} \tag{5.22}$$

where subscripts 1 and 2 of Δ indicate the differential fractional frequency shifts of the first and second interleaved measurements, respectively. Since $\Delta\alpha'_{E1}$ depends on the lattice laser frequency, I expressed it in terms of the partial derivation of the laser frequency and the frequency detuning. ν_{l1} and ν_{l2} are lattice laser frequencies of the first and second interleaved measurements, respectively. According to Eq. 5.22, $\partial\Delta\alpha'_{E1}/\partial\nu_l$ can be determined since all other quantities can be obtained through measurements, such as sideband spectroscopy measurements.

According to the measurements in Figure 5.8 and Eq. 5.22, the resulting slope of differential electric dipole polarizability is 16(5) µHz/MHz which is consistent with the measurement results from Refs. [85] and [90]. The primary source of uncertainty ($>90\%$) of this method comes from differential lattice shift measurements, which could be significantly reduced by additional repeated measurements. On the basis of this method, the slope of the differential electric dipole polarizability can be easily measured with high accuracy, thus accurately determining the lattice AC Stark shift.

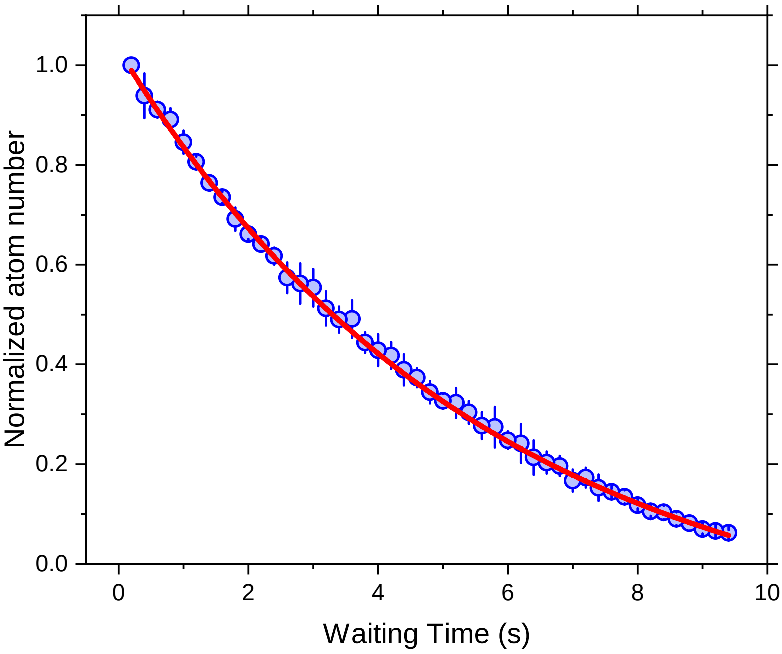

Figure 5.9: The background gas limited lifetime measurement. The blue circular points are experimental data and the red line is the exponential decay function. The $1/e$ decay time defines the lifetime, which is 5.7(1) s here.

5.6 Background gas collision shift

Even though the vacuum pressure in the science chamber is less than 10^{-10} mbar (based on the ion pump current), there are still some residual room-temperature gases, mainly H_2 molecules. The collision between lattice-trapped cold strontium atoms and room-temperature H_2 molecules causes a frequency shift, named the background gas collision frequency shift, which is studied and evaluated in Ref. [91]. For a background gas limited 1 s lifetime, the shift is

$$\frac{\Delta\nu_{bg}}{\nu_0} = -30(3) \times 10^{-18} \tag{5.23}$$

The background gas limited lifetime of SOC2 is 5.7(1) s, measured by magnetic trap, as shown in Figure 5.9. Thus, the background gas collision frequency shift of SOC2 is $-5.3(5) \times 10^{-18}$.

5.7 Frequency shifts due to other effects

DC-Stark shift. The electric field around the cold atom can cause a frequency shift which is independent of the clock cycle time T_c and the interrogation time T_π. Although the current T_c and T_π are different from those used in Ref. [16], the DC-Stark shift should remain at the same level, which is $\sim -2(2) \times 10^{-18}$, since the conditions of electric potential around the science chamber are the same.

Servo error. The cavity-stabilized clock laser usually has a frequency drift because of the length drift of the cavity. The time delay between the atomic interrogation and the frequency correction feedback to the clock laser causes a frequency offset between the atomic resonance frequency and the clock laser frequency, called servo error. The servo error due to the linear frequency drift of the optical resonator can be eliminated by compensating the clock laser frequency. However, the nonlinear frequency drift cannot be easily compensated, leading to servo error [92]. Fortunately, during the operation of the SOC2 clock, the clock laser is phase-locked to the PTB stationary clock laser, which is stabilized to the PTB stationary clock (Sr3). Therefore, there is essentially no frequency drift, and thus the servo error is zero.

Effect	Correction (mHz)	Uncertainty (mHz)
BBR shift (environment)	2236.8	4.9
BBR shift (oven)	0	0
Lattice AC Stark shift	15.3	9.4
Probe light AC Stark shift	485.8	9.6
Cold collision shift	8.7	2.7
Quadratic Zeeman shift	6341.3	22.1
Background gas collision shift	2.3	0.2
DC Stark shift	0.8	0.1
Servo error	0	0
Total	9091.0	26.5
Fractional frequency (10^{-17})	2118.0	6.2

Table 5.1: The typical uncertainty budget of the SOC2 clock at a low atom number ($\sim$ 240). The clock laser is phase-locked to PTB 48 cm room-temperature ULE cavity and then transfer-locked to PTB 21 cm cryogenic silicon cavity via an optical comb.

5.8 Systematic uncertainty budget of the SOC2 clock

By now, I have characterized and analyzed all the effects on the SOC2 clock. The uncertainty budget of SOC2 is shown in Table 5.1 with a low atom number (24(5) counts), and the main contribution is from the quadratic Zeeman shift. Since, while running the SOC2 clock, the atom number was not stabilized and had a large fluctuation, this fluctuation would significantly affect the collision shift. Thus, the uncertainty budget would undergo a significant change. Here, Table 5.2 shows the budget at high atom number (225(37) counts[13]). Directly from the table, the main contribution of the uncertainty budget is from the lattice AC Stark shifts. However, the noise source of the lattice AC Stark shifts at a high atom number comes from the collision shift which is more significant than in the low atom number case and thus worsens the uncertainty of the SOC2 clock. The uncertainty of the count number represents the standard deviation.

5.9 Isotope shift between strontium-88 and -87 neutral atoms of clock transitions

5.9.1 Gravitational redshift

In order to have the isotope shift between strontium-88 and -87 atoms by the SOC2 and Sr3 [19] frequency comparison, the frequency shift due to the gravitational potential difference

Effect	Correction (mHz)	Uncertainty (mHz)
BBR shift (environment)	2232.2	5.0
BBR shift (oven)	0.5	0.2
Lattice AC Stark shift	38.3	42.7
Probe light AC Stark shift	485.8	9.6
Cold collision shift	80.1	22.4
Quadratic Zeeman shift	6341.3	22.1
Background gas collision shift	2.3	0.2
DC Stark shift	0.8	0.1
Servo error	0	0
Total	9181.3	54.1
Fractional frequency (10^{-17})	2139.0	12.6

Table 5.2: The typical uncertainty budget of SOC2 clock at a high atom number (~ 2250). The clock laser is the same as that used in Table 1.1.

should be considered. The gravitational redshift $\Delta\nu$ can be described by the gravitational potential difference ΔU as

$$\frac{\Delta\nu}{\nu_0} = \frac{\Delta U}{c^2} \tag{5.24}$$

where ν_0 is the frequency of clock transition, and c is the speed of light. The SOC2 and Sr3 clocks are located in neighboring labs and the gravitational redshift between them can be expressed as

$$\frac{\Delta\nu_{soc}}{\nu_{^{88}Sr}} - \frac{\Delta\nu_{Sr3}}{\nu_{^{87}Sr}} = \frac{\Delta U_{soc}}{c^2} - \frac{\Delta U_{Sr3}}{c^2} \tag{5.25}$$

Since the clock transitions $\nu_{^{88}Sr} \approx \nu_{^{87}Sr}$, the gravitational redshift can be reduced to

$$\frac{\Delta\nu}{\nu_{^{88}Sr}} = \frac{g\Delta h}{c^2} \tag{5.26}$$

where g is the local gravitational acceleration and Δh is the height difference between cold-atom ensembles of SOC2 and Sr3 clocks. There is a geopotential reference marker in the laboratory building where both clocks are located. The heights of SOC2 and Sr3 to the marker are measured with standard geometric leveling, using a spirit level and a ruler [29] and they are 1007(5) mm and 703(3) mm for the cold-atom ensembles of SOC2 and Sr3, respectively. The difference is 304(6) mm, resulting gravitational redshift difference of 0.0143(3) Hz, which corresponds to $3.32(6) \times 10^{-17}$ in relative frequency.

5.9.2 Isotope shift

The typical statistical and systematic uncertainties of the Sr3 clock can be found in Ref. [19]. After considering the gravitational shift and systematic shifts of the SOC2 and Sr3 clocks, the isotope shift was measured and shown in Figure 5.10a. The measurements were implemented on four different days with different atom numbers. The common uptime of the SOC2 and Sr3 clocks is 19.2 hours. The measurements on 60374 and 60375 Modified Julian Date (MJD) are with low atom number and their corresponding systematic uncertainties are listed in Table 5.1. On the other hand, measurements with high atom numbers are conducted as well on 60383 and 60384 MJD with corresponding systematic uncertainty list in Table 5.2. Obviously, the uncertainties of the isotope shift with more atoms are more significant than those with fewer atoms because of the density shift. In the four frequency comparison data, the daily error bars represent the total uncertainties, which are the quadrature sum of statistical and systematic uncertainties. The total uncertainties are used as weights to average the daily data. The weighted average of the isotope shift in the four measurements is 62 188 134.032(35) Hz, which agrees well with the value recently reported as shown in Figure 5.11. To obtain the uncertainty of the weighted average here, the systematic frequency shifts are treated as fully correlated between the measurements; however, the statistical uncertainties are treated as uncorrelated.

The frequency ratio between strontium-88 and -87 atoms of clock transitions is shown in Figure 5.10b. The weighted average is 1.000 000 144 883 682 842(82), which is consistent with the 2021 recommended frequency values of CIPM (International Committee for Weights and Measures) [93].

Meanwhile, PTB transportable strontium optical lattice clock (Sr4) was also operating [14]. The common uptime between the SOC2 and Sr4 clocks is 12.6 hours. The resulting frequency ratio and isotope shift between them are 1.000 000 144 883 682 832(77) and 62 188 134.027(33) Hz, respectively. The isotope shift is also shown in Figure 5.11 to compare with the results of other groups.

The systematic uncertainty of the SOC2 clock dominates the uncertainties of the frequency ratio and isotope shift.

The systematic uncertainty of the SOC2 clock dominates the uncertainties of the frequency ratio and isotope shift. They are higher with respect to Sr3 than to Sr4. The deviations are at 10^{-17} level, which may be attributed to an unidentified systematic frequency shift of Sr3 [98] or the systematic uncertainty of the SOC2 clock.

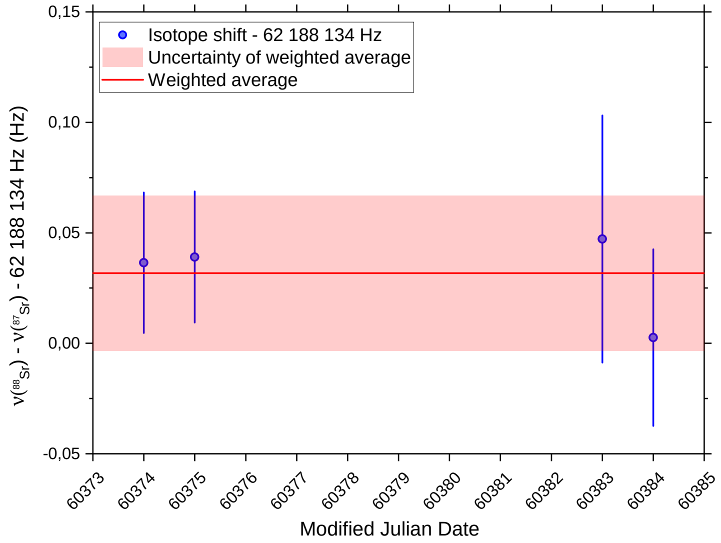

(a) Isotope shift

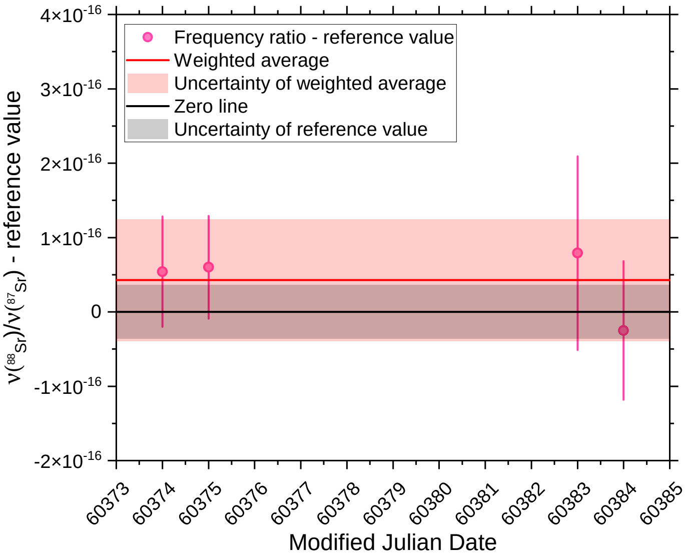

(b) Frequency ratio

Figure 5.10: Isotope shift and frequency ratio between strontium-88 and -87 atoms of the clock transitions by comparing the SOC2 and the Sr3 clocks. Error bars represent the quadrature sum of statistical and systematic uncertainties. The daily statistical uncertainties are less than 1×10^{-17} and total uncertainties are dominated by the systematic uncertainty of the SOC2 clock. (a) Isotope shift measurements. The weighted average is 62 188 134.032(35) Hz. (b) Frequency ratio results. The weighted average is 1.000 000 144 883 682 842(82), which is consistent with the 2021 recommended frequency values of CIPM (International Committee for Weights and Measures) [93]. The reference value is the frequency ratio from Table B1 in [93].

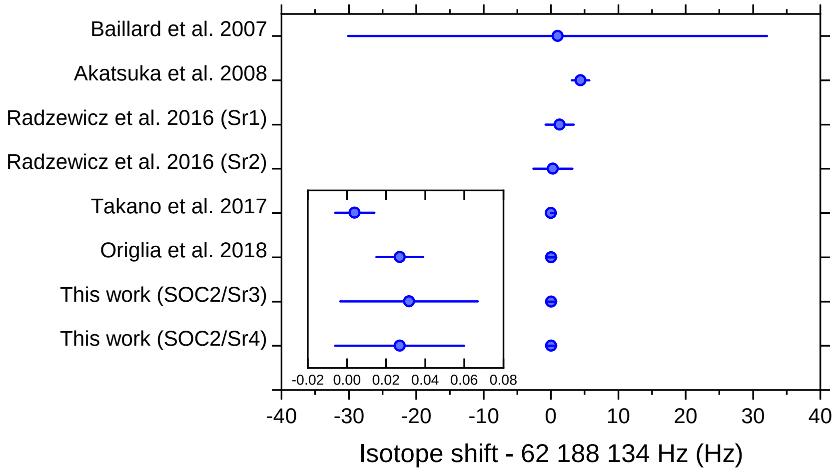

Figure 5.11: Isotope shift comparison with published values. The insert box shows the recently reported results. The results in this dissertation agree well with the values recently reported [16][94]. Baillard et al. [95] and Radzewicz et al. [96] derived the isotope shifts from the absolute frequency measurements of the ^{88}Sr clock transition. Takano et al. [94] measured the isotope shift by alternatively interrogating ^{88}Sr and ^{87}Sr atoms in the same vacuum system. Akatsuka et al. [97], Origlia et al. [16], and our work implemented direct frequency comparison between independent ^{88}Sr and ^{87}Sr clocks to measure the isotope shifts.

5.10 The frequency ratios of strontium-88 neutral atom to ytterbium-171 and indium-115 ions

In addition to strontium optical lattice clocks, there are also many optical ion clocks operating at PTB, for instance, $^{171}\mathrm{Yb}^+$ (ytterbium-171 ion) clock [99] [100], $^{115}\mathrm{In}^+$ (indium-115 ion) clock [98], $^{27}\mathrm{Al}^+$ (aluminum-27 ion) clock. During the SOC2 clock operation in early 2024, the $^{171}\mathrm{Yb}^+$ and $^{115}\mathrm{In}^+$ clocks were also operated.

The common uptimes of $^{88}\mathrm{Sr}$ to $^{171}\mathrm{Yb}^+$ and $^{115}\mathrm{In}^+$ clocks are 16.3 hours and 1.2 hours, respectively. Frequency ratios of $^{88}\mathrm{Sr}$ with respect to the electric octupole ($E3$) transition in $^{171}\mathrm{Yb}^+$ are shown in Figure 5.12. The weighted average is 1.495 991 401 800 156 81(12), which is consistent with the 2021 recommended frequency values of CIPM.

Frequency ratio of $^{88}\mathrm{Sr}$ with respect to $^{115}\mathrm{In}^+$ is 2.952 748 322 069 809 39(22), as shown in Figure 5.13. The ratio uncertainty of $^{88}\mathrm{Sr}$ to $^{115}\mathrm{In}^+$ has improved over the reference value by a factor of approximately 60. The reference value is the frequency ratio from Table B1 in [93].

The fractional uncertainties of the ratios of $^{88}\mathrm{Sr}$ to $^{171}\mathrm{Yb}^+$ and $^{115}\mathrm{In}^+$ are 8.2×10^{-17} and 7.5×10^{-17}, which are dominated by the systematic uncertainty of the SOC2 clock. To our knowledge, these direct optical frequency ratios of $^{88}\mathrm{Sr}$ to $^{171}\mathrm{Yb}^+$ and $^{115}\mathrm{In}^+$ are reported for the first time.

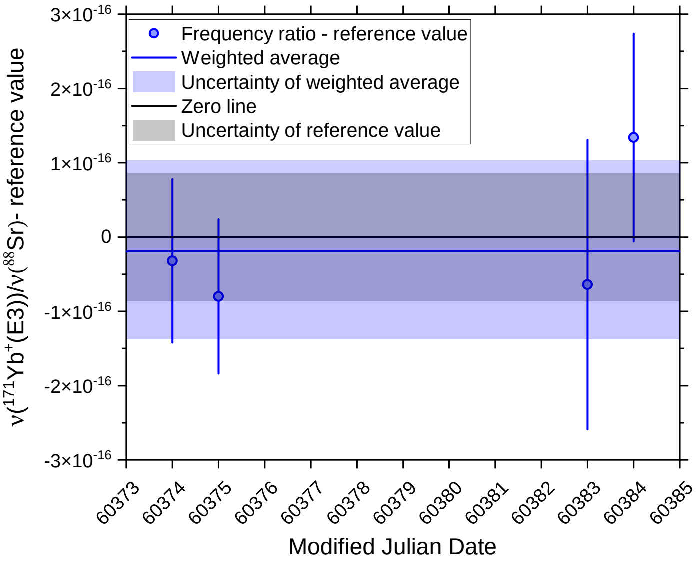

Figure 5.12: Frequency ratio of ^{88}Sr with respect to the electric octupole ($E3$) transition in ^{171}Yb^{+}. The weighted average is 1.495 991 401 800 156 81(12), which is consistent with the 2021 recommended frequency values of CIPM (International Committee for Weights and Measures) [93]. The reference value is the frequency ratio from Table B1 in [93].

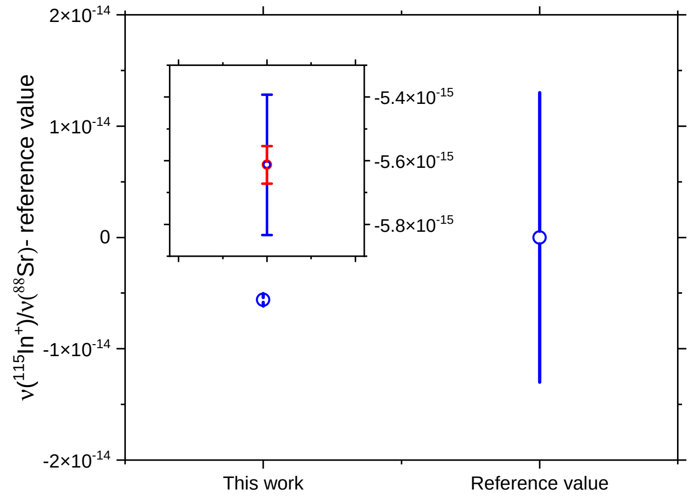

Figure 5.13: Frequency ratio of ^{88}Sr with respect to ^{115}In^{+}. The insert box shows the total uncertainty (blue error bar) and the statistical uncertainty (red error bar) of this work. The ratio is 2.952 748 322 069 809 39(22), which is consistent with the 2021 recommended frequency values of CIPM (International Committee for Weights and Measures) [93]. The reference value is the frequency ratio from Table B1 in [93].

Chapter 6

Potential Improvements of the SOC2 Clock

In the preceding chapters, a transportable 1-D optical lattice clock based on neutral strontium-88 atoms (SOC2) is shown. After careful characterizations, the instability of the clock is 6×10^{-17} at 100 s, 1×10^{-17} at 1 hour, which satisfies the technical requirements of the FOR 5456 project (shown in Chapter 1). However, the long-term instability at an averaging time of 2 days is not shown due to the lack of long-term clock operation, which has not yet been achieved. It is related to another main technical requirement of SOC2 clock: uninterrupted operation for at least 1 week. Moreover, the systematic uncertainty of SOC2 also does not meet the technical requirement, which is $\leq 1 \times 10^{-17}$. Some potential optimizations of the SOC2 clock could be implemented to meet the project goals.

6.1 BBR shift

The blackbody radiation shift is an important effect that often limits the performance of an optical clock. This is especially true if the objective is to achieve an overall uncertainty at the level of 10^{-18}. Most optical clock groups implement a water cooling system to stabilize the temperature and reduce the temperature gradient of the science chamber, where the cold atoms are interrogated. Additionally, some groups utilize a cryogenic BBR shield to achieve an uncertainty of less than 2×10^{-18} on the BBR shift. For the SOC2 clock, an approach suitable for transport is required. It should be as reliable and straightforward as possible. Therefore, we[13] designed a simple, compact, and low-power-consumption temperature control (TC) system based on eight thermoelectric cooling (TEC) elements, each with an independent controller. Additionally, an independent monitoring system was also built. With this overall system, I demonstrated a temperature gradient of approximately 220 mK, corresponding to an uncertainty on the BBR shift of 4×10^{-18}. The variation of no more

---

[13] Stefano Origlia designed the printed circuit board (PCB) of the controller and I tested and debugged the PCB. More details can be found in Appendix B. After the controller became functional, I built a box for it, shown in Figure 6.3a.

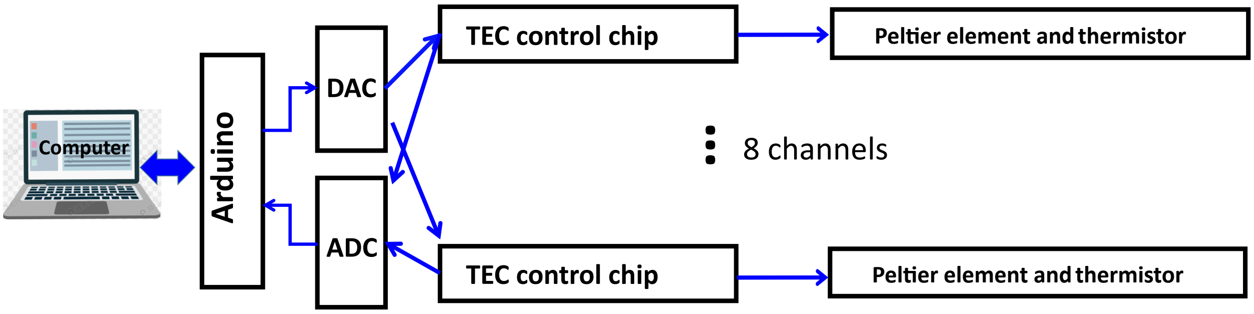

Figure 6.1: The scheme of the temperature control system. More details in text. TEC: thermoelectric cooling element; ADC: analog-to-digital converter; DAC: digital-to-analog converter.

than 20 mK over two days in the average temperature was obtained.

6.1.1 Temperature controller of the science chamber

The TC system features eight independent channels, each equipped with a TEC control chip, a Peltier element, and a thermistor. The temperature setpoint and actual temperature can be optimized independently via the DAC (digital-to-analog converter) and ADC (analog-to-digital converter) and can also be monitored using an Arduino. The scheme is shown in Figure 6.1.

The Peltier elements and thermistors are distributed around the science chamber, as shown in Figure 6.2. The heat pipes and a heat sink located on top of the rack are used to dissipate the heat generated by the Peltier elements.

The electronic part of the TC system is housed in a compact box, which includes TEC control chips, an Arduino module, an ADC, and a DAC, as shown in Figure 6.3. There are eight switches on the front panel of the control box that can be used to turn each control channel on or off independently. On the front panel, eight LEDs indicate the status of the actual temperature. When the LED turns on, the actual temperature has reached the temperature setpoint.

In order to measure the mean temperature of the chamber and its gradient, seventeen temperature sensors (thin film RTDs, PT100) are installed outside the science chamber and monitored by a precision temperature scanner (Fluke 1586A). Together, they form the monitoring system. The scanner is employed to read the temperature of each sensor. With this approach, we expect to also obtain a relatively accurate picture of the thermal environment of the atoms inside the chamber. The exact positions of these sensors are shown in Figure 6.4. All sensors are carefully calibrated and a calibration uncertainty of 15 mK was obtained [16].

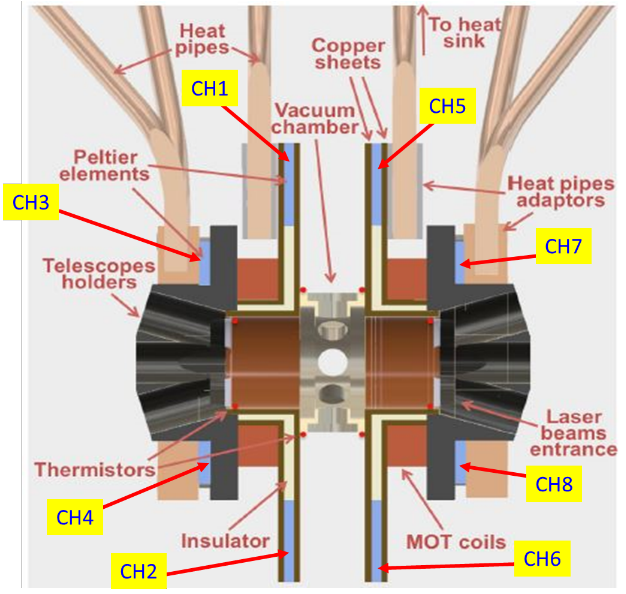

Figure 6.2: The cross-section of the science chamber and the distribution of 8 channels peltier elements and thermistors.

The calibration procedure was performed using procedures developed by PTB.

6.1.2 Operation of the temperature control system

All channels of this system are operated independently. I use one channel as an example to demonstrate how to operate this system, setting the temperature to 25 °C. The DAC (AD5669R) and TEC controllers (TECA1-5V-5V-D) are employed to set the temperature. For a desired temperature, e.g., 25 °C, an appropriate voltage V_{OUT} must be supplied to the TEC chip, as specified in its datasheet. The relationship between setpoint temperature and voltage can be obtained from its datasheet. For 25 °C, the setpoint voltage is 1.5 V. Then the decimal equivalent D of the binary code for DAC has to be calculated based on the formula

$$V_{OUT} = V_R \times \frac{D}{2^N} \tag{6.1}$$

and then loaded to the DAC register via the Arduino module. N is the resolution of the DAC chip and V_R is the reference voltage on the chip. For our case, N is 16 and $V_R = 3\,\mathrm{V}$, so $D = 32768$ for 25 °C. After loading the code into the DAC register, the setpoint temperature is changed. Some time later, the LED on the front panel lights up and the actual temperature has reached 25 °C which is acquired via the thermistors and the ADC (ADS1115).

(a) Control box.

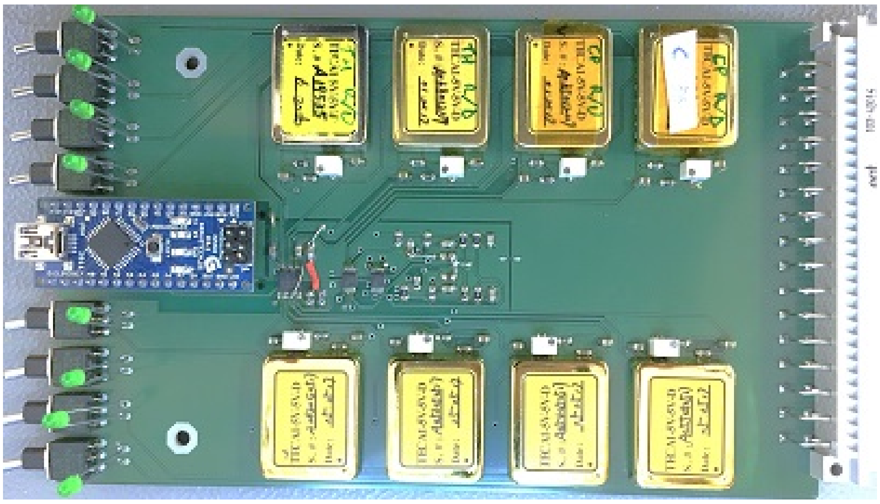

(b) The printed circuit board (PCB) in the box.

Figure 6.3: The electronics part of the temperature control system.

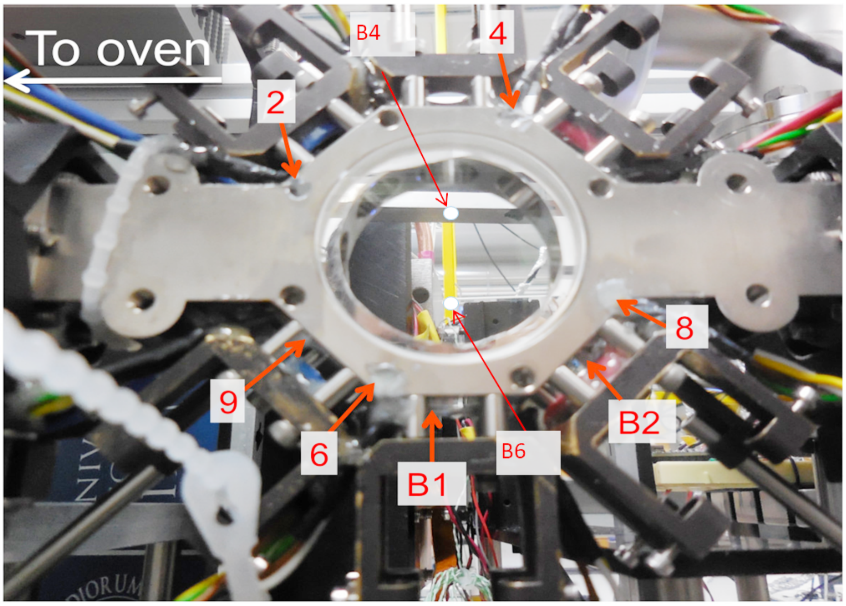

(a) Right side of the science chamber.

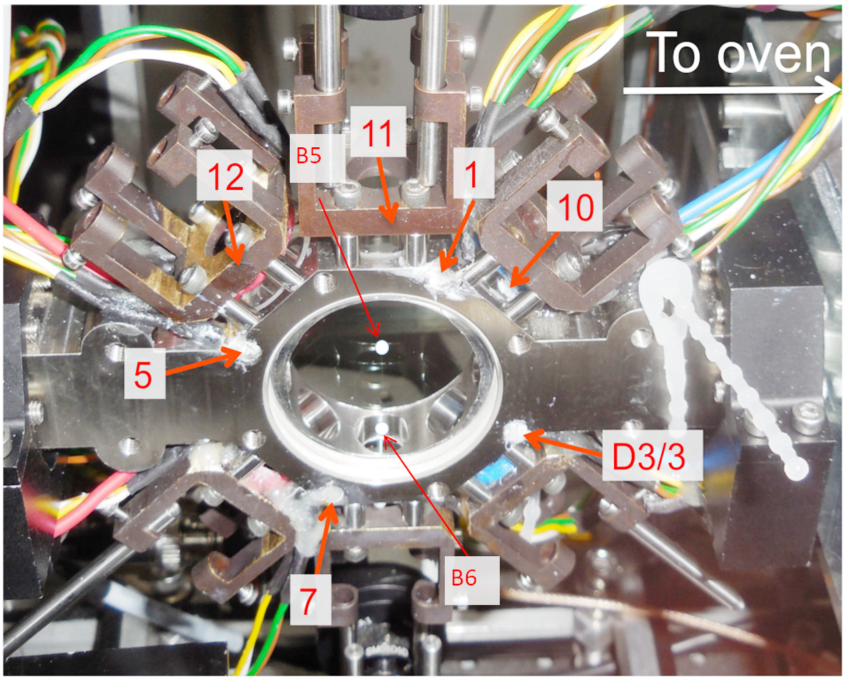

(b) Left side of the science chamber.

Figure 6.4: The positions of the PT100 sensors.

6.1.3 Temperature data from monitoring system

After completing the hardware construction and computer code, I run the TC system with the clock control sequence enabled, which means that the magnetic field coils are supplied with current. The corresponding heat load leads to a temperature gradient δT defined as the difference between T_c and T_w across the science chamber,

$$\delta T(t) = T_c(t) - T_w(t) \tag{6.2}$$

For the first run with the control sequence on, all the channels are set to the same setpoint, $D = 21845$, corresponding to a setpoint temperature of 21.5 °C. Since the temperature scanner can only read up to 10 sensors simultaneously, to measure 17 sensors, it is necessary to remove and replace the cables manually. It then takes less than 10 minutes to read all 17 channels. I performed this procedure several times on the first days of testing and then chose 10 of the 17 sensors that show significant temperature changes and large temperature differences to be monitored for a long-term measurement. The science chamber temperature of approximately 21.5 °C was obtained. I also immediately obtained a gradient of 250 mK before any further adjustments. Since the eight control channels are independent, I manually optimized the individual coefficients of all eight controllers. After optimization of the temperature setpoints of the eight TEC channels, a slightly smaller temperature gradient, approximately 220 mK, was obtained, as shown in Figures 6.5 and 6.6.

A typical temperature time series showing overall behavior is reported in Figure 6.5. At the beginning of the trace, the clock sequence is activated (the current of the MOT coils is turned on). Therefore, the temperature of the science chamber rapidly increases and reaches a new equilibrium of around 23 °C, due to the heat produced by the MOT coils located near the science chamber. Two hours later, the TC is activated and the temperature rapidly stabilizes approximately at 21.5 °C. When the TC is first turned on, its power consumption is 53.5 W, but this high power level only lasts 1 min and then decreases to 2.2 W when the temperature has stabilized at 21.5 °C. This power consumption would vary with different heat loads produced by the coils. The consumption could be proportional to the difference between the temperature when the coils are on (and the TC is off) and the setpoint temperature.

The gradient was subsequently optimized by adjusting the setpoint temperatures of eight control channels in the time interval from 6 h to 12 h shown in Figure 6.5. After optimization, a temperature gradient of approximately 220 mK is achieved.

Figure 6.6 shows an additional measurement, over a time interval of 55 h. Here, the temperature gradient is also approximately 220 mK.

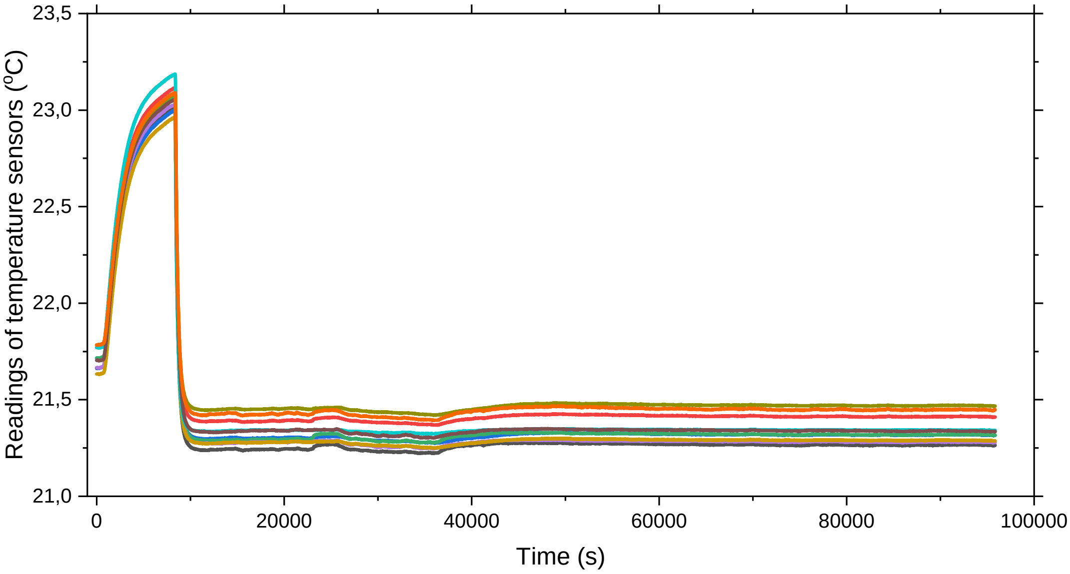

Figure 6.5: The typical temperature curves from the sensors before and after turning on the temperature control system.

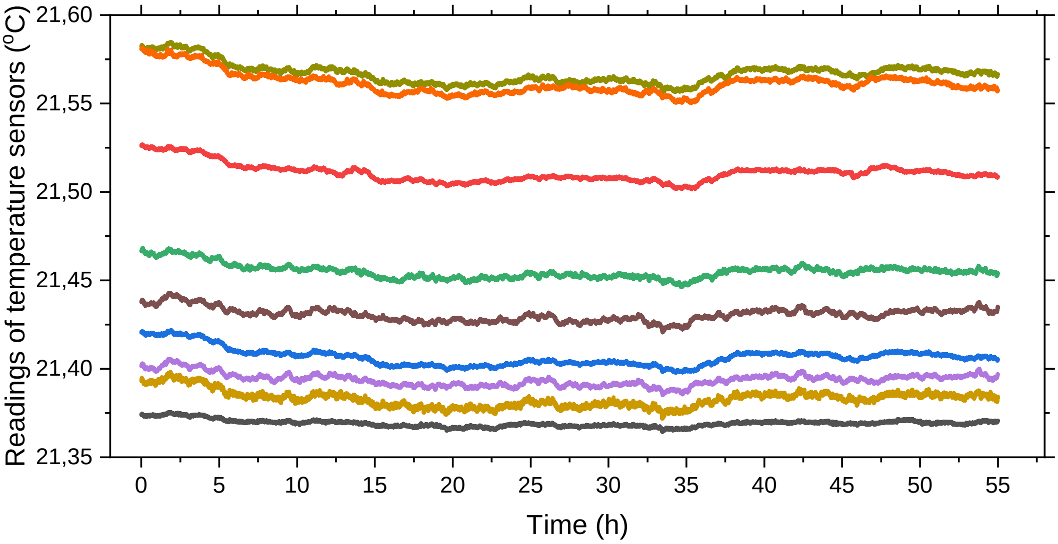

Figure 6.6: A long-term temperature recording.

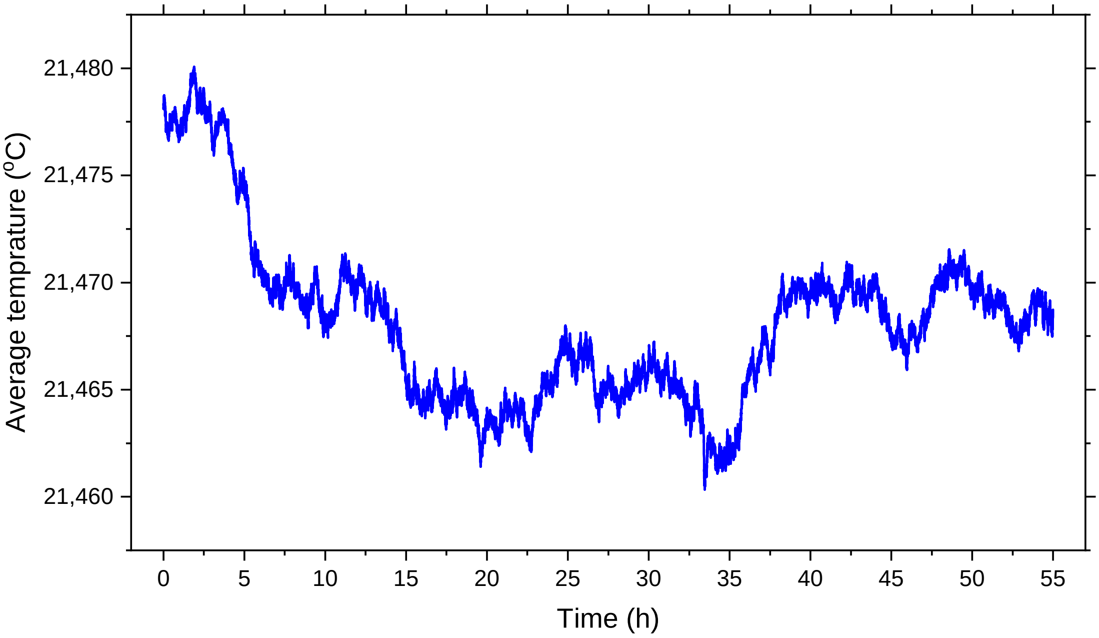

Figure 6.7: The variation of the average temperature.

An average temperature is defined as

$$T_{avg}(t) = \frac{T_c(t) + T_w(t)}{2} \tag{6.3}$$

Figure 6.7 shows the average temperature of the measurement in Figure 6.6. Its variation remains within 20 mK over more than two days.

6.1.4 Analysis

In the previous section, I measured the temperatures of the coolest and warmest points in the vacuum chamber. T_{min} indicates the minimum value of T_c over the measurement interval and T_{max} for the maximum value of T_w. Assuming a rectangular probability distribution for the temperature seen by the atoms, the representative temperature is $T = (T_{min} + T_{max})/2$ and the uncertainty $\Delta T = (T_{max} - T_{min})/\sqrt{12}$. The values for T and ΔT are ~ 294.62 K and ~ 63.5 mK, respectively, resulting in a BBR shift of 4.929×10^{-15} and corresponding fractional frequency uncertainty of 4×10^{-18}, according to Eq. 5.1.

6.1.5 Conclusion

A simple, compact, low-power-consumption temperature control system based on TECs was constructed and demonstrated. A temperature gradient of approximately 220 mK and a average temperature instability of less than 20 mK were obtained over days, implying less than the fractional frequency uncertainty of 4×10^{-18} due to the BBR shift. It shows the temperature controller of the science chamber can reduce the BBR shift of the SOC2 clock from 1.14×10^{-17} to 4×10^{-18}.

6.2 BBR shift from the oven

The BBR shift from the oven also significantly contributes to the clock frequency shift. To eliminate this BBR shift, one atomic beam shutter was installed, as shown in Figure 3.3. However, in the last part of this dissertation, the shutter is broken. Thus, the result in Table 5.2 is with the BBR shift from the oven. If the shutter is enabled, the BBR shift from the oven should be zero, as shown in Table 5.1.

6.3 Probe light shift and quadratic Zeeman shift

The SOC2 clock is based on bosonic strontium atoms, ^{88}Sr, whose clock transition $^1S_0 \rightarrow {}^3P_0$ is doubly forbidden. To excite it, magnetic field-induced spectroscopy is used; however, significant quadratic Zeeman shift and probe light AC Stark shift are present as a consequence. For example, in this dissertation, the quadratic Zeeman shift and the probe light shift are $-1477(5) \times 10^{-17}$ and $-113(2) \times 10^{-17}$, respectively. To eliminate these shifts, several variants of Ramsey spectroscopy are investigated, including hyper-Ramsey spectroscopy and other modifications using composite Ramsey pulse [101][102][103][104] and generalized auto-balanced Ramsey spectroscopy and combined error signal [105][106][107], et al.

6.3.1 Modified hyper-Ramsey spectroscopy

The systematic uncertainty budget shows that the high contributions of the frequency shift apart from BBR are from probe light shift and quadratic Zeeman shift in Tables 5.1 and 5.2. In this section, I will discuss how we can suppress these two effects.

In addition to Rabi spectroscopy used in this dissertation, Ramsey spectroscopy is also applied to the clock spectroscopy, which is a scheme of separating oscillatory fields to interrogate atoms. In standard Ramsey spectroscopy, two $\pi/2$ pulses exciting atoms are

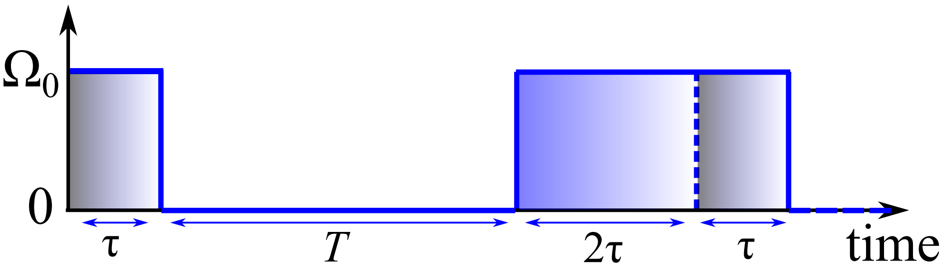

Figure 6.8: Pulse pattern of the hyper-Ramsey spectroscopy. Ω_0 is the Rabi frequency when the laser detuning is zero from the unperturbed clock transition resonance. τ is the pulse length duration of $\pi/2$ pulse, $\Omega_0\tau = \pi/2$. Thus, both the first and third pulse areas are $\pi/2$, while the second pulse area is π. T is the dark time. The phase of each pulse of "hyper-Ramsey type A" spectroscopy: $\pm\pi/2$ for the first pulse, π for the second pulse, and 0 for the third pulse. In "hyper-Ramsey type B" spectroscopy, the phase step $\pm\pi/2$ is implemented in the third pulse instead of the first.

separated by a long dark time. To suppress the probe light shift and the quadratic Zeeman shift, a modified Ramsey spectroscopy was proposed [103][108], in which a frequency step Δ_{st} is applied to the probe laser to compensate exactly for the shift Δ_{sh}. However, the shift Δ_{sh} cannot be known exactly in practice. Thus a residual uncompensated shift $\Delta = \Delta_{st} - \Delta_{sh}$ remains and causes the frequency shift of the Ramsey fringe [103].

To reduce the sensitivity to a residual uncompensated shift Δ, hyper-Ramsey spectroscopy was proposed [101][103], in which there are three pulses with individually tailored durations, phases and frequencies. The pulse pattern of the hyper-Ramsey scheme is shown in Figure 6.8. The first pulse has a pulse length τ and a phase $\pm\pi/2$, then a dark time T is used for free evaluation of atoms, and finally a pair of pulses of length 2τ and τ and phase π, 0 is applied [103]. The pulse length τ satisfies $\Omega_0\tau = \pi/2$, where Ω_0 is the Rabi frequency when laser detuning is zero from the unperturbed clock transition resonance. Thus, both the first and third pulse areas are $\pi/2$, while the second pulse area is π. This hyper-Rmasey scheme is called "hyper-Ramsey type A" spectroscopy (HRA) [103]. To stabilize the clock, the interleaving a sequence of the HRAn with the phase $+\pi/2$ of the first pulse, followed by one sequence of the HRAp with the phase $-\pi/2$ of the first pulse, the excitation fraction difference of HRAn and HRAp is feedback to the clock frequency [103]. However, the clock residual frequency shift is still cubic dependence on Δ. To further reduce the sensitivity to Δ, the "hyper-Ramsey type B" spectroscopy (HRB) was suggested [103], in which the phase step $\pm\pi/2$ is implemented in the third pulse instead of the first. A mix of both HRA and HRB spectroscopy is used to ultimately eliminate all dependence of the locked clock on Δ.

Modified hyper-Ramsey spectroscopy was demonstrated on ^{88}Sr optical lattice clock by Hobson et al.[103] to eliminate the probe light AC Stark shift. To stabilize the clock, the interleaving a sequence of the HRAn with the phase $+\pi/2$ of the first pulse, followed by one sequence of the HRBp with the phase $-\pi/2$ of the third pulse, the excitation fraction difference of HRAn and HRBp is feedback to the clock frequency [103]. A significant 2×10^{-13} probe light AC Stark shift is suppressed to below 1×10^{-16}. In theory, this method should eliminate the Stark shift to zero; however, experiments indicate that a residual shift remains, as reported in [103]. This may be due to sampling asymmetry in the error signal and an imperfect realization of the hyper-Ramsey pulse.

We could also implement modified hyper-Ramsey spectroscopy on the SOC2 apparatus to eliminate the AC Stark shift of the probe light. However, the quadratic Zeeman shift must be considered with caution at the same time. To estimate the operational parameters for this method on the SOC2 clock, the original probe shift and the ratio of the total interrogation time to π pulse are the same as in Ref. [103]. With the probe shift of 2×10^{-13}, the probe light intensity should be approximately 4.8 W/cm^2 corresponding to the probe beam power of 92 µW which is achievable by removing the ND filter. To facilitate easy comparison with Rabi spectroscopy used in this dissertation, the total interrogation time is maintained at 1 s. Thus the π pulse length is $T_\pi = 111$ ms and the free evaluation time is $T = 556$ ms. According to the relationship among Rabi frequency, π pulse, probe light intensity, and magnetic field strength, the strength of the magnetic field should be 0.329 mT, and the corresponding quadratic Zeeman shift is approximately 6×10^{-15}. In these conditions, after the implementation of modified hyper-Ramsey spectroscopy, it is achievable that the probe light shift is less than 1×10^{-16} and the quadratic Zeeman shift is approximately 6×10^{-15}.

To further reduce the quadratic Zeeman shift to be less than 1×10^{-16}, e.g. 6×10^{-17}, the magnetic field strength should be decreased by a factor of 10. There are two scenarios here. First scenario: increase T_π by a factor of 10 to still keep the probe light at 2×10^{-13}, thus $T_\pi = 1.11$ s. The total interrogation time should be approximately 10 s. This scenario can only be achieved using PTB cryogenic Silicon cavity [7]. Second scenario: increase the probe light intensity by a factor of 100 to maintain $T_\pi = 111$ ms. In this case, the probe light intensity should be approximately 480 W/cm^2 corresponding to the probe beam power of 9.2 mW which cannot be achieved in our current clock laser system due to a lack of total laser power to atoms (~ 1 mW). The beam power can be easily obtained from a laser diode HL70021DG, with a maximum output power of 210 mW, from USHIO. It may also be possible to simultaneously vary both the intensity of the probe light and the interrogation time to achieve both the probe light shift and the quadratic Zeeman shift at a level of less than 1×10^{-16}. By well controlling the probe light power and magnetic field strength, the uncertainties of the probe light AC Stark shift and quadratic Zeeman shift can easily be less than 1×10^{-18}.

6.4 Cold collision shift

The frequency shift of the clock transition caused by collisions between cold atoms in a single lattice site is also a significant contribution to optical lattice clocks. In the SOC2 system, the cold collision shift was examined in both shallow and deep lattices, as illustrated in Section 5.4. The clock is usually operated at a low lattice depth (approximately $30E_r$) and with a low number of atoms (fewer than 1000), resulting in a collision shift coefficient of less than -1×10^{-16}.

We need to consider increasing the number of atoms to take advantage of the optical lattice, which can reduce quantum projection noise and improve clock stability. However, a higher atomic number will result in a greater cold collision shift. To reduce the cold collision shift, we can implement photoassociation of strontium-88 atoms, allowing multiple atoms at a single lattice site to form molecules. These are then expelled from the trap, maintaining fewer than two atoms in each lattice site to prevent collisions between cold atoms.

6.4.1 Photoassociation

A photon can be absorbed by two colliding lattice-trapped atoms, which photoassociate to form a least-bound, electronically excited molecule. Then, the excited bound molecule spontaneously emits a photon and becomes a pair of hot atoms or possibly a cold molecule with enough kinetic energy to escape the trap. In this way, the colliding atoms can be eliminated from the lattice trap, leaving either one or no atom per lattice site to prevent atom collisions.

To reduce the cold collision shift between strontium-88 atoms in the SOC2 system, photoassociation (PA) spectroscopy is performed near the ${}^1S_0 - {}^3P_1$ intercombination transition. The PA line at interatomic separation $R(a_0) = 84$ and the detuning of $\sim 222\,\text{MHz}$ from the transition of ${}^1S_0 - {}^3P_1$ [109]is employed.

The PA laser beam is produced by two cascaded injection locking lasers, shown in Figure 6.9. The master laser and the first slave laser are used as a laser cooling beam for the red MOT. The detailed scheme of this distribution breadboard is shown in Figure 3.11 of Chapter 3. The second slave laser is located on the stirring laser distribution breadboard, which can be used as a cooling beam for strontium-87 atoms. The light that has passed twice through the AOM provided by the second slave laser serves as PA light and has a detuning of approximately $\sim 222\,\text{MHz}$ from the intercombination transition. Figure 6.10 shows the

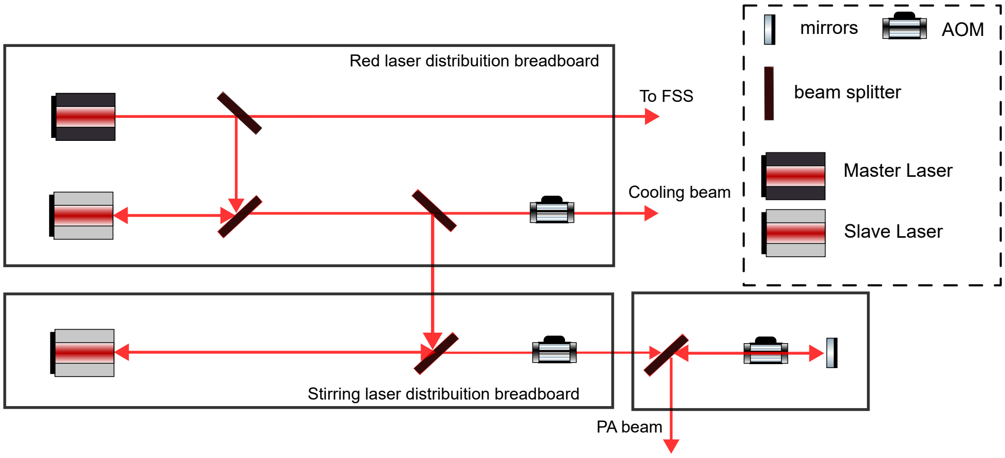

Figure 6.9: The schematics of optics path of PA beam. The first order diffracted beam of each AOM is shown here. The other beam dumps are left out for clarity. More details in the text. PA: photoassociation; FSS: frequency stabilization system; AOM: Acousto-Optic modulation.

PA spectroscopy by scanning the double-pass AOM. The asymmetric shape of the PA line is a result of thermal effects [109].

6.4.2 Clock transition after the implementation of photoassociation

During clock operation, a PA beam is inserted before clock interrogation, as shown in Figure 6.11. Figure 6.12 shows the clock transitions with and without photoassociations. With photoassociation, the broadening of the linewidth due to collisions is reduced, and the clock transition is also shifted by $\sim 1\,\text{Hz}$, as shown in Figure 6.12. If all lattice sites are filled with one or no atoms per site after implementing photoassociation, the collision shift can be entirely eliminated.

The collision shift could also be suppressed using an auto-compensation method proposed by Yudin et al. [110].

6.5 Clock transition shifts due to other effects

Lattice light shift

To reduce the AC Stark shift of the clock transition caused by the lattice laser, one may operate the lattice clock at a low trap depth according to Eq. 5.21; however, a lower trap depth results in a higher tunneling rate. Therefore, one must balance the lattice AC Stark shift and tunneling under operational conditions. Moreover, the differential electric dipole

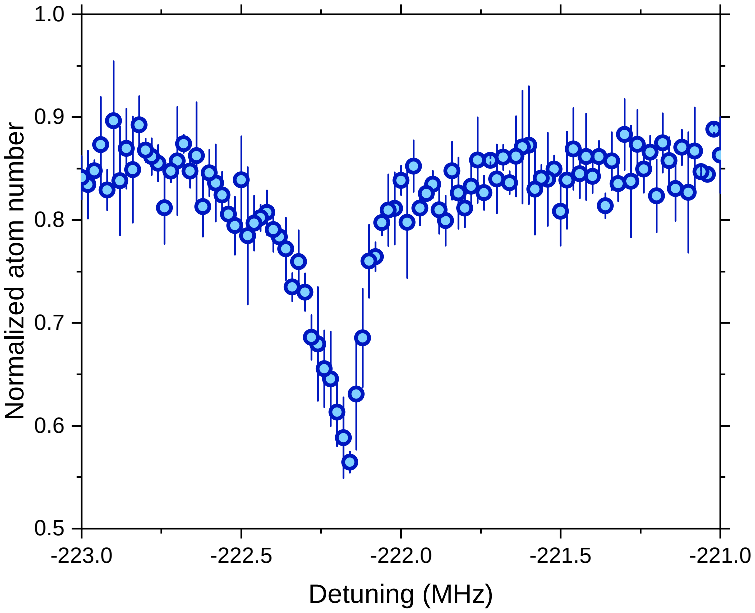

Figure 6.10: PA spectroscopy at the detuning approximately 222 MHz from the intercombination transition. The asymmetric shape of the PA line is a result of thermal effects.

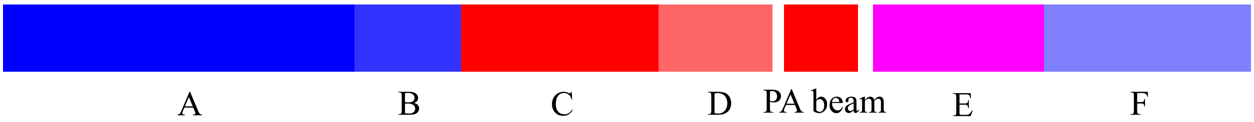

Figure 6.11: The timing sequence of clock operation with PA beam. From pahse A to D, atoms are cooled down and loaded into the optical lattice. Then, a PA beam that is on resonance with the PA line which is $\sim 222\,\mathrm{MHz}$ detuning from the ${}^1S_0 \leftrightarrow {}^3P_1$ transition is delivered into the lattice. E and F are the interrogation and detection phases. More details of A to F in Figure 3.21.

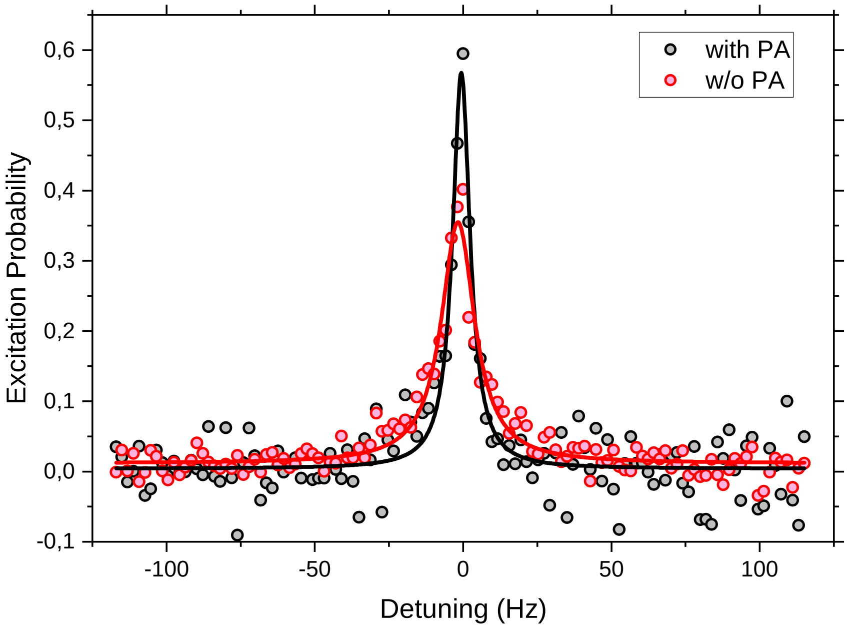

Figure 6.12: The clock transitions with and without photoassociation.

polarizability, magnetic dipole, electric quadrupole polarizability, and hyperpolarizability must be precisely known to accurately determine the lattice AC Stark shift. Another approach involves implementing serial measurements of the AC Stark shifts at various lattice depths with the lattice laser frequencies close to the effective magic wavelength, where prior knowledge of polarizabilities is unnecessary, according to Eq. 5.20. However, before that, the linear scaling of the atom temperature with lattice depth U_0 should be carefully examined.

Background gas collision shift

An experimental observation of the strong dependence of the lifetime on the pressure of the vacuum system was made in the SOC2 system [29]. The lattice lifetime was improved by 10 times by reducing the pressure from $\sim 1 \times 10^{-9}$ mbar to $\sim 1 \times 10^{-10}$ mbar. A more powerful ion pump could remove more background gas, further enhancing the pressure in the science chamber and reducing the frequency shift caused by background gas.

DC Stark shift

DC-Stark shift is due to the residual electric field in the interrogation phase, which causes a frequency shift of the clock transition. In the SOC2 system, a pair of large non-conductive chamber windows (diameter 40 mm) are placed on the horizontal plane and as close as 7 mm to the cold atoms. Electric charges can accumulate on the windows and produce a DC-

Effect	Achieved frequency shift	 uncertainty	Attainable uncertainty	Notes
BBR shift	-521.12	1.14	<0.5	
BBR oven	0	0	0	
Lattice AC Stark shifts	-3.56	2.19	<0.1	
Probe light AC Stark shift	-113.18	2.24	<0.1	
Cold collision shift	-2.03	0.63	0	
Quadratic Zeeman shift	-1477.37	5.15	<0.1	
Background gas collision shift	-0.54	0.05	$<$ 0.05	
DC Stark shift	-0.19	0.02	0	
Servo error	0	0	0	
Total	-2117.99	6.17	<0.54	

Table 6.1: Uncertainty budget for the SOC2 clock with achievable uncertainty without significant unnecessary system upgrades. All values are to be multiplied by 10^{-17}. The achieved uncertainty budget corresponds to Table 5.1.

Stark shift. To reduce the DC-Stark shift, a pair of windows with a conductive coating can replace the non-conductive chamber windows, thereby removing the residual electric field. For example, Indium Tin Oxide (ITO) coatings offer advantages such as higher electrical conductivity and optical transparency, making them suitable for use in SOC2 systems.

6.6 The achievable uncertainty of the SOC2 clock

The achievable uncertainty budget of the SOC2 clock is shown in Table 6.1 with comparison of achieved results. If we carefully control all the effects, the systematic uncertainty of less than 5.4×10^{-18} is reachable. Less noise from all the effects also improves the clock instability, making the clock more stable. Currently, we are also optimizing the laser systems with high-power 461 nm and 689 nm laser diodes, which are NDB4916 (from NICHIA) with a maximum output power of 600 mW, and HL69001DG (from USHIO) with a maximum output power of 210 mW, respectively. We are trying to make the laser system more robust, and aiming for long-term running, i.e. longer than 1 week with a large uptime fraction. Based on the discussion in previous sections, it is possible to meet the project goals.

Chapter 7

Conclusion

In this dissertation, I reported a transportable optical lattice clock (SOC2) based on strontium-88 neutral atoms, which aims to investigate relativistic geodesy by time comparison in the framework of the DFG research unit "Clock Metrology: A Novel Approach to TIME in Geodesy".

The principle of the strontium optical lattice clock was discussed, and the compact physics package and compact, modular-designed laser systems of the SOC2 clock were introduced. Then the noise contributions to the clock instability were analyzed, for example, the noises from quantum projection, Dick effect of the probe laser, bias field, probe laser power, lattice laser power, detection noise, etc. The estimated contribution to the instability from all noise sources together with the contribution of the Sr3 clock is $\sim 2.7 \times 10^{-16}/\sqrt{\tau}$. However, the measured instability of the SOC2 clock against the Sr3 clock is $\sim 5.7 \times 10^{-16}/\sqrt{\tau}$. Therefore, there are still unidentified noise sources that contribute to the instability of the SOC2 clock.

The frequency shifts due to all relevant effects were carefully characterized, for instance, blackbody radiation shift, quadratic Zeeman shift, probe light AC Stark shift, lattice light AC Stark shift, cold collision shift, background gas collision shift, etc. The systematic uncertainty of the clock is 6.2×10^{-17} at low atom number (~ 240), and the main contribution stems from the quadratic Zeeman shift; however, at high atom number (~ 2250), the systematic uncertainty is 1.26×10^{-16} with a high contribution from the lattice AC Stark shifts. The noise source of the lattice AC Stark shift originates from the collisions of cold atoms: the collision shift contribution in the lattice AC Stark shift measurement with a high atom number is more significant than in the low atom number case, and thus worsens the uncertainty of the SOC2 clock.

By frequency comparison between the SOC2 and Sr3 clocks, the isotope shift between ^{88}Sr and ^{87}Sr was also obtained, which is $62\,188\,134.032(35)$ Hz. The result agrees with the recently reported values. The frequency ratio between strontium-88 and -87 clocks is $1.000\,000\,144\,883\,682\,842(42)$, which is consistent with the recommended value of CIPM [93]. The isotope shift is also obtained by frequency comparison with the transportable optical lattice clock (Sr4) of PTB. The two measured isotope shifts are consistent with each other.

The frequency ratios of ^{88}Sr with respect to the electric octupole ($E3$) transition in ^{171}Yb^{+} and ^{115}In^{+} are also reported in this dissertation. The frequency ratio of ^{171}Yb^{+}($E3$)/^{88}Sr is measured to be 1.495 991 401 800 156 81(12), and the frequency ratio of ^{115}In^{+}/^{88}Sr is 2.952 748 322 069 809 39(22). Both of them are consistent with the 2021 recommended frequency values of CIPM. The reference value is the frequency ratio from Table B1 in [93]. Based on these two ratios, the ratio ^{115}In^{+} to ^{171}Yb^{+}($E3$) can be obtained, which is consistent with the value reported in Ref. [98]. The ratio uncertainty of ^{115}In^{+} to ^{88}Sr has improved over the reference value by a factor of approximately 60. To our knowledge, these direct optical frequency ratios of ^{88}Sr to ^{171}Yb^{+} and ^{115}In^{+} are reported for the first time.

In order to further improve the clock performance, some potential optimizations of the SOC2 clock were discussed, for example, reducing the BBR shift to 4×10^{-18} by better controlling the temperature of the science chamber; suppressing the quadratic Zeeman shift and probe light shift by implementing modified hyper-Ramsey spectroscopy [103]; controlling the cold collision shift by photoassociation of cold atoms in the same lattice site; etc. The achievable uncertainty of the SOC2 clock is less than 5.4×10^{-18}, if all the effects are carefully controlled, which meets the project goals.

Currently, we are optimizing and upgrading the laser systems with high-power 461 nm and 689 nm laser diodes, trying to make the system more robust and reliable, and aiming for long-term clock operation, i.e., longer than 1 week with a large uptime fraction. The new transportable clock laser based on the NEXCERA material was transported from HHU to PTB last year and was integrated into the SOC2 setup.

At the end of 2025, the SOC2 clock is planned to be transported to Wettzell, to define the GOW time scale, and to be an enabling element for time transfer between GOW and Potsdam, in order to investigate relativistic geodesy via ACES.

Bibliography

[1] *Historical perspective: Unit of time, second.* https://www.bipm.org/en/history-si/second. Accessed: 2024-09-02 (cit. on p. 1).

[2] Sigfrido Leschiutta. “The definition of the ‘atomic’ second”. In: *Metrologia* 42.3 (Jan. 2005), S10. DOI: 10.1088/0026-1394/42/3/S03 (cit. on p. 1).

[3] N Dimarcq et al. “Roadmap towards the redefinition of the second”. In: *Metrologia* 61.1 (Jan. 2024), p. 012001. DOI: 10.1088/1681-7575/ad17d2 (cit. on pp. 1, 6, 16).

[4] L Essen and J V L Parry. “An atomic standard of frequency and time interval: A cæsium resonator”. en. In: *Nature* 176.4476 (Aug. 1955), pp. 280–282 (cit. on p. 1).

[5] Fritz Riehle. “Towards a redefinition of the second based on optical atomic clocks”. In: *Comptes Rendus Physique* 16.5 (2015). The measurement of time / La mesure du temps, pp. 506–515. ISSN: 1631-0705. DOI: https://doi.org/10.1016/j.crhy.2015.03.012 (cit. on p. 1).

[6] Th Udem, R Holzwarth, and T W Hänsch. “Optical frequency metrology”. en. In: *Nature* 416.6877 (Mar. 2002), pp. 233–237 (cit. on p. 2).

[7] D. G. Matei et al. “1.5 μm Lasers with Sub-10 mHz Linewidth”. In: *Phys. Rev. Lett.* 118 (26 June 2017), p. 263202. DOI: 10.1103/PhysRevLett.118.263202 (cit. on pp. 2, 51, 88, 89, 142).

[8] Sofia Herbers et al. “Transportable clock laser system with an instability of 1.6×10^{-16}”. In: *Opt. Lett.* 47.20 (Oct. 2022), pp. 5441–5444. DOI: 10.1364/OL.470984 (cit. on p. 3).

[9] J. R. Vig. *Quartz crystal oscillators and resonators.* https://www.ieee-uffc.org/fc. October 1999. SLCET-TR-88-1 (Rev. 8.3.9) (cit. on p. 3).

[10] Alexander Aeppli et al. “Clock with 8×10^{-19} Systematic Uncertainty”. In: *Phys. Rev. Lett.* 133 (2 July 2024), p. 023401. DOI: 10.1103/PhysRevLett.133.023401 (cit. on pp. 4, 5).

[11] Mason C. Marshall et al. “High-Stability Single-Ion Clock with 5.5×10^{-19} Systematic Uncertainty”. In: *Phys. Rev. Lett.* 135 (3 July 2025), p. 033201. DOI: 10.1103/hb3c-dk28 (cit. on p. 4).

[12] Jacopo Grotti et al. “Geodesy and metrology with a transportable optical clock”. en. In: *Nat. Phys.* 14.5 (May 2018), pp. 437–441 (cit. on p. 4).

[13] J. Grotti et al. “Long-distance chronometric leveling with a portable optical clock”. In: *Phys. Rev. Appl.* 21 (6 Jan. 2024), p. L061001. DOI: 10.1103/PhysRevApplied.21.L061001 (cit. on pp. 4, 6).

[14] I. Nosske et al. *Transportable strontium lattice clock with 4×10^{-19} blackbody radiation shift uncertainty*. 2025. arXiv: 2507.14030 `[physics.atom-ph]` (cit. on pp. 4, 5, 127).

[15] International Clock and Oscillator Networking (ICON) Collaboration. *International comparison of optical frequencies with transportable optical lattice clocks*. 2024. arXiv: 2410.22973 `[physics.atom-ph]` (cit. on pp. 4–6).

[16] S. Origlia et al. “Towards an optical clock for space: Compact, high-performance optical lattice clock based on bosonic atoms”. In: *Phys. Rev. A* 98 (5 Nov. 2018), p. 053443. DOI: 10.1103/PhysRevA.98.053443 (cit. on pp. 4, 5, 31, 109, 111, 124, 129, 133).

[17] Masao Takamoto et al. “Test of general relativity by a pair of transportable optical lattice clocks”. en. In: *Nat. Photonics* 14.7 (July 2020), pp. 411–415. DOI: 10.1038/s41566-020-0619-8 (cit. on pp. 4–6).

[18] Feng Guo et al. “A proof-of-concept model of compact and high-performance 87Sr optical lattice clock for space”. In: *AIP Advances* 11.12 (Dec. 2021), p. 125116. ISSN: 2158-3226. DOI: 10.1063/5.0064087. eprint: https://pubs.aip.org/aip/adv/article-pdf/doi/10.1063/5.0064087/12935173/125116_1_online.pdf (cit. on p. 4).

[19] Roman Schwarz. *A cryogenic Strontium lattice clock*. PhD thesis, University of Hannover, 2022 (cit. on pp. 5, 23–25, 125, 127).

[20] Grégoire Vallet et al. “Study of Accuracy and Stability of Sr Lattice Clocks at LNE-SYRTE”. In: *2018 Conference on Precision Electromagnetic Measurements (CPEM 2018)*. 2018, pp. 1–2. DOI: 10.1109/CPEM.2018.8500833 (cit. on p. 5).

[21] Noriaki Ohmae et al. “Transportable strontium optical lattice clocks operated outside laboratory at the level of 10^{-18} uncertainty”. en. In: *Adv. Quantum Technol.* (May 2021), p. 2100015 (cit. on p. 5).

[22] Nils Nemitz et al. “Absolute frequency of ^{87}Sr at 1.8×10^{-16} uncertainty by reference to remote primary frequency standards”. In: *Metrologia* 58.2 (Feb. 2021), p. 025006. DOI: 10.1088/1681-7575/abc232 (cit. on p. 5).

[23] Yusuke Hisai et al. “Improved frequency ratio measurement with ^{87}Sr and ^{171}Yb optical lattice clocks at NMIJ”. In: *Metrologia* 58.1 (Jan. 2021), p. 015008. DOI: 10.1088/1681-7575/abc104 (cit. on p. 5).

[24] Bing-Kun Lu et al. “Improved Evaluation of BBR and Collisional Frequency Shifts of NIM-Sr2 with 7.2×10^{-18} Total Uncertainty”. In: *Chinese Physics Letters* 39.8 (June 2022), p. 080601. DOI: 10.1088/0256-307X/39/8/080601 (cit. on p. 5).

[25] Xiao-Tong Lu et al. “NTSC SrII optical lattice clock with uncertainty of 2×10^{-18}”. In: *Metrologia* 62.3 (June 2025), p. 035007. DOI: 10.1088/1681-7575/addc77 (cit. on p. 5).

[26] Zhi-Peng Jia et al. *Improved systematic evaluation of a strontium optical clock with uncertainty below* 1×10^{-18}. 2025. arXiv: `2509.13991 [physics.atom-ph]` (cit. on p. 5).

[27] Piotr Morzyński et al. “Intercontinental frequency ratio measurement of ^{171}Yb and ^{88}Sr optical lattice clocks”. In: *Metrologia* 61.4 (Aug. 2024), p. 045009. DOI: 10.1088/1681-7575/ad6a1e (cit. on p. 5).

[28] *BIPM Time Department Data Base*. https://webtai.bipm.org/database/d_plot.html. Accessed: 2025-04-14 (cit. on p. 6).

[29] Stefano Origlia. *A high-performance bosonic optical lattice clock*. PhD thesis, University of Düsseldorf, 2018 (cit. on pp. 6, 27, 29, 33, 38, 39, 43, 51, 57, 90, 95, 126, 146).

[30] M. Filzinger et al. “Improved Limits on the Coupling of Ultralight Bosonic Dark Matter to Photons from Optical Atomic Clock Comparisons”. In: *Phys. Rev. Lett.* 130 (25 June 2023), p. 253001. DOI: 10.1103/PhysRevLett.130.253001 (cit. on p. 6).

[31] *DFG Research Unit 5456 Clock Metrology: A Novel Approach to TIME in Geodesy*. https://clockmetrology.de/en/. Accessed: 2025-08-06 (cit. on p. 7).

[32] Stephan Schiller. *Project Proposal: Performance optimization of the optical clock “SOC2”, installation and operation at Wettzell for geodesy and fundamental physics studies*. https://gepris.dfg.de/gepris/projekt/513190936. Accessed: 2025-06-26 (cit. on pp. 7–9).

[33] K Ulrich Schreiber and Jan Kodet. “The application of coherent local time for optical time transfer and the quantification of systematic errors in satellite laser ranging”. In: *Space Sci. Rev.* 214.1 (Feb. 2018) (cit. on p. 10).

[34] Nandan Jha. *A high-performance magnesium lattice clock: stability and accuracy analysis*. PhD thesis, Universität Hannover, 2022 (cit. on p. 12).

[35] Carsten Degenhardt et al. “Calcium optical frequency standard with ultracold atoms: Approaching 10^{-15} relative uncertainty”. In: *Phys. Rev. A* 72 (6 Dec. 2005), p. 062111. DOI: 10.1103/PhysRevA.72.062111 (cit. on p. 12).

[36] Juan A. Muniz et al. “Cavity-QED measurements of the ^{87}Sr millihertz optical clock transition and determination of its natural linewidth”. In: *Phys. Rev. Res.* 3 (2 May 2021), p. 023152. DOI: 10.1103/PhysRevResearch.3.023152 (cit. on pp. 12, 16).

[37] R Drozdowski et al. “Radiative lifetimes of the lowest 3P1 metastable states of Ca and Sr”. en. In: *Z. Phys. D At. Mol. Clust.* 41.2 (June 1997), pp. 125–131 (cit. on p. 12).

[38] Robin Santra, Kevin V. Christ, and Chris H. Greene. “Properties of metastable alkaline-earth-metal atoms calculated using an accurate effective core potential”. In: *Phys. Rev. A* 69 (4 Apr. 2004), p. 042510. DOI: 10.1103/PhysRevA.69.042510 (cit. on pp. 12, 16).

[39] Maxime Favier. *Mercury optical lattice clock: From high-resolution spectroscopy to frequency ratio measurements.* PhD thesis, Université Pierre et Marie Curie, 2017 (cit. on p. 12).

[40] A. Yamaguchi et al. “Narrow-line Cooling and Determination of the Magic Wavelength of Cd”. In: *Phys. Rev. Lett.* 123 (11 Sept. 2019), p. 113201. DOI: 10.1103/PhysRevLett.123.113201 (cit. on p. 12).

[41] Wesley Brand. *A transportable yetterbium optical lattice clock with eighteen digits of accuracy.* PhD thesis, University of Colorado, 2024 (cit. on p. 12).

[42] J. E. Sansonetti and G. Nave. “Wavelengths, Transition Probabilities, and Energy Levels for the Spectrum of Neutral Strontium (SrI)”. In: *Journal of Physical and Chemical Reference Data* 39.3 (Aug. 2010), p. 033103. ISSN: 0047-2689. DOI: 10.1063/1.3449176. eprint: https://pubs.aip.org/aip/jpr/article-pdf/doi/10.1063/1.3449176/15763928/033103_1_online.pdf (cit. on pp. 13, 16, 17).

[43] T.W. Hänsch and A.L. Schawlow. “Cooling of gases by laser radiation”. In: *Optics Communications* 13.1 (1975), pp. 68–69. ISSN: 0030-4018. DOI: https://doi.org/10.1016/0030-4018(75)90159-5 (cit. on p. 13).

[44] Harold J Metcalf and Peter Van Der Straten. *Laser Cooling and Trapping.* en. 1st ed. Graduate Texts in Contemporary Physics. New York, NY: Springer, Apr. 2000 (cit. on p. 13).

[45] Andrew D. Ludlow et al. “Optical atomic clocks”. In: *Rev. Mod. Phys.* 87 (2 June 2015), pp. 637–701. DOI: 10.1103/RevModPhys.87.637 (cit. on p. 13).

[46] C.J. Foot. *Atomic Physics.* Oxford Master Series in Physics. OUP Oxford, 2005. ISBN: 9780198506959 (cit. on pp. 14, 15).

[47] Masami Yasuda and Hidetoshi Katori. “Lifetime measurement of the 3P2 metastable state of strontium atoms”. en. In: *Phys. Rev. Lett.* 92.15 (Apr. 2004), p. 153004 (cit. on p. 17).

[48] P H Moriya et al. “Comparison between 403 nm and 497 nm repumping schemes for strontium magneto-optical traps”. In: *Journal of Physics Communications* 2.12 (Dec. 2018), p. 125008. DOI: 10.1088/2399-6528/aaf662 (cit. on p. 18).

[49] Simon Stellmer. *Degenerate quantum gases of strontium*. PhD thesis, University of Innsbruck, 2013 (cit. on pp. 18, 38).

[50] Naohiro Okamoto, Takatoshi Aoki, and Yoshio Torii. “Limitation of single-repumping schemes for laser cooling of Sr atoms”. In: *Phys. Rev. Res.* 6 (4 Nov. 2024), p. 043088. DOI: 10.1103/PhysRevResearch.6.043088 (cit. on p. 18).

[51] R. Hobson et al. “Midinfrared magneto-optical trap of metastable strontium for an optical lattice clock”. In: *Phys. Rev. A* 101 (1 Jan. 2020), p. 013420. DOI: 10.1103/PhysRevA.101.013420 (cit. on p. 18).

[52] Tomoya Akatsuka et al. “Three-stage laser cooling of Sr atoms using the $5s5p^3P_2$ metastable state below Doppler temperatures”. In: *Phys. Rev. A* 103 (2 Feb. 2021), p. 023331. DOI: 10.1103/PhysRevA.103.023331 (cit. on p. 18).

[53] Eugene Demler. *Strongly correlated systems in atomic and condensed matter physics*. Lecture notes for Physics 284. Harvard University, 2014 (cit. on p. 18).

[54] Jean Dalibard. *Optical lattices*. Lecure series 2012-13. Collège de France, 2012 (cit. on p. 18).

[55] Hélène Perrin. *Optical Lattices*. Les Houches lectures on optical lattices. Université Paris 13, 2019 (cit. on p. 19).

[56] D. Leibfried et al. “Quantum dynamics of single trapped ions”. In: *Rev. Mod. Phys.* 75 (1 Mar. 2003), pp. 281–324. DOI: 10.1103/RevModPhys.75.281 (cit. on p. 22).

[57] Saumitra S. Phatak et al. “A Generalized Theory for Optical Cooling of a Trapped Atom with Spin”. In: *arXiv* (2024). arXiv: 2406.19153 `[physics.atom-ph]` (cit. on p. 22).

[58] S. Blatt et al. “Rabi spectroscopy and excitation inhomogeneity in a one-dimensional optical lattice clock”. In: *Phys. Rev. A* 80 (5 Nov. 2009), p. 052703. DOI: 10.1103/PhysRevA.80.052703 (cit. on pp. 24, 70, 73–75).

[59] Pierre Lemonde and Peter Wolf. “Optical lattice clock with atoms confined in a shallow trap”. In: *Phys. Rev. A* 72 (3 Sept. 2005), p. 033409. DOI: 10.1103/PhysRevA.72.033409 (cit. on p. 25).

[60] Wilhelm Zwerger. "Mott–Hubbard transition of cold atoms in optical lattices". In: *Journal of Optics B: Quantum and Semiclassical Optics* 5.2 (Apr. 2003), S9. DOI: 10.1088/1464-4266/5/2/352 (cit. on p. 25).

[61] Masao Takamoto et al. "An optical lattice clock". In: *Nature* 435 (May 2005), pp. 321–324. DOI: 10.1038/nature03541 (cit. on p. 27).

[62] Hidetoshi Katori et al. "Ultrastable Optical Clock with Neutral Atoms in an Engineered Light Shift Trap". In: *Phys. Rev. Lett.* 91 (17 Oct. 2003), p. 173005. DOI: 10.1103/PhysRevLett.91.173005 (cit. on p. 27).

[63] Tomoya Akatsuka, Masao Takamoto, and Hidetoshi Katori. "Three-dimensional optical lattice clock with bosonic ^{88}Sr atoms". In: *Phys. Rev. A* 81 (2 Feb. 2010), p. 023402. DOI: 10.1103/PhysRevA.81.023402 (cit. on pp. 27, 28).

[64] Ch. Lisdat et al. "Blackbody radiation shift in strontium lattice clocks revisited". In: *Phys. Rev. Res.* 3 (4 Dec. 2021), p. L042036. DOI: 10.1103/PhysRevResearch.3.L042036 (cit. on pp. 27, 107, 108).

[65] A. V. Taichenachev et al. "Magnetic Field-Induced Spectroscopy of Forbidden Optical Transitions with Application to Lattice-Based Optical Atomic Clocks". In: *Phys. Rev. Lett.* 96 (8 Mar. 2006), p. 083001. DOI: 10.1103/PhysRevLett.96.083001 (cit. on pp. 28, 29, 90, 95, 110, 114, 162).

[66] Tao Hong et al. "Optical Clocks Based on Ultranarrow Three-Photon Resonances in Alkaline Earth Atoms". In: *Phys. Rev. Lett.* 94 (5 Feb. 2005), p. 050801. DOI: 10.1103/PhysRevLett.94.050801 (cit. on p. 29).

[67] Junyu He et al. "Coherent Three-Photon Excitation of the Strontium Clock Transition". In: *arXiv:2406.07530* (2024). arXiv: 2406.07530 `[cond-mat.quant-gas]` (cit. on p. 29).

[68] Samuel P. Carman et al. "Collinear three-photon excitation of a strongly forbidden optical clock transition". In: *arXiv:2406.07902* (2024). arXiv: 2406.07902 `[physics.atom-ph]` (cit. on p. 29).

[69] Robin Santra et al. "High-Accuracy Optical Clock via Three-Level Coherence in Neutral Bosonic ^{88}Sr". In: *Phys. Rev. Lett.* 94 (17 May 2005), p. 173002. DOI: 10.1103/PhysRevLett.94.173002 (cit. on p. 30).

[70] N Poli et al. "A transportable strontium optical lattice clock". en. In: *Appl. Phys. B* 117.4 (Dec. 2014), pp. 1107–1116 (cit. on p. 31).

[71] Kai Bongs et al. “Development of a strontium optical lattice clock for the SOC mission on the ISS”. en. In: *Comptes Rendus. Physique* 16.5 (2015), pp. 553–564. DOI: 10.1016/j.crhy.2015.03.009 (cit. on pp. 31, 54).

[72] Gregor Mura et al. “A transportable optical lattice clock using 171Yb”. In: *2013 Joint European Frequency and Time Forum and International Frequency Control Symposium (EFTF/IFC)* (2013), pp. 376–378. DOI: 10.1109/EFTF-IFC.2013.6702292 (cit. on p. 31).

[73] Ian R Hill et al. “Zeeman slowers for strontium based on permanent magnets”. In: *Journal of Physics B: Atomic, Molecular and Optical Physics* 47.7 (Mar. 2014), p. 075006. DOI: 10.1088/0953-4075/47/7/075006 (cit. on pp. 35, 36).

[74] A. Nevsky et al. “Robust frequency stabilization of multiple spectroscopy lasers with large and tunable offset frequencies”. In: *Opt. Lett.* 38.22 (Nov. 2013), pp. 4903–4906. DOI: 10.1364/OL.38.004903 (cit. on pp. 35, 40, 53).

[75] Lyndsie Laura Smith. *A tranportable strontium optical lattice clock towards space*. PhD thesis, University of Birmingham, 2016 (cit. on p. 38).

[76] M. Schioppo et al. “A compact and efficient strontium oven for laser-cooling experiments”. In: *Review of Scientific Instruments* 83.10 (Oct. 2012), p. 103101. ISSN: 0034-6748. DOI: 10.1063/1.4756936. eprint: https://pubs.aip.org/aip/rsi/article-pdf/doi/10.1063/1.4756936/14133321/103101_1_online.pdf (cit. on p. 38).

[77] S Vogt et al. “Demonstration of a transportable 1 Hz-linewidth laser”. en. In: *Appl. Phys. B* 104.4 (Sept. 2011), pp. 741–745 (cit. on p. 51).

[78] Sebastian Häfner. *Ultra-stabile lasersysteme für weltraum- und bodenanwendungen*. PhD thesis, University of Hannover, 2015 (cit. on p. 51).

[79] Tomasz M Brzozowski et al. “Time-of-flight measurement of the temperature of cold atoms for short trap-probe beam distances”. In: *Journal of Optics B: Quantum and Semiclassical Optics* 4.1 (Jan. 2002), p. 62. DOI: 10.1088/1464-4266/4/1/310 (cit. on p. 62).

[80] Fritz Riehle. *Frequency Standards*. Wiley-VCH, Berlin, 2004. ISBN: 9783527402304 (cit. on p. 75).

[81] Ali Al-Masoudi et al. “Noise and instability of an optical lattice clock”. In: *Phys. Rev. A* 92 (6 Dec. 2015), p. 063814. DOI: 10.1103/PhysRevA.92.063814 (cit. on pp. 79, 81–83, 86, 87, 104).

[82] G.J. Dick. *Local oscillator induced instabilities in trapped ion frequency standards*. Proceedings of 19th Annu. Precise Time and Time Interval Meeting, Redendo Beach, 1987. US Naval Observatory, Wahington, DC, 1988 (cit. on pp. 86, 87).

[83] Ali Khalas Anfoos Al-Masoudi. *A strontium lattice clock with reduced blackbody radiation shift*. PhD thesis, University of Hannover, 2016 (cit. on p. 87).

[84] Richard Hobson. *An Optical Lattice Clock with Neutral Strontium*. PhD thesis, University of Oxford, 2016 (cit. on p. 87).

[85] Ichiro Ushijima, Masao Takamoto, and Hidetoshi Katori. "Operational Magic Intensity for Sr Optical Lattice Clocks". In: *Phys. Rev. Lett.* 121 (26 Dec. 2018), p. 263202. DOI: 10.1103/PhysRevLett.121.263202 (cit. on pp. 103, 121, 122).

[86] Thomas Middelmann et al. "High Accuracy Correction of Blackbody Radiation Shift in an Optical Lattice Clock". In: *Phys. Rev. Lett.* 109 (26 Dec. 2012), p. 263004. DOI: 10.1103/PhysRevLett.109.263004 (cit. on pp. 107, 108).

[87] R. C. Brown et al. "Hyperpolarizability and Operational Magic Wavelength in an Optical Lattice Clock". In: *Phys. Rev. Lett.* 119 (25 Dec. 2017), p. 253001. DOI: 10.1103/PhysRevLett.119.253001 (cit. on pp. 118, 121).

[88] Jie Li et al. "A strontium lattice clock with both stability and uncertainty below $5{\times}10^{-18}$". In: *Metrologia* 61.1 (Jan. 2024), p. 015006. DOI: 10.1088/1681-7575/ad1a4c (cit. on p. 121).

[89] Tobias Bothwell et al. "JILA SrI optical lattice clock with uncertainty of 2.0×10^{-18}". In: *Metrologia* 56.6 (Oct. 2019), p. 065004. DOI: 10.1088/1681-7575/ab4089 (cit. on p. 121).

[90] Kyungtae Kim et al. "Evaluation of Lattice Light Shift at Low 10^{-19} Uncertainty for a Shallow Lattice Sr Optical Clock". In: *Phys. Rev. Lett.* 130 (11 Mar. 2023), p. 113203. DOI: 10.1103/PhysRevLett.130.113203 (cit. on p. 122).

[91] B. X. R. Alves et al. "Background Gas Collision Frequency Shift on Lattice-Trapped Strontium Atoms". In: *2019 Joint Conference of the IEEE International Frequency Control Symposium and European Frequency and Time Forum (EFTF/IFC)*. 2019, pp. 1–2. DOI: 10.1109/FCS.2019.8856042 (cit. on p. 123).

[92] St Falke et al. "The 87Sr optical frequency standard at PTB". In: *Metrologia* 48.5 (Sept. 2011), p. 399. DOI: 10.1088/0026-1394/48/5/022 (cit. on p. 124).

[93] H S Margolis et al. "The CIPM list 'Recommended values of standard frequencies': 2021 update". In: *Metrologia* 61.3 (Apr. 2024), p. 035005. DOI: 10.1088/1681-7575/ad3afc (cit. on pp. 127, 128, 130, 131, 148, 149).

[94] Tetsushi Takano, Ray Mizushima, and Hidetoshi Katori. "Precise determination of the isotope shift of 88Sr–87Sr optical lattice clock by sharing perturbations". In: *Applied Physics Express* 10.7 (June 2017), p. 072801. DOI: 10.7567/APEX.10.072801 (cit. on p. 129).

[95] Xavier Baillard et al. "Accuracy evaluation of an optical lattice clock with bosonic atoms". In: *Opt. Lett.* 32.13 (July 2007), pp. 1812–1814. DOI: 10.1364/OL.32.001812 (cit. on p. 129).

[96] Czesław Radzewicz et al. "Accuracy budget of the 88Sr optical atomic clocks at KL FAMO". In: *Physica Scripta* 91.8 (Nov. 2016), p. 084003. DOI: 10.1088/0031-8949/91/8/084003 (cit. on p. 129).

[97] Tomoya Akatsuka, Masao Takamoto, and Hidetoshi Katori. "Optical lattice clocks with non-interacting bosons and fermions". en. In: *Nat. Phys.* 4.12 (Dec. 2008), pp. 954–959 (cit. on p. 129).

[98] H. N. Hausser et al. "$^{115}\mathrm{In}^{+}$–$^{172}\mathrm{Yb}^{+}$ Coulomb Crystal Clock with 2.5×10^{-18} Systematic Uncertainty". In: *Phys. Rev. Lett.* 134 (2 Jan. 2025), p. 023201. DOI: 10.1103/PhysRevLett.134.023201 (cit. on pp. 127, 130, 149).

[99] N. Huntemann et al. "Single-Ion Atomic Clock with 3×10^{-18} Systematic Uncertainty". In: *Phys. Rev. Lett.* 116 (6 Feb. 2016), p. 063001. DOI: 10.1103/PhysRevLett.116.063001 (cit. on p. 130).

[100] Christian Sanner et al. "Optical clock comparison for Lorentz symmetry testing". en. In: *Nature* 567.7747 (Mar. 2019), pp. 204–208 (cit. on p. 130).

[101] V. I. Yudin et al. "Hyper-Ramsey spectroscopy of optical clock transitions". In: *Phys. Rev. A* 82 (1 July 2010), p. 011804. DOI: 10.1103/PhysRevA.82.011804 (cit. on pp. 140, 141).

[102] N. Huntemann et al. "Generalized Ramsey Excitation Scheme with Suppressed Light Shift". In: *Phys. Rev. Lett.* 109 (21 Nov. 2012), p. 213002. DOI: 10.1103/PhysRevLett.109.213002 (cit. on p. 140).

[103] R. Hobson et al. "Modified hyper-Ramsey methods for the elimination of probe shifts in optical clocks". In: *Phys. Rev. A* 93 (1 Jan. 2016), p. 010501. DOI: 10.1103/PhysRevA.93.010501 (cit. on pp. 140–142, 149).

[104] Thomas Zanon-Willette et al. "Composite laser-pulses spectroscopy for high-accuracy optical clocks: a review of recent progress and perspectives". In: *Reports on Progress in Physics* 81.9 (Aug. 2018), p. 094401. DOI: 10.1088/1361-6633/aac9e9 (cit. on p. 140).

[105] Christian Sanner et al. “Autobalanced Ramsey Spectroscopy”. In: *Phys. Rev. Lett.* 120 (5 Jan. 2018), p. 053602. DOI: 10.1103/PhysRevLett.120.053602 (cit. on p. 140).

[106] V. I. Yudin et al. “Generalized Autobalanced Ramsey Spectroscopy of Clock Transitions”. In: *Phys. Rev. Appl.* 9 (5 May 2018), p. 054034. DOI: 10.1103/PhysRevApplied.9.054034 (cit. on p. 140).

[107] V I Yudin et al. “Combined error signal in Ramsey spectroscopy of clock transitions”. In: *New Journal of Physics* 20.12 (Dec. 2018), p. 123016. DOI: 10.1088/1367-2630/aaf47c (cit. on p. 140).

[108] A V Taichenachev et al. “Compensation of field-induced frequency shifts in Ramsey spectroscopy of optical clock transitions”. en. In: *JETP Lett.* 90.11 (Feb. 2010), pp. 713–717 (cit. on p. 141).

[109] T. Zelevinsky et al. “Narrow Line Photoassociation in an Optical Lattice”. In: *Phys. Rev. Lett.* 96 (20 May 2006), p. 203201. DOI: 10.1103/PhysRevLett.96.203201 (cit. on pp. 143, 144).

[110] V.I. Yudin et al. “Auto-Compensation of Collisional Shift in Atomic Clocks Based on Bosonic Atoms in an Optical Lattice”. In: (2021), pp. 1–2. DOI: 10.1109/EFTF/IFCS52194.2021.9604346 (cit. on p. 144).

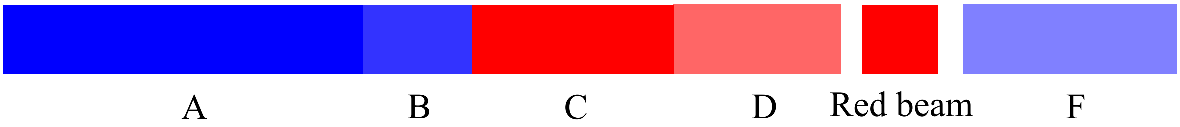

Figure A.1: The timing sequence of detecting ${}^1S_0 \leftrightarrow {}^3P_1$ transition. From phase A to D, atoms are cooled down and loaded into the optical lattice. Then, a red beam that is on resonance with the ${}^1S_0 \leftrightarrow {}^3P_1$ transition is delivered into the lattice. Detection phase F is applied, which follows the red beam to detect the remaining atoms in the lattice. More details of phase A to D and F in Figure 3.21.

Appendix A The compensation of the perpendicular background magnetic field

To compensate for the background magnetic field $\overrightarrow{B}_\perp$ which is perpendicular to the quantization axis as shown in Figure 5.2, I used the ${}^1S_0 \leftrightarrow {}^3P_1$ transition to monitor the magnetic field and apply three orthogonal pairs of coils with a Helmholtz configuration to create a compensating magnetic field. First, the atoms are slowed down, cooled, and trapped in the MOT, then loaded into the optical lattice. Then, a red beam that is in resonance with the ${}^1S_0 \leftrightarrow {}^3P_1$ transition is delivered into the lattice. The atoms in the lattice are kicked out of the lattice by the resonant laser. After that, the detection pulse addressing the ${}^1S_0 \leftrightarrow {}^1P_1$ transition is applied to detect the remaining atoms in the lattice. Figure A.1 shows the timing sequence.

Figure A.2 shows the remaining atoms in the optical lattice after using the red beam. There are two drops that correspond to ${}^1S_0 \leftrightarrow {}^3P_1, m_J = \pm 1$ transitions. Based on the ${}^1S_0 \leftrightarrow {}^3P_1$ transition signals, I can easily estimate the magnetic field and then apply the compensation field created by three pairs of Helmholtz coils to compensate the background field to ~ 0. Figure A.3 shows the spectra of ${}^1S_0 \leftrightarrow {}^3P_1$ transition with the gradually increasing compensation magnetic field (Figure A.3a-c). In the end, the background field is compensated to approximately zero, and the two transition lines are overlapped (Figure A.3c).

To evaluate the residual background field, I modeled the line shape as the sum of two Lorentzian components with negative signs (dips) to fit the experimental data:

$$\widetilde{N}(\nu) = 1 - \frac{A\gamma_1^2}{(\nu-\nu_0)^2+\gamma_1^2} - \frac{A\gamma_2^2}{(\nu-\nu_0-\Delta\nu)^2+\gamma_2^2} \tag{A.1}$$

where $\widetilde{N}(\nu)$ is the fractional atom number remaining in the lattice after using the red beam; ν_0 is the center frequency of one transition line and $\Delta\nu$ is the center frequency separation

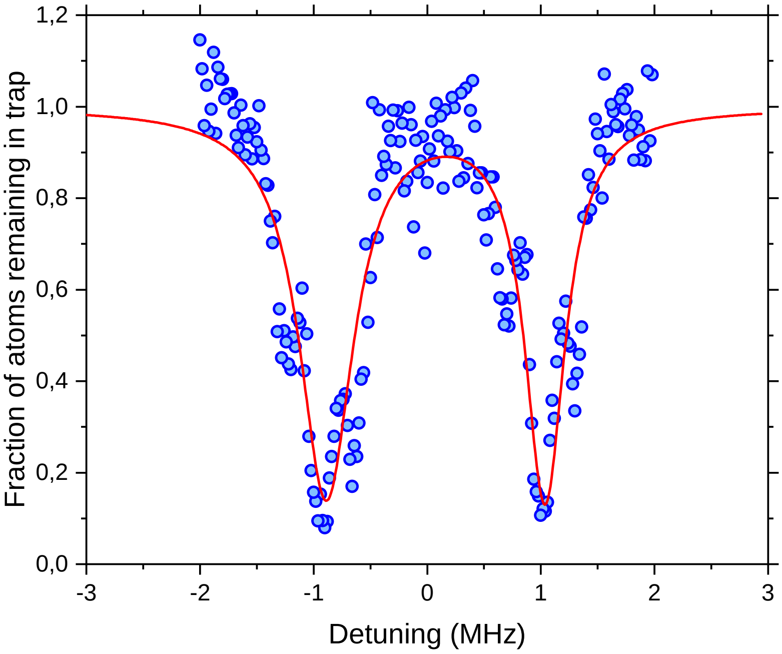

Figure A.2: The remaining atoms in the optical lattice after using the red beam. Two main drops correspond to $^1S_0 \leftrightarrow {}^3P_1, m_J = \pm 1$ transitions. The blue dots are experimental data, while the red curve is a fit of Eq. A.1 to the data.

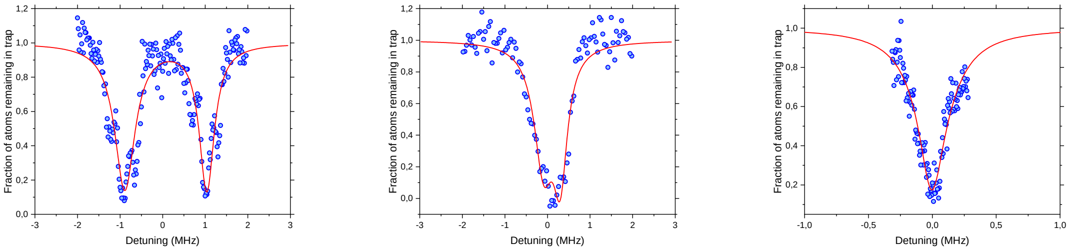

(a)

(b)

(c)

Figure A.3: The spectra of $^1S_0 \leftrightarrow {}^3P_1$ transition with the gradually increasing compensation magnetic fields, from (a) to (c). The blue dots are experimental data, while the red curves are fits of Eq. A.1 to the data. (a) is the same plot with Figure A.2.

Parameters	Figure A.3a	Figure A.3b	Figure A.3c
The height A	0.85(3)	0.76(4)	0.41(1)
The center frequency ν_0 (MHz)	-0.89(1)	-0.09(2)	-0.01(1)
FWHM/2 γ_1 (MHz)	0.29(2)	0.28(3)	0.21(2)
FWHM/2 γ_2 (MHz)	0.22(1)	0.20(3)	0.10(2)
The frequency separation $\Delta\nu$ (MHz)	1.925(16)	0.390(21)	0.018(22)

Table 1: The fitted results of the spectra in Figure A.3. FWHM is the full width at half maximum. After the background magnetic field compensation, the frequency separation is 0.018(22) MHz, shown in Figure A.3c, corresponding to 0.43 µT of residual magnetic field.

of the two transition lines; A is the height at $\nu = \nu_0$; γ_1 and γ_2 are half of the full width at half maximum (FWHM) of two transition lines, respectively. The fitted parameters are listed in Table 1. After the background magnetic field compensation, the frequency separation is 0.018(22) Hz, shown in Figure A.3c. The Zeeman splitting coefficient between $^1S_0 \leftrightarrow {}^3P_1, m_J = \pm 1$ transitions can be theoretically calculated, which is 4.2 kHz/mG. Thus, the residual magnetic field is 0.43 µT after compensation. According to magnetic-field-induced spectroscopy [65], the quadratic Zeeman shift coefficient of the clock transition is -23.3 MHz/T^2. Therefore, the quadratic Zeeman shift due to the residual magnetic field is -4(17) µHz, corresponding to $-9(40) \times 10^{-20}$ in fractional units. Compared to the quadratic Zeeman shift due to the bias magnetic field ($\sim -1477.4(52) \times 10^{-17}$), shown in Section 5.2, this contribution from residual perpendicular magnetic field is negligible.

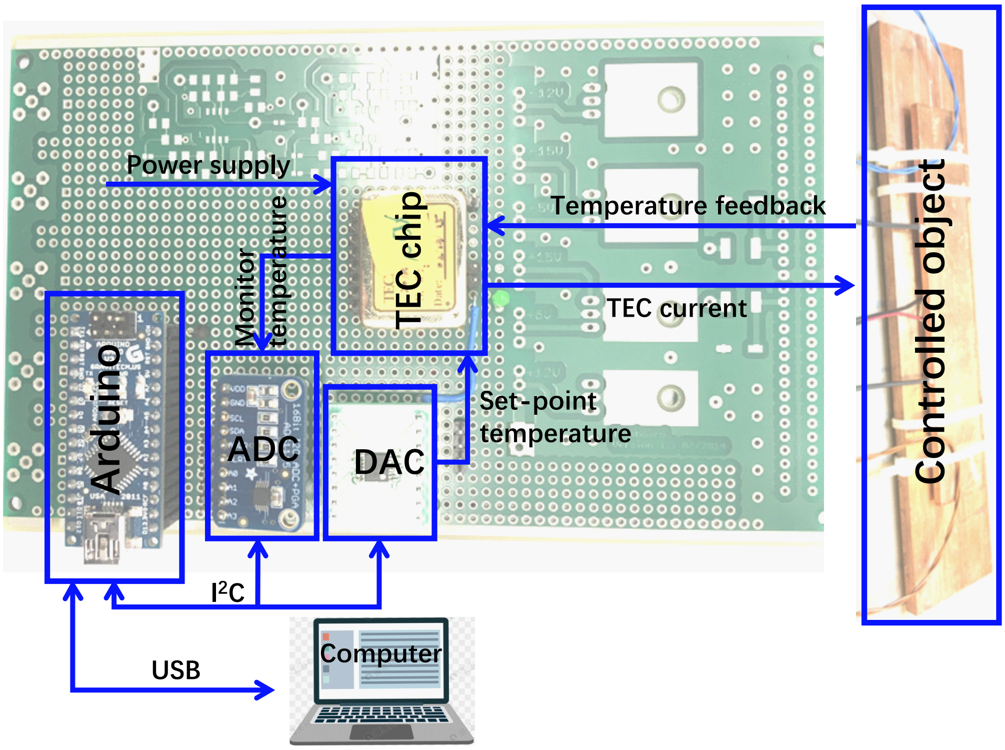

Figure B.1: The test board for a single TEC chip. An Arduino sends the set-point temperature to the TEC chip and receives the actual temperature via DAC and ADC, respectively. The TEC chip reads the temperature from the thermistor on the controlled object and compares the setpoint with the actual temperature to modulate the current to the Peltier element, which is located between two copper plates (controlled object). The communication between Arduino and ADC/DAC is through the I^{2}C protocol. The Python code is uploaded to the Arduino via USB. TEC: thermoelectric cooling element; ADC: analog-to-digital converter; DAC: digital-to-analog converter.

Appendix B Test and debug of the temperature controller of the science chamber

In order to test the TEC chips and the Arduino program, I built a test board in which the two copper plates are used as controlled object, shown in Figure B.1. The Arduino sends the set-point temperature to the TEC chip and receives the actual temperature via DAC and ADC, respectively, through the I^{2}C protocol. TEC chip reads the temperature from the thermistor on the controlled object and compares it to the setpoint. The difference between the desired temperature and the setpoint is used to modulate the current to the Peltier element, which is located between the two copper plates. A computer communicates with the Arduino via USB to upload the Python program and to read out the data from the Arduino and display the monitored temperature. The overall photo and schematics of the

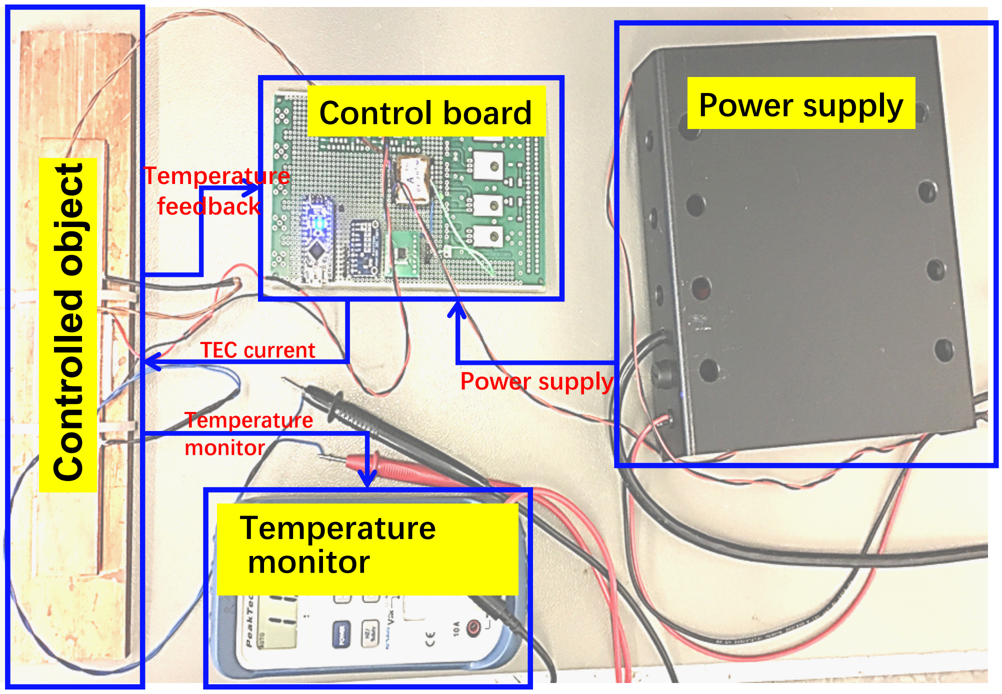

Figure B.2: Photo and schematics of the test system. To simplify the system, the computer is not shown here. A multimeter is applied to monitor the out-of-loop temperature of the controlled object. Power supply with eight-channel outputs is located on the right side of the photo. The details of the control board is illustrated in Figure B.1.

test system are shown in Figure B.2. In addition to the components shown in Figure B.1, a multimeter is applied to monitor the out-of-loop temperature of the controlled object. A power supply with eight-channel outputs is located on the right side of the photo.

After testing each TEC chip and software, I used the controller for the science chamber to replace the test board to debug the printed circuit board (PCB), shown in Figure B.3, and test the controller channel by channel. I found many mistakes in the PCB board and corrected them by adding wires, changing resistors and capacitors, etc. Figure B.4 shows more details of the modifications after debugging. After ensuring that all eight channels work well, I integrated the controller into our setup to control the temperature of the science chamber.

In the end, the temperature gradient of the science chamber is approximately 220 mK around the average temperature 294.65 K, with continuous monitoring of the temperature for 55 hours. The resulting BBR shift is 4.929×10^{-15} corresponding fractional frequency uncertainty of 4×10^{-18}. More details can be found in Chapter 6.

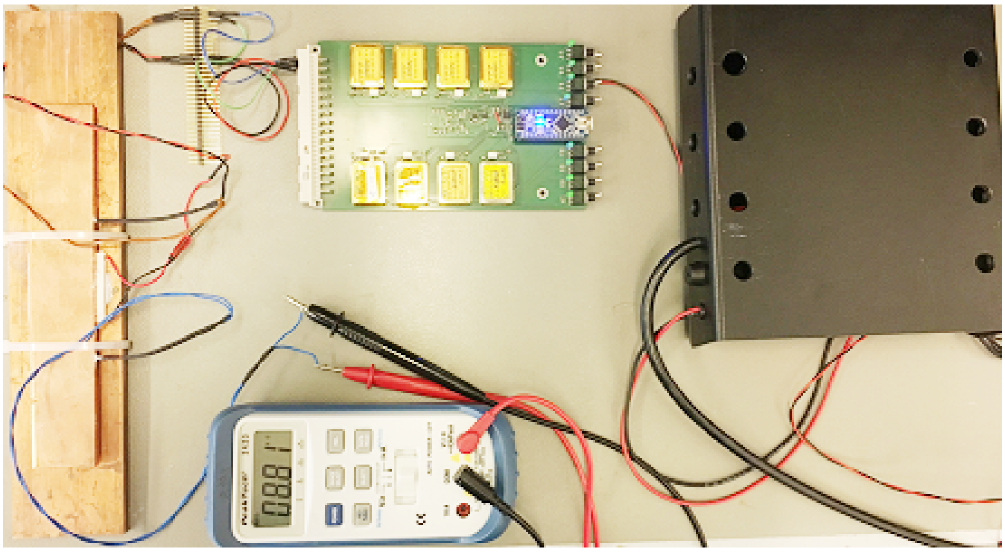

Figure B.3: Photo of the temperature controller of the science chamber under testing. Here the controller replaces the test board and the other components are kept the same as in Figure B.2.

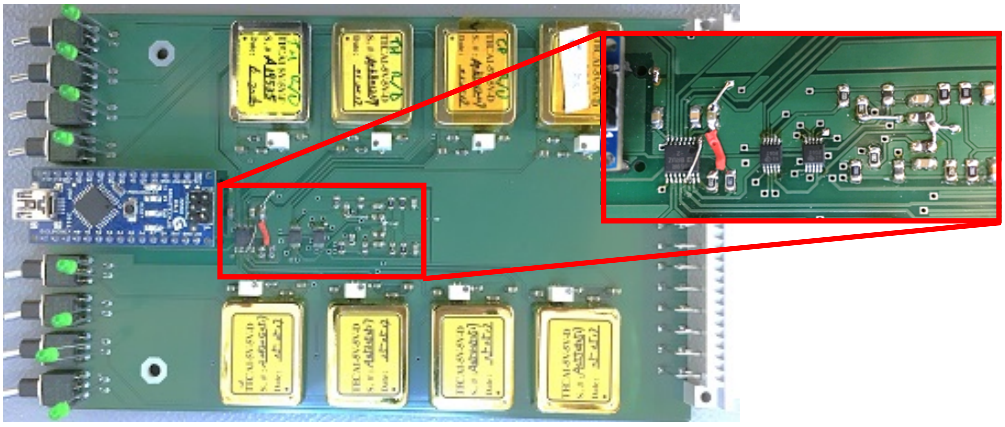

(a) The top side.

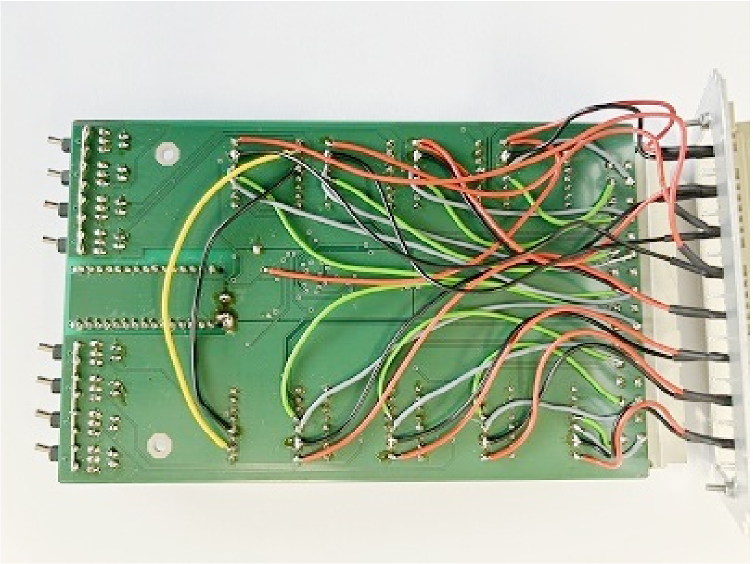

(b) The bottom side.

Figure B.4: The printed circuit board (PCB) of the temperature controller of the science chamber after debugging the errors. The insert of (a) shows the details of the modification of the PCB top side.

ACKNOWLEDGEMENTS

Writing this dissertation has been a journey made possible by the incredible support of so many people, and I'm deeply grateful to each of you.

First and foremost, I owe my deepest thanks to my supervisor, Prof. Stephan Schiller, for believing in me, guiding me through this project, and sharing your patience and encouragement—especially during the toughest moments. I'm especially thankful to Prof. Axel Görlitz for kindly agreeing to be my thesis reviewer—your perspective meant a great deal.

To the SOC2 team: I'm truly grateful to Pramod Mysore Srinivas for collaborating on the clock development, René Oswald for the software development and his meticulous feedback on my manuscript and endless patience, and Chang Jian Kwong, Victor Vogt, Dr. Eugen Wiens and Dr. Michael Hansen for your insightful discussions and unwavering help. Special thanks to Victor Vogt for his invaluable assistance with the dissertation defence and publication processes.

Thank you to Ulrich Rosowski and Dmitri Iwaschko for your expert support with electronic hardware, and to Beate Rödding for handling administrative tasks with such efficiency. To all other members of the Institute for Experimental Physics for their supports and contributions to SOC2 project.

To the colleagues in Department 4.3 at PTB: Your camaraderie and support made this journey not just possible, but joyful. I couldn't have finished without you.

My sincere thanks to: Dr. Christian Lisdat for your brilliant insights during group meetings; Dr. Uwe Sterr for your inspiring discussions and invaluable advice; Dr. Sören Dörscher for always being there to discuss ideas—especially for hosting the wonderful Ask-a-Post-Doc sessions where I could ask all my "naive" questions! Dr. Sofia Herbers for co-organizing the APD meetings and helping with optical cavity locking; Dr. Ingo Nosske for your exceptional support—both professionally and personally, and for your thoughtful feedback on my manuscript; Dr. Roman Schwarz, Dr. Chetan Vishwakarma, Tim Lücke, Joshua Klose, and Kilian Stahl for your thoughtful discussions and suggestions; Andre Uhde, Mandy Rindermann, Ali Alkasabra, Klemens Budin, Andreas Koczwara, and Mattias Misera for providing essential mechanical and electronic components; Dr. Chun Yu Ma, Dr. Jialiang Yu, Jingxian Ji, and Dr. Suo Zhang (Menlo Systems), Mona Kempkes for your helpful suggestions and conversations; Ute Krüger for dealing administrative issues with such efficiency; all other members of Department 4.3 for their supports and contributions to SOC2 project.

A special thank you to Dr. Erik Benkler for operating the frequency comb, and to the Yb team (PTB, Department 4.4)—Dr. Nils Huntemann, Melina Filzinger, and Martin Steinel—for their work on the Yb ion clock. I'm also grateful to the In team (PTB, QUEST Institute)—Prof. Tanja Mehlstäubler, Dr. Jonas Keller, Dr. Hartmut Hausser, and Ingrid Maria Richter—for their expertise with the In ion clock.

Finally, to my family: Thank you for your unconditional love, endless encouragement, and for being my anchor through every challenge. This milestone is as much yours as it is mine.

This journey wouldn't have been possible without you all. I'm so grateful.